Abstract

This thesis raises the concept of aggregated Structural Health Monitoring (SHM). Such systems exploit heterogeneous sensing techniques (e.g. dynamic, static, chemical, environmental) to attain both global and local damage detection capabilities. As examples of particularly proficient approaches, modal analysis and seismic interferometric methods are investigated in this thesis as two complementary techniques offering both global and local damage identification. This materializes into dense sets of time series from which miscellaneous damage-sensitive features can be extracted. On this basis, physics-informed digital twins are investigated to translate the extracted feature maps into local model parameters reflecting the actual health condition of the physical asset. In particular, research efforts focus on the use of computationally efficient surrogate models to bypass high-fidelity numerical models. In this light, the optimization problem derived from the inverse model calibration (model updating) can be conducted in real- or quasi-real time. Time series of model parameters can be thus continuously extracted and used to complement the experimental data, hence providing a comprehensive image of the health condition of the asset. Finally, the damage assessment problem is solved through a statistical pattern recognition framework. The developed methodology is materialized in two software suites for an easy technological transfer. When installed on an instrumented structure, the software autonomously interrogates the health condition of the asset by fusing arbitrary combinations of damage-sensitive features through quality control charts. The effectiveness of the developed methodology is demonstrated in a number of real-world in-operation civil engineering structures. Thereby, this thesis and the developed techniques are envisaged to represent disruptive tools for infrastructure managers to enable the extensive implementation of SHM methods into complete infrastructural systems.

October 2022

Online damage identification of structures via continuous in-operation ambient vibration monitoring

Author: E. García-Macías; Tutor: F. Ubertini; Int. tutor: A. E. Martínez-Castro

University of Perugia
Department of Civil and Environmental Engineering

INTERNATIONAL DOCTORAL PROGRAM
IN CIVIL AND ENVIRONMENTAL ENGINEERING

PhD thesis
XXXV cycle

Online damage identification of structures via continuous in-operation ambient vibration monitoring

PhD Candidate
Enrique García-Macías

Tutor
Filippo Ubertini

International Tutor
Alejandro E. Martínez-Castro

University of Perugia
Department of Civil and Eviromental Engineering

INTERNATIONAL DOCTORAL PROGRAM

IN CIVIL AND ENVIRONMENTAL ENGINEERING

PhD thesis
XXXV cycle

Online damage identification of structures via continuous in-operation ambient vibration monitoring

PhD Candidate
Enrique García-Macías

Tutor
Filippo Ubertini

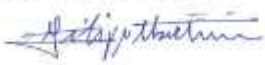

International Tutor
Alejandro E. Martínez-Castro

unipg
DIPARTIMENTO DI INGEGNERIA CIVILE E AMBIENTALE
DIPARTIMENTO DI ECCELLENZA

UNIVERSIDAD DE GRANADA

International Faculty Board

PhD Coordinator

Prof. Filippo Ubertini

Italian members

Belardi Paolo
Bianconi Fabio
Brunone Bruno
Breccolotti Marco
Cavalagli Nicola
Cerni Gianluca
Cluni Federico
Falcinelli Stefano
Ferrante Marco
Flammini Alessia
Formisano Antonio
Fornaciari Da Passano
Gigliotti Giovanni
Gioffrè Massimiliano
Giorgi Giacomo
Gusella Vittorio
Kenny Jose Maria
Manciola Piergiorgio
Materazzi A. Luigi
Meniconi Silvia
Menchetelli Valeria
Mochi Giovanni
Morbidelli Renato
Orlandi Fabio
Pezzolla Daniela
Puglia Debora
Salciarini Diana
Saltalippi Carla
Terenzi Benedetta
Torre Luigi
Valentini Luca
Venanzi Ilaria
Ventura Flaminia

International members

Arwade Sanjay
Caracoglia Luca
Covas Didia
Denoël Vincent
Glisic Branko
Grigoriu Mircea
Halevi Yoram
Laflamme Simon
Rodríguez-Tembleque Luis
Sáez Andrés
Sritharan Sri

Funding: Part of this thesis was supported by the Italian Ministry of Education, University and Research (MIUR) through the funded Project of Relevant National Interest "DETECT-AGING - Degradation effects on structural safety of cultural heritage constructions through simulation and health monitoring" (protocol no. 201747Y73L). The financial support and access to the monitoring data of the Trigno Bridge by Anas S.p.A are gratefully acknowledged.

Data Availability Statement: The scientific results of this thesis have been disseminated through peer-reviewed scientific articles, data repositories, and social media.

• Peer-reviewed publications:

☐ García-Macías, E., Kita, A., & Ubertini, F. (2020). Synergistic application of operational modal analysis and ambient noise deconvolution interferometry for structural and damage identification in historic masonry structures: three case studies of Italian architectural heritage. Structural Health Monitoring, 19(4), 1250-1272. DOI: 10.1177/1475921719881450

☐ García-Macías, E., & Ubertini, F. (2020). MOVA/MOSS: Two integrated software solutions for comprehensive Structural Health Monitoring of structures. Mechanical Systems and Signal Processing, 143, 106830. DOI: 10.1016/j.ymssp.2020.106830

☐ García-Macías, E., & Ubertini, F. (2020). Automated operational modal analysis and ambient noise deconvolution interferometry for the full structural identification of historic towers: A case study of the Sciri Tower in Perugia, Italy. Engineering Structures, 215, 110615. DOI: 10.1016/j.engstruct.2020.110615

☐ García-Macías, E., Venanzi, I., & Ubertini, F. (2020). Metamodel-based pattern recognition approach for real-time identification of earthquake-induced damage in historic masonry structures. Automation in Construction, 120, 103389. DOI: 10.1016/j.autcon.2020.103389

☐ García-Macías, E., Ierimonti, L., Venanzi, I., & Ubertini, F. (2021). An innovative methodology for online surrogate-based model updating of historic buildings using monitoring data. International Journal of Architectural Heritage, 15(1), 92-112. DOI: 10.1080/15583058.2019.1668495

☐ García-Macías, E., & Ubertini, F. (2021). Structural assessment of bridges through ambient noise deconvolution interferometry: application to the lateral dynamic behaviour of a RC multi-span viaduct. Archives of Civil and Mechanical Engineering, 21(3), 1-20. DOI: 10.1007/s43452-021-00273-9

☐ Giglioni, V., García-Macías, E., Venanzi, I., Ierimonti, L., & Ubertini, F. (2021). The use of receiver operating characteristic curves and precision-versus-recall curves as performance metrics in unsupervised structural damage classification under changing environment. Engineering Structures, 246, 113029. DOI: 10.1016/j.engstruct.2021.113029

☐ Ierimonti, L., Cavalagli, N., Venanzi, I., García-Macías, E., & Ubertini, F. (2021). A transfer Bayesian learning methodology for structural health monitoring of monumental structures. Engineering Structures, 247, 113089. DOI: 10.1016/j.engstruct.2021.113089

☐ García-Macías, E., & Ubertini, F. (2022). Least Angle Regression for early-stage identification of earthquake-induced damage in a monumental masonry palace: Palazzo dei Consoli. Engineering Structures, 259, 114119. DOI: 10.1016/j.engstruct.2022.114119

☐ García-Macías, E., & Ubertini, F. (2022). Real-time Bayesian damage identification enabled by sparse PCE-Kriging meta-modelling for continuous SHM of large-scale civil engineering structures. Journal of Building Engineering, 105004. DOI: 10.1016/j.jobe.2022.105004

• Under review peer-reviewed publications:

☐ García-Macías, E., Ruccolo, A., Angelo Zanini, M., Pellegrino, C., Gentile, C., Ubertini, F., & Mannella, P. P3P – A software suite for autonomous SHM of bridge networks. Journal of Civil Structural Health Monitoring, 2022.

☐ García-Macías, E., Hernández-González, I. A., Puertas, E., Gallego, R., Castro-Triguero, R., & Ubertini, F. Digital twin for vibration-based damage identification of a 13th-century rammed earth tower in the Alhambra monumental complex in Granada, Spain. International Journal of Architectural Heritage, 2022.

• Book chapters:

☐ García-Macías, E., & Ubertini, F. (2022). Integrated SHM Systems: Damage Detection Through Unsupervised Learning and Data Fusion. In Structural Health Monitoring Based on Data Science Techniques (pp. 247-268). Springer, Cham.

• Data bases:

☐ Mendeley data: DOI: 10.17632/d25khz772v.4

☐ Website of the Laboratory of Structural Health Monitoring and Earthquake Engineering: https://shmlab.weebly.com

☐ GitHub repository: https://github.com/EnriqueGarMac?tab=repositories

☐ Personal website: https://enriquegarma.com

• Social Media:

☐ ResearchGate Profile:
https://www.researchgate.net/profile/Enrique-Garcia-Macias

☐ Youtube Channel:
https://www.youtube.com/channel/UCDmxeWIk0IOiEz_wEtX8jzQ

Acknowledgments: Foremost, I would like to express my deep gratitude to Ubertini's research group in general, and to Prof. Ubertini in particular, for the great opportunity of developing my academic career at the University of Perugia. It would be a tremendous challenge to express in words the innumerable lessons learned during the last three years, not only from a scientific point of view, but also from a human perspective. I carry with me a sincere appreciation for the outstanding generosity and the enthusiasm of Prof. Ubertini, which have irrevocably contributed to convert these years of intense work into a continuous and exciting quest for scientific excellence and personal development. I would also like to acknowledge the unconditional support of my international tutor, Alejandro E. Martínez-Castro, who has been and will always be a reference of rigor and professionalism. Finally, I would like to express the great honor and blessing of having formed part of the University of Perugia, an institution (and a city) that will undoubtedly represent a fundamental landmark in my future academic endeavors. Last but not least, I would like to give a special thanks to my family and friends for their unconditional support and affection. I would like to especially mention my beloved parents, Concepción and Jorge, to whom I owe everything and who have always offered their unconditional support. Finally, a especial thanks is dedicated to Sabrina for her endless patience, love and support.

Contents

1. Introduction

1.1. Abstract

This thesis raises the concept of aggregated Structural Health Monitoring (SHM). Such systems exploit heterogeneous sensing techniques (e.g. dynamic, static, chemical, environmental) to attain both global and local damage detection capabilities. As examples of particularly proficient techniques, modal identification and seismic interferometric methods are investigated in this thesis as two complementary techniques offering both global and local damage identification. This materializes into dense sets of time series from which miscellaneous damage-sensitive features can be extracted. On this basis, physics-informed digital twins are investigated to translate the extracted feature map into local model parameters reflecting the actual health condition of the physical asset. In particular, research efforts focus on the use of computationally efficient surrogate models to bypass high-fidelity numerical models. In this light, the optimization problem derived from the inverse calibration of the model (model updating) can be conducted in real- or quasi-real time. Time series of model parameters can be thus continuously extracted and used to complement the experimental data, hence providing a comprehensive image of the health condition of the asset. Finally, the damage assessment problem is solved through a statistical pattern recognition framework. The developed methodology is materialized in two software suites for an easy technological transfer. When installed on an instrumented structure, the software autonomously interrogates the health condition of the asset by fusing arbitrary combinations of damage-sensitive features through quality control charts. The effectiveness of the developed methodology is demonstrated in a number of real-world in-operation civil engineering structures. Thereby, this thesis and the developed techniques are envisaged to

represent disruptive tools for infrastructure managers to enable the extensive implementation of SHM techniques into complete infrastructural systems.

1.2.State of the Art and Motivation

The management of aging infrastructures represents one of the most pressing challenges of Structural Engineering. Recent tragic collapses like the I-35 W Mississippi river in 2007 or the Genoa bridge in 2018 (Fig. 1.1) have revealed the fundamental challenge posed by aging civil infrastructure and the need to prioritize its management in the political agenda. Nevertheless, the urging need to tackle such a serious challenge had been widely exposed by the scientific community in the last decades. Indeed, a sizable proportion of European civil infrastructures were built during the economic growth of the 1930s, thus they are currently approaching their design service life. A remarkable evidence of this is the last Infrastructure Report Card recently released in 2021 by the American Society of Civil Engineers (ASCE) [1], which detected that 7.5% of the more than 600,000 American highway bridges are in poor conditions and estimated the nation's backlog of bridge repair at $123 billion. The EU-funded BRIME project [2] in 2001 revealed a similar picture across the European highway bridges, with deficiency rates among the surveyed countries ranging between 26 and 39%. This circumstance explains the increasing rates of bridge collapses registered in the last decades (Fig. 1.2 (a)), with many structures failing with ages even below 50 years (Fig. 1.2 (b)).

The daunting challenge of aging infrastructures has promoted a vast volume of research on SHM. While the first works date back to the 80s, the field of SHM has experienced an outstanding boost in recent years with a number of scientific articles that has multiplied by 50 in the last two decades (see Fig. 1.2 (c)). Fundamental research has been also accompanied by important R&D actions in diverse areas of sensing, analytics, communication and computing technologies, making the market volume related to SHM experience a steady increase in the last years with forecasts of increases of 5 times the volume of 2015 by 2025 (see Fig. 1.2 (d)). Such a considerable research and technology effort has materialized in the publication of a multitude of technical standards of SHM worldwide [3]. These comprise from the first SHM guide in 2001 by the ISIS Canada Research Network [4], until the last guidelines of the monitoring of viaducts published by the Italian Ministry of Infrastructure and Transport [5]. There is also a growing awareness on the limitations of classical periodic bridge maintenance policies based on visual inspections to provide efficient assessment of early-stage pathologies. It is worth noting the survey report published by the US Department of Transportation in 2001 [6], which concluded that inspection reports may considerably differ depending on the lighting conditions, fear of traffic, and experience of the inspectors. In this light, condition-based maintenance strategies within the framework of SHM constitute a powerful alternative. Through permanent monitoring and suitable damage detection tools, rehabili-

tation tasks can be scheduled according to the real-time condition of structures, thereby minimizing the number of inspections, reducing service disruptions, and anticipating the appearance of risky pathologies that may eventually lead to the collapse of the structure (e.g. those in Fig. 1.1).

Fig. 1.1: Catastrophic failures of the I-35 W Mississippi river in 2007 (constructed between 1964 and 1967 in Minneapolis, Minnesota, US) (source: [7]) (a) and the Morandi Bridge in 2018 (constructed between 1963 and 1967 in Genoa, Italy) (source: EFE agency).

Vibration-based SHM systems have become specially popular owing to their effectiveness for non-destructive global damage detection and minimum intrusiveness [8]. Such systems rely on the identification of the modal features (i.e. resonant frequencies, damping ratios, and mode shapes), which depend upon the intrinsic stiffness and energy dissipation mechanisms of structures. Therefore, the appearance of damage affecting the overall stiffness of structures can be detected by means of variations in the modal properties. In this line, monitoring systems based on Output-only or Operational Modal Analysis (OMA) are specially engaging. These rely on the assessment of ambient vibrations without the need of any artificial excitement source, thereby the monitoring can be performed in operative conditions without interfering with the normal functioning of structures [9]. Such systems are notably well-suited for cultural heritage structures, where monitoring must not only ensure that safety needs are met, but also they must respect the architectural value of the structure. In this light, numerous successful applications can be found in manifold structural typologies, such as bridges [10], dams [11], wind turbines [12], and historic constructions [13].

Despite the large research efforts made in the field, the routine implementation of SHM is marginal and classical periodic bridge maintenance policies remains being extensively adopted [15]. Among the reasons explaining the slow technological transfer of SHM to industry, it is worth stressing the lack of stan-

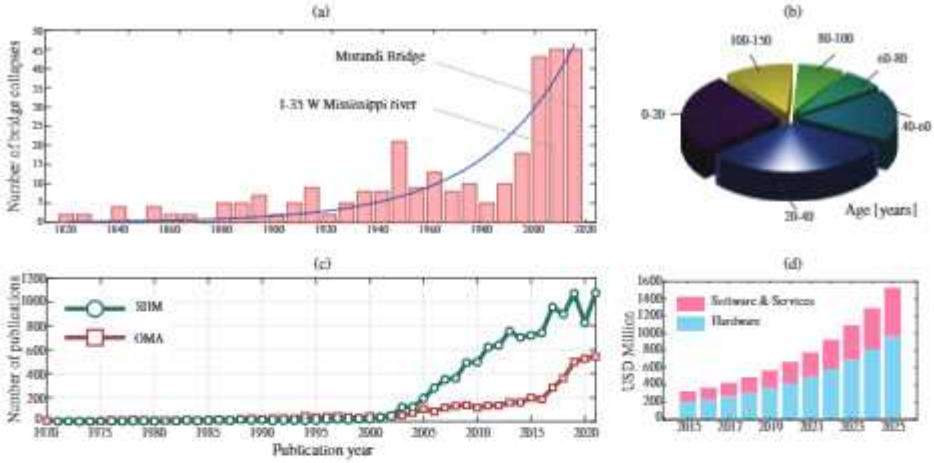

Fig. 1.2: Number of catastrophic collapses of bridges (a), and age at failure (b) (source: [14]). Number of published research works containing the keywords SHM and OMA (c) (source: Scopus), and SHM market size (d) (source: Grand View Research Inc.).

dardized solutions for continuous data processing and automated data-driven decision-making, important initial investments on monitoring equipment, data management, as well as the assistance of highly qualified specialized professionals and in-house software platforms. Specifically, the key limitations hampering the technological transfer of SHM include:

- Difficult automation of damage detection algorithms. Damage detection using vibration-based SHM is usually performed by tracking the time series of certain statistical distances of the resonant frequencies with respect to a baseline undamaged condition. Such distances are plotted in a control chart along with a user-defined threshold indicating some statistical confidence level. In this way, damage detection reduces to a two-class classification problem (i.e. Undamaged or Damaged). This leads to elevated false alarm rates and requires the assistance of highly qualified operators.

- Limited effectiveness at detecting local pathologies. While vibration-based SHM systems are proficient for detecting global defects, local damage sources with minimum impact on the overall stiffness of structures are hardly identifiable. A wide variety of local deterioration processes can be found in common practice, such as, among others, chemical (e.g. carbonation, chloride penetration, sulphate attacks, freezing/thawing deterioration, etc.) and electrochemical (corrosion) attacks. Such phenomena are more effectively detected by non-vibration non-destructive testing techniques (e.g. static monitoring, electrical resistivity measurements, acous-

tic emission, etc.).

- Troublesome application for damage localization. The applicability of vibration-based SHM systems often limit to damage detection. Higher levels in the damage identification problem such as localization typically imply the inverse calibration of a numerical model. In this line, some successful applications can be found in the literature on laboratory specimens and simple structures, although the continuous calibration of realistic 3D models for damage identification remains poorly explored. This is primarily due to the geometrical complexity and fine meshing demands of such models, whose large computational burdens preclude the application to online model identification.

1.3. Objectives, Methodology, and Organization of the thesis

In view of the previous state-of-the-art review, the main aim of this thesis is the development of novel solutions for *autonomous aggregated SHM* systems with superior damage detection and localization capabilities. The general concept of aggregated SHM raised in this thesis is sketched in Fig. 1.3. Such systems combine heterogeneous sensing technologies with digital twining techniques to achieve complete damage identification capabilities, that is detection, localization, and quantification. On one hand, the use of heterogeneous sensing techniques (e.g. dynamic, static, chemical, environmental) empowers the SHM system to detect both global and local structural pathologies. On the other hand, the adoption of physics-informed digital twins allows translating monitoring data into local parameters of the structure, hence providing the SHM system with damage localization and quantification capabilities. The outcome of such systems materializes in dense sets of time series involving manifold physical quantities of the structural response as well as local model parameters extracted by inverse calibration of the digital twin. The processing of such a dense set of time series provides a rich database of damage-sensitive features, offering a comprehensive image of the health condition of the physical asset. When introduced into a statistical pattern recognition framework, damage assessment can be conducted by exploiting multiple quality control charts assessing the appearance of anomalies in arbitrary combinations of features. The automation of the whole process constitutes a cornerstone in this thesis as an effort to systematize the implementation of aggregated SHM systems to diverse structural typologies with minimal intervention of expert judgment.

To achieve the global objective above, key elements in the design of the research plan of this thesis included: (i) to develop signal processing techniques capable of fusing monitoring data from heterogeneous sensing solutions to attain both global and local and damage detection capabilities; (ii) to automate the whole SHM process from data acquisition to damage identification; (iii) to develop model updating approaches compatible with real-time SHM; (iv) to

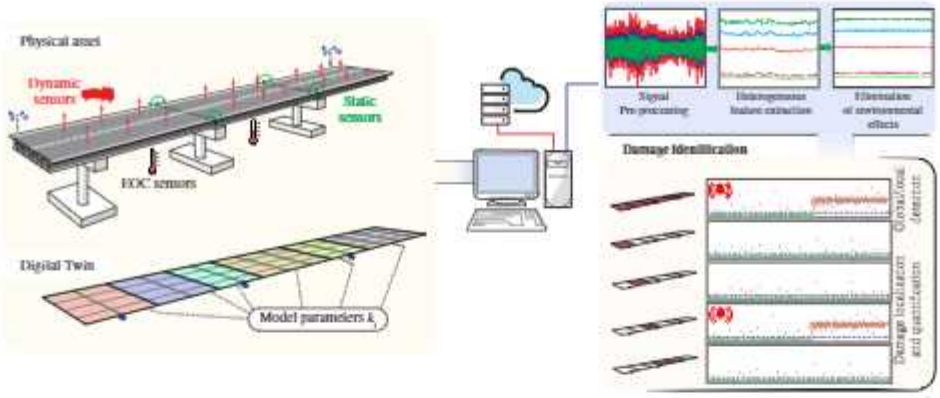

Fig. 1.3: Schematic representation of the concept of aggregated SHM.

validate the fundamental developments with data from real in-operation civil engineering structures; (v) to guarantee the technological transfer of the scientific achievements into a software platform. These key elements have been materialized in four strategic objectives (OB), namely:

- **OB-I**: Development of automated normalization (elimination of operational and environmental effects), pattern recognition and novelty analysis techniques for aggregated SHM systems. This involves the development of new software solutions for the development of autonomous SHM systems involving heterogeneous sensing techniques.

- **OB-II**: Development of new semi-supervised classification algorithms for multi damage detection of aggregated SHM systems. Through non-parametric clustering, efforts will be devoted to the development of automatic pattern recognition of multiple damage sensitive features. These include not only modal information, but also monitoring data from different sensing technologies.

- **OB-III**: Development of new data fusion techniques capable of performing pattern recognition of multiple long-term monitoring systems. Most efforts will be devoted to the identification/elimination of environmental/operational factors and automated non-parametric clustering for multi-damage detection of multiple damage sensitive features.

- **OB-IV**: Development of surrogate-based model updating approaches for automated online damage identification. Particularly framed on geometrically complex historic masonry structures, this objective is aimed at developing computationally efficient surrogate models for online calibration of intensive 3D numerical models, so attaining real-time damage localization and quantification capabilities.

The methodology has been designed to achieve a leading-edge technological transfer. This includes not only all the fundamental aspects involved in the previously listed objectives, but also their direct application on real infrastructures. Specifically, the research plan has been organized according to four work packages covering the previously stated objectives.

- **WP-I**: Software solutions for automated signal processing, data normalization, pattern recognition and novelty analysis. The code to be developed must allow the automatic analysis of multiple damage sensitive features and perform parallel novelty analyses.
- **WP-II**: Development of new techniques for automated elimination of environmental and operational effects from monitoring data. These techniques should allow to accommodate varying environmental regimes as well as incremental damage events.
- **WP-III**: New data fusion techniques to exploit multi-dimensional time series of monitoring data for pattern recognition and data normalization. In this framework, the use of ambient noise deconvolution interferometry (ANDI) is investigated as a complementary technique to OMA.
- **WP-IV**: Development of efficient meta-modeling techniques apt for real-time damage identification (detection, localization and quantification) of large-scale civil engineering structures.

1.4.Organization of the Thesis

The thesis is organized in seven main chapters covering the theoretical fundamentals and scientific results obtained in the pursuit of the aforementioned objectives. In general terms, the main goal of this thesis regards the development of next-generation aggregated SHM systems. In this context, four fundamental elements have been identified in this thesis as sketched in Fig. 1.4. These include the analysis of the SHM process as a statistical pattern recognition problem in Chapter 2, development of new automated OMA techniques in Chapter 3, use of ANDI as a complementary technique to OMA in Chapter 4, and finally, the development of digital twins compatible with real-time SHM in Chapter 5. The fundamental achievements obtained all throughout this thesis have been systematically incorporated in two software platforms, namely MOVA/MOSS and P3P as reported in Chapter 6. Finally, Chapter 7 presents the main conclusions of the thesis and presents the future perspectives of the investigation.

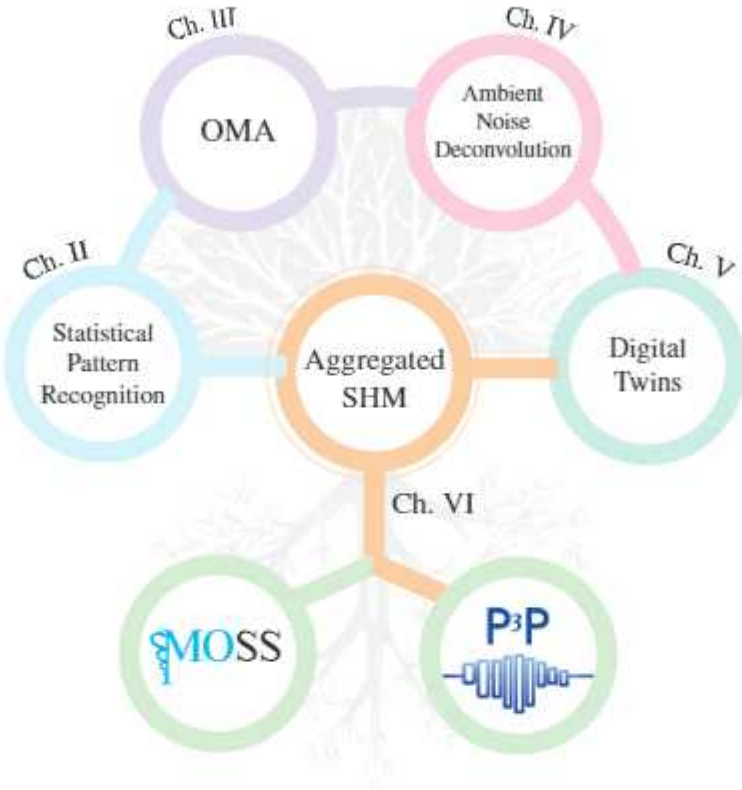

Fig. 1.4: Organization of the thesis.

1.5. Description of investigated case studies

As an effort to attain maximum technological transfer, an application case-oriented philosophy has been a fundamental cornerstone in the course of all the works conducted in this thesis. This has motivated the investigation of a considerable number of real in-operation civil engineering structures where the fundamental developments of this thesis have been tested and validated. In particular, these include three bridges, three historical towers, a basilica and a monumental palace. Table 1.1 summaries the investigated case studies and the conducted analyses. For the sake of readability and better organization of the remainder of this thesis, the architectural and structural description of the structures, as well as the implemented monitoring systems are presented in the following subsections.

Table 1.1: Investigated case studies.

Case study	Description	Location	SHM system	Conducted analyses
Z-24 Bridge (Section 1.5.1)	Post-tensioned concrete box girder bridge	Canton Bern (Switzerland)	Dynamic/Env.	OMA
San Pietro bell-tower (Section 1.5.2)	Historic masonry tower	Perugia (Italy)	Dynamic/Env.	OMA, ANDI
Santa Maria degli Angeli (Section 1.5.2)	Masonry basilica	Assisi (Italy)	Dynamic/Env.	OMA
Sciri Tower (Section 1.5.4)	Historic masonry tower	Perugia (Italy)	Dynamic/Env.	OMA, DT, ANDI
Consoli Palace (Section 1.5.5)	Historic masonry palace	Gubbio (Italy)	Dynamic/Static/Env.	OMA, DT, ANDI
Muhammad Tower (Section 1.5.6)	Historic rammed earth tower	Granada (Spain)	Dynamic/Env.	OMA, DT
Chiaravalle Bridge (Section 1.5.7)	Reinforced concrete multispan viaduct	Marche region (Italy)	Dynamic	OMA, ANDI
Trigno V Bridge (Section 1.5.8)	Concrete-girder highway bridge	Abruzos (Italy)	Dynamic	OMA

1.5.1.Z-24 Bridge

The Z-24 Bridge represents the most extensively investigated benchmark case study in the literature on SHM. Before demolition in 1998, the bridge was extensively instrumented and tested with the purpose of providing a benchmark case study for vibration-based SHM as reported for the first time by Peeters and De Roeck [16]. The Z-24 Bridge was a post-tensioned concrete box girder bridge composed of a main span of 30 m and two side-spans of 144 m, as depicted in Fig. 1.5 (a). A continuous monitoring system was installed in the bridge from November 11$^{\text{th}}$ 1997 until September 10$^{\text{th}}$ 1998. Artificially controlled damage was introduced in the bridge in the last month of operation. In particular, 14 different damage conditions were induced in the bridge, including different settlements, tilting of one of the piers, failure of anchor heads and rupture of tendons [17, 18]. The monitoring database is available to the scientific community by the structural mechanics section of KU Leuven. It includes 5556 computer files of ambient vibration records with 65536 samples ($\approx$ 11 min), acquired at a sampling rate of 100 Hz with a periodicity of 1 hour from November 10$^{\text{th}}$ 1997 until September 4$^{\text{th}}$ 1998. Accelerations were recorded by 8 sensors deployed on the bridge according to the layout in Fig. 1.5 (b). In addition, the database also includes records of environmental data, comprising temperature (46 channels), wind and humidity sensors at several locations. The structural mechanics section of KU Leuven is gratefully acknowledged for providing access to the Z24 Bridge data-set.

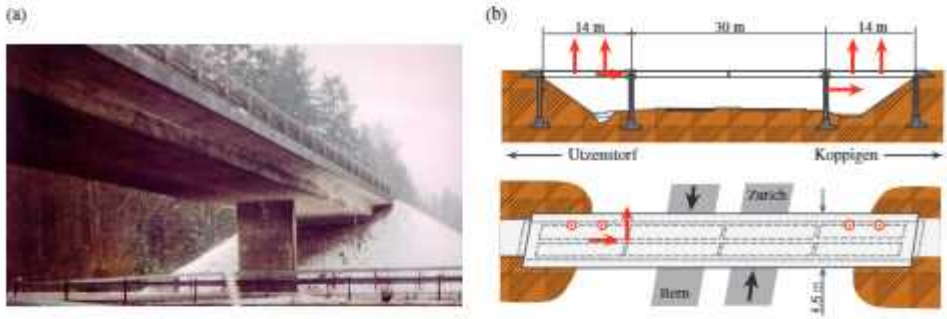

Fig. 1.5: General view of the Z-24 Bridge (a) and sensors layout (b).

1.5.2.San Pietro bell-tower

The bell-tower of the Basilica of San Pietro is located in the southern part of the city of Perugia, Italy (see Fig. 1.6 (c)). The construction of the monastery dates back to around 996, although the bell-tower was not erected until the 13^{th} century. The Benedictine abbey is an architectural ensemble arranged around three main cloisters, comprising the basilica, a convent and other more recent buildings. Over the centuries, the bell-tower has been subjected to several architectural alterations and restoration interventions. The current configuration dates back to the 15^{th} century, and the design is attributed to the architect Bernardo Rossellino. Three main structural portions can be identified in the tower, including the shaft, the belfry and the cusp. Firstly, the shaft stands 26 m high and has a dodecagonal cross-section. The bulk of the shaft is made of stone masonry with large external portions of brick masonry as a result of several rehabilitation operations. Rising up to a height of 40.8 m, an hexagonal belfry sits on top of the shaft. The belfry is made of brick masonry covered with an external curtain of stone, and large Gothic mullioned windows characterize its architecture. Finally, a brick masonry cusp completes the tower with a total height of 61.4 m. The bell-tower stands out between the basilica and other branches of the abbey, being its first 17 m restrained by the adjoining buildings. In 1997, the tower was severely damaged after the Umbria–Marche earthquake, so it was painstakingly restored and consolidated in 2001.

As reported by Ubertini *et al.* [19], the 2016 Central Italy seismic sequence produced moderate damage in the bell-tower with permanent variations in its modal properties. The seismic sequence consisted of the Accumoli M_w 6.0 earthquake of August 24^{th}, followed by the Ussita M_w 5.9 and Norcia M_w 6.5 earthquakes of October 26^{th} and 30^{th}, respectively. Albeit only small peak ground accelerations of 30 cm/s^2 were measured in the vicinity of the tower (85 km far from the epicentre of the first major shock), the OMA of acceleration records demonstrated accumulated permanent decays in the natural frequencies of the tower [19]. While no significant damages could be visually identified, the

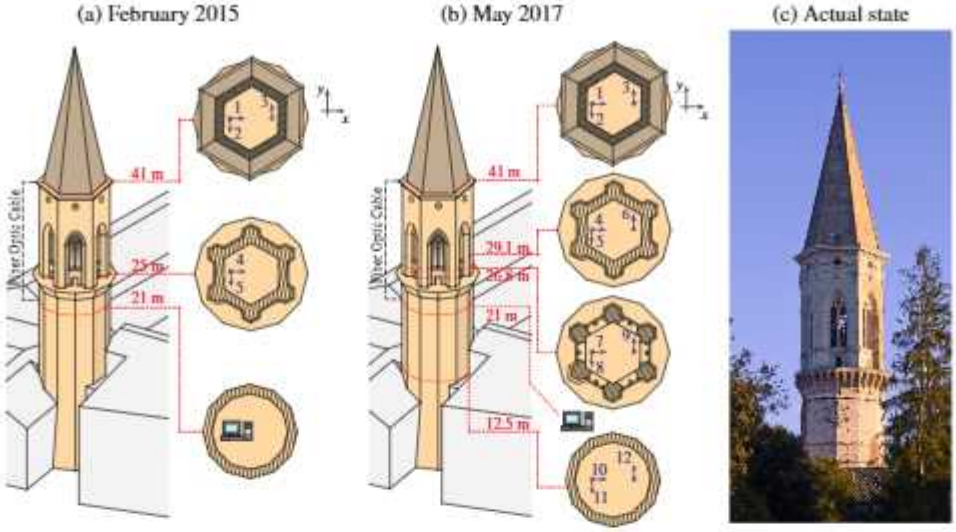

Fig. 1.6: Sketch of the AVT conducted in February 2015 (a), May 2017 (b), and view of the masonry bell-tower of the Basilica of San Pietro (c).

non-linear finite element simulations by Cavalagli *et al.* [20] corroborated the experimental results and reported the development of microcracks at the base of the columns of the belfry. In this light, this case study constitutes a remarkable example of the effectiveness of SHM for early-stage earthquake-induced damage detection.

The monitoring system comprises three high-sensitivity (10 V/g) accelerometers model PCB 393B12 installed at the base of the cusp (labeled with A1 to A3 in Fig. 1.6), as well as a data acquisition (DAQ) system located at $z = 21$ m. In addition, two ambient vibration tests (AVTs) were carried out before and after the 2016 Central Italy seismic sequence. As sketched in Fig. 1.6 (a), the first AVT was carried out in February 2015 by using five accelerometers (model PCB 393B12) placed at two different levels, namely $z = 41$ m and $z = 25$ m. On the other hand, the second AVT was carried out in May 2017 and consisted of twelve accelerometers model PCB 393B12 deployed at four different levels as sketched in Fig. 1.6 (b), namely $z = 41$ m, $z = 29.1$ m, $z = 26.8$ m and $z = 12.5$ m. In both cases, the ambient vibrations were recorded for 30 minutes at a sampling frequency of 100 Hz.

1.5.3. Basilica of Santa Maria degli Angeli

The Basilica of Santa Maria degli Angeli in Assisi (Fig. 1.7 (a)) was built between 1569 and 1679. The basilica has a 126×65 m Latin cross plan, with a nave, two aisles, and a semicircular apse. The central core, at the intersection of the transept and the nave, consists of four pillars bearing the triumphal arches and the drum-dome structure. The single-shell dome of the Basilica has

inner diameter of about 20 m and variable thickness from 1.60 to 0.70 m. The inner and outer perimeters of the drum are circular and octagonal, respectively. Pilasters at the angles of the octagon become stiffening ribs which join together at the oculus, the base of the lantern, giving a total height of about 75 m to the structure.

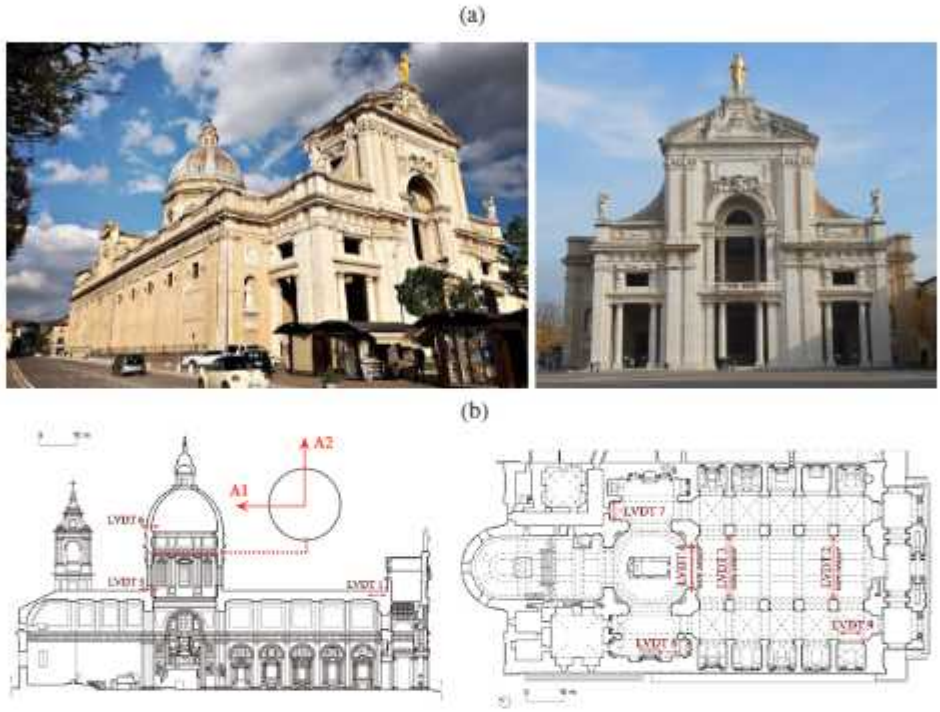

Fig. 1.7: Basilica of Santa Maria degli Angeli (a) and sensors' layout (b).

A permanent SHM system has been uninterruptedly monitoring the static, dynamic and environmental behavior of the Basilica since 2017 [21]. The monitoring system comprises 2 high sensitivity uniaxial PCB 393B12 accelerometers (labeled with A1 and A2), 9 LVDTs, 2 inclination sensors, 2 K-type thermocouples, and one laser displacement sensor (see Fig. 1.7 (b)).

1.5.4.Sciri Tower

The Sciri Tower (*Torre degli Sciri*) is a 41 m high civic tower located in the historical centre of Perugia in Italy. Its construction dates back to the late 13th century and, nowadays, the Sciri Tower is the only one preserved intact among the numerous towers erected during the medieval period of the city. The tower was owned by the noble family of Oddi until 1488, when it was transferred to the Sciri family (who gave it its current name) after violent disputes between noble clans that forced the Oddi family into exile. In 1680, the tower and the adjoining building were gifted to the Franciscan Third Order until 2011,

when the ensemble became property of the Municipality of Perugia. Important conservative restoration works were conducted in the building ensemble by the municipality in 2015, although neither the building aggregate nor the tower experienced significant structural modifications.

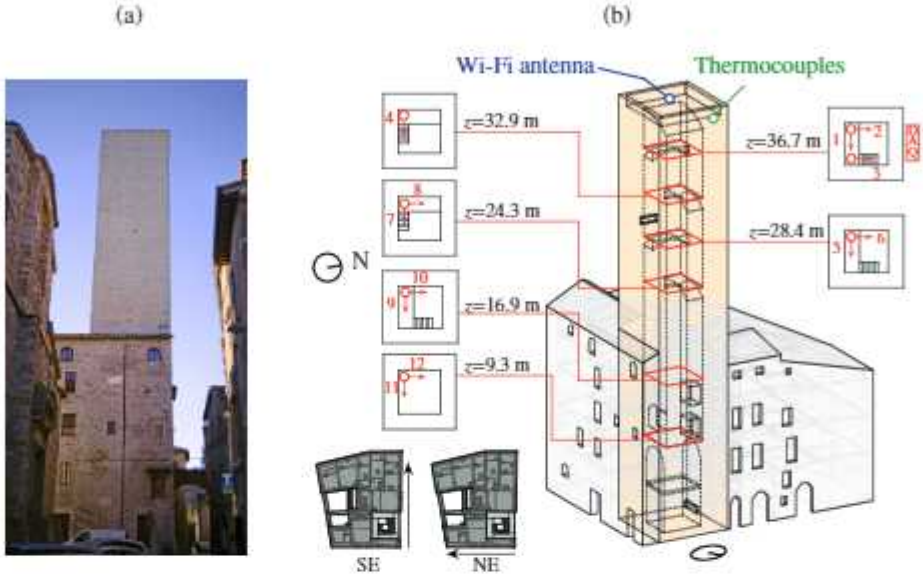

Fig. 1.8: View of the Sciri Tower (a) and layout of the dynamic monitoring system installed in the Sciri Tower with sensors positions (labeled from 1 to 12) (b).

The Sciri Tower is inserted into a building ensemble with approximate plan dimensions of 22×25 m. The tower is made of homogeneous squared white limestone blocks and has a hollow rectangular cross-section of 7.15×7.35 m, with three façades connected to the adjacent masonry buildings up to a height of 17 m, and a fourth one remaining unconstrained all along its height. The tower can be ideally split into two structural portions beneath and above the height level of 8.4 m. The lower part has wall thicknesses between 1.68 m and 2.1 m, and culminates with a stone masonry vaulted slab standing over an old chapel. On the other hand, the upper part has slender continuous walls (with thickness varying in height from 1.6 m to 1.4 m), and houses a metal staircase resting on four 1.5 m wide masonry vaulted slabs at different heights. Finally, a brick masonry ceiling vault completes the tower, and a 0.5 m thick parapet along the edges of a panoramic terrace rises up to a total height of 41 m.

With the aim of identifying the modal features and wave propagation properties of the Sciri Tower, a continuous ambient vibration testing was performed for three weeks, from February 13^{th} until March 10^{th} 2019. To this end, a total of 12 high sensitivity (10 V/g) uniaxial PCB 393B12 accelerometers were installed at four different heights of the tower, namely $z = 40.5$ m, $z = 33.5$ m, $z = 24.0$ m and $z = 8.4$ m, as shown in Figure 1.8. Ambient vibrations were

recorded at three different sampling frequencies to evaluate the robustness of the wave identification, including 200 Hz, 1000 Hz, and 5000 Hz. In addition, two K-type thermocouples were also installed at the level $z = 40.5$ m (indoor and outdoor) and temperature was recorded at a sampling frequency of 0.4 Hz. Field data were acquired using a multi-channel data acquisition system (DAQ) model NI CompactDAQ-9184 located at the level $z = 36.7$ m, equipped with NI 9234 data acquisition modules for accelerometers (24-bit resolution, 102 dB dynamic range and anti-aliasing filters) and NI 9219 modules for thermocouples (24-bit resolution, ± 60 V range, 100 S/s). A LabView toolkit was implemented for data acquisition and preliminary real-time processing, including amplitude and spectral plots for quality-control inspections. Data were recorded in separate files containing 30-min long acceleration and temperature time series, and transferred in real-time through Wi-Fi connection to the Laboratory of Structural Dynamics of the University of Perugia, 2.5 km far from the tower.

1.5.5. Consoli Palace

The Consoli Palace is the most emblematic building in the medieval town of Gubbio in central Italy. The palace forms part of a monumental ensemble built in the 14$^{\text{th}}$ century together with the Podestà Palace and a vaulted hanging square, named "Piazza Grande" (see Fig. 1.9 (a)). Although originally dedicated to host the legislative/executive and judicial courts, the Consoli and the Podestà palaces respectively house the Civic Museum and the municipality headquarters of Gubbio since the early nineties. The Consoli Palace presents a 40×20 m rectangular plan and it is structurally constituted by calcareous stone masonry thick bearing walls and vaulted ceilings. The foundations of the building are placed on two levels with a drop of approximately 10 m to accommodate the steep slope of the terrain (see Fig. 1.9 (b)), giving the building an irregular distribution in height. The south façade includes a panoramic loggia and stands 60 m from the ground level until a 13 m high bell-tower rising from the roof level, while the north façade has a height of about 30 m between the square's level and the roof. As an extraordinary example of a monumental masonry structure, the Consoli Palace has been the case study of a number of research projects (see [22, 23, 24, 25]).

Gubbio is located on the Umbria-Marche Apennine Mountains, an area of almost continuous seismicity and cataloged as a natural laboratory for seismic studies (TABOO - Alto Tiberina Near Fault Observatory). The seismic activity in this area is dominated by the Gubbio fault on which the city rises. The Gubbio fault is a 22-km-long normal fault pertaining to a set of active SW-dipping sub-parallel normal faults known as the seismogenic Umbria Fault System (UFS) [26]. The UFS faults are antithetic splays located in the hanging wall of the regional Alto Tiberina Fault (ATF), a major east-dipping low-angle (20°) normal fault. Geophysical data and seismological studies characterized the geometry of the Gubbio fault, revealing a listric trend and the intersection

with the ATF at a depth of 6 km [27]. The strongest registered earthquake to date was on April 29th 1984 (Mw 5.6) with epicenter located ≈10 km south of the town of Gubbio [28] and causing important damage to the Consoli Palace. Later on, an intense seismic activity started on August 26th 2013 with a Mw 3.8 event and followed by several aftershocks with 3<Mw<4.9 through the entire 2014. Since then, the seismic activity has been quite constant, with one single major event occurred on October 2016 with a magnitude Mw 3.0 [28].

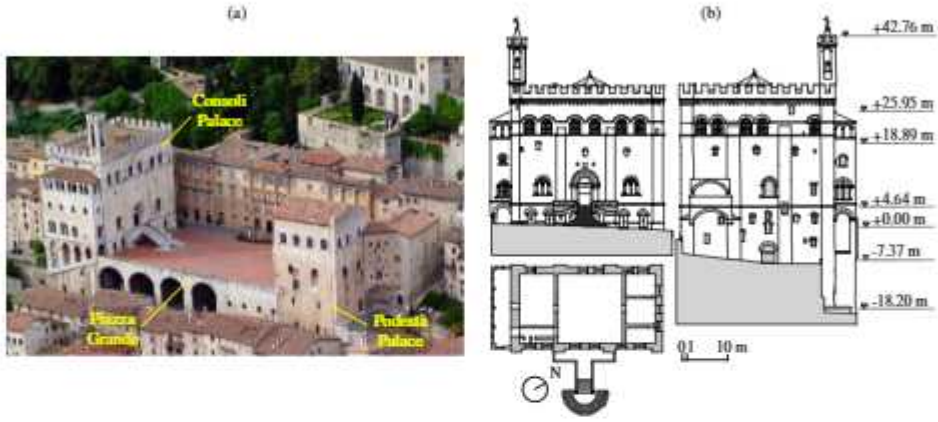

Fig. 1.9: Aerial view of the monumental ensemble of the Consoli Palace, the Podestà Palace and the Piazza grande (a); Plan and elevation views of the Consoli Palace (b).

Within the framework of the research project "DETECT-AGING - Degradation effects on structural safety of cultural heritage constructions through simulation and health monitoring" (protocol no. 201747Y73L) funded by the Ministry of Education, University and Research (MIUR), an aggregated SHM system involving dynamic, static and environmental sensors was installed in the Consoli Palace in July 2017 and remained active until July 2020. The original monitoring system comprised three uni-axial accelerometers, two Linear Variable Displacement Transducers (LVDTs), and two temperature sensors. The analysis of the monitoring data acquired during this first phase of the SHM system was reported by Kita and co-authors [24]. Nonetheless, an important upgrade of the system was carried out in July 2020 with a considerable increase in the number of sensors, which remains active up to date. The layout of the system is sketched in Fig. 1.10 (b) and comprises: twelve accelerometers, four LVDTs, six temperature sensors, and a data acquisition system (DAQ). The accelerometers, labeled with A1 to A12 in Fig. 1.10 (b) and shown in Fig. 1.10 (a), are high-sensitivity uni-axial piezoelectric accelerometers model PCB393B12 (10 V/g, broadband resolution 800 µg, and ± 0.5 g measurement range). They are deployed in the two main floors of the building and on the roof level, namely at heights of +4.64 m (Arengo Hall), +18.89 m (Nobili Hall), and +29.77 m. Three accelerometers are located in each floor, with a

biaxial station in the south façade and a mono-axial station in the north façade monitoring ambient accelerations along the y-direction. Such a configuration is aimed at characterizing rigid diaphragm motions of the floors and global torsional rotations of the building. A similar scheme has been also considered on the roof level but with the consideration of two accelerometers (A11 and A12) located at the centre of the east and west façades, respectively, with the aim of monitoring out-of-plane bending movements. Four S-series LVDTs (50 mm measurement range and < 0.3 µm resolution), labeled with D1 to D4 in Fig. 1.10 (b), are also installed monitoring the opening/cracking of two major cracks previously identified in reference [24]. Specifically, LVDTs D1 and D3 monitor two cracks in the second level of the palace, whose origin is possibly related to the overturning mechanism of the loggia in the south façade. Instead, LVDTs D2 and D4 monitor the movements at two levels (second and third floors) of a second major crack located in the north façade of the palace and propagating downwards until reaching the west façade. The origin of the latter may be indicative of the initiation of a failure mechanism of overturning of the northern part of the west façade. Finally, six K-type thermocouples, labeled with T1 to T6, are also deployed in the palace. Thermocouples T1 to T4 are located aside LVDTs D1 to D4 measuring the surface temperature of the masonry, while thermocouples T5 and T6 monitor the ambient temperature at the roof level and the third level, respectively. The accelerometers, thermocouples T1 and T2, and LVDTs D1 and D2 are connected to a DAQ system located in the third level and powered from an uninterruptible power supply. (Fig. 1.10 (a.4)). The DAQ, model NI Compact DQ-9132 (1.33 GHz Dual-Core Atom, 4 slots, Windows Embedded Standard 7, 16 GB SD storage), is equipped with three NI 9234 acceleration acquisition modules (4 channels, 24-bit resolution, 102-dB dynamic range and anti-aliasing filters) and a NI 9219 acquisition module for LVDTs and thermo-couples (4 channels, 24-bit resolution, ± 60 V range, 100 S/s). Conversely, the monitoring records of crack-meters D3 to D4 and thermo-couples T3 to T6 are transferred through wireless communication to a wifi router (Fig. 1.10 (a.3)).

Ambient vibrations are sampled at 40 Hz, and crack amplitudes and temperatures from channels D1-D2 and T1-T2 are sampled at 0.1 Hz. The monitoring records are stored in separate binary data files containing 30-min-long recordings. A Labview script is used for data acquisition and quality control from remote, including amplitude and spectral plots. Single acquisitions from sensors D3-D4 and T3-T6 are taken every 30 minutes and collected in common text files on a daily basis. The recorded data are sent through the internet to a cloud archive, where they are accessed by a remote server computer in the Laboratory of Structural Dynamics of the University of Perugia. In addition, a dense AVT was conducted at 13:00 pm CEST on May 7$^{\text{th}}$ 2021 in order to characterize the modal signatures of the Consoli Palace. The test comprised 19 uni-axial piezoelectric accelerometers (same technical specifications as those used for the

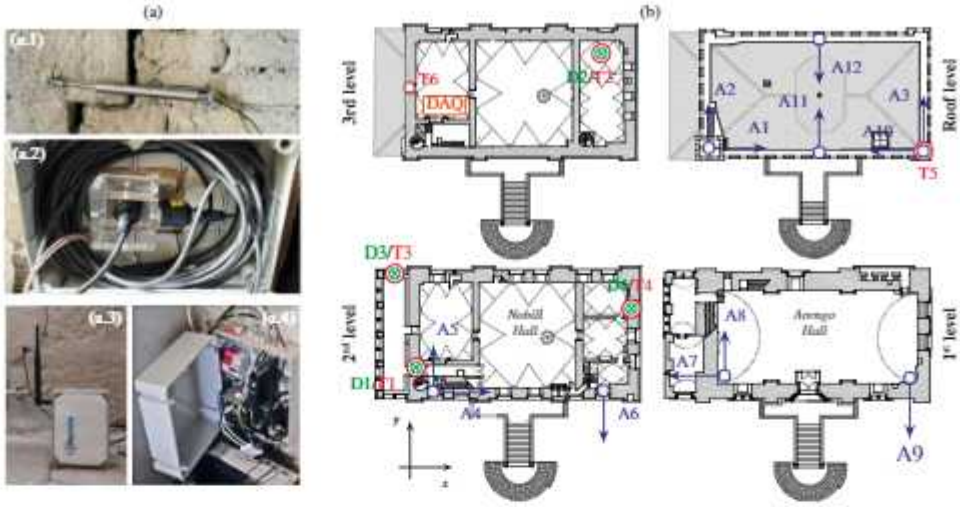

Fig. 1.10: Views of the monitoring and acquisition equipment (a; a.1 - LVDT, a.2 - Accelerometer, a.3 - wireless data transmission, a.4 - DAQ), and layout of the continuous monitoring system (b).

continuous monitoring) with positions sketched in Fig. 1.11. Specifically, the accelerometers layout used in the continuous monitoring system (Fig. 1.11 (a)) was complemented with nine accelerometers covering the two orthogonal directions of the palace at the roof level, and three stations at the top level of the bell-tower to monitor rigid-diaphragm motions. Such a configuration was designed with a twofold purpose: firstly to identify the interaction of the bell-tower with the main body of the palace and so to distinguish between local, global and mixed modes; secondly, to assess the degree of rigidity of the roof level of the palace and the possible appearance of out-of-plane bending modes in the main façades of the palace. Recordings from channels A7, A8 and A9 are omitted in the dynamic identification, both in the AVT and the continuous monitoring, and reserved for monitoring ground motions. The reason is that the excitation level in the first floor of the palace under normal conditions is extremely low, so these accelerometers simply record noise when no seismic actions are present. Two asynchronous 30 minutes long acquisitions were carried out and ambient vibrations were recorded at a sampling rate of 10652.89 Hz (the maximum rate allowed by the DAQ). The test was conducted under normal operating conditions, with micro-tremors induced by traffic in the neighboring roads and wind forces as the main sources of excitation. The mean environmental temperature during the test was 17.2° and the average wind speed was equal to 6.4 km/h as measured from the meteorological observatory of Gubbio center, only 500 m from the palace. Such moderately strong wind speeds favored the dynamic identification of the palace, reaching maximum accelerations of about 0.8 cm/s^2, while average ambient vibrations during the continuous monitoring

are typically around 0.2 cm/s^2.

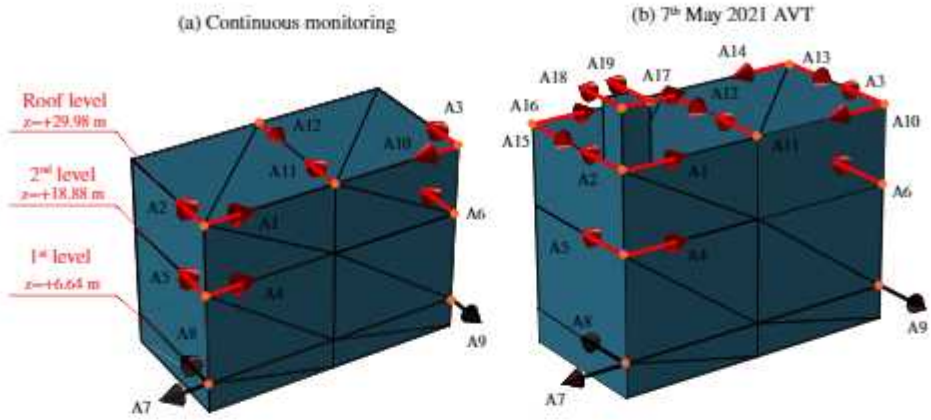

Fig. 1.11: Comparison of the accelerometers layout during the continuous monitoring of the Consoli Palace (a) and the dense AVT performed on May 7th 2021 (b).

Seismic sequence occurred in May 2021

A seismic sequence of small intensity recently hit the palace between May 15th and May 27th 2021. The seismic sequence comprised six earthquakes of moderate intensity, with the strongest shock of magnitude Mw 4.0 at 07:56 UTC. Ground motion records for these earthquakes have been obtained from the data provided by the Italian Strong Motion Network (RAN) of the Department of Civil Protection (DPC) and the Italian Seismic Network (RSN) of the National Institute of Geophysics and Vulcanology (INGV). Specifically, seismic records have been taken from the Gubbio Parcheggio Santa Lucia station, which is located only 600 m far from the Consoli Palace. Figure 1.12 (a) shows the geographical location of the epicenter of the main shock and the location of the palace, and the waveforms recorded at the Gubbio Parcheggio Santa Lucia station are presented in Fig. 1.12 (b). Table 1.2 reports the registered seismic events, including their PGA, depth and distance from the seismic station. Note that the Consoli Palace is located at a distance of less than 3 km from the epicenters, thereby this case study represents a unique example of a monumental building subjected to impulsive near-field earthquakes. The location of the epicenter is almost identical to the seismic sequences started on December 18th 2013 with a major shock of similar intensity Mw 3.9, followed by seven aftershocks with intensities between Mw 2.9 and 3.6. Therefore, it is conceivable that this new sequence may have been originated by the same activation mechanism of the Gubbio fault.

Table 1.2: Seismic events registered in May 2021 at the Gubbio Parcheggio Santa Lucia station (Latitude: 43.3558, Longitude: 12.5717, Elevation: 515 m). Source: Italian Strong Motion Network (RAN).

Event	Date	Mw	PGA [cm/s^2]	Depth [km]	Dist. epic. [km]
E1	15/05/21 07:56:01 UTC	4.0	102.4	9.9	1.4
E2	15/05/21 08:07:20 UTC	3.1	35.3	9.6	1.0
E3	15/05/21 10:19:17 UTC	3.0	18.07	10.5	2.4
E4	15/05/21 21:27:25 UTC	2.8	18.07	9.4	2.2
E5	23/05/21 20:51:22 UTC	3.0	17.38	8.1	1.8
E6	27/06/21 13:27:16 UTC	3.0	7.65	6.8	2.2

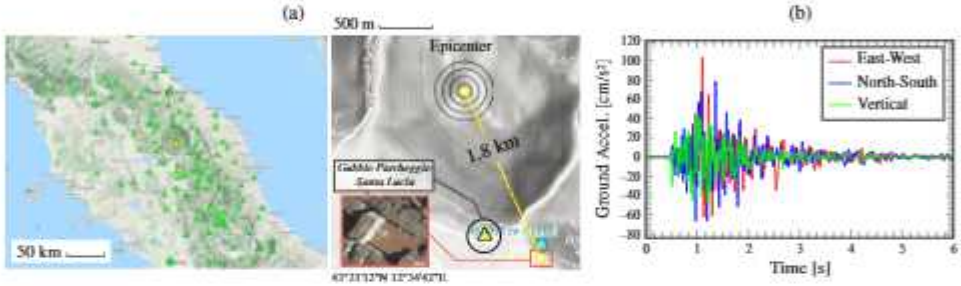

Fig. 1.12: Geographical map highlighting the epicenter of the earthquake from May 15$^{\text{th}}$ 2021 at 07:56:01 UTC (a), and E-W, N-S and vertical components of the near-field accelerations recorded by the Gubbio Parcheggio Santa Lucia station (200 Hz sampling frequency) (b).

1.5.6.Muhammad Tower

The Muhammad Tower in Fig. 1.13 (a,c) (also referred to as the Hontiveros Tower and the Tower of the Hens) is the westernmost tower of the monumental complex of the Alhambra (Fig. 1.13 (b)), which is currently one of the few preserved palatine cities of the medieval Islamic period in Europe (8^{th}-15^{th} centuries). The Alhambra overlooks the city of Granada (Andalusia) on top of the Sabika Hill at the foot of the Sierra Nevada Mountains in South-East Spain (see Fig. 1.13 (b)). Originally constructed as a military enclosure, the Alhambra became a fortified palatine city during the Nasrid dynasty in the mid-13^{th} century. Designated as a world heritage site by UNESCO in 1984, the Alhambra monumental complex is the second most visited monument in Spain and attracts more than 3 million tourists every year.

Inserted in the walls of the Alhambra Fortress between the Tower of the Cube and the Mexuar Palace, the Muhammad Tower was erected in the 13^{th}-century by Muhammad II to control the access to the royal palaces. The tower has an approximately rectangular cross-section (6.6×9.0 m) composed of 1.3-1.9 m thick RE and brick masonry walls. Along its height, the tower has two vaulted

floors and a terrace rising 11.6 m above the foundation, including a 0.80 m tall parapet and 1.2 m tall battlements (Fig. 1.13 (d)). The three levels of the tower are connected by masonry staircases at the south-West façade of the tower. The foundations lay on a geological formation of conglomerates with intercalated sands and clays of the Pliocene and Lower Pleistocene, known as the Alhambra Formation. Although there are evidences of numerous modifications of the tower over the centuries, it is only after the 50s that rehabilitation interventions start being documented. These include the underpinning and consolidation of the foundations of the tower by the architect Francisco Prieto-Moreno Pardo in 1975 to rehabilitate the tower after a long period of abandonment in the 19^{th} century.

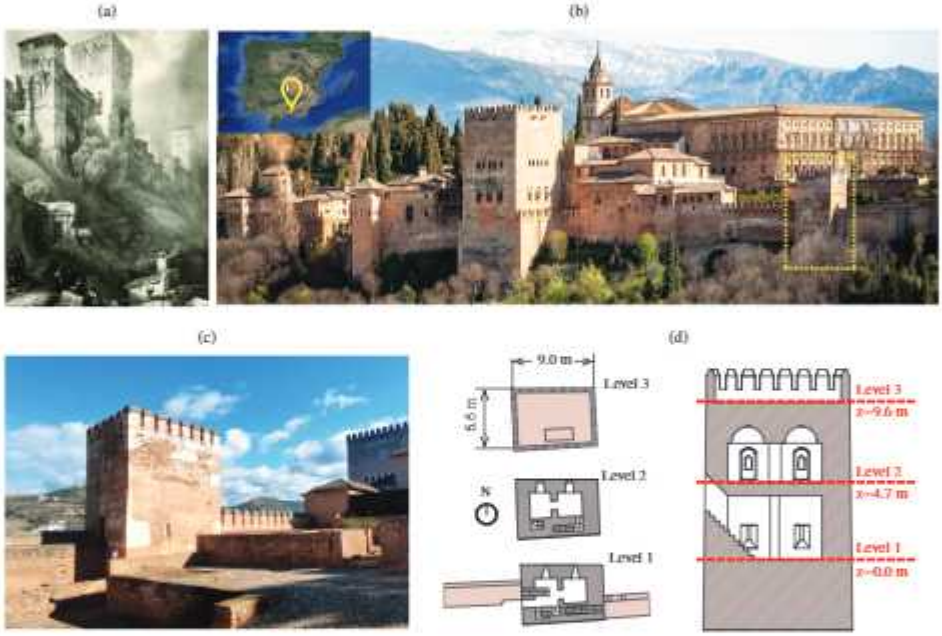

Fig. 1.13: Drawing of the fortress of the Alhambra by David Roberts 1835 (from the Library of the Patronato of the Alhambra and Generalife) (a). Panoramic view of the Alhambra and its geographic position (b). View of the Muhammad Tower (c), plan and elevation views (d).

With the aim of assessing the structural condition of the tower, a vibration-based SHM system was installed from January until March 2022. The monitoring system comprises 8 high-sensitivity piezoelectric accelerometers model PCB393B31 (μ5% 10.0 V/g, broadband Resolution: 1 μg rms and ±0.5 g pk) installed on the three main levels of the tower as shown in Fig. 1.14 (a). The sensors, labeled with A1 to A8, are deployed forming a biaxial station in the East façade and a mono-axial one in the North façade (except for the first level where only a bi-axial station is installed). Such a configuration is aimed

at characterizing the rigid diaphragm motions of the floors and the global torsional rotations of the tower. Ambient vibrations are sampled at 200 Hz through the LMS Test.Xpress software and stored in separate data files containing 30-min-long records. The acceleration signals are recoded by a data acquisition system (DAQ) model LMS SCADAS located in the second level, and a portable WiFi router is used for data transfer and remote control of the system. Environmental data are retrieved from the Granada-Albayzín meteorological station managed by the Department of Mineralogy and Petrology from the University of Granada, located only 280 m far from the tower. Environmental data include air temperature, relative humidity, wind speed, and atmospheric pressure with an acquisition frequency of 10 min.

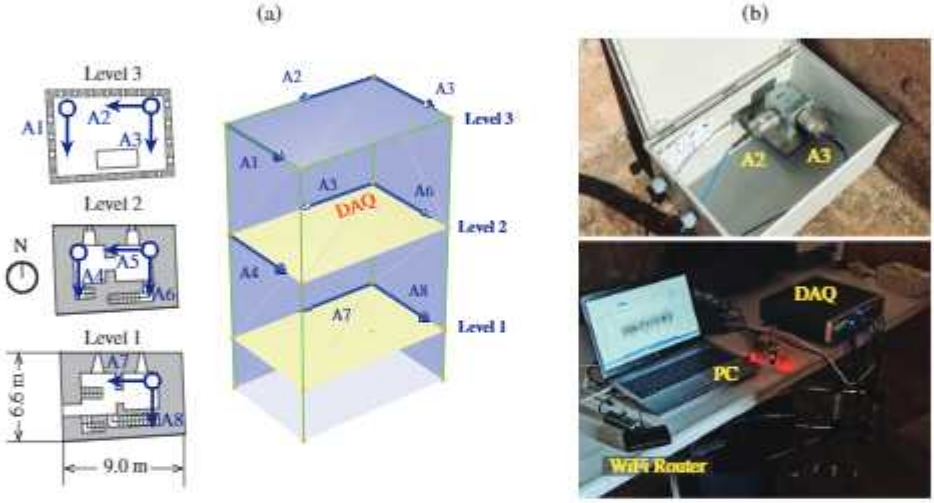

Fig. 1.14: Layout of the continuous monitoring system (a) and views of the sensors and the DAQ equipment (b).

1.5.7. Chiaravalle bridge

The Chiaravalle viaduct links the state road 76 (SS76) and the Marche airport (also known as the Raffaello Sanzio Airport) straddling the municipalities of Falconara Marittima and Chiaravalle in central Italy (Fig. 1.15). The viaduct has been studied in several research works in the literature, so interested readers can find further information on the bridge structure in references [29, 30, 31, 32, 33]. The overall length of the viaduct is 875 m and it consists of four kinematic chains (KC#), separated by structural joints (Fig. 1.16). The KCs, involving 13, 10, 3 and 5 spans, respectively, are constituted by simply supported girders connected by steel post-tensioned tendons at the level of the concrete slab. The span length is 27.5 m with exception of the span between piers 24 and 25, crossing the Orte-Falconara Marittima railway line, which has a total length of 51.80 m. The layout of the viaduct consists of a horizontally curved alignment

between piers 17 and 29 with radius of curvature of 425 m, and joined to two tangent straight segments of 495 m and 55 m along the center-line.

Fig. 1.15: Geographic position of the Chiaravalle viaduct (a,b) (from Google Maps); photo evidence of the viaduct (c).

Fig. 1.16: Plan location of the KCs (from Google Maps) (a); view of the column-bent piers (b); wall pier (P17) (c); and pier 24 (d).

The deck along the viaduct is 12.10 m wide and is constituted by three twin simply supported V-shaped prestressed concrete beams underlying a 0.25 m thick concrete slab (Fig. 1.17 (a)). The span between piers 24 and 25 is an exception, because its deck consists in an adjacent box beam ending with two Gerber saddles (Fig. 1.17 (b)), on which the trapezoidal beams of the adjacent spans are connected. The substructure of the viaduct was originally defined by column bent piers constituted by two circular columns with a diameter of 1.4 m (Figs. 1.17 (c,d)), with the exception of pier 17, which is characterized by a single wall pier with a rounder rectangular cross section. The foundations of

the piers were originally defined by 1.70×9.00×5.00 m plinths on two rows of three ∅1000 mm piles. Nonetheless, the viaduct, built in the early 1990s, was seismically upgraded in 2017 after a survey campaign evidenced the presence of advanced surface degradation of the viaduct [29]. The degradation was particularly acute in the foundation structures where coring samples revealed low values of concrete compressive strength, with reductions in the piles of up to 70% of the project design values. The seismic upgrading works considered a new foundation structure constituted by ∅300 mm micropiles in the perimeter of the rafts, new rafts superimposed to the original ones, and 0.3 m thick concrete jacketing of the pillars [30]. The upgrading also included the substitution of steel-teflon elastomeric bearings with double concave friction pendulum isolators, as well as auxiliary dissipative viscous dampers between the deck and the substructure on the abutments and pier 17. The final configuration of the piers has heights ranging between 6.25~8.72 m for KC1, 8.60~10.75 m for KC2, 8.95~11.42 m for KC3, and 4.50~9.01 m for KC4.

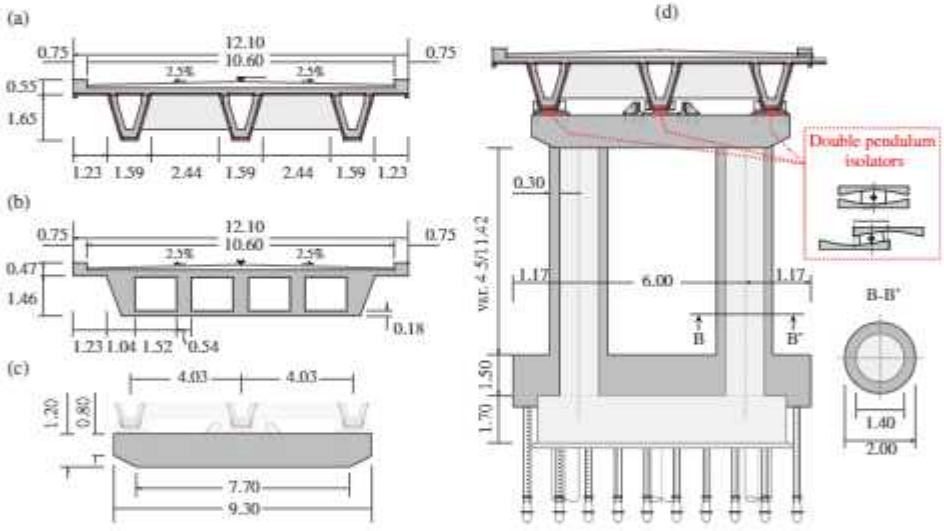

Fig. 1.17: Viaduct dimensions: (a) V-shaped reinforced concrete beams cross-section; (b) adjacent box beam cross-section; (c) columns bent; (d) lateral view of the pier-deck system (units in [m]).

Ambient vibration tests (AVTs) were performed to evaluate the dynamic behavior of the viaduct on February 4th and 7th 2020. The monitoring instrumentation consisted of high sensitivity (10 V/g) uniaxial PCB 393B12 accelerometers fastened to steel supports by threaded screws (Fig. 1.18 (a)). The accelerometers were placed on the curb side of the bridge deck, and connected by coaxial cables to a data acquisition system (DAQ) model NI cDAQ-9188 with NI 9234 modules (24-bit resolution, 102 dB dynamic range and anti-aliasing filters) (Fig. 1.18 (b)). Because of limited availability of sensors, three different

Fig. 1.18: Photographs of an accelerometer fixed to a steel support (a) and the DAQ (b).

sensor configurations were adopted to achieve a sufficient spatial coverage of the viaduct as illustrated in Fig. 1.19. Note that the adopted sensor layout has been designed similar to the one installed by Gara *et al.* [33] for subsequent comparison purposes. The first set-up was aimed at characterizing the dynamic behavior of KC1, and included 14 accelerometers aligned in the transverse direction of the bridge center-line and located on the piers and the first abutment, as well as 3 accelerometers aligned in the longitudinal direction on piers 6 and 13. The second set-up focused on KC2, including 12 accelerometers aligned in the transverse direction on the piers, and 3 aligned in the longitudinal direction on piers 13, 18 and 23. Channels 1, 2 and 13, coincident with channels 13, 14, and 17 from the first set-up, are used as reference sensors to evaluate any degree of continuity of the modes between the kinematic chains. From preliminary numerical analyses and previous literature on the viaduct, one single roving sensor (Ch. 14) was assumed sufficient to characterize both the longitudinal mode shapes and wave velocities of KC2. Finally, the third set-up covered KC3 and KC4, comprising 10 accelerometers on the piers and aligned in the transverse direction, and 4 accelerometers in the longitudinal direction on piers 23, 26, 28, and the second abutment. In this set-up, channels 12, 13 and 14 are used as reference sensors coincident with channels 11, 12 and 15 from the previous one. For each set-up, 30 minutes of ambient vibrations were recorded by two asynchronous acquisitions at a sampling frequency rate of 1652.89 Hz (the largest rate allowed by the data acquisition equipment). A LabView toolkit was implemented for data acquisition and preliminary real-time processing, including amplitude and spectral plots for quality-control inspections. With regard to the environmental conditions, February 4^{th} was characterized by strong winds with speeds up to about 15 m/s in the transverse direction of the bridge, and environmental temperatures in the order of 10-15°C . Conversely, almost no wind was present on February 7^{th} and cooler temperatures ranging between 5 and 10°C were registered.

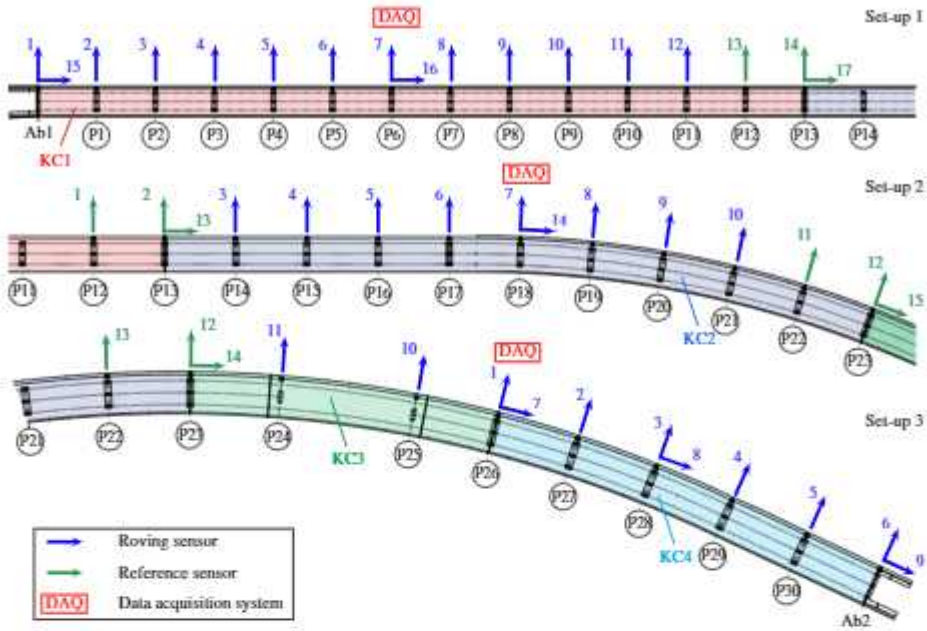

Fig. 1.19: Sensors layout for the different KCs.

1.5.8. Trigno V Bridge

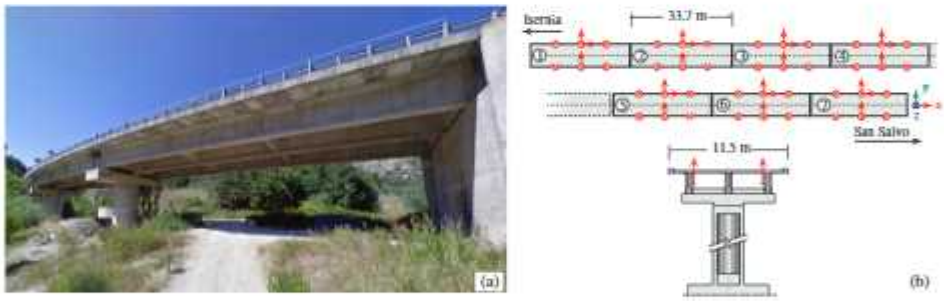

Fig. 1.20: General view of the Trigno Bridge (a) and sensors layout (b).

The Trigno V Bridge is a seven span simply supported concrete-girder highway bridge (7×33.7 m long) located in the Italian region of Abruzos between the municipalities of Isernia and San Salvo (Fig. 1.20 (a)). The isostatic spans are nominally equal with length of 33.7 m and width of 11.5 m (Fig. 1.20 (b)). Each span is made of three longitudinal I-shaped pre-stressed girders separated by 3.8 m between axes and connected to a 0.25 m thick reinforced concrete deck slab and transverse tie diaphragms with a spacing of 11.2 m. Within the development framework of P3P, a dense dynamic monitoring system was installed in the bridge on October 13^{th} 2021. The system comprised 50 MEMS-based

accelerometers covering 81 measurement channels (see Fig. 1.20 (b)). Four asynchronous 30 min long acquisitions were acquired between 11:00 a.m. and 12:30 p.m. at a sampling rate of 200 Hz and under normal operating conditions, with wind and traffic as the main sources of excitation. In this thesis work, only the vertical accelerations are processed. This amounts to 42 channels (6 channels per span) as illustrated in the modal geometry defined in P3P and shown in Fig. 1.21.

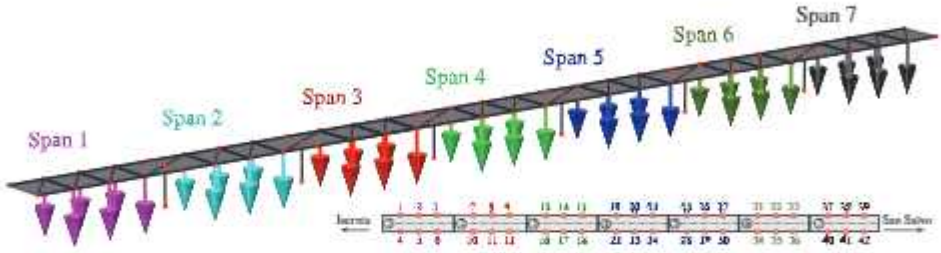

Fig. 1.21: Modal geometry of the Trigno Bridge.

2. Structural Health Monitoring: The Statistical Pattern Recognition Paradigm

2.1. Introduction

In its broadest sense, SHM can be defined as the process of implementing a continuous damage identification strategy for an engineering infrastructure. Damage can be conceived in this context as any disruptive event affecting the system's performance such as, for instance, alterations of the material and/or geometrical properties, or changes to the boundary conditions/connectivity [34]. In this light, the final aim of SHM is to track anomalies in the structural performance caused by damage and, desirably, to predict damage evolution and structural life expectancy [8]. Among the broad variety of existing sensing techniques, ambient vibration-based SHM systems have become particularly widespread owing to their non-destructive nature and minimum intrusiveness, without requiring heavy and costly excitation devices. Such techniques have proven proficiency to correctly assess global damage, although their ability to detect local defects with minimal effect upon the overall stiffness is rather limited (e.g. freezing/thawing cycles, chemical attack, corrosion) [35]. In this regard, static monitoring such as the assessment of crack widths, displacements or tilts is typically more effective [36]. Moreover, it is often convenient to also monitor the environmental and operational conditions (EOC) of structures to facilitate the discrimination of damage from normal operational conditions. In this light, it follows that the use of integrated monitoring systems encompassing diverse sensing solutions results crucial to attain effective local/global damage

detection capabilities [37]. The implementation of such systems comprising dense sensor networks is becoming economically viable in engineering practice thanks to the major advances and progressive cheapening of sensor technology in recent years. Under these circumstances, the integration of all these monitoring data turns the damage identification task into a Big Data problem where the use of Data Science and Machine Learning becomes increasingly necessary.

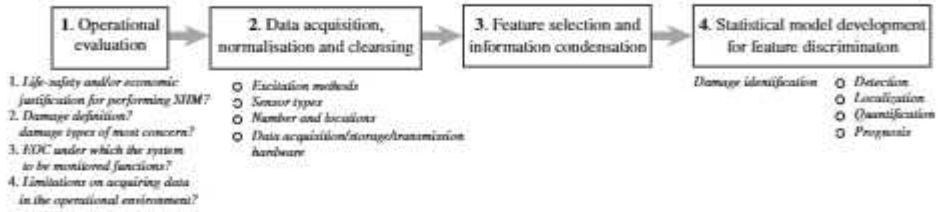

Fig. 2.1: Statistical pattern recognition paradigm for SHM.

The comprehensive approach to SHM through the pattern recognition paradigm has been particularly successful. This framework was first formalized by Farrar *et al.* [38] around the idea that one can learn how to assign damage states or classes to monitoring data through the study of relations or patterns in the response of the monitored structure. The general methodology comprises four stages as sketched in Fig. 2.1:

1. Operational Evaluation: The first stage sets boundaries to the problem and aids at tailoring the subsequent damage identification process by addressing four questions. These include the motivation and economic justification for the implementation of an SHM system, the definition of the different sources of damage that may arise in the structure to be monitored, EOC in which the system may operate, and the data acquisition limitations under operating conditions.

2. Data acquisition/normalization and cleansing: The data acquisition process concerns the selection of suitable excitation methods, sensor types and coverage (number and location), and data acquisition, storage, and transmission. Data normalization regards the ability of separating changes in sensor readings caused by damage from those caused by varying EOC. Finally, data cleansing regards the process of phasing out corrupted or uninformative data from the feature selection process.

3. Feature extraction and information condensation: This stage relates the identification of data features that allow one to distinguish between the undamaged and damaged conditions. Inherent in the feature selection process, the information condensation step deals with the minimization of redundant features and dimensionality reduction.

4. Statistical model development: This last stage concerns the implementation of statistical models mapping between the extracted features and the diagnosis, that is to say, the class or tag assignment. Such models are thus intended to enable the discrimination between features related to undamaged and damaged classes. Generally, statistical models are classified in three categories: unsupervised learning, supervised learning, and semi-supervised learning as an intermediate solution. A pattern recognition model can be trained in a supervised learning fashion when data are available from both the undamaged and damaged structure. Conversely, when no information is available on the damaged structure, the algorithms fall into the category of unsupervised learning. In semi-supervised learning, a minimum amount of tagged training data (data labeled as "damaged") is available, but not sufficient for a full supervised learning. In this regard, Transfer learning is a popular alternative to supervised learning, where tagged data are generated through a digital twin of the structure (virtual damage scenarios). In either way, statistical pattern recognition models analyze statistical distributions of the measured or derived features with the aim of performing damage identification. The damage identification process is commonly organized in a hierarchical structure of increasing complexity discussed by Rytter [39] as sketched in Fig. 2.2: **Level I**: Detection; **Level II**: Localization; **Level III**: Classification; **Level IV**: Extension; and **Level IV**: Prognosis. All things considered, the final outcome of the paradigm of statistical pattern recognition is a set of classes from which decisions can be made, closing the data to decision (D2D) chain.

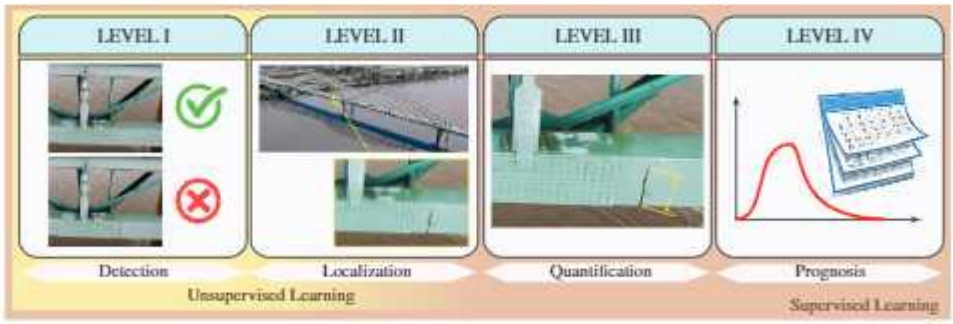

Fig. 2.2: Damage Identification problem in SHM.

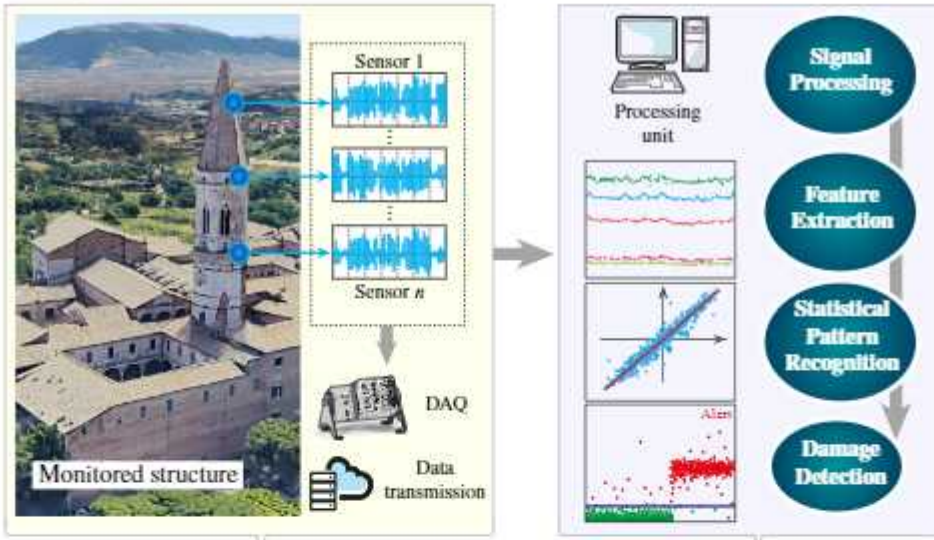

Fig. 2.3: General work-flow of the SHM of historic constructions under the paradigm of statistical pattern recognition.

Unsupervised learning techniques have been more extensively reported in the literature given the difficulty in obtaining monitoring data from damage conditions in civil engineering structures. Note that data from every conceivable damage scenario must be available to effectively apply supervised learning, which is always a challenging task, either through modeling or experiments. Modeling approaches such as finite element modeling also represents a formidable problem, since civil engineering structures are usually characterized by geometrical and material complexities. The modeling of damage itself is even more intricate, being possible to find multiple damage mechanisms with highly nonlinear behaviors, not to mention the frequent existence of previous damage with uncertain origin, extension and evolution. A major drawback of unsupervised learning is that it usually limits to damage detection, and damage can only be located to some extent in some particular cases. Nonetheless, level 1 diagnostic often suffices for the maintenance of singular constructions, whose high economic value and impact across infrastructure networks justifies the execution of in-situ inspections every time any fault is detected. In this light, the statistical pattern recognition paradigm previously depicted in Fig. 2.1 can be materialized in the shape of hardware and software components as sketched in Fig. 2.3:

- Hardware component: The hardware part is generally composed of a heterogeneous sensor network, a data transmission system (wired or wireless), and a data acquisition (DAQ) system that permanently collects the monitoring data. Computer files containing records of certain time duration

are locally processed or sent through the internet or another transmission system to a server or the cloud.

- Software component: This component comprises a sequence of pattern recognition algorithms designed to translate the signals acquired by the sensing interface into condition classes (damaged or undamaged). The computer implementation follows the statistical pattern recognition paradigm previously sketched in Fig. 2.1: (i) Signal processing; (ii) Feature Extraction; (iv) Statistical Pattern Recognition; and (iv) Damage detection.

All the scientific achievements made in this thesis have been framed within the paradigm of statistical pattern recognition given its intrinsic conception of SHM as a compound of monitoring techniques and algorithms enabling long-term automated condition-based maintenance. In this light, the fundamental stages in SHM are further described in the following sections, namely the concept of feature extraction in Section 2.2, data cleansing in Section 2.3, data normalization in Section 2.4, novelty analysis in Section 2.5, and automated anomaly detection in Section 2.6. Finally, Section 2.7 illustrates all these steps with an application case study of the damage identification of the Consoli Palace after the seismic sequence occurred in May 2021. While methodological advances have been achieved in all these elements all throughout the course of this thesis, the main scientific contribution regards the assembling of all these tools into a common an automated procedure in the software codes later introduced in Chapter 6.

2.2.Feature Extraction

In the fields of Statistics and Machine Learning, feature selection and extraction are two approaches for dimension reduction aimed at producing the possible most informative, distinctive, and compact set of features to improve the success of data storage and processing applications [40]. On one hand, feature selection relates the process of selecting the most relevant attributes of a database, overlooking redundant or non-informative features. On the other hand, feature extraction creates low-dimensional data-sets by functional mapping of the original features. In the realm of SHM, feature extraction relates the identification process of certain physical signatures or variables that are sensitive to the appearance of damage from the raw measurements [41]. The effectiveness of the adopted feature extraction approach largely determines the success of the damage assessment and the subsequent decision-making process, since it is a fundamental axiom of SHM that sensors cannot directly measure damage [42]. The design of the feature extraction strategy is conditioned by the operational evaluation. This includes aspects such as the employed sensing technology, accessibility limitations, the specific structural typology and engineering materials, and, most importantly, the damage mechanisms of concern

in the particular monitored system. The ideal outcome is a low-dimensional feature set that is highly sensitive to the condition of the structure. Such a selection is often not a trivial task, being necessary to combine robust signal processing techniques with a priori statistics and engineering judgment. A wide variety of damage-sensitive features can be found in the literature such as simple signal statistics (e.g. averages, max/min and root-mean-squared (rms) values), frequency spectra, time-frequency analysis features, or modal properties and derived signatures (e.g. mode shape curvature, modal strain energy or flexibility) [41, 43, 44]. Model updating [8, 45] and time-series modeling [46] methods represent other useful approaches for model-based and data-driven feature extraction, respectively. In essence, these techniques construct (or learn) a physics- or data-based model of the monitored structure by exploiting monitoring data. Then, the model parameters or the residuals between new experimental data and the model predictions can be used as damage-sensitive features [41]. In general, it is convenient to count on heterogeneous damage-sensitive features to attain both local and global damage identification.

In the context of vibration-based SHM systems, it is common to employ modal properties (resonant frequencies, damping ratios, and mode shapes) as damage-sensitive features (DSF). To do so, a variety of automated OMA procedures have been proposed in the literature [47, 48]. Given the utmost importance of such techniques in the context of this thesis, readers are referred to Chapter 5 where a full description is presented. These techniques allow to automatically extract time series of modal signatures as illustrated in Fig. 2.4 for the Consoli Palace (Section 1.5.5). It may be also useful to utilize mode shapes as damage sensitive features. These are usually less affected by environmental conditions compared to resonant frequencies, although the number of sensors required for their correct characterization is usually larger. This motivates the use of mode shape components for damage detection, particularly during the first months of monitoring when acquired data is not enough for cleansing time series of natural frequencies from environmental effects. Mode shapes can be characterized using several metrics, although the use of MAC values between the identified modes and the reference ones is the most common approach. This statistical indicator appraises the coherence or similarity between two arbitrary complex mode shapes $\boldsymbol{\varphi}_r$ and $\boldsymbol{\varphi}_q$ as [49]:

$$MAC\left(\boldsymbol{\varphi}_r, \boldsymbol{\varphi}_q\right) = \frac{\left|\boldsymbol{\varphi}_r^{\mathrm{T}} \boldsymbol{\varphi}_q^*\right|^2}{\left(\boldsymbol{\varphi}_r^{\mathrm{T}} \boldsymbol{\varphi}_r^*\right)\left(\boldsymbol{\varphi}_q^{\mathrm{T}} \boldsymbol{\varphi}_q^*\right)}, \tag{2.1}$$

where the asterisk denotes the complex conjugate. A MAC value of 1 indicates perfect correlation between the mode shapes, while a value of 0 evidences no correlation. The assessment of MAC values may be also used as a diagnostic tool to detect faulty sensors; whose effect is often not so evident in terms of

resonant frequencies. To illustrate this, Fig. 2.5 (a) furnishes the time series of MAC values of the modes of the Consoli Palace previously reported in Fig. 2.4. It is noted in this figure that a sudden drop in the MAC values was found between August 30th and October 20th 2020. During in-situ inspections, it was found out that the slot of channel 6 in the acquisition module of accelerometers had been damaged during a storm event, although it was working in an apparently normal way. This was confirmed by a statistical analysis of the mode shapes as shown in Fig. 2.5 (b). In this figure, the modal components (normalized to a maximum amplitude of 1) of the 12 channels of the SHM system are analyzed during three different stages; Stage 1 July 17th-August 29th 2020 (before fault), Stage 2 August 29th-October 20th 2020 (faulty period), and Stage 3 October 20th-November 16th 2020 (after fault). Substantial differences in the modal components of channel 6 are noted between Sets 1 and 2. Once the slot was repaired in Set 3, the modal component of channel 6 went back to its correct value. This analysis allowed us to disregard the acceleration records of channel 6 during the faulty period as a feature selection procedure for the subsequent pattern recognition steps.

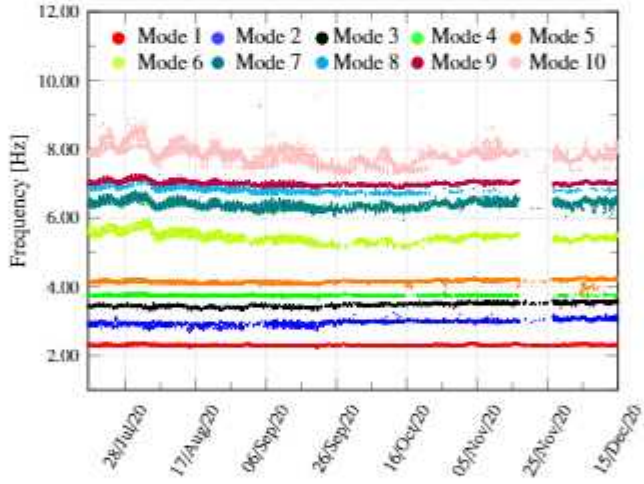

Fig. 2.4: Time series of identified resonant frequencies by automated OMA of the Consoli Palace by automated Covariance-Driven Stochastic Subspace Identification (Cov-SSI) from July to December 2020.

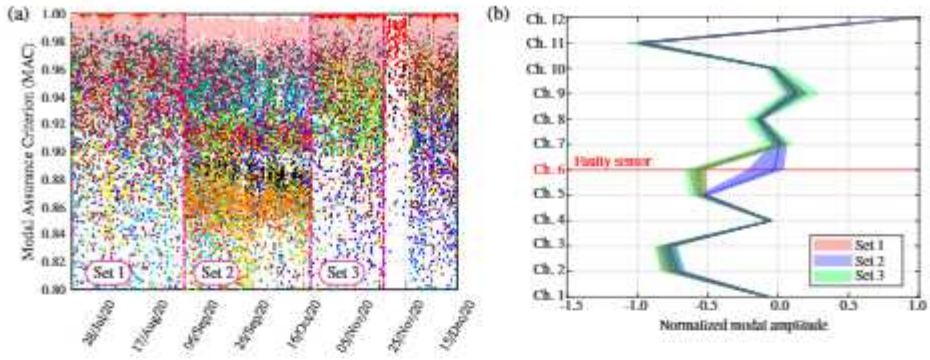

Fig. 2.5: Time series of MAC values (a) and analysis of the modal components of the fundamental mode (b) in the Consoli Palace. The shaded areas in (b) represent the 95% confidence level of the modal amplitudes.

2.3.Data cleansing

Outliers are always present to a certain degree in every feature set in SHM, being the result of manifold sources such as noise, identification errors, faulty sensors, imperfect mounting of sensors, and more. The presence of such outliers in the training data-set has two major pernicious effects. On one hand, outliers affect the effectiveness of statistical models for pattern recognition, biasing the model parameters. On the other hand, the ability of damage classification methods based upon novelty analysis to detect early-stage damage is also affected by outliers. As it will be discussed in Section 2.5, novelty analysis techniques heavily rely on the determination of statistical moments of the damage-sensitive features in the training population. The presence of outliers will bias such moments, reducing the damage sensitivity of the classification.

An extensive variety of methodologies for outlier elimination can be found in the literature, including statistical, clustering, graph, ensemble, and learning methods (refer to [50] for a comprehensive overview). It is worth noting among them a simple but particularly effective methodology based upon the Minimum Covariance Determinant (MCD) method. The MCD method introduced by Rousseau [51] is a robust estimator of multivariate location and scatter commonly used for outlier detection. Assuming Gaussian-distributed data, the MCD method seeks a subset of given size with lowest sample covariance. In the context of this work, the presence of outliers ought to be minimized in the training population $\mathbf{Y}_{tp}$. Let $H_1 \subset \{1,\dots,t_p\}$ be an h-subset with $|H_1| = h$, and $\boldsymbol{\mu}_1 = (1/h)\sum_{i\in H_1}\mathbf{y}_i$ and $\boldsymbol{\Sigma}_1 = [1/(h-1)]\sum_{i\in H_1}(\mathbf{y}_i-\boldsymbol{\mu}_1)(\mathbf{y}_i-\boldsymbol{\mu}_1)^{\mathrm{T}}$ being the empirical mean and covariance matrix of the data in H_1, respectively. The Mahalanobis distances of all the data samples in the training population read:

$$d_1(\mathbf{y}_i) = \sqrt{(\mathbf{y}_i-\boldsymbol{\mu}_1)^{\mathrm{T}}\boldsymbol{\Sigma}_1^{-1}(\mathbf{y}_i-\boldsymbol{\mu}_1)} \quad \text{for} \quad i = 1,\dots,t_p. \tag{2.2}$$

Now take H_2 another h-subset such that $\{d_1(i)\,;\, i \in H_2\} := \{(d_1)_{1:t_p}, \ldots, (d_1)_{h:t_p}\}$ where $(d_1)_{1:t_p} \leq (d_1)_{2:t_p} \leq \ldots \leq (d_1)_{t_p:t_p}$ are the ordered distances, and compute $\boldsymbol{\mu}_2$ and $\boldsymbol{\Sigma}_2$ based on H_2. Then $\det(\boldsymbol{\Sigma}_2) \leq \det(\boldsymbol{\Sigma}_1)$ holds with equality if and only if $\boldsymbol{\mu}_2 = \boldsymbol{\mu}_1$ and $\boldsymbol{\Sigma}_2 = \boldsymbol{\Sigma}_1$. This process, also known as the concentration step (C-step), can be iteratively repeated as follows:

1. Select h observations from the training data-set $\mathbf{Y}_{tp}$ conforming H_s.
2. Compute the empirical covariance $\boldsymbol{\mu}_s$ and $\boldsymbol{\Sigma}_s$.
3. Compute the Mahalanobis distances $d_s(\mathbf{y}_i)$, $i = 1, \ldots, t_p$.
4. Sort the Mahalanobis distances, and select the h observations having the smallest distances to form H_{s+1}.
5. Stop if $\det(\boldsymbol{\Sigma}_{s+1}) = 0$ or $\det(\boldsymbol{\Sigma}_{s+1}) = \det(\boldsymbol{\Sigma}_s)$, otherwise go to step 2.

The sequence $\det(\boldsymbol{\Sigma}_1) \geq \det(\boldsymbol{\Sigma}_2) \geq \det(\boldsymbol{\Sigma}_3) \geq \det(\boldsymbol{\Sigma}_4) \geq \ldots$ is non-negative, so the algorithm always converges in finite steps as there is a finite number of h-subsets [50]. Nevertheless, the final calculation of the covariance matrix may not converge to the global minimum since it highly depends upon the definition of the initial subset H_1. The evaluation of all $\binom{t_p}{h}$ subsets of size h may lead to prohibitive computational costs as the number of data samples in the training period is usually large. As an alternative solution, Rousseau and Driessen [52] proposed a Fast-MCD algorithm based upon the application of the raw MCD to a large number of initial candidates for H_1. Specifically, the algorithm comprises three sequential stages when the number of samples is considerably large ($t_p > 600$ [52]): Firstly, several disjoint subsets are drawn from the data-set (a recommended number of $n+1$ subsets [50]) and several C-steps are applied to each subset keeping the solutions with lowest determinants. Secondly, the subsets are pooled together forming a merged set, and the previously obtained best h-subsets are used as the initial subset H_1. For every initial subset, several C-steps are applied and the solutions with lowest determinants are kept. Finally, the raw MCD method is applied to the full data-set keeping the solution with lowest determinant obtained by considering the previously obtained solutions as initial subsets H_1. The algorithm is given in detail in references [52, 50, 53, 54].

For illustration purposes, Fig. 2.6 shows a toy example of outlier detection using the MCD method. The Fast-MCD algorithm is applied to a dataset of $t_p = 1250$ observations and $n = 2$ variables, in which 1000 and 250 (outliers) observations were drawn from two bi-variate normal distributions $\mathcal{N}_1$ and $\mathcal{N}_2$:

$$\mathcal{N}_1\left(\begin{bmatrix}0\\0\end{bmatrix}, \begin{bmatrix}1 & 1.5\\1.5 & 3\end{bmatrix}\right), \quad \mathcal{N}_2\left(\begin{bmatrix}2\\-2\end{bmatrix}, \begin{bmatrix}1 & -0.5\\-0.5 & 1\end{bmatrix}\right). \tag{2.3}$$

The dimension h of the subsets has been selected according to the recommendation by Rousseau and Driessen [52] as $h \approx (n+p+1)/2 = 626$. The Fast-MCD algorithm has been applied to the synthetic data-set starting from five subsets with 300 samples, and the obtained analysis results are shown in Fig. 2.6. The scatter plot in Fig. 2.6 (a) shows the optimal h-set and the remaining $t_p - h$ samples with blue and red solid points, respectively. In this figure, the 99% tolerance ellipses are also shown. Figure 2.6 (b) depicts the distance-distance plot, which represents the robust Mahalanobis distances (based upon the mean and covariance estimates after applying the MCD method) versus the distances computed from the complete data-set. On both axes, threshold limits corresponding to a 99% confidence level and defined as $\sqrt{\chi^2_{2,0.99}} = 3.0349$ are also indicated. It is clear in this figure that the MCD concentrates the data samples drawn from $\mathcal{N}_1$ in the h-subset, while isolating most of the samples from $\mathcal{N}_2$ as outliers. From the analysis of Fig. 2.6 (b), it is found that the classification using the MCD method identifies 231 outliers, while the direct analysis of the data-set only leads to 26 outliers.

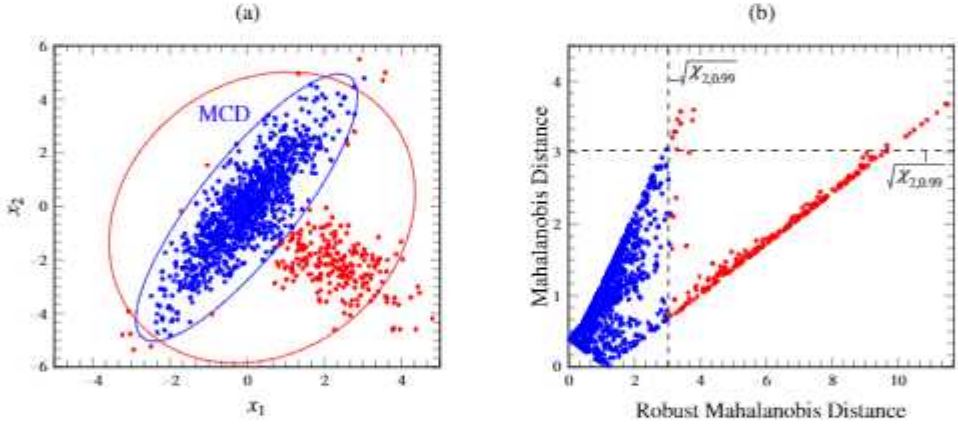

Fig. 2.6: Toy example of two overlapping bi-variate Gaussian distributions: scatter plot with 99% tolerance ellipses before and after the application of the MCD method (a), and distance-distance plot (b).

The previous approach was implemented in reference [55] to identify the presence of outliers in the time series of resonant frequencies obtained in the Consoli Palace as shown in Fig. 2.7. In particular, the dimension of the subsets has been selected according to the recommendation by Rousseau and Driessen [52] as $h = (n+p+1)/2 = (12878+6+1)/2 \approx 6443$. Once the optimal h-subset is found, all the data samples are sorted according to their Mahalanobis distances from the optimal set. Afterward, 20% of the data points with largest distances are considered as outliers and disregarded in the subsequent data normalization. It is important to remark that no outliers elimi-

nation was conducted beyond the training period leaving the time series intact. This is crucial to prevent the erroneous elimination of nonconformities that may stem from any structural pathology.

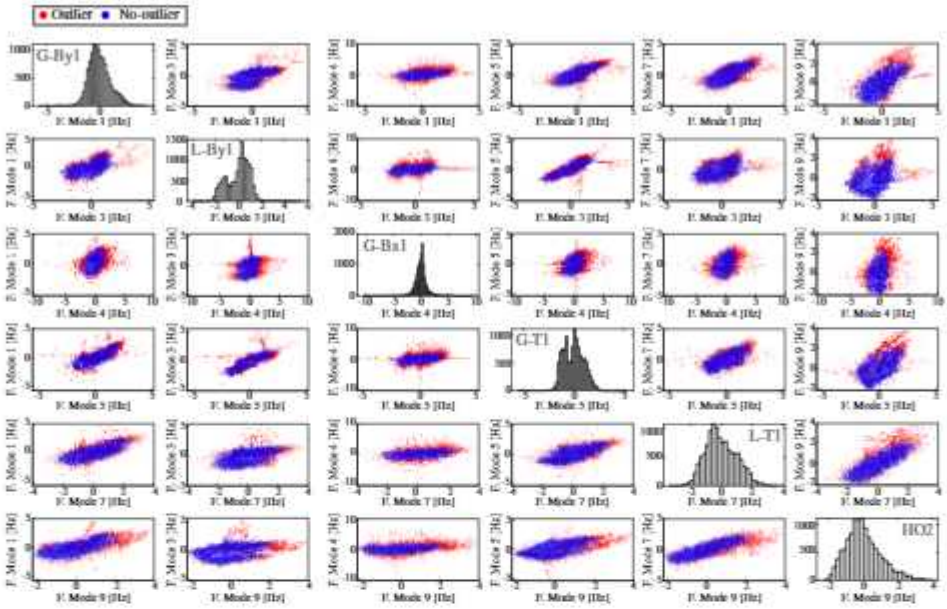

Fig. 2.7: Correlation analysis between the resonant frequencies of the Consoli Palace and outliers detection results. Twenty percent of the data points with largest Mahalanobis distances to optimal h-subset selected by MCD are considered as outliers. (Modes G-By1/Mode 1, L-T1/Mode 3, G-Bx1/Mode 4, G-T1/Mode 5, L-T1/Mode 7, and HO2/Mode 9).

2.4.Data normalization

Data normalization constitutes the process of eliminating the variability in the selected features due to variations in EOC [41]. Such variations may play a leading role in the variance of the selected features, exceeding in many cases the effects caused by damage, especially at initial stages. For instance, Peeters and De Roeck [16] found variations up to 18% in the first four resonant frequencies of the well-known case study of the Z24-Bridge as shown in Fig. 2.8. In the context of historic structures, positive correlations be-

Fig. 2.8: Fundamental frequency versus wearing surface temperature from the healthy condition of the Z-24 Bridge (Ref: [16]).

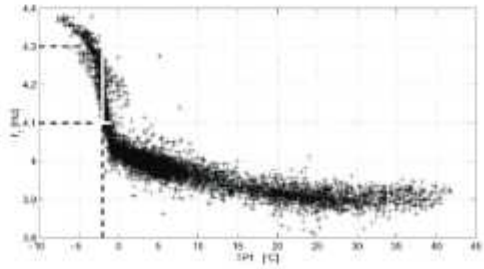

tween environmental temperature and resonant frequencies are often observed in masonry structures, which is usually ascribed to thermal-induced crack closure phenomena [56, 57, 58]. This is for instance the case of the Basilica of Santa Maria degli Angeli (Section 1.5.3) as shown in Fig. 2.9. It is noted in this figure that the resonant frequencies of the first three modes exhibit both daily and seasonal fluctuations. Specifically, mean variation ranges of 11.0%, 14.3%, 17.3% are found per year for Modes 1, 2, and 3, respectively. A similar behavior can be also observed in terms of displacements measured by two LVDTs bridging the crack faces of two major cracks of the Basilica (refer to reference [21] for further details on the monitoring system). However, completely different correlations can be found in practice as shown in the work by Gentile *et al.* [57] on the SHM of the Milan Cathedral in Italy. Their results showed a negative correlation between resonant frequencies and temperature, which was ascribed to the actions exerted by metallic tie-rods in the building. Such negative correlations are also common in reinforced-concrete and steel structures due to decreases in the material Young's modulus with increasing temperature [59, 10], such as for instance asphalt concrete pavements in roadway bridges. In general, many different situations can be found depending on the specific structural typology, solar radiation and thermal capacitance, as well as other environmental factors such as humidity, wind, snow or rain, or operational actions like traffic or human-structure interactions. These effects translate into daily and seasonal fluctuations in the selected features that may mask the appearance of damage, whereby their elimination through data normalization represents a crucial step to ensure the effectiveness of the damage identification.

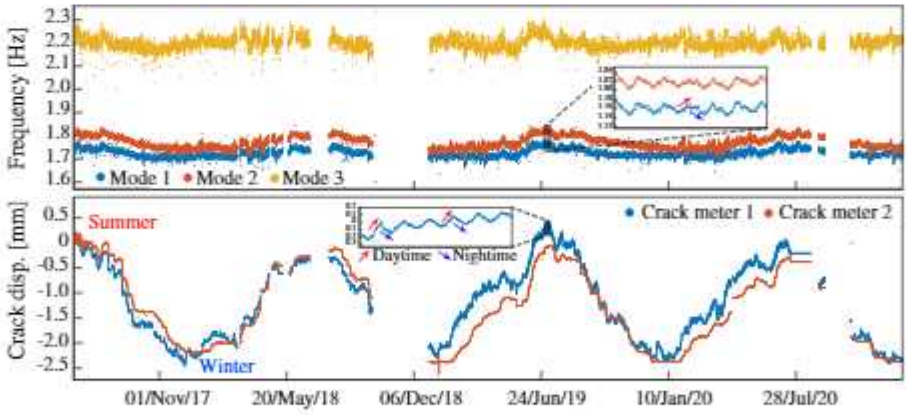

Fig. 2.9: Time series of resonant frequencies and crack displacements of the Basilica of Santa Maria degli Angeli from 2017 until 2020.

The general work-flow of the data normalization process is sketched in Fig. 2.10. The general idea is to develop a certain statistical model capable of

predicting the DSFs as a function of any combination of predictors independent from any damage condition, thus characterizing the variance in the DSFs purely driven by EOC. Let us denote $\mathbf{Y}$ the observation matrix containing the selected DSFs (static and/or dynamic features). Let us also denote a control period of t_p feature samples, usually referred to as the *training period*. This baseline data-set must statistically represent the healthy state of the structure under all the possible EOC, including both daily and seasonal fluctuations (typically one year). Generally, two different strategies can be employed for data normalization: when monitoring data of EOC are available (Input-Output) and when they are not (Output only). A wide variety of statistical models can be found for each category, amongst which some of the most commonly used ones are listed below [60, 61]:

- Input-Output regression models: Multiple Linear Regression (MLR) [62], AutoRegressive with eXogenous input model (ARX) [63], artificial neural networks [64], support vector regression [65].
- Output only regression models: Principal Component Analysis (PCA) [62], Kernel PCA (KPCA) [66], Factor Analysis (FA) [67], Autoassociative Neural Networks (ANNs) [68], time-series models [69], Cointegration (CI) [70].

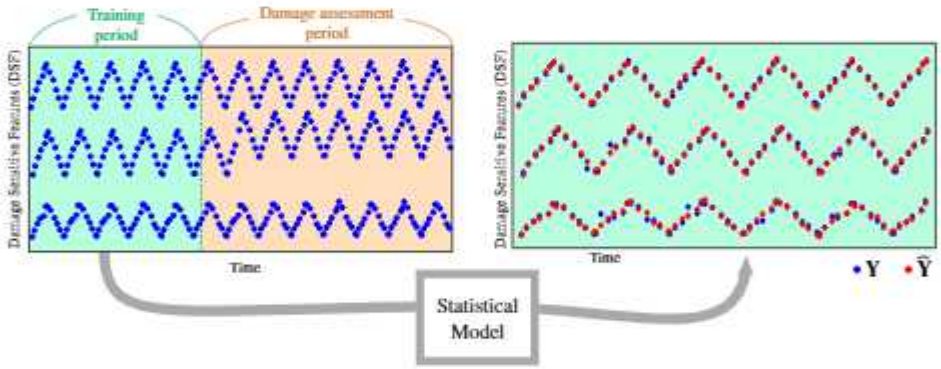

Fig. 2.10: Flowchart of data normalization through statistical pattern recognition.

In general, Output only regression models exploit correlations between the selected DSFs, in such a way that structural defects affecting such correlations will rise an anomaly. Nevertheless, since these models do not rely on predictor variables independent from structural damage, the physical interpretation of anomalies may be cumbersome and some structural defects may go unnoticed. Input-output models instead exploit correlations between DSFs and EOC. Although this approach requires monitoring data from EOC with the subsequent larger archive storage, the physical interpretation of anomalies is straightforward

since model predictions are built on variables that are intrinsically independent from any structural damage.

Given the extensive use of MLR and PCA models in the literature, their theoretical fundamentals are presented in Sections 2.4.1 and 2.4.2, respectively. In addition, two novel approaches developed in this thesis are presented afterward. These include a sparse MLR model for automated selection of predictors in Section 2.4.3 and reported in reference [55], and a general non-linear extension of statistical pattern recognition models through cluster-wise expansions in Section 2.4.4 and reported in references [71, 72].

2.4.1.MLR

MLR models exploit linear correlations between the n selected features (estimators or dependent variables) and a set of p independent exploratory variables (predictors or independent variables), which are typically taken from monitoring data of EOC (e.g. environmental temperatures, humidity, wind intensity, etc., as well as delayed variations to account for capacitance effects). The predictions $\hat{\mathbf{Y}}$ by MLR of the observation matrix $\mathbf{Y}$ are obtained as:

$$\hat{\mathbf{Y}} = [\mathbf{1}_{N\times 1}, \mathbf{X}] \begin{bmatrix} \boldsymbol{\beta}_0 \\ \boldsymbol{\beta} \end{bmatrix}, \tag{2.4}$$

where $\mathbf{1}_{N\times 1}$ is a column vector of ones and $\mathbf{X} = \left[\mathbf{x}_1, \ldots, \mathbf{x}_p\right] \in \mathbb{R}^{N\times p}$ is an observation matrix with columns containing the time series of the p selected predictors. Term $\boldsymbol{\beta}_0 \in \mathbb{R}^{1\times n}$ is a row vector of intercept terms and $\boldsymbol{\beta} = \left[\boldsymbol{\beta}_1, \ldots, \boldsymbol{\beta}_p\right] \in \mathbb{R}^{p\times n}$ is a matrix of linear regression coefficients. Let us first consider centered and normalized versions of the predictors $\mathbf{x}_j$ in $\mathbf{X}$ arranged in a normalized predictor matrix $\mathbf{X}_n$, as well a centered version of an arbitrary i-th estimator $\mathbf{y}_i$ in $\mathbf{Y}$:

$$\mathbf{x}_j^n = \frac{\mathbf{x}_j - \overline{\mathbf{x}}_j}{\sigma_{x_j}},\ j = 1, \ldots, p, \quad \mathbf{y}_i^n = \mathbf{y}_i - \overline{\mathbf{y}}_i,\ i = 1, \ldots, n, \tag{2.5}$$

with

$$\sigma_{x_j} = \sqrt{\frac{1}{N-1}\left(\mathbf{x}_j - \overline{\mathbf{x}}_j\right)\left(\mathbf{x}_j - \overline{\mathbf{x}}_j\right)^{\mathrm{T}}}. \tag{2.6}$$

A regression method estimates the coefficients vector $\boldsymbol{\beta}_i^*$ relating the normalized predictor matrix $\mathbf{X}_n$ and the i-th normalized output $\mathbf{y}_i^n$ as:

$$\mathbf{y}_i^n = \mathbf{X}_n \boldsymbol{\beta}_i^*. \tag{2.7}$$

The matrix of regression coefficients $\boldsymbol{\beta}^*$ can be readily obtained as the ordinary least squares estimator as:

$$\boldsymbol{\beta}^* = \left(\mathbf{X}_n^{\mathrm{T}}\mathbf{X}\right)^{-1}\mathbf{X}_n^{\mathrm{T}}\mathbf{Y}_n. \tag{2.8}$$

Once determined, the coefficients in $\boldsymbol{\beta}_i^*$ can be readily converted to the original scaled model as $\boldsymbol{\beta}_i = \sigma_{x_j}\boldsymbol{\beta}_i^*$, and the i-th intercept term can be computed as $\boldsymbol{\beta}_{0,i} = \bar{\mathbf{y}}_i - \bar{\mathbf{X}}\boldsymbol{\beta}_i^*$.

As an example, Fig. 2.11 shows the results of MLR analysis of the resonant frequency of the fourth mode of vibration (second flexural mode) of the San Pietro bell-tower (Section 1.5.2) from 2018 until 2020. In the analysis, the ambient temperature measurements by two thermocouples installed at the base of the cusp of the tower (T_1 indoor, T_2 outdoor) are used as predictors. Note that the model must be linear in its coefficients contained in matrix $\boldsymbol{\beta}$, while arbitrary non-linear transformations such as exponential or logarithmic functions can be applied to the predictors. As an example, the results of the MLR model using both linear and quadratic temperature values are also depicted in Fig. 2.11. Ideally, the obtained residuals should be normally distributed, thereby statistical tests assessing the gaussianity of the residuals can be used to evaluate the quality of a statistical model for data normalization. To this aim, a variety of statistical metrics can be used from simple statistics to dedicated normality tests such as the Kolmogorov-Smirnov or the Shapiro-Wilk tests. For illustrative purposes, Fig. 2.12 shows the analysis of the residuals obtained from the results in Fig. 2.11. It is noted that, although the standard deviation of the residuals decreases when quadratic terms are involved in the MLR, the kurtosis of the distribution of the residuals moves away from 3 (theoretical value for an ideal Gaussian distribution) compared to the model with linear terms, which indicates some over-fitting degree.

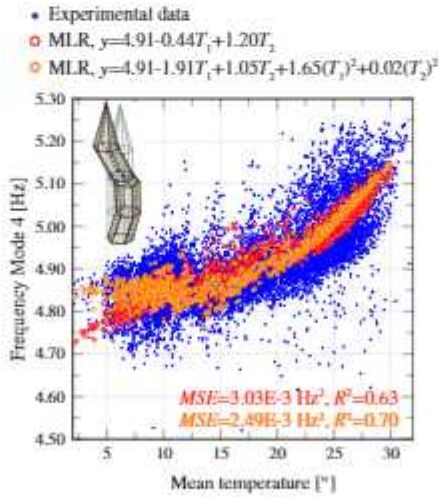

Fig. 2.11: Multiple Linear Regression analysis of the resonant frequency of the fourth mode of vibration of the San Pietro bell-tower from 2018 until 2020.

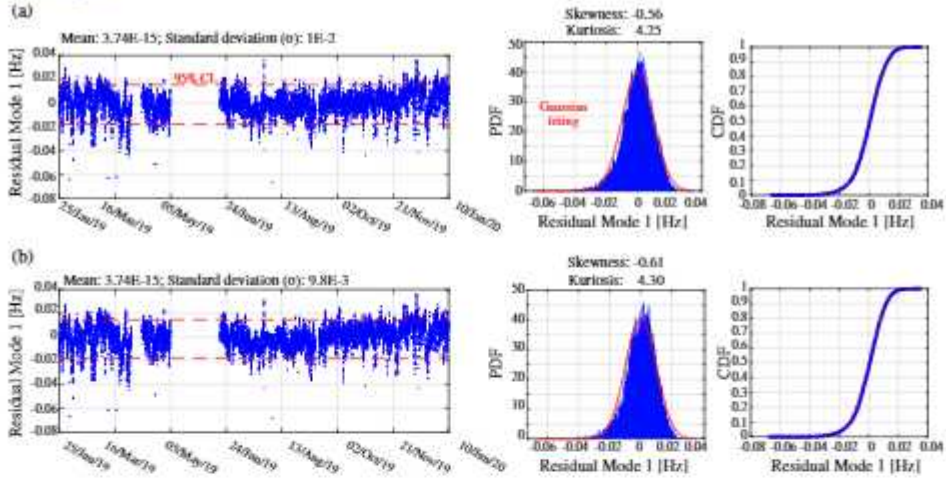

Fig. 2.12: Analysis of residuals of the statistical predictions by MLR of the fundamental frequency of the San Pietro bell-tower from 2018 until 2020. Models accounting for linear (a) and quadratic (b) temperature values.

2.4.2.PCA

PCA is a dimensionality-reduction technique used to transform databases into lower dimensional subspaces without significant losses in data variance. Mathematically, PCA is defined as an orthogonal linear transformation that converts the data to a new coordinate system where the greatest variance of the data lies on the first coordinate (called the first principal component), the second greatest variance on the second coordinate, and so on. Principal components (PCs) are the eigenvectors of the covariance matrix of the original data, thereby PCs constitute an orthogonal basis of uncorrelated components. Denoting by $\mathbf{Y}_n$ the normalized version of matrix $\mathbf{Y}$ (i.e. the feature time series are transformed to have zero mean and unit variance) and $\mathbf{\Sigma_Y} = \mathbf{Y}_n^{\mathrm{T}}\mathbf{Y}_n/(N-1) \in \mathbb{R}^{n\times n}$ its covariance matrix, the PCs can be obtained by the eigenvalue-eigenvector decomposition of $\mathbf{\Sigma_Y}$ as:

$$\mathbf{\Sigma_Y U} = \mathbf{U S}^2, \tag{2.9}$$

where the eigenvectors of $\mathbf{\Sigma_Y}$ are the columns of $\mathbf{U}$ (loading matrix) and represent the PCs, and the eigenvalues are the diagonal terms of $\mathbf{S}^2$. The PCs are sorted in descending order according to the diagonal terms of $\mathbf{S}^2$, which represent the proportion of total variance in $\mathbf{Y}$ (i.e. $\mathrm{tr}\,(\mathbf{\Sigma_Y}) = n$) explained by the PCs. The transformed data matrix $\mathbf{T} \in \mathbb{R}^{N\times n}$ (scores matrix) is the projection of the original data in $\mathbf{Y}_n$ over the space spanned by the PCs in $\mathbf{U}$:

$$\mathbf{T} = \mathbf{Y}_n\mathbf{U}. \tag{2.10}$$

In the realm of SHM, PCs providing the largest contributions to the variance are assumed to encapsulate the effects of EOC on the features matrix $\mathbf{Y}$. In this

light, matrix $\overline{\mathbf{Y}}$ can be estimated by mapping back the reduced subset of PCs onto the original data space. Specifically, if only the first l columns of matrix $\mathbf{U}$ are collected into a reduced matrix $\overline{\mathbf{U}} \in \mathbb{R}^{n \times l}$, matrix $\widehat{\mathbf{Y}}_n$ (normalized) can be obtained as:

$$\widehat{\mathbf{Y}}_n = \mathbf{Y}_n \left(\overline{\mathbf{U}}\, \overline{\mathbf{U}}^{\mathrm{T}} \right). \tag{2.11}$$

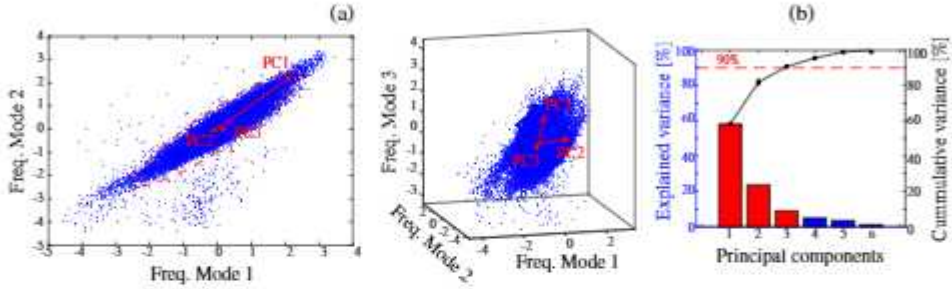

Fig. 2.13: Principal Components Analysis of the resonant frequencies of the San Pietro bell-tower. Principal components (a), and variance analysis (b). Resonant frequencies are reported in normalized values.

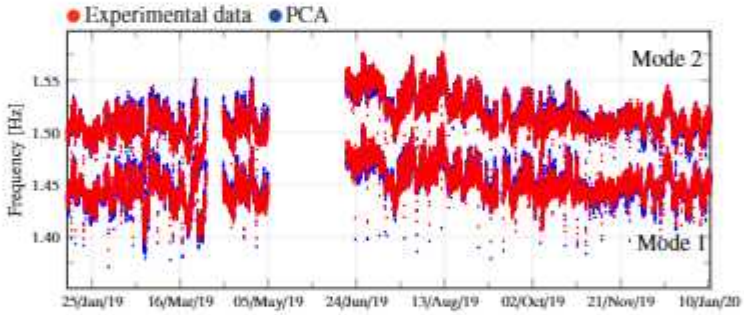

Fig. 2.14: Comparison between experimental data and predictions by PCA of the first two resonant frequencies of the San Pietro bell-tower.

The number l of PCs to be retained must be chosen according to their relative contributions to the variance in the data. If this dimension is too small, part of the EOC will not be properly captured, while an excessively large number of retained PCs will make the model suffer from over-fitting with the subsequent loss of generality. As an example, Fig. 2.13 shows the results of the PCA of six resonant frequencies of the San Pietro bell-tower identified in the frequency broadband of 1 to 12 Hz. It is noted that three PCs suffice to explain more than 90% of the variance in the resonant frequencies. The comparison of the experimental identification results of the first two resonant frequencies of

the tower and the predictions by PCA using three PCs is depicted in Fig. 2.14. It is noted that the PCA model can reproduce both the seasonal and the daily fluctuations in the resonant frequencies induced by EOC.

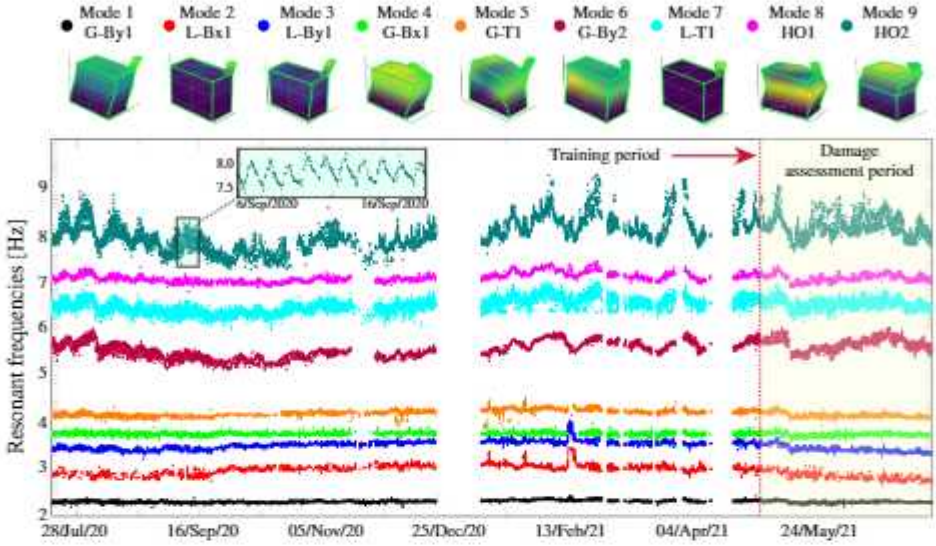

Fig. 2.15: Tracking of the resonant frequencies of the Consoli Palace from July 2020 until July 2021.

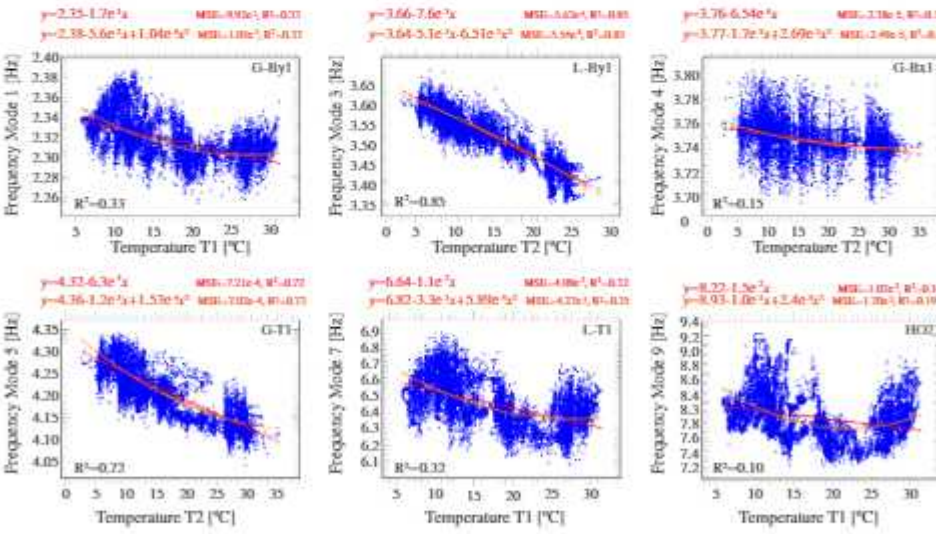

Fig. 2.16: Correlations between the natural frequencies of the Consoli Palace and the environmental temperature in the training period from July 14th 2020 until May 3rd 2021 (12878 data samples).

2.4.3.Sparse MLR (SMLR)

The quality of MLR models for feature normalization is highly dependent upon the quality of the predictor selection. The selection of such predictors is however a major difficulty in practice. To illustrate this, Figures 2.15 and 2.16 respectively furnish the time series of identified resonant frequencies of the Consoli Palace (Section 1.5.5) and their correlation with temperature. Firstly, let us note that negative frequency/temperature correlations are found in all the modes. This indicates that the global stiffness of the palace decreases as temperature rises. As previously discussed, such a trend is quite uncommon in masonry structures. In the case of the Consoli Palace, negative frequency/temperature correlations were previously found by Kita *et al.* [24]. Those authors attributed this trend to temperature-induced slackening of some metallic tie rods installed in the Arengo hall to restrain the lateral thrusts exerted by the barrel-vault ceiling, as well as the possible contribution of the existing macro cracks. Overall, considerably linear frequency-temperature correlations are observed in the natural frequencies of Modes 3 and 4, whereas noticeably non-linear correlations are identified instead for Modes 1, 5, 7 and 9, which may be ascribed to the existence of complex temperature-driven mechanisms or a strong dependence on unmonitored EOC. The large scatter in the correlation plots of Modes 1, G-x1, and L-T1 may indicate the presence of thermal capacitance effects, that is some delays in heat transfer from the position of the thermocouples through the cross-sections of the masonry walls.

Intricate correlations such as those in Fig. 2.16, which are indeed quite common in civil engineering structures, motivate the interest for developing automated procedures for optimal predictors selection. In reference [55], a novel methodology of sparse MLR was proposed for that aim. In general, let us consider a univariate linear model defined as $\mathbf{y} = \mathbf{X}\beta + \varepsilon$, with ε being a zero mean error term. Let us also consider that matrix $\mathbf{X}$ contains a large database of potential predictors variables including all the available monitoring data from EOC plus algebraic (e.g. exponential functions) and time-shifted variations with varying delays to accommodate capacitance effects. It is thus reasonable to consider that some of these predictors provide no contribution to the variance of $\mathbf{y}$, being the variability mostly explained by a reduced subset of them. In this light, it is considered that the linear model in Eq. (2.7) is sparse, in such a way that the coefficients in β are non-zero for the most representative predictors, while the remaining coefficients corresponding to the least influential ones are zero. Let use denote the active set $\mathcal{A}$ as the indices in β corresponding to non-zero elements, and the inactive set $\mathcal{I}$ as the complementary set of $\mathcal{A}$. Also, let us note $\mathbf{X}_{\mathcal{A}}$ consisting of a subset of predictors obtained by extracting from $\mathbf{X}$ the columns corresponding to the indexes in $\mathcal{A}$. Among the variety of sparse regression methods available in the literature (see e.g. [73]), the least-angle regression (LAR) model has proved particularly efficient. The LAR algorithm is a forward stepwise regression approach set out by Efron *et al.* [74]. The

active set is initialized to be empty, $\mathcal{A} = \emptyset$, and the indexes of all the predictors are included in the inactive set, i.e. $\mathcal{I} = \{1, \ldots, p\}$. The algorithm starts by assuming the coefficient vector $\boldsymbol{\beta}^{(0)} = \mathbf{0}$ and, thus, the residual $\boldsymbol{\varepsilon}_0 = \mathbf{y} - \hat{\mathbf{y}}^{(0)}$, with $\hat{\mathbf{y}}^{(0)} = \mathbf{0}$ being the initial prediction of the linear model. The first predictor to be included in the active set is the one which has the largest correlation with the current residual, that is:

$$c = \max_{i \in \mathcal{I}} \left| \mathbf{x}_i^{\mathrm{T}} \boldsymbol{\varepsilon}_0 \right|. \tag{2.12}$$

Let us assume the index j is the one corresponding to c, and thus the index to be added to the active set $\mathcal{A}$. Then, the regression coefficients are moved towards their least-square value, until some other predictor has as much correlation with the current residual. This corresponds to an updating of the form:

$$\boldsymbol{\beta}^{(1)} = \boldsymbol{\beta}^{(0)} + \gamma \left(\boldsymbol{\beta}_{OLS}^{(1)} - \boldsymbol{\beta}^{(0)} \right), \tag{2.13}$$

with $\boldsymbol{\beta}_{OLS}^{(1)}$ being the ordinary least-squares (OLS) solution:

$$\boldsymbol{\beta}_{OLS}^{(1)} = \left(\mathbf{X}_{\mathcal{A}}^{\mathrm{T}} \mathbf{X}_{\mathcal{A}} \right)^{-1} \mathbf{X}_{\mathcal{A}}^{\mathrm{T}} \mathbf{y}, \tag{2.14}$$

and γ the step length $0 < \gamma \leq 1$. Accordingly, the prediction by the linear model and the residual are updated as $\hat{\mathbf{y}}^{(1)} = \hat{\mathbf{y}}^{(0)} + \gamma \left(\hat{\mathbf{y}}_{OLS}^{(1)} - \hat{\mathbf{y}}^{(0)} \right)$ and $\boldsymbol{\varepsilon}_1 = \mathbf{y} - \hat{\mathbf{y}}^{(1)}$, respectively, with $\hat{\mathbf{y}}_{OLS}^{(1)}$ being the least squares solution, i.e. $\hat{\mathbf{y}}_{OLS}^{(1)} = \mathbf{X}_{\mathcal{A}} \boldsymbol{\beta}_{OLS}^{(1)}$. In order to determine the value of γ, one seeks the smallest positive value where correlations with the current residual become equal, i.e. $\mathbf{x}_{i \in \mathcal{I}}^{\mathrm{T}} \boldsymbol{\varepsilon}_1 = \mathbf{x}_j^{\mathrm{T}} \boldsymbol{\varepsilon}_1$, leading to:

$$\mathbf{x}_{i \in \mathcal{I}}^{\mathrm{T}} \left[\mathbf{y} - \hat{\mathbf{y}}^{(0)} - \gamma \left(\hat{\mathbf{y}}_{OLS}^{(1)} - \hat{\mathbf{y}}^{(0)} \right) \right] = \mathbf{x}_j \left[\mathbf{y} - \hat{\mathbf{y}}^{(0)} - \gamma \left(\hat{\mathbf{y}}_{OLS}^{(1)} - \hat{\mathbf{y}}^{(0)} \right) \right]. \tag{2.15}$$

Solving the expression in Eq. (2.15) for γ, one gets:

$$\gamma = \frac{\left(\mathbf{x}_i - \mathbf{x}_j \right)^{\mathrm{T}} \left(\mathbf{y} - \hat{\mathbf{y}}^{(0)} \right)}{\left(\mathbf{x}_i - \mathbf{x}_j \right)^{\mathrm{T}} \left(\hat{\mathbf{y}}_{OLS}^{(1)} - \hat{\mathbf{y}}^{(0)} \right)} = \frac{\left(\mathbf{x}_i - \mathbf{x}_j \right)^{\mathrm{T}} \boldsymbol{\varepsilon}_0}{\left(\mathbf{x}_i - \mathbf{x}_j \right)^{\mathrm{T}} \mathbf{d}}, \tag{2.16}$$

where $\mathbf{d} = \hat{\mathbf{y}}_{OLS}^{(1)} - \hat{\mathbf{y}}^{(0)}$ is the direction of the walk. Note that $\mathbf{d}$ is orthogonal to $\boldsymbol{\varepsilon}_0$, therefore we have $\mathbf{x}_i \boldsymbol{\varepsilon}_0 = \mathbf{x}_i \mathbf{d} \equiv c$. Since the predictors in $\mathbf{X}$ are assumed to be normalized, i.e. $|\mathbf{x}_i| = 1$, the condition in Eq. (2.15) may be interpreted in terms of dot products as $\mathbf{x}_i^{\mathrm{T}} \boldsymbol{\varepsilon}_1 = \cos \theta_i = \mathbf{x}_j^{\mathrm{T}} \boldsymbol{\varepsilon}_1 = \cos \theta_j$, i.e. $\theta_i = \theta_j$. This bisection condition is equivalent to imposing the movement of the predictor coefficients along the equiangular direction between the predictors $\mathbf{x}_i$ and $\mathbf{x}_j$

and the current residual ε_1, i.e. the least angle direction. Furthermore, since the sign of the correlation between variables is irrelevant, Eq. (2.16) can be in general written as:

$$\gamma = \min_{i \in \mathcal{I}} \left\{ \frac{\mathbf{x}_i^{\mathrm{T}} \varepsilon_0 - c}{\mathbf{x}_i^{\mathrm{T}} \mathbf{d} - c}, \frac{\mathbf{x}_i^{\mathrm{T}} \varepsilon_0 + c}{\mathbf{x}_i^{\mathrm{T}} \mathbf{d} + c} \right\}, \quad 0 < \gamma \leq 1. \tag{2.17}$$

This process can be performed iteratively $p-1$ times according to the following steps:

1. Initialize the coefficient vector $\beta^{(0)} = \mathbf{0}$, the fitted vector $\hat{\mathbf{y}}^{(0)} = \mathbf{0}$, the active set $\mathcal{A} = \emptyset$ and the inactive set $\mathcal{I} = \{1, \ldots, p\}$.
2. **for** k = 0 to p-2 **do**
3. Update the residual $\varepsilon_k = \mathbf{y} - \hat{\mathbf{y}}^{(k)}$.
4. Find the maximum correlation $c = \max_{i \in \mathcal{I}} \left| \mathbf{x}_i^{\mathrm{T}} \varepsilon_k \right|$.
5. Move variable corresponding to c from $\mathcal{I}$ to $\mathcal{A}$.
6. Compute the least squares solutions $\beta_{OLS}^{(k+1)} = \left(\mathbf{X}_{\mathcal{A}}^{\mathrm{T}} \mathbf{X}_{\mathcal{A}} \right)^{-1} \mathbf{X}_{\mathcal{A}}^{\mathrm{T}} \mathbf{y}$ and $\mathbf{y}_{OLS}^{(k+1)} = \mathbf{X}_{\mathcal{A}} \beta_{OLS}^{(k+1)}$.
7. Compute the direction of the walk $\mathbf{d} = \hat{\mathbf{y}}_{OLS}^{(k+1)} - \hat{\mathbf{y}}^{(k)}$.
8. Compute the step length $\gamma = \left\{ \frac{\mathbf{x}_i^{\mathrm{T}} \varepsilon_k - c}{\mathbf{x}_i^{\mathrm{T}} \mathbf{d} - c}, \frac{\mathbf{x}_i^{\mathrm{T}} \varepsilon_k + c}{\mathbf{x}_i^{\mathrm{T}} \mathbf{d} + c} \right\}, \quad 0 < \gamma \leq 1.$
9. Update the regression coefficients: $\beta^{(k+1)} = \beta^{(k)} + \gamma \left(\beta_{OLS}^{(k+1)} - \beta^{(k)} \right)$.
10. Update the fitted vector: $\hat{\mathbf{y}}^{(k+1)} = \hat{\mathbf{y}}^{(k)} + \gamma \left(\hat{\mathbf{y}}_{OLS}^{(k+1)} - \hat{\mathbf{y}}^{(k)} \right)$.
11. **end for**

The algorithm at step p is completed with the full OLS solution, i.e. $\beta^{(p)} = \left(\mathbf{X}^{\mathrm{T}} \mathbf{X} \right)^{-1} \mathbf{X}^{\mathrm{T}} \mathbf{y}$. The main output is the series of coefficients $\mathcal{B} = \left\{ \beta^{(0)}, \ldots, \beta^{(p)} \right\}$, which represent different linear models with decreasing level of sparsity. Finally, the best regression model in $\mathcal{B}$ can be selected according to certain quality criteria such as the maximum number of selected predictors or the minimum residual sum-of-squares (RSS), or information based statistical criteria like the Bayesian Information Criterion (BIC) [75] or the Akaike Information Criterion (AIC) [76]. To better illustrate the working mechanism of the LAR algorithm, Fig. 2.17 presents the geometrical interpretation of the determination of the coefficient parameters in the case of 3 covariates $\mathbf{x}_1$, $\mathbf{x}_2$, and $\mathbf{x}_3$. In the initial step $k = 0$ in Fig. 2.17 (a), $\mathbf{x}_1$ is selected as the first predictor since it has the largest correlation with the initial residue $\varepsilon_0 = \mathbf{y}$. Therefore, $\beta^{(1)} = \gamma \beta_{OLS}^{(1)}$, and we need to determine the step length γ. To do so, we need to apply the equiangular condition in Eq. (2.16). In this initial case ($k = 0$), this equation reduces to:

$$\mathbf{x}_1 \underbrace{\left(\mathbf{y} - \gamma \beta_{OLS}^{(1)} \right)}_{\varepsilon_{12}} = \mathbf{x}_2 \underbrace{\left(\mathbf{y} - \gamma \beta_{OLS}^{(1)} \right)}_{\varepsilon_{12}}, \tag{2.18}$$

and

$$\mathbf{x}_1 \underbrace{\left(\mathbf{y} - \gamma\boldsymbol{\beta}_{OLS}^{(1)}\right)}_{\boldsymbol{\varepsilon}_{13}} = \mathbf{x}_3 \underbrace{\left(\mathbf{y} - \gamma\boldsymbol{\beta}_{OLS}^{(1)}\right)}_{\boldsymbol{\varepsilon}_{13}}. \tag{2.19}$$

The bisection condition in Eq. (2.18) leads to a solution where the residue vector $\boldsymbol{\varepsilon}_{12}$ has the same angle α_{12} with the inactive predictor $\mathbf{x}_2$ and the active predictor $\mathbf{x}_1$. Similarly, Eq. (2.19) leads to a different solution where the residue vector $\boldsymbol{\varepsilon}_{13}$ has the same angle α_{13} with $\mathbf{x}_3$ and $\mathbf{x}_1$. In this example, $\mathbf{x}_3$ has the least angle ($\boldsymbol{\varepsilon}_{13} < \boldsymbol{\varepsilon}_{12}$) and, therefore, Eq. (2.19) determines the step length γ. In the second step ($k = 1$), the direction of the walk is given by the OLS projection of $\mathbf{y}$ onto the active set defined by $\mathbf{x}_1$ and $\mathbf{x}_3$, i.e. $\hat{\mathbf{y}}_{OLS}^{(2)}$. This procedure is repeated until reaching the full OLS as shown in Fig. 2.17 (b), where covariates $\mathbf{x}_1$, $\mathbf{x}_3$, and $\mathbf{x}_2$ are added sequentially to the regression. Variables $\hat{\mathbf{y}}_{OLS}^{(1)}$ and $\hat{\mathbf{y}}_{OLS}^{(2)}$ represent the partial OLS solutions on $\mathbf{x}_1$ and $\{\mathbf{x}_1, \mathbf{x}_3\}$, respectively, while $\hat{\mathbf{y}}_{OLS}^{(3)} = \hat{\mathbf{y}}^{(3)}$ represents the full OLS solution.

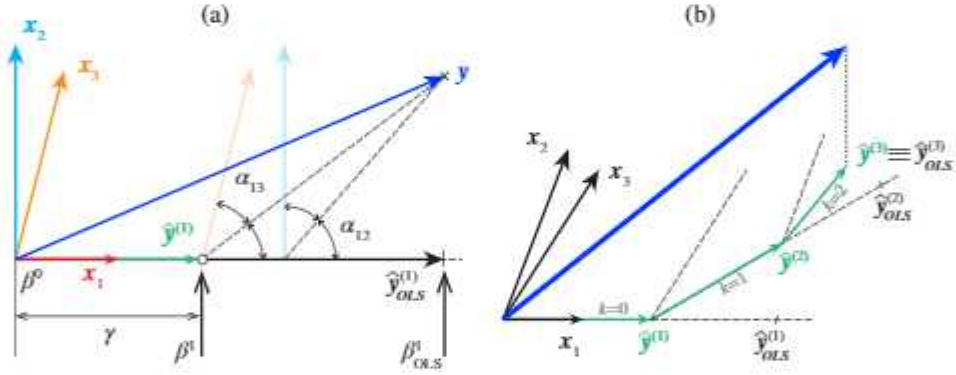

Fig. 2.17: Geometric representation of the LAR algorithm in the case of 3 covariates. (a) Initial step $k = 0$, and (b) determination of the complete solution path.

This formulation was applied to remove the EOC effects from the resonant frequencies of the Consoli Palace previously reported in Fig. 2.16. To do so, a total of 48 potential predictors were considered. These comprised linear and quadratic (denoted with the subscript 2) versions of the time series of environmental temperatures by thermo-couples T1, T2 and T3. Additionally, with the aim of accommodating potential thermal capacitance effects in the palace, time delayed versions of the previous time series were also accounted for. These included delays of 30 min (2 samples), 1 hour (4 samples), 2 hours (8 samples), 5 hours (20 samples), 12 hours (48 samples), 24 hours (96 samples), and 48 hours (192 samples). On this basis, Figs. 2.18 (a,b) show the coefficients of the LAR regressions obtained for the resonant frequency of Mode

1 (G-By1). It is noted in Fig. 2.18 (a) how the number of predictors with non-zero regression coefficients β_i increases as the LAR algorithm progresses. Note that the proposed method is capable of automatically finding correlations with delayed predictors, making the statistical model dynamic in nature. In order to select the optimal model and, therefore, the optimal set of predictors, several metrics have been implemented, namely RSS, BIC, and AIC. In general, the BIC and AIC criteria yielded similar solutions in all the considered estimators, while the RSS led to less sparse solutions as it is the case in Fig. 2.18 (b). For the sake of minimizing over-fitting limitations, the solution obtained by minimizing the BIC criterion has been retained.

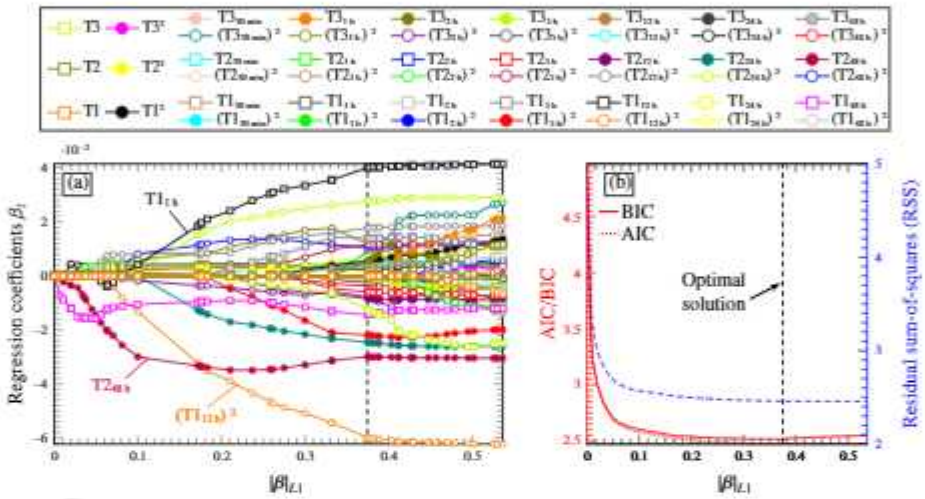

Fig. 2.18: LAR analysis of the experimentally identified resonant frequencies of Mode G-By1 (a,b). Evolution of the regression coefficients β_i versus the L1 norm ($|\boldsymbol{\beta}|_{L1} = \sum_{i=1}^{p} |\beta_i|$) (a), and selection of optimal set of predictors based upon the residual sum-of-squares (RSS), and Bayesian Information Criterion (BIC) and Akaike Information Criterion (AIC) (b). (Training period from July 14th 2020 until May 3rd 2021 (12878 data samples)).

2.4.4. Cluster-wise nonlinear regression

A common circumstance in SHM regards the appearance of diverse environmental regimes manifesting in the shape of non-linear EOC correlations. This is the case, for instance, of masonry structures experiencing freezing conditions during the winter, when the icing of pore water in masonry leads to a dramatic change in temperature/stiffness relationship. As an illustrative example, Fig. 2.19 shows the time series of resonant frequencies of the Consoli Palace identified through automated OMA between July 2017 and June 2019. It is interesting to note that local sudden increases in the resonant frequencies were found during the time period from February 25th to March 1st 2017. Freezing air temperatures were registered during these days, thereby such in-

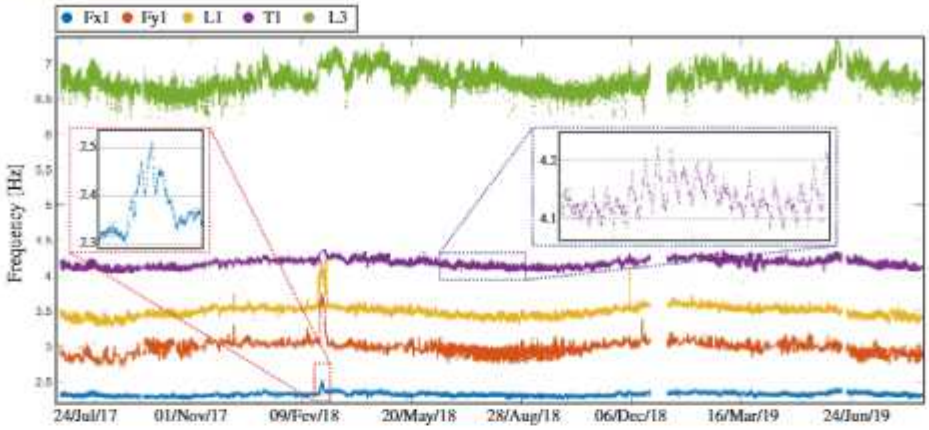

Fig. 2.19: Frequency tracking results since July 2017 until January 2019 of the permanent SHM system installed in the Consoli Palace. Modes Fx1 (first global bending mode in the $x-$direction), Fy1 (first global bending mode in the $y-$direction), L1 (first order local mode related to the interaction between the palace and the bell-tower), T1 (global torsional mode), and L3 (third order local mode).

creases are conceivably due to the formation of ice in the micro porosity of the mortar joints and the consequent stiffening effect. Such transient variations cannot be reproduce by any of the aforementioned statistical pattern recognition. To address this issue, a general cluster-wise non-linear extension using a Gaussian Mixture Model (GMM) was proposed in reference [71] and later used and validated to identify damage in the Z-24 Bridge and the Consoli Palace in reference [72]. The general idea is that the DSFs experiencing distinct environmental regimes can be approximately identified through different multi-dimensional Gaussian distributions with different mean vectors and covariance matrices. Once identified, any of the previously mentioned normalization techniques can be implemented in a cluster-wise fashion, thus achieving non-linear simulation capabilities.

The GMM model assumes that the probability density function $p(\mathbf{x})$ of the data set in the training period $\mathbf{X}$ (in general, non-normally distributed) can be represented as a linear superposition of K Gaussian components as [77]:

$$p(\mathbf{x}) = \sum_{k=1}^{K} \pi_k \mathcal{N}\left(\mathbf{x} \,|\boldsymbol{\mu}_k, \boldsymbol{\Sigma}_k\right). \tag{2.20}$$

where each component of the mixture is defined as a Gaussian distribution $\mathcal{N}\left(\mathbf{x} \,|\boldsymbol{\mu}_k, \boldsymbol{\Sigma}_k\right)$ with mean and covariance matrix denoted by $\boldsymbol{\mu}_k$ and $\boldsymbol{\Sigma}_k$, respectively. The parameters $\boldsymbol{\pi} = [\pi_1, \ldots, \pi_K]^{\mathrm{T}}$ in Eq. (2.20) are called the mixing coefficients, and they range between 0 and 1 ($0 \leq \pi_k \leq 1$) and sum to one ($\sum_{k=1}^{K} \pi_k = 1$). The model parameters, $\boldsymbol{\mu}_k$,$\boldsymbol{\Sigma}_k$ and π_k, are fitted by

minimizing the log-likelihood function:

$$\ln p(\mathbf{X}\,|\boldsymbol{\pi},\boldsymbol{\mu},\boldsymbol{\Sigma}) = \sum_{n=1}^{t_p} \ln \left\{ \sum_{k=1}^{K} \pi_k \mathcal{N}\left(\mathbf{x}_n\,|\boldsymbol{\mu}_k,\boldsymbol{\Sigma}_k\right) \right\}. \tag{2.21}$$

The maximum likelihood solution for the parameters ($\boldsymbol{\mu}$,$\boldsymbol{\Sigma}$ and $\boldsymbol{\pi}$) is estimated using the iterative Expectation-Maximization (EM) algorithm. In the expectation (E) step, the parameters (initial guess at the beginning) are held fixed and the posterior probability of assigning $\mathbf{x}_n$ to the k's cluster is given by the so-called responsibilities $\gamma(z_{nk})$ as:

$$\gamma(z_{nk}) = \frac{\pi_k \mathcal{N}\left(\mathbf{x}_n\,|\boldsymbol{\mu}_k,\boldsymbol{\Sigma}_k\right)}{\sum_{j=1}^{K} \pi_j \mathcal{N}\left(\mathbf{x}_n\,|\boldsymbol{\mu}_j,\boldsymbol{\Sigma}_j\right)}, \tag{2.22}$$

where z_{nk} is an element of a K-dimensional binary random variable $\mathbf{z}$ with a 1-of-K representation. Only one element in $\mathbf{z}$ is equal to 1 and all other elements are 0. Then, in the maximization (M) step, the parameters are re-estimated using the posterior probability calculated in the previous E step as follows:

$$\boldsymbol{\mu}_k^{\text{new}} = \frac{1}{N_k} \sum_{n=1}^{t_p} \gamma(z_{nk}) \mathbf{x}_n, \tag{2.23}$$

$$\boldsymbol{\Sigma}_k^{\text{new}} = \frac{1}{N_k} \sum_{n=1}^{t_p} \gamma(z_{nk}) \left(\mathbf{x}_n - \boldsymbol{\mu}_k^{\text{new}}\right) \left(\mathbf{x}_n - \boldsymbol{\mu}_k^{\text{new}}\right)^{\mathrm{T}}, \tag{2.24}$$

$$\pi_k^{\text{new}} = N_k/N, \quad N_k = \sum_{n=1}^{t_p} \gamma(z_{nk}). \tag{2.25}$$

The log-likelihood in Eq. (2.21) can then be evaluated. Convergence of either the parameters of the log likelihood is checked, and if the criteria are not satisfied, the process is iterated using the updated data values until the criteria are met. Once the K clusters have been defined in the training period, new data samples are assigned to the cluster with the least Mahalanobis distance.

To illustrate the potential of the previous approach, Fig. 2.20 presents the fundamental frequency of the Consoli Palace versus environmental temperature throughout the training period of one year. In this figure, the presence of freezing conditions is evident in the shape of hasty frequency increases. Moreover, it is noted that the frequency-temperature relationship is not linear, but describes a non-linear behavior with certain hysteresis. Such a behavior may be due to the intricate geometry and distribution of volumes of the palace, which presumably originate the presence of complex temperature/humidity gradients throughout the building. In this case, the use of clustering approaches for the

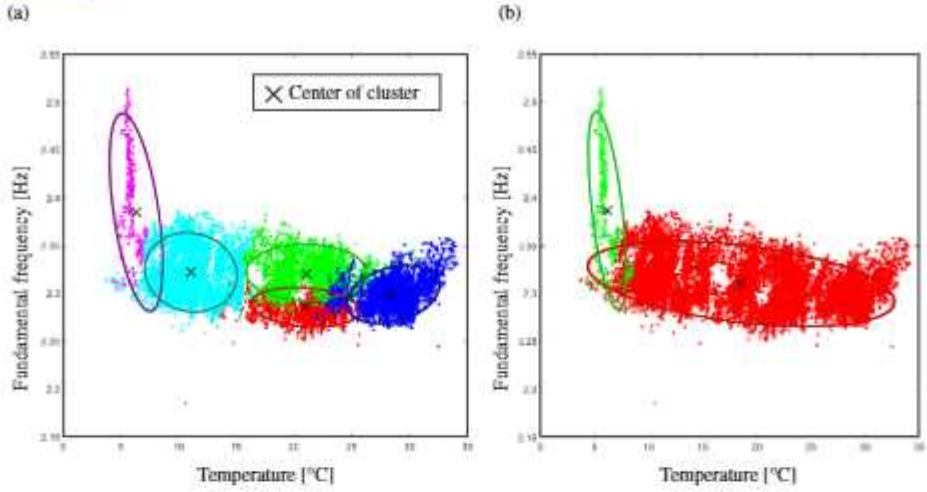

Fig. 2.20: Clustering results of the resonant frequencies of the Consoli Palace using the GMM model considering five clusters (a) and two clusters (b).

discrimination of different environmental regimes becomes imperative. Specifically, two different GMM models have been investigated, one using 5 clusters in Fig. 2.20 (a) and a second one only using 2 clusters in Fig. 2.20 (b). It is noted that the database corresponding to the frequencies under freezing conditions is well captured by both models. Additionally, it is interesting to note that the GMM model with the largest number of clusters differentiate four clusters in the frequency-temperature hysteresis cycles. Two clusters (cyan and blue) collect the data samples with minimum/maximum temperature values, while two other clusters (green and red) separate the two branches closing the hysteresis cycles. This fact may indicate the existence of distinct cooling and heating mechanisms. It is also straightforward to implement an automated identification of the optimal number of clusters by means of a certain statistical quality metric such as the BIC or AIC criteria.

2.5.Novelty Analysis

Once the statistical pattern recognition model has been trained, it can be used to filter out the effects of EOC from the selected DSFs. To do so, the residual matrix $\mathbf{E} \in \mathbb{R}^{n \times N}$ between the features in $\mathbf{Y}$ and the predictions made by the statistical model $\widehat{\mathbf{Y}}$ can be obtained as (see Fig. 2.21 (a)):

$$\mathbf{E} = \mathbf{Y} - \widehat{\mathbf{Y}}, \tag{2.26}$$

Note that matrix $\widehat{\mathbf{Y}}$ condenses the part of the variance of the features in $\mathbf{Y}$ driven by EOC. It is important to recall that the statistical model was trained considering the distribution of DSFs within a certain training period (healthy condition) and, thus, its predictions are not affected by any damage condition.

Hence, when the system remains healthy, matrix $\mathbf{E}$ only contains the residual variance stemming from modeling errors. Conversely, if a certain damage develops, this only affects the data contained in $\mathbf{Y}$ while matrix $\hat{\mathbf{Y}}$ remains unaltered. Therefore, matrix $\mathbf{E}$ concentrates the damage-induced variance and is apt for being used for damage identification.

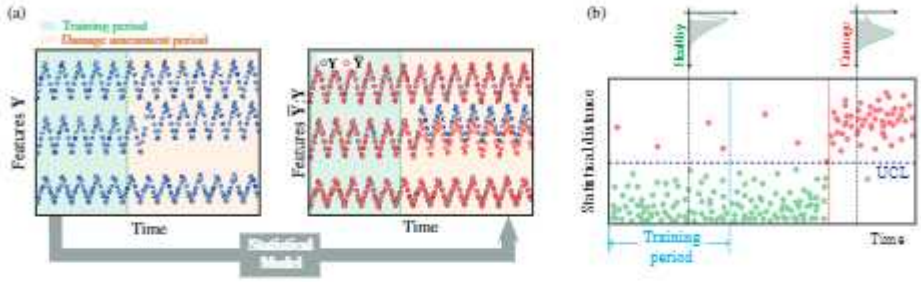

Fig. 2.21: Flowchart of data normalization through statistical pattern recognition (a), and schematic representation of damage detection using control charts (b).

Once the residual error matrix $\mathbf{E}$ is computed, the appearance of damage can be detected through novelty analysis of control charts as sketched in Fig. 2.21 (b). These furnish in time a certain statistical distance accounting for disturbances in the distribution of the residuals contained in $\mathbf{E}$. By defining an in-control region, the appearance of out-of-control processes, possibly associated to damage, is detected in the shape of data points violating the in-control region. A wide variety of control charts has been reported in the literature, although the Hotelling's T^2, Multivariate Cumulative Sum (MCUSUM), and Multivariate Exponentially Weighted Moving Average (MEWMA) control charts are the most popular ones in the realm of SHM. Below the reader may find a concise overview of the theoretical formulation of these control charts. These statistical distances are positive by definition, so an in-control region can be defined by an interval $[0, UCL]$, with the upper control limit UCL relating the statistical distance associated with a certain confidence level for the distribution of data within the training period. On this basis, control charts constitute an easily automatable and intuitive tool to conduct damage detection. The user can identify the appearance of an anomalous condition through persistent accumulations of data points violating the in-control region as illustrated in Fig. 2.21 (b).

- *Hotelling's* T^2: The Hotelling's T^2 control chart is one of the the most extensively used in the realm of SHM. The analyzed statistical distance is the squared Mahalanobis distances of the residuals in $\overline{\mathbf{E}}$ as [78]:

$$T_i^2 = r\left(\overline{\mathbf{E}} - \overline{\overline{\mathbf{E}}}\right)^{\mathrm{T}} \boldsymbol{\Sigma}_0^{-1}\left(\overline{\mathbf{E}} - \overline{\overline{\mathbf{E}}}\right), \; i = 1, 2, \ldots, N/r, \tag{2.27}$$

where r is an integer parameter referred to as subgroup size, $\overline{\mathbf{E}}$ is the mean of the residuals in the subgroup of the last r observations, while $\overline{\overline{\mathbf{E}}}$ and $\mathbf{\Sigma}_0$ are the mean values and the covariance matrix of the residuals statistically estimated in the training period.

- *Multivariate Cumulative Sum (MCUSUM)*: This control chart appears as an improvement of the sensitivity of the T^2 control chart to detect small shifts in the mean of the statistical process, and it is based upon the principle of accumulating information of past observations. Among the different versions of this control chart available in the literature, the MCUSUM method proposed by Crosier [79] is one of the most popular approaches and is given by:

$$MCUSUM_i = \left(r\, \mathbf{S}_i^{\mathrm{T}}\, \mathbf{\Sigma}_0^{-1}\, \mathbf{S}_i \right)^{1/2}, \; i = 1, 2, \ldots, N/r, \tag{2.28}$$

with

$$\begin{aligned} C_i &= \left[r \left(\mathbf{S}_{i-1} + \overline{\mathbf{E}} - \overline{\overline{\mathbf{E}}} \right)^{\mathrm{T}} \mathbf{\Sigma}_0^{-1} \left(\mathbf{S}_{i-1} + \overline{\mathbf{E}} - \overline{\overline{\mathbf{E}}} \right) \right]^{1/2}, \\ \mathbf{S}_0 &= \mathbf{0}, \\ \mathbf{S}_i &= \begin{cases} \mathbf{0}, & \text{if} \quad C_i \leq k, \\ \left(\mathbf{S}_{i-1} + \overline{\mathbf{E}} - \overline{\overline{\mathbf{E}}} \right) \left(1 - k/C_i \right), & \text{if} \quad C_i > k, \end{cases} \end{aligned} \tag{2.29}$$

where k is a constant parameter. Specific expressions for setting k can be found in reference [79].

- *Multivariate Exponentially Weighted Moving Average (MEWMA)*: Originally proposed by Lowry *et al.* [80], the MEWMA control chart represents an intermediate solution between the T^2 and the MCUSUM control charts. Alike the MCUSUM control chart, the MEWMA method also accounts for the information from past observations, although it gives weights decreasing in a geometric progression from the most recent observation to the first one. The statistical distance used in the MEWMA control chart reads:

$$MEWMA_i = \left(r\, \mathbf{z}_i^{\mathrm{T}}\, \mathbf{\Sigma}_{z_i}^{-1} \mathbf{z}_i \right)^{1/2}, \; i = 1, 2, \ldots, N/r, \tag{2.30}$$

with

$$\begin{aligned} \mathbf{z}_i &= \lambda\left(\overline{\mathbf{E}} - \overline{\overline{\mathbf{E}}}\right) + (1-\lambda)\mathbf{z}_{i-1}, \\ \mathbf{\Sigma}_{z_i} &= \lambda\frac{1-(1-\lambda)^{2i}}{2-\lambda}\mathbf{\Sigma}_0, \end{aligned} \tag{2.31}$$

where λ is a smoothing constant with $0 \leq \lambda \leq 1$. Practically, the most often used value of λ is 0.1.

2.6.Automated damage detection

An alarm system based upon the detection of outliers in the control chart would result in an excessive number of false alarms. Note that the control limit UCL is defined for a certain confidence level α, so such a system would signal a proportion of $1-\alpha$ alerts even when the structure remains in healthy condition (see Fig. 2.21 (b)). While control charts represent intuitive visual tools, it would be desirable to count on suitable algorithms capable of automating the interpretation, especially for the management of complete structural networks with numerous monitored assets. To this aim, a simple detection algorithm was proposed in reference [25] to automatically identify the appearance of damage-induced anomalies in the statistical distribution of the statistical distances in control charts. The proposed algorithm represents an extension of the pruned exact linear time (PELT) method proposed by Killick and co-authors [81]. This algorithm searches for a change-point or time instant at which some statistical property of a signal changes abruptly. In particular, we focus on the detection of mean shifts in the time series of residuals in $\mathbf{E}$. Considering a certain row of the error residual matrix $\mathbf{E}$ as a signal $x_1, x_2, ..., x_N$, the algorithm finds a position cp in a time series that minimizes the following cost function:

$$\begin{aligned} J = &\sum_{i=1}^{cp-1}\left(x_i - \frac{1}{cp-1}\sum_{r=1}^{cp-1}x_r\right)^2 + \\ &+\sum_{i=cp}^{N}\left(x_i - \frac{1}{N-cp+1}\sum_{r=cp}^{N}x_r,\right)^2. \end{aligned} \tag{2.32}$$

To do so, the PELT algorithm iteratively segments the time series until finding the optimal solution. Through the use of dynamic programming and pruning, it can be proved that the computational cost of the PELT method is linear in the number of data points (refer to [81]). This approach is automatically launched every time a new monitoring data-set arrives to the system

and the corresponding DSFs are collected in a new column of the residual matrix **E**. The positions of the change-points detected by the PELT method are arranged in a matrix $\mathbf{P} \in \mathbb{R}^{n \times N}$, and the number of repetitions (i.e. number of consecutive times that the PELT algorithm finds the same change-point) are collected in a vector $\mathbf{N} \in \mathbb{R}^{n}$. When a change-point is detected within the training period t_p, a zero value is assigned to the corresponding position in **P**. The algorithm stops and signals an alarm when any of the elements of **N** reaches an user-defined maximum number of repetitions cp_{max}. For clarity, the algorithm is illustrated in the following pseudo-code:

Algorithm 1 Pseudo-code for online damage detection using the PELT method.

for $i \leftarrow 1, n$ **do**
    PELT method $\leftarrow cp_i$
    if $cp_i \leq t_p$ **then**
        $\mathbf{P}_{N+1,i} = 0$
    else
        $\mathbf{P}_{N+1,i} = cp_i$
    end if
    if $\mathbf{P}_{N+1,i} = \mathbf{P}_{N,i}$ **then**
        $\mathbf{N}_i = \mathbf{N}_i + 1$
    else
        $\mathbf{N}_i = 0$
    end if
end for
if $\max(\mathbf{N}) = cp_{max}$ **then**
    Signal alarm
end if

2.7. Application case study: Consoli Palace

As a comprehensive illustrative example of the theoretical concepts overviewed above, this section presents a concise overview of the research works conducted in reference [55] on the damage identification of the Consoli Palace (Section 1.5.5) after the seismic sequence occurred on May 15th 2021 (Section 1.5.5). In that work, the benefits of the SMLR approach previously presented in Section 2.4.3 to conduct automated selection of optimal predictor sets were demonstrated. Most importantly, the presented numerical results and discussion demonstrated the fundamental role of SMLR not only to detect damage, but also to quantify the effects upon the modal properties and the permanent variations in the width of some major cracks in the building.

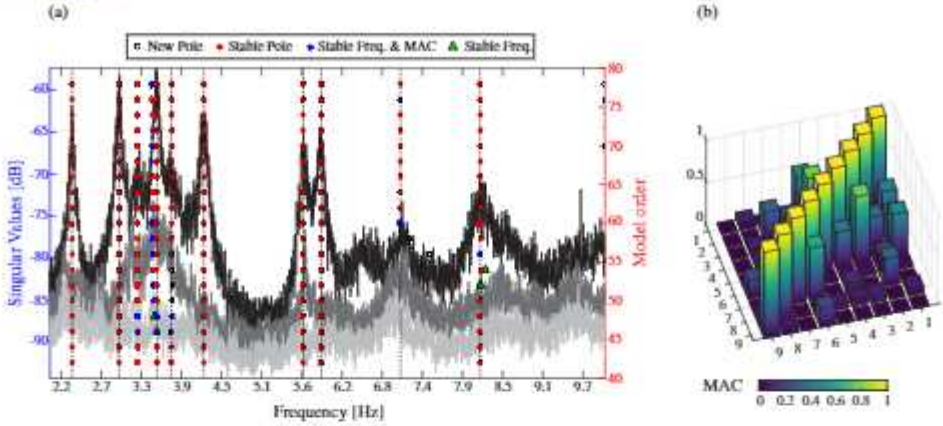

Fig. 2.22: Stabilization diagram obtained using Cov-SSI of the Consoli Palace during the AVT conducted on May 7$^{\text{th}}$ 2021 ($j = 1200$, $t_{lag} = 6$ s) (a), and MAC matrix plot (b).

Figure 2.22 (a) furnishes one of the stabilization diagrams obtained using Cov-SSI of the ambient accelerations recorded during the AVT conducted on May 7$^{\text{th}}$ 2021 (time lag of 6 s). The modal identification was performed using the automated OMA procedure presented later in Chapter 3. In the identification, we defined block rows/columns numbers j_b ranging from 301 ($t_{lag} = 6s$) to 401 ($t_{lag} = 8s$) with steps $\Delta j_b = 5$. Then, for every value of j_b, the modal identification was performed considering model orders ranging from 40 to 80 with steps of 2. Afterward, all the poles were collected and a first cleansing procedure is applied consisting of eliminating complex conjugate poles and poles with damping ratios above 10%. Finally, structural poles were distinguished from spurious ones by applying the hierarchical clustering approach reported in [47]. Threshold parameters to identify clusters of poles included relative variations of resonant frequencies $\Delta f < 1\%$, damping ratios $\Delta\zeta < 3\%$, and Modal Assurance Criterion (MAC) values $MAC > 0.99$. Nine modes have been identified in the frequency range up to 10 Hz and highlighted with thick dashed lines in Fig. 2.22 (a), and the corresponding MAC matrix plot is furnished in Fig. 2.22 (b). The identified modal signatures (resonant frequencies, damping ratios, and Mode Phase Collinearities (MPC)) are collected in Table 2.1 and the first seven mode shapes are shown in Fig. 2.23. The modes have been classified as global (G), local (L), or high order models (HO) according to the interpretation of the mode shapes shown in Fig. 2.23. Specifically, four global modes have been identified and labeled with G-By1, G-T1, G-Bx1, and G-By2 in Fig. 2.23 and Table 2.1. Modes G-By1 and G-Bx1 correspond to first order bending modes along the y- and the x-directions of the building (refer to Fig. 1.10 (b)), respectively, mode G-By2 refers to a second-order bending mode along the y-direction, and mode G-T1 corresponds to the global torsional mode

of the palace. Modes L-Bx1 and L-By1 refer to the first order bending modes of the bell-tower along the x- and the y- directions, while mode L-T1 corresponds to the first torsional mode of the bell-tower. Note that mode L-By1 involves certain torsion in the main body of the palace (see Fig. 2.23). Finally, modes HO1 and HO2 show complex interactions between the main body of the palace, including some out-of-plane deformation of the roof level. Specifically, modes HO1 and HO2 respectively show symmetric and anti-symmetric movements of the point locations of channels A11 and A12. These results were later used to define the baseline modal features of the palace to be tracked during the continuous monitoring, obtaining the time series previously shown in Fig. 2.18.

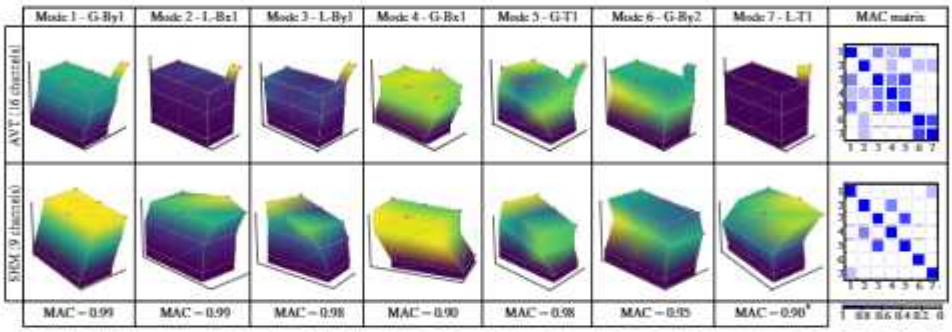

Fig. 2.23: First seven mode shapes identified in the dense AVT and consistently tracked in the continuous monitoring of the Consoli Palace. The mode shapes representative of the continuous monitoring were extracted from the identification of the accelerations recorded on July 17th 2020 12:30 pm CEST. *In the comparison of Mode L-T1 between the AVT and the SHM campaign, only the modal displacements at the roof level were considered in the computation of the MAC value since, given the local nature of this mode, only marginal values were obtained at the first and second floors in the AVT.

Table 2.1: Comparison of the experimentally identified modal signatures of the Consoli Palace in the dense AVT and continuous monitoring using the Cov-SSI method.

		AVT - 13:00 pm CEST May 7th 2021			Continuous monitoring - July 2020/May 2021		
Mode No.	Label	Frequency [Hz]	Damping ratio [%]	MPC [%]	SR* [%]	Mean Frequency [Hz]	Variation range [Hz]
1	G-By1	2.32	0.98	98.3	85.5	2.32	2.18 (-5.80%) - 2.44 (+5.10%)
2	L-Bx1	2.99	0.92	100.0	36.25	3.02	2.75 (-8.65%) - 3.45 (+14.29%)
3	L-By1	3.54	0.78	99.9	49.57	3.53	3.32 (-8.54%) - 4.02 (+14.10%)
4	G-Bx1	3.75	2.76	99.0	56.08	3.75	3.51 (-6.36 %) - 3.97 (+5.77%)
5	G-T1	4.22	0.95	99.9	70.94	4.2	3.86 (-8.28%) - 4.51 (+7.34 %)
6	G-By2	5.65	0.72	99.8	57.3	5.53	5.10 (-7.78%) - 5.97 (+8.02 %)
7	L-T1	5.91	0.69	99.8	76.2	6.46	5.96 (-7.75 %) - 7.00 (+8.27%)
8	HO1	7.05	1.65	97.2	43.61	7.05	6.77 (-4.07%) - 7.41 (+5.00%)
9	HO2	8.20	1.67	96.3	76.61	7.97	7.23 (-9.29%) - 9.23 (15.89%)

* *Success ratio in the identification*

In this light, the predictions of the SMLR model previously reported in Section 2.4.3 are shown in Fig. 2.24. It is evident in this figure that after the seismic sequence initiated on May 15th 2021, some drops are found in

most of the experimental resonant frequencies. Instead, note that the SMLR model does not predict any drop, which facilitates the identification of damage-induced anomalies in the residuals. This is particularly evident in mode L-By1, where the experimental data follow a shifted parallel tendency to the statistical predictions.

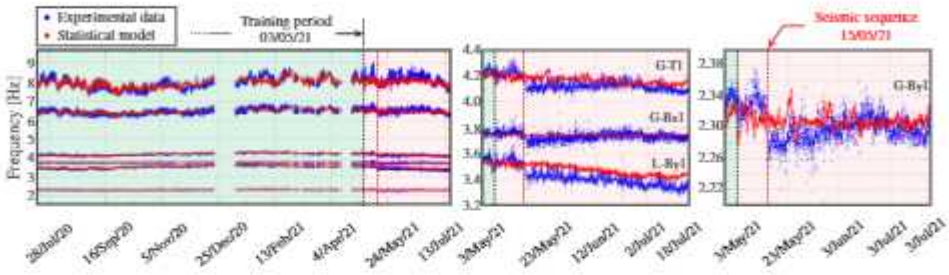

Fig. 2.24: Prediction of the resonant frequencies of the Consoli Palace using SMLR (a) and PCA (3 PCs) (b) using a training period from July 14th 2020 until May 3rd 2021 (12878 data samples) followed by a damage assessment period until July 18th 2021 (3631 data samples).

Afterward, novelty analyses were conducted following the theoretical framework previously overviewed in Section 2.5. The Hotelling's T^2 control chart in terms of resonant frequencies is furnished in Fig. 2.25. For comparison purposes, the control chart obtained using SMLR is benchmarked again against the one resulting from using PCA (3 PCs, explaining more than 90% of the variance). In this figure, a marked anomaly is clearly observable after May 15th, either using SMLR or PCA. In both cases, the T^2 distances experience a shift right after the onset of the seismic sequence, although some slightly better results are visible when using SMLR. Specifically, in the case of SMLR, the number of out-of-control processes overpassing the 95% UCL amounts to 8.55% until May 15th 2021, and increases up to 71.95% in the remaining damage assessment period. Instead, in the case of PCA, the number of outliers amount to 7.85% and 68.8% before and after the seismic sequence for the same confidence level. The quality of the damage classifications by SMLR and PCA is also appraised in Fig. 2.25 (b) through the assessment of the confusion matrices, including receiver operating characteristic (ROC) and Precision/Recall (PR) curves (refer to [25] for a complete description of these classification assessment tools). For their calculation, a dense range of UCL values is swept and the frequency of outliers is computed and stored independently before and after the seismic sequence. Then, outliers before May 15th are assumed as false positives, while those arising after May 15th are considered true positives. The analyses were also performed considering PCA and SMLR without outliers elimination to demonstrate the importance of cleansing the training data-set. Finally, with the aim of providing further insight into the effective-

ness of the classifications, the areas under the ROC (AUC) and Precision-Recall (PAUC) were also computed as comprehensive quality metrics. All things considered, it is evident in Fig. 2.25 (b) that the pattern recognition including data cleansing (denoted with solid lines) proves far better performance using both SMLR or PCA. Indeed, the classification conducted without outliers elimination achieves limited areas of AUC=0.8698 and PAUC=0.5463 in the case of SMLR, and AUC=0.8811 and PAUC=0.5002 in the case of PCA. Instead, when the cleansing of the training population is included, the classifications using both SMLR (AUC=0.9749, PAUC=0.8766) or PCA (AUC=0.9739, PAUC=0.8834) approach the perfect classifier (AUC=PAUC=1.0). With regard to the comparison between SMLR and PCA, very limited differences are found in terms of ROC/PR curves when all the selected resonant frequencies are included in the classification. Nevertheless, larger differences arise when inspecting the classifications obtained accounting for an increasing number of features as shown in Fig. 2.26. It is noted in Fig. 2.26 (a) that almost equally effective classifications are obtained using SMLR for every subset of features, while the classification using PCA in Fig. 2.26 (b) cannot achieve a comparable effectiveness until including all the modes in the classification. Indeed, a comparable classification is only found when including high-order Mode 9 (HO2). This is also confirmed by examining the AUCs of the previous ROC curves in Fig. 2.26 (c), which demonstrates that the damage classification using SMLR considerably outperforms the one obtained by PCA.

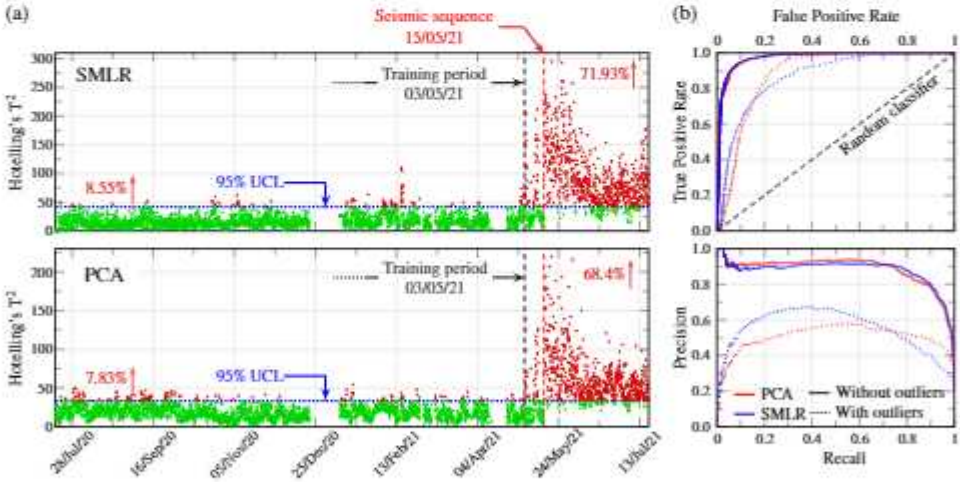

Fig. 2.25: Hotelling's T^2 control charts of the residuals of the resonant frequencies of the Consoli Palace considering SMLR and PCA (3 PCs) (a), and quality assessment in terms of ROC/PR curves (b).

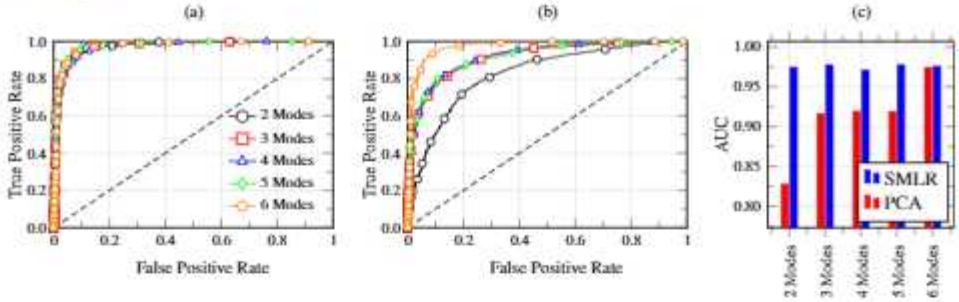

Fig. 2.26: ROC curves considering an increasing number of resonant frequencies using SMLR (a) and PCA (b) (3 PCs), and comparison in terms of AUCs (c). Modes are included in the classification in increasing order of frequency.

Given that the predictions of the proposed SMLR only depends upon environmental factors (completely independent from any damage condition), the sign of anomalies from the analysis of the residuals derived from Fig. 2.24 can be readily interpreted and related to physical phenomena. In this light, the characterization of the earthquake-induced decays in the first three resonant frequencies of the Consoli Palace is reported in Fig. 2.27 (a). The analysis was performed by the individualized study of the residuals. To facilitate the identification of shifts and minimize the effects of residual EOC variability, moving averages of order 192 (4 days) are included with solid black lines. It is clear in Fig. 2.25 (a) the appearance of sudden and stable decays starting right after the onset of the seismic sequence. Note that the signs of the shifts are all negative, indicating the appearance of earthquake-induced stiffness losses in the palace. The earthquake-induced variations in the correlations between the resonant frequencies and the environmental temperature are investigated in Fig. 2.27 (b). Data samples before and after the seismic sequence are denoted in this figure with Regions I and II, respectively. In these analyses, the variation range of environmental temperature (channel T1) has been divided into 50 equally spaced disjoint intervals, and the statistical distribution of resonant frequencies has been described interval-wise through a frequentistic analysis. In is noted in this figure that an almost constant decay is found in Mode 3 throughout all the temperature range. Conversely, decays in Modes 1 and 4 concentrate in the temperature range up to 20°, while almost no variation is observed at higher temperatures.

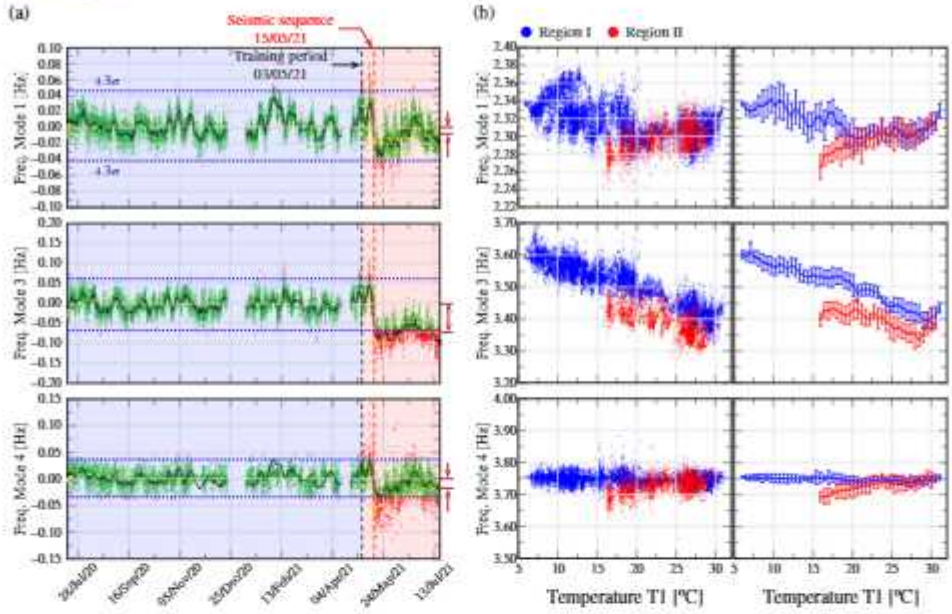

Fig. 2.27: Characterization of the earthquake-induced variations in the three considered resonant frequencies of the Consoli Palace (a) and in the frequency/temperature correlations (b). Black solid lines in (a) represent the moving averages of the residuals (order 192, 4 days). Regions I and II in (b) denote the data samples before and after the seismic sequence, respectively, and error bars indicate standard deviation.

The same methodology was also applied to investigate the appearance of damage-induced anomalies in the static monitoring data. In particular, the time series of the crack displacements recorded by LVDTs D1, D2, and the temperature readings by thermo-couples T1, T2, and T3 (refer to Fig. 1.10 in Section 1.5.5) are shown in Figs. 2.28 (a) and (b), respectively. The recordings by LVDTs D1 and D2 exhibit similar behaviors, with amplitudes ranging between a closing of 0.112 mm to an opening of 0.25 mm with respect to the initial state of the monitored cracks. The analysis also evidences the strong effect of environmental temperature in Fig. 2.28 (b) upon the crack displacements in Fig. 2.28 (a), exhibiting both seasonal and daily fluctuations. The monitored cracks tend to open during the winter, while closing during the summer. Also the breathing behaviors of the cracks can be observed in the zoom inserts in Fig. 2.28 (a), with closing during the day-time and opening during the night-time. After the implementation of the developed SMLR pattern recognition approach, the obtained residuals of crack amplitudes D1 and D2 and the analysis of their correlations with the environmental temperature (channel T1) are furnished in Figs. 2.29 (a) and (b), respectively. It can be clearly concluded from Fig. 2.29 (a) that crack amplitudes D1 (in the south façade of the palace) experienced almost no variation after the seismic sequence, while

a steep and stable shift is found in D2 (in the north façade of the palace). This fact is also confirmed when analyzing the correlations with environmental temperature in Fig. 2.29 (b), where consistent decreases (closing) are found in the whole temperature range.

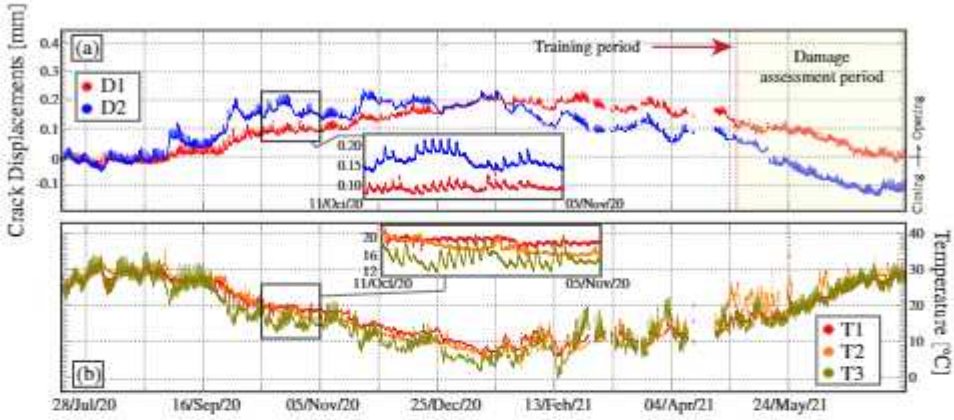

Fig. 2.28: Time series of crack amplitudes of channels D1 and D2 (a), and time series of environmental temperatures of channels T1, T2, and T3 (b) from July 2020 to July 2021.

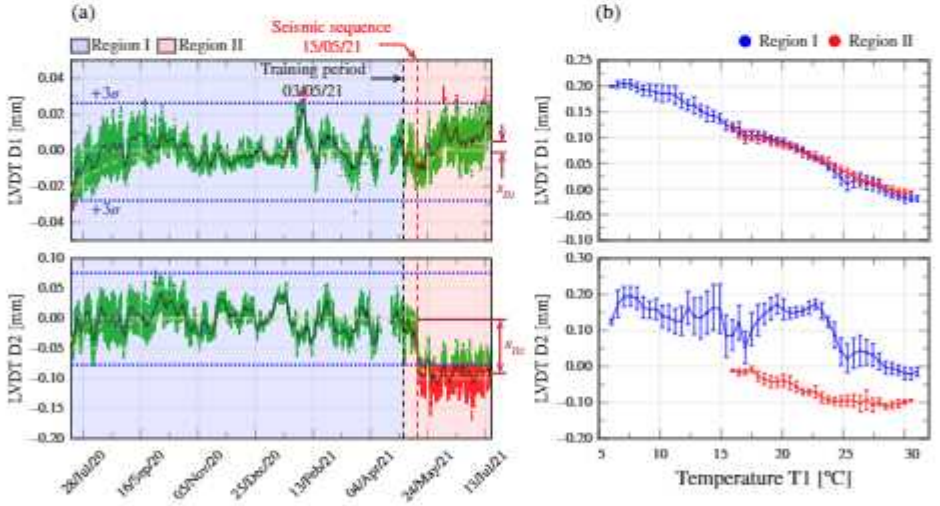

Fig. 2.29: Residuals of crack amplitudes D1 and D2 of the Consoli Palace using SMLR (a), and identification of earthquake-induced variations in the crack/temperature correlations (b).

Table 2.2: Characterization of the shifts in the resonant frequencies and crack amplitudes of the Consoli Palace after the May 15th 2021 seismic sequence. Subscripts I and II relate the statistical moments calculated before and after the seismic sequence, respectively. Quantities in parentheses indicate the standard deviations of the empirical mean values computed in the bootstrap repetitions

	July 17th 2020 to May 15th 2021		May 15th 2021 to July 18th 2021		Comparison	
Estimator **y**	Mean $\mathbf{y}_I$	Std. dev. $\sigma_{\mathbf{y},I}$	Mean $\mathbf{y}_{II}$	Std. dev. $\sigma_{\mathbf{y},II}$	$100\cdot(\mathbf{y}_{II}-\mathbf{y}_I)/\mathbf{y}_I$	MAC
Mode 1 (G-By1) [Hz]	2.319 (±1.33E-04)	0.020	2.304 (±3.37E-04)	0.016	-0.62	0.977
Mode 3 (L-By1) [Hz]	3.514 (±1.99E-04)	0.068	3.442 (±4.26E-04)	0.041	-2.04	0.943
Mode 4 (G-Bx1) [Hz]	3.750 (±1.20E-04)	0.014	3.730 (±4.69E-04)	0.027	-0.54	0.903
Mode 5 (G-T1) [Hz]	4.186 (±2.38E-04)	0.057	4.147 (±6.39E-04)	0.031	-0.93	0.974
Mode 7 (L-T1) [Hz]	6.477 (±8.03E-04)	0.136	6.479 (±1.79E-03)	0.110	0.04	0.962
Mode 9 (NO2) [Hz]	7.971 (±1.61E-03)	0.292	8.020 (±3.57E-03)	0.248	0.62	0.977
Crack D1 [mm]	0.115 (±7.20E-05)	0.074	0.122 (±1.93E-04)	0.037	-	-
Crack D2 [mm]	0.120 (±2.21E-04)	0.072	0.031 (±4.26E-04)	0.036	-	-

From the previous analysis, the earthquake-induced damage in the Consoli Palace could be identified as reported in Table 2.2. To compute the earthquake-induced shifts in the considered estimators (resonant frequencies and crack displacements), the statistical moments of the residuals presented in Figs. 2.27 and 2.29 were estimated by non-parametric bootstrap with 800 repetitions. In terms of resonant frequencies, it can be observed in Table 2.2 that decays concentrated in Modes 3 (L-T1), 5 (G-T1), 1 (G-By1) and 4 (G-Bx1) in decreasing order. Note that, given the relative orientation of the palace with respect to the epicenter of the main shock (see Fig. 1.12 (a)), damage is expected to concentrate along the y-direction of the building, primarily affecting the first bending mode along that direction (G-By1) as well as the torsional modes (L-T1 and G-T1). This claim is supported by the results reported in Table 2.2, where the decays in the first order bending modes along the y- and x-directions amount to 0.62 and 0.54%, respectively. Besides, the largest decays are found for torsional Modes 3 (local) and 5 (global) with values of 2.04 and 0.93%, respectively, indicating that the seismic events had largest influence upon the torsional stiffness of the palace. Interestingly, an increase of 0.62% is found for local Mode 9, which may indicate some earthquake-induced rearrangement of the tower/building interaction. It is important to remark that no significant variations were found in the MAC values between the mode shapes after and before the seismic sequence, with values very close to 1 as reported in Table 2.2. This circumstance may indicate the registered damage is very moderate and sustains no severe structural risk to the palace. In fact, preliminary in-situ inspections revealed no new pathologies in the palace, which suggests that the developed damage remained at a degree not observable by visual examinations. With regard to the crack amplitudes, the results in Table 2.2 confirm that crack D1 was not affected by the seismic sequence, while a clear closure of crack D2 of about 8.9E-2 mm was found. Note that LVDT D2 is located bridging a major crack located in the north façade of the building, which was presumably originated as a result of an incipient overturning failure mechanism

of the western façade. Instead, LVDT D1 is monitoring a crack relating the local overturning of the loggia in the south façade. Following the previous discussion on the incidence direction of the seismic shocks, it is reasonable to state that these will mainly affect the north façade of the palace. Finally, it is important to emphasize that, whilst the detected anomaly in D2 is significant in relatively terms, the closure of crack D2 is very limited and supports the previous statement on the mild severity of the earthquake-induced damage.

3. Operational Modal Analysis

3.1. Introduction

Among the broad variety of sensing solutions in the realm of SHM, ambient vibration-based techniques are particularly popular and constitute one of the most active areas of research in the last decades in the field of Structural Engineering. While signal processing in vibration-based SHM is convoluted and requires the assistance of specialized technicians, its minimal intrusiveness, fully non-destructive character, global damage detection capabilities, easy implementation into pre-existing assets and high compatibility with continuous monitoring schemes make it an ideal monitoring solution for many civil engineering structures [82]. These techniques exploit ambient acceleration records under normal operating conditions to extract the modal features of a system through output-only OMA, namely natural frequencies, mode shapes, and damping ratios [83, 48]. The basic premise is that, since modal features are functions of the mass, stiffness, and energy dissipation mechanisms of the monitored structure, the appearance of damage can be inferred by tracking permanent variations in its modal parameters [84, 19]. Numerous recent works report the successful application of this technology to diverse structural typologies, including bridges [85], dams [86], buildings [87], stadiums [88], naval vessels [89], or aircraft structures [90]. Vibration-based SHM is also becoming increasingly popular for preventive conservation of Cultural Heritage (CH) structures. The monitoring of such structures must have a minimum impact on their architectural and cultural value, for which OMA-based SHM represents an ideal solution. In this context, plenty of successful applications can be found in the literature, including CH bridges [91, 92], towers [93], churches [57], and buildings [94, 24].

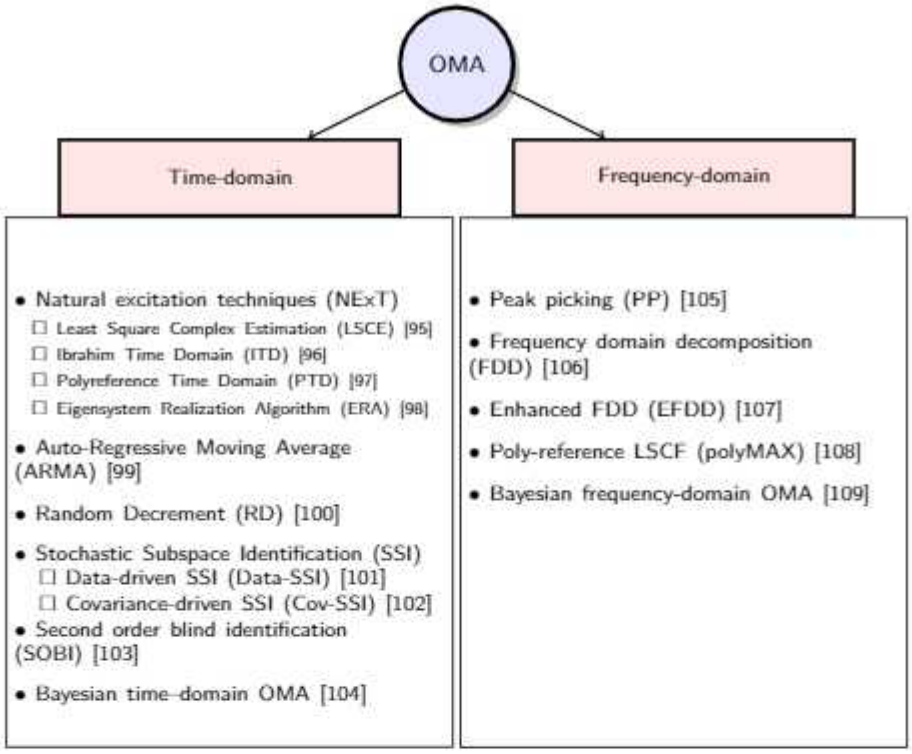

Fig. 3.1: Identification techniques most commonly used in OMA.

Considerable research has been devoted in the last decades to the development of diverse time-domain and frequency-OMA techniques. The most popular approaches in the realm of civil engineering structures are presented in Fig. 3.1, and readers may find several comprehensive reviews in the literature discussing on their advantages and disadvantages (see e.g. [110, 111, 112, 113]). Nonetheless, in the most recent years, most research efforts have been devoted to the development of automated OMA procedures apt for continuous SHM schemes [114, 47, 115]. These enable early detection of damage by tracking anomalies in time series of continuously identified modal features. In particular, a number of approaches have been proposed in the literature for the automated interpretation of stabilization diagrams obtained by time domain-based Stochastic Subspace Identification (SSI) methods. These include, among others, hierarchical clustering [47, 116], fuzzy clustering [117], Gaussian Mixture Models (GMM) [118], density-based clustering [119], and blind k-means [120]. Such techniques allow to conduct automated and quasi real-time identification of stable modal poles, which can be then used to trace time series of modal signatures of the monitored structure through a frequency tracking approach. In this light, an increasing number of publications reporting on the successful application of vibration-based SHM systems for damage identification of in-service civil engineering structures are being presented in the

literature. In particular, the Z24-Bridge (Section 1.5.1) represents one of the most prominent examples. Peeters and De Roeck [16] successfully detected the artificial damage imposed to the Z24-Bridge by analyzing the residuals between experimental resonant frequencies and statistical predictions obtained by an autoregressive model. Kullaa [121] and Yan and co-authors [122] also worked on the Z24 Bridge and showed that damage can be also detected through control charts and PCA. Ubertini *et al.* [19] reported the damage detection of the bell-tower of the Basilica of San Pietro in Perugia after the 2016 Central Italy seismic sequence through MLR/PCA-based novelty analysis of the time series of resonant frequencies. Hu *et al.* [123] reported the vibration-based SHM of a prestressed-concrete box girder bridge in Berlin over 14 years. Through MLR filtering of the environmental effects, those authors found a progressive increase in the number of outliers in the control charts from 1.35% in 2000/2001 to 21.58% after 2008.

Even though the development of new OMA techniques remains an open research field, the considerable amount of successful field implementations in the literature demonstrate the high level of maturity of vibration-based SHM. This circumstance contrasts with the slow technological transfer of vibration-based SHM to routine engineering practice, being mostly implemented for AVT and only by few highly specialized companies and research centers. This is mainly due to the difficulties involved in the automation of the OMA procedures and their connection with the remaining chains in the statistical pattern recognition paradigm. In this light, the main contribution of this thesis regards the connection of most state-of-the-art OMA techniques into the SHM software suite later presented in Chapter 6. This chapter presents the theoretical fundamentals of the implemented techniques, as well as some other methodological innovations achieved during the course of this thesis, with particular emphasis on the automation of SSI methods and modal tracking. Specifically, Section 3.2 overviews the fundamentals of dynamic equilibrium of Linear Time Invariant (LTI) systems. Section 3.3 overviews the fundamentals of the most popular frequency- and time-domain OMA methods. Sections 3.4 and 3.5 reports the formulation of automated SSI methods for long-term SHM and of modal tracking techniques, respectively. Finally, Section 3.6 presents the analysis of the Z-24 Bridge from reference [124] as a comprehensive example to illustrate the introduced OMA techniques and their use into the statistical pattern recognition paradigm previously reported in Chapter 2.

3.2.Fundamentals of LTI dynamic systems

The differential equation of equilibrium of a dynamic system discretized into a finite number of n_2 degrees of freedom (DOFs) can be written as:

$$\mathbf{M}\ddot{\mathbf{q}}(t) + \mathbf{C}\dot{\mathbf{q}}(t) + \mathbf{K}\mathbf{q}(t) = \mathbf{f}(t) = \mathbf{B}_2\mathbf{u}(t), \tag{3.1}$$

where $\mathbf{M}, \mathbf{C}, \mathbf{K} \in \mathbb{R}^{n_2 \times n_2}$ are the mass, damping and stiffness matrices of the

system. Terms $\ddot{\mathbf{q}}(t)$, $\dot{\mathbf{q}}(t)$, $\mathbf{q}(t), \in \mathbb{R}^{n_2}$ denote the acceleration, velocity, and displacement vectors as functions of time t, and term $\mathbf{f}(t) \in \mathbb{R}^{n_2}$ is a column vector containing the forces applied to the system. Since not all the DOFs of the system are commonly excited, $\mathbf{f}(t)$ can be replaced by a vector $\mathbf{u}(t) \in \mathbb{R}^{m}$ of lower dimensions ($m < n_2$) concentrating the time evolution of the m applied forces. Then, $\mathbf{u}(t)$ is multiplied by a conversion matrix $\mathbf{B}_2 \in \mathbb{R}^{n_2 \times m}$ that maps the m input forces into the n_2 DOFs of the system. Matrix $\mathbf{B}_2$ is composed of zeroes and ones, the latter at those positions B_2^{ij} where the force component u_j corresponds to the i-the DOF of the system. When a reduced set of DOFs of the system are monitored, the second-order system of differential equations in Eq. (3.1) can be transformed after some manipulation into a first-order one referred to as the continuous state-space form:

$$\begin{aligned} \dot{\mathbf{x}}(t) &= \mathbf{A}_C \mathbf{x}(t) + \mathbf{B}_C \mathbf{u}(t), \\ \mathbf{y}(t) &= \mathbf{C}_C \mathbf{x}(t) + \mathbf{D}_C \mathbf{u}(t), \end{aligned} \tag{3.2}$$

where $\mathbf{A}_C \in \mathbb{R}^{2n_2 \times 2n_2}$, $\mathbf{B}_C \in \mathbb{R}^{2n_2 \times n_i}$, $\mathbf{C}_C \in \mathbb{R}^{l \times 2n_2}$, and $\mathbf{D}_C \in \mathbb{R}^{l \times n_i}$ are designated the state matrix, input matrix, output matrix, and direct transmission matrix, respectively. Vectors $\mathbf{x}(t) \in \mathbb{R}^{2n_2}$ and $\mathbf{y}(t) \in \mathbb{R}^{l}$ denote the state and observation vectors, respectively. The state vector $\mathbf{x}(t)$ contains the displacements and velocities of the DOFs of the system, while the observation vector $\mathbf{y}(t)$ contains a subset of l measured outputs. The first line in Eq. (3.2), called the state equation, relates n_i inputs (loads) applied to the system and contained in vector $\mathbf{u}(t) \in \mathbb{R}^{n_i}$ to the state vector $\mathbf{x}(t)$. On the other hand, the second line in Eq. (3.2) is called the observation equation and establishes a relation between the observation vector $\mathbf{y}(t)$ and the state vector $\mathbf{x}(t)$. The relationship between the system matrices of the dynamic system and the state/input matrices can be obtained by simple matrix algebra as [125]:

$$\mathbf{A}_C = \begin{bmatrix} \mathbf{0}_{2n_2 \times 2n_2} & \mathbf{I}_{2n_2 \times 2n_2} \\ -\mathbf{M}^{-1}\mathbf{K} & -\mathbf{M}^{-1}\mathbf{C} \end{bmatrix}, \tag{3.3}$$

$$\mathbf{B}_C = \begin{bmatrix} \mathbf{0}_{2n_2 \times 2n_2} \\ \mathbf{M}^{-1}\mathbf{B}_2 \end{bmatrix}. \tag{3.4}$$

The modal features of the system can be extracted from the eigenvalue decomposition of the state matrix $\mathbf{A}_C$ as $\mathbf{A}_C = \mathbf{\Psi}\mathbf{\Lambda}_C\mathbf{\Psi}^{-1}$. Matrices $\mathbf{\Lambda}_C$ and $\mathbf{\Psi}$ containing the eigenvalues and eigenvectors of $\mathbf{A}_C$, respectively, present the

following structure [126]:

$$\begin{gathered}\boldsymbol{\Lambda}_C = \begin{bmatrix} \boldsymbol{\Lambda} & 0 \\ 0 & \boldsymbol{\Lambda}^* \end{bmatrix}, \boldsymbol{\Psi} = \begin{bmatrix} \boldsymbol{\Theta} & \boldsymbol{\Theta}^* \\ \boldsymbol{\Theta}\boldsymbol{\Lambda} & \boldsymbol{\Theta}^*\boldsymbol{\Lambda}^* \end{bmatrix}, \\ \boldsymbol{\Lambda} = \begin{bmatrix} \ddots & & \\ & \lambda_k & \\ & & \ddots \end{bmatrix}, \boldsymbol{\Theta} = \begin{bmatrix} \dots & \boldsymbol{\phi}_k & \dots \end{bmatrix}, k = 1, .., n_2 \end{gathered} \tag{3.5}$$

where $\bullet^*$ denotes complex conjugate. Parameters λ_k are related to the resonant frequencies (ω_k - natural frequencies in rad/s) and the modal damping ratios (ζ_k) of the system as:

$$\lambda_k = -\zeta_k \omega_k + \mathrm{i}\sqrt{1-\zeta_k^2}\omega_k, \tag{3.6}$$

with i denoting the imaginary unit. The mode shapes are represented in Eq. (3.5) by $\boldsymbol{\phi}_k \in \mathbb{R}^{n_2}$. However, since only a subset of l DOFs is measured, the observable modal matrix $\boldsymbol{\Phi} \in \mathbb{R}^{l \times n_2}$ is given by:

$$\boldsymbol{\Phi} = \mathbf{C}_C \boldsymbol{\Psi}. \tag{3.7}$$

In practice, recorded analogue signals are digitized by an analogue-to-digital converter (A/D), so the available information is discrete in time. Such a process is conducted by sampling the signals at a certain sampling frequency $f_s = 1/\Delta t$, with Δt being the adopted sampling interval. Therefore, the time functions $\mathbf{x}(t)$ and $\mathbf{y}(t)$ in Eq. (3.2) must be replaced by their values at discrete time instants $k\Delta t$ with k being an integer, i.e. $\mathbf{y}_k = \mathbf{y}(k\Delta t)$, $\mathbf{x}_k = \mathbf{x}(k\Delta t)$. In addition, in the context of OMA, the system inputs in $\mathbf{u}(t)$ are unknown (unmeasured) and must be represented through stochastic processes. On this basis, the discrete stochastic state-space model reads:

$$\begin{aligned} \mathbf{x}_{k+1} &= \mathbf{A}\mathbf{x}_k + \mathbf{w}_k, \\ \mathbf{y}_k &= \mathbf{C}\mathbf{x}_k + \mathbf{v}_k, \end{aligned} \tag{3.8}$$

here, vectors $\mathbf{w}_k \in \mathbb{R}^{2n_2}$ and $\mathbf{v}_k \in \mathbb{R}^l$ represent white noise processes accounting for the effect of unknown outputs as well as the effects of process noise (modelling inaccuracies) and measurement noise, respectively. Both noise vectors are assumed to be zero-mean realizations of stochastic processes with the following correlation matrices:

$$E\left(\begin{bmatrix} \mathbf{w}_p \\ \mathbf{v}_p \end{bmatrix} \begin{bmatrix} \mathbf{w}_q^{\mathrm{T}} & \mathbf{v}_q^{\mathrm{T}} \end{bmatrix}\right) = \begin{bmatrix} \mathbf{Q} & \mathbf{S} \\ \mathbf{S}^{\mathrm{T}} & \mathbf{R} \end{bmatrix} \delta_{pq}, \tag{3.9}$$

where sub-indexes p and q denote generic time instants, δ_{pq} is the Kronecker delta, and E is the expected value operator.

It can be demonstrated that the eigenvectors of matrix $\mathbf{A}$ coincide with those of the continuous counterpart $\mathbf{A}_C$ and, since $\mathbf{C}$ equals $\mathbf{C}_C$, the modal matrix is given by Eq. (3.7) [125]. In addition, the eigenvalues of the discrete model μ_k are related to those of the continuous model λ_k as [125]:

$$\mu_k = e^{\lambda_k \Delta t} \Leftrightarrow \lambda_k = \frac{\ln(\mu_k)}{\Delta t}. \tag{3.10}$$

Therefore, the natural frequencies and model damping ratios can be readily obtained from the eigenvalues of matrix $\mathbf{A}$ using Eqs. (3.6) and (3.10).

An important property of stochastic state-space models regards the relation between the correlation matrix of the measurement records and the state-space matrices [126]:

$$\mathbf{R}_j = \mathbf{C}\mathbf{A}^{j-1}\mathbf{G}, \tag{3.11}$$

with $\mathbf{R}_j$ being the output correlation matrix for a time lag $\tau = j\Delta t$, and $\mathbf{G}$ being the next state-output covariance matrix given by:

$$\mathbf{G} = E\left[\mathbf{x}_{k+1}\mathbf{y}_k^{\mathrm{T}}\right]. \tag{3.12}$$

3.3. Operational Modal Analysis methods

3.3.1. Frequency-domain models

Enhanced Frequency Domain Decomposition (EFDD)

The Frequency Domain Decomposition (FDD) method is based on the input/output relationship of linear time-invariant systems as [127]:

$$\mathbf{G}_{yy}(\omega) = \mathbf{H}(\omega)\mathbf{G}_{uu}(\omega)\mathbf{H}(\omega)^{\mathrm{H}}, \tag{3.13}$$

where $\bullet^{\mathrm{H}}$ denotes complex conjugate (Hermitian) transpose. Matrices $\mathbf{G}_{uu}(\omega) \in \mathbb{C}^{r_c \times r_c}$ and $\mathbf{G}_{yy}(\omega) \in \mathbb{C}^{l \times l}$ represent the Power Spectral Density (PSD) matrices of the inputs and outputs, respectively, with r_c being the number of inputs (references), and $\mathbf{H}(\omega) \in \mathbb{C}^{r_c \times l}$ is the Frequency Response Function (FRF) matrix. In practice, the PSDs are commonly computed using the Welch's method. Then, the singular value decomposition (SVD) of $\mathbf{G}_{yy}$ is performed as:

$$\mathbf{G}_{yy}(\omega_j) = \mathbf{U}_j\mathbf{S}_j\mathbf{U}_j^{\mathrm{H}}, \tag{3.14}$$

where $\mathbf{U}_j$ is an orthonormal matrix ($\mathbf{U}_j\mathbf{U}_j^{\mathrm{H}} = \mathbf{I}$) containing the singular vectors of $\mathbf{G}_{yy}(\omega_j)$, and $\mathbf{S}_j$ is a diagonal matrix holding the corresponding singular values (SVs). On this basis the resonant frequencies can be estimated by

picking the peaks of the first SV, while the mode shapes are obtained as the first singular vector evaluated at the formerly picked frequency values.

The EFDD method represents an improved version of the FDD that allows to identify damping ratios and more accurate estimates of resonant frequencies. To do so, the singular value data around the resonance peaks are selected, typically according to a limit MAC value. Once selected, these spectrum segments are converted to the time domain in order to get auto-correlation functions for each mode. Finally, the corresponding resonant frequencies and damping ratios can be obtained by fitting the expression for the impulse response of a single-degree-of-freedom system. Alternatively, MOVA and MOSS implement the Single-Input-Multiple-Output (SIMO) version of the Ibrahim Time Domain (ITD) technique to extract the natural frequencies and damping ratios from the computed auto-correlation functions [128].

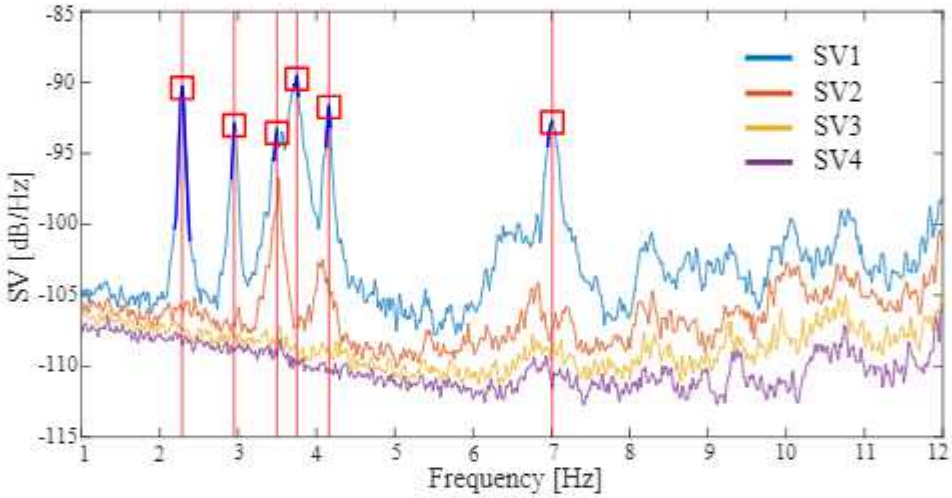

Fig. 3.2: Dynamic identification of the Consoli Palace using EFDD.

Figure 3.2 presents the first four SVs of the spectral matrix calculated from the acceleration time-series recorded during the AVT of the Consoli Palace. These were calculated with the Welch's method using time segments with 2048 points, and Hanning windows with an overlapping of 50%. The application of the SVD decomposition to the spectral matrix evaluated at all the discrete frequencies between 0 and 12 Hz produces 9 SVs for each frequency. The spectrum of the first singular values exhibits six peaks that are associated with main modes of the Consoli Palace within the frequency band under analysis as later reported in Section 3.3.3. The points of the singular value spectra are selected for the application of the ITD method using a limit for the MAC of 0.8.

Polyreference Least Squares Complex Frequency Domain method (p-LSCF)

The Polyreference Least Squares Complex Frequency Domain method (p-LSCF) is a parametric frequency-domain method developed by Peeters and Van der Auweraer [108]. The p-LSCF models the positive half-spectrum matrix using a right-matrix fraction model as:

$$\mathbf{G}_{yy}^{+}(\omega_j) = \mathbf{B}(\omega_j)\left[\mathbf{A}(\omega_j)\right]^{-1} = \left[\sum_{r=0}^{p} \mathbf{B}_r \Omega_r(\omega_j)\right]\left[\sum_{r=0}^{p} \mathbf{A}_r \Omega_r(\omega_j)\right]^{-1}, \quad (3.15)$$

where matrices $\mathbf{B}_r$, $\mathbf{A}_r \in \mathbb{R}^{l \times l}$ are model parameter matrices to be determined, $\Omega_r(\omega_j)$ are polynomial basis functions, and p is the polynomial order. The p-LSCF model is expressed in the discrete z-domain (i.e. a frequency-domain model derived from a discrete-time model), so the polynomial basis functions take the form $\Omega_r(\omega_j) = e^{i\omega_j \Delta t r}$. The method seeks matrices $\mathbf{B}_r$ and $\mathbf{A}_r$ that minimize in a non-linear least-squares sense the error matrix $\mathbf{E}^{NLS}(\omega_j) = \mathbf{G}_{yy}^{+}(\omega_j) - \hat{\mathbf{G}}_{yy}^{+}(\omega_j)$, which involves the difference between $\mathbf{G}_{yy}^{+}$ and the half-spectrum matrix $\hat{\mathbf{G}}_{yy}^{+}$ estimated from the measurement records. Nevertheless, the right multiplication of $\mathbf{E}^{NLS}(\omega_j)$ by matrix $\mathbf{A}(\omega_j)$ leads to more convenient linear least-squares equation errors as:

$$\mathbf{E}^{LS}(\omega_j) = \left[\sum_{r=0}^{p} \mathbf{B}_r \Omega_r(\omega)\right] - \hat{\mathbf{G}}_{yy}^{+}(\omega_j)\left[\sum_{r=0}^{p} \mathbf{A}_r \Omega_r(\omega)\right], \quad (3.16)$$

where $\mathbf{E}^{LS}(\omega_j) \in \mathbb{C}^{l \times l}$ contains the errors (E_{ij}) to be minimized. The minimization problem can be written in a more compact form after some transformations. In particular, an arbitrary line o of the error matrix at all the discrete frequency values from ω_1 to ω_{N_f} can be stacked in a matrix $\mathbf{E}_o^{LS} \in \mathbb{C}^{N_f \times l}$:

$$\mathbf{E}_o^{LS}(\boldsymbol{\beta}_o, \boldsymbol{\alpha}) = \begin{bmatrix} E_{o1}(\omega_1) & \dots & E_{ol}(\omega_1) \\ E_{o1}(\omega_2) & \dots & E_{ol}(\omega_2) \\ \dots & \dots & \dots \\ E_{o1}(\omega_{N_f}) & \dots & E_{ol}(\omega_{N_f}) \end{bmatrix} = \begin{bmatrix} \mathbf{X}_o & \mathbf{Y}_o \end{bmatrix} \begin{bmatrix} \boldsymbol{\beta}_o \\ \boldsymbol{\alpha} \end{bmatrix}, \quad (3.17)$$

with

$$\begin{gathered}\boldsymbol{\Omega}(\omega_j) = \left[\Omega_0(\omega_j)\,\Omega_2(\omega_j)\,\ldots\,\Omega_p(\omega_j)\right] \in \mathbb{C}^{p+1},\\ \mathbf{Y}_o = \begin{bmatrix} \Omega_0(\omega_1)\hat{\mathbf{S}}^+_{yyo} & \Omega_1(\omega_1)\hat{\mathbf{S}}^+_{yyo} & \ldots & \Omega_p(\omega_1)\hat{\mathbf{S}}^+_{yyo} \\ & \vdots & \ldots & \\ \Omega_0(\omega_{N_f})\hat{\mathbf{S}}^+_{yyo} & \Omega_1(\omega_{N_f})\hat{\mathbf{S}}^+_{yyo} & \ldots & \Omega_p(\omega_{N_f})\hat{\mathbf{S}}^+_{yyo} \end{bmatrix} \in \mathbb{C}^{N_f \times l(p+1)},\\ \mathbf{X}_o = \begin{bmatrix} \boldsymbol{\Omega}(\omega_1) \\ \vdots \\ \boldsymbol{\Omega}(\omega_{n_f}) \end{bmatrix} \in \mathbb{C}^{N_f \times (p+1)},\ \boldsymbol{\beta}_o = \begin{bmatrix} \mathbf{B}_{0o} \\ \mathbf{B}_{1o} \\ \ldots \\ \mathbf{B}_{po} \end{bmatrix} \in \mathbb{R}^{(p+1)\times l},\ \boldsymbol{\alpha} = \begin{bmatrix} \mathbf{A}_0 \\ \mathbf{A}_1 \\ \ldots \\ \mathbf{A}_p \end{bmatrix} \in \mathbb{R}^{l(p+1)\times l}, \end{gathered} \tag{3.18}$$

where $\hat{\mathbf{S}}^+_{yyo}$ and $\mathbf{B}_{ro}$ represent the o lines of matrices $\hat{\mathbf{S}}^+_{yy}$ and $\mathbf{B}_r$, respectively. Finally, a scalar cost function can be constructed as the sum of the squared elements of the error matrix as:

$$\begin{aligned}\varepsilon(\boldsymbol{\beta}_o, \boldsymbol{\alpha}) &= \sum_{o=1}^{l} \mathrm{tr}\left\{\mathbf{E}_o(\boldsymbol{\beta}_o, \boldsymbol{\alpha})^{\mathrm{H}}\mathbf{E}_o(\boldsymbol{\beta}_o, \boldsymbol{\alpha})\right\} = \\ &= \sum_{o=1}^{l} \mathrm{tr}\left\{ \begin{bmatrix} \boldsymbol{\beta}_o^{\mathrm{T}} & \boldsymbol{\alpha}^{\mathrm{T}} \end{bmatrix} \begin{bmatrix} \mathbf{R}_o & \mathbf{S}_o \\ \mathbf{S}_o^{T} & \mathbf{T}_o \end{bmatrix} \begin{bmatrix} \boldsymbol{\beta}_o \\ \boldsymbol{\alpha} \end{bmatrix} \right\},\end{aligned} \tag{3.19}$$

with $\mathbf{R}_o = \mathrm{Re}(\mathbf{X}_o^{\mathrm{H}}\mathbf{X}_o) \in \mathbb{R}^{(p+1)\times(p+1)}$, $\mathbf{S}_o = \mathrm{Re}(\mathbf{X}_o^{\mathrm{H}}\mathbf{Y}_o) \in \mathbb{R}^{(p+1)\times l(p+1)}$, $\mathbf{T}_o = \mathrm{Re}(\mathbf{Y}_o^{\mathrm{H}}\mathbf{Y}_o) \in \mathbb{R}^{l(p+1)\times l(p+1)}$, and tr denoting the trace operator. The unknown model parameters in $\mathbf{B}_r$ and $\mathbf{A}_r$ can be obtained by forcing the derivatives of the cost function with respect to $\boldsymbol{\alpha}$ and $\boldsymbol{\beta}_o$ to be zero. This leads to the following reduced system of equations:

$$\begin{aligned} &2(\mathbf{R}_o\boldsymbol{\beta}_o + \mathbf{S}_o\boldsymbol{\alpha}) = \mathbf{0} \Leftrightarrow \boldsymbol{\beta}_o = -\mathbf{R}_o^{-1}\mathbf{S}_o\boldsymbol{\alpha},\\ &2\textstyle\sum_{o=1}^{l}\left(\mathbf{T}_o - \mathbf{S}_o^{\mathrm{T}}\mathbf{R}_o^{-1}\mathbf{S}_o\right)\boldsymbol{\alpha} = 0 \Leftrightarrow \mathbf{M}\boldsymbol{\alpha} = 0, \end{aligned} \tag{3.20}$$

where matrix $\mathbf{M} \in \mathbb{C}^{l(p+1)\times l(p+1)}$ can be computed from the output half-spectrum matrix estimated from the measurement records. In order to avoid the trivial solution of the previous equation ($\boldsymbol{\alpha} = \mathbf{0}$), a constraint has to be imposed. This is typically conducted by forcing either $\mathbf{A}_o$ or $\mathbf{A}_p$ to be the identity matrix. In particular, clearer stabilization diagrams have been reported to be found when $\mathbf{A}_o = \mathbf{I}$ [83]. Then, the resolution of the system of equations

reads:

$$\mathbf{M}\boldsymbol{\alpha} = \mathbf{0} \leftrightarrow \left[\begin{array}{c|c} \mathbf{M}_{aa} & \mathbf{M}_{ab} \\ \hline \mathbf{M}_{ba} & \mathbf{M}_{bb} \end{array}\right] \left[\begin{array}{c} \mathbf{I} \\ \hline \boldsymbol{\alpha}_b \end{array}\right] = \left[\begin{array}{c} \mathbf{0} \\ \hline \mathbf{0} \\ \vdots \\ \mathbf{0} \end{array}\right] \leftrightarrow \boldsymbol{\alpha}_b = -\mathbf{M}_{bb}^{-1}\mathbf{M}_{ba} \leftrightarrow \boldsymbol{\alpha} = \left[\begin{array}{c} \mathbf{I} \\ \hline -\mathbf{M}_{bb}^{-1}\mathbf{M}_{ba} \end{array}\right], \tag{3.21}$$

where $\mathbf{M}_{ba}$ contains the first l columns and the last pl lines of $\mathbf{M}$, $\mathbf{M}_{bb}$ contains the last pl columns and rows of $\mathbf{M}$, and $\boldsymbol{\alpha}_b$ contains the last pl rows of $\boldsymbol{\alpha}$. Once matrix $\boldsymbol{\alpha}$ is determined, matrix $\boldsymbol{\beta}_o$ is directly obtained using the relation between $\boldsymbol{\alpha}$ and $\boldsymbol{\beta}_o$ in Eq. (3.20). With this step, the model parameter matrices $\mathbf{A}_r$ and $\mathbf{B}_r$ are determined and the identification problem is solved. Then, the modal features can be obtained through the transposition equations from right matrix-fraction models to state-space models, leading to the following state-space matrices [129]:

$$\begin{aligned}
\mathbf{A}_C &= \begin{bmatrix} -\mathbf{A}_p^{-1}\mathbf{A}_{p-1} & -\mathbf{A}_p^{-1}\mathbf{A}_{p-2} & \dots & -\mathbf{A}_p^{-1}\mathbf{A}_1 & -\mathbf{A}_p^{-1}\mathbf{A}_0 \\ \mathbf{I} & \mathbf{0} & \dots & \mathbf{0} & \mathbf{0} \\ \vdots & \ddots & \dots & \vdots & \vdots \\ \mathbf{0} & \mathbf{0} & \dots & \mathbf{I} & \mathbf{0} \end{bmatrix}, \\
\mathbf{B}_C &= \begin{bmatrix} \mathbf{A}_p^{-1} \\ \mathbf{0} \end{bmatrix}, \\
\mathbf{C}_C &= \begin{bmatrix} \mathbf{B}_{p-1} - \mathbf{B}_p\mathbf{A}_p^{-1}\mathbf{A}_{p-1} & \dots & \mathbf{B}_0 - \mathbf{B}_p\mathbf{A}_p^{-1}\mathbf{A}_0 \end{bmatrix}, \\
\mathbf{D}_C &= \mathbf{B}_p\mathbf{A}_p^{-1}.
\end{aligned} \tag{3.22}$$

Finally, the modal features can be readily determined through the eigenvalue decomposition of matrix $\mathbf{A}$. At this point, separation of physical and spurious modes becomes crucial. This is commonly performed through stabilization diagrams representing the modal parameters estimated considering p-LSCF models with increasing polynomial orders p. The concept of stabilization diagrams will is explained in more detail in Section 3.4 when discussing on the automation of OMA. Figure 3.3 shows the stabilization diagram obtained using the p-LSCF method for the ambient vibration data-set recorded during the AVT of the Consoli Palace. To do so, the cross half-spectra of the nine time series of ambient vibrations were obtained using the Welch's method considering time segments with 2048 points and 50% overlap. Afterward, the model conversion in Eq. (3.22) was constructed by adopting polynomial orders between 20 and 120. It is noted in Fig. 3.3 that six clear columns of stable poles are found at frequency values corresponding to the main natural frequencies of the Consoli

Palace in the considered frequency range. These results exemplify one of the main advantages of the p-LSCF method, which regards the generation of very clear stabilization diagrams. Indeed, it has been previously reported in the literature that most of the spurious poles appear with negative damping ratios when using the p-LSCF method, thereby they are directly eliminated before constructing the stabilization diagram [126].

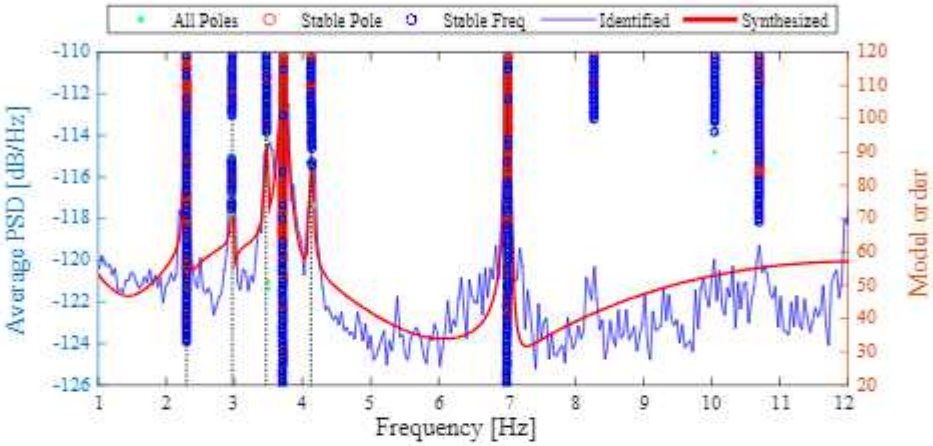

Fig. 3.3: Dynamic identification of the Consoli Palace using p-LSCF.

3.3.2. Stochastic Subspace Identification

Cov-SSI

The Cov-SSI method identifies a stochastic state-space model from the output covariance matrix (or correlation, as the mean of the signals is assumed to be zero). It starts by computing the output correlation matrix for positive time lags varying from Δt to $(2j_b - 1)\Delta t$ represented by $\mathbf{R}_1$ to $\mathbf{R}_{2j_b-1}$. Afterward, the covariance matrix is organized in a lj_b-by-lj_b block Toeplitz matrix (sketched in Fig. 3.4) as:

$$\mathbf{T}_{1|j_b} = \begin{bmatrix} \mathbf{R}_{j_b} & \mathbf{R}_{j_b-1} & \cdots & \mathbf{R}_1 \\ \mathbf{R}_{j_b+1} & \mathbf{R}_{j_b} & \cdots & \mathbf{R}_2 \\ \cdots & \cdots & \cdots & \cdots \\ \mathbf{R}_{2j_b-1} & \mathbf{R}_{2j_b-2} & \cdots & \mathbf{R}_{j_b} \end{bmatrix}. \tag{3.23}$$

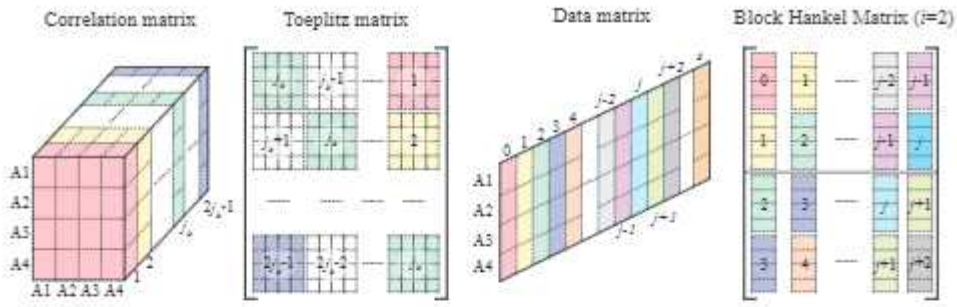

Fig. 3.4: Schematic representation of the construction of the Toeplitz matrix and block Hankel matrix for Cov-SSI and Data-SSI, respectively.

Applying the factorization property of the correlation matrix in Eq. (3.11) to all the R_j matrices stored in the Toeplitz matrix, $T_{1|_{j_b}}$ can be decomposed in the product of the following matrices:

$$\mathbf{T}_{1|_{j_b}} = \begin{bmatrix} \mathbf{C} \\ \mathbf{CA} \\ \dots \\ \mathbf{CA}^{j_b-1} \end{bmatrix} \begin{bmatrix} \mathbf{A}^{j_b-1}\mathbf{G} & \dots & \mathbf{AG} & \mathbf{G} \end{bmatrix} = \mathbf{O\Gamma}. \tag{3.24}$$

The second equality in Eq. (3.24) defines the following matrices: $\mathbf{O}$- extended observability matrix; and $\mathbf{\Gamma}$- reversed extended stochastic controllability matrix. The first one is a column of j_b blocks with dimensions l-by-n (n is the dimension of the state-space model). The second one is formed by j_b n-by-l matrices organized in a row. According to the previous equation, the Toeplitz matrix results from the product of a matrix with n columns by a matrix with n rows. Therefore, if $n < lj_b$, the rank of $T_{1|_{j_b}}$ is equal to n. Then, the SVD of the block Toeplitz matrix is calculated:

$$\mathbf{T}_{1|_{j_b}} = \mathbf{USV}^{\mathrm{T}} = \begin{bmatrix} \mathbf{U}_1 & \mathbf{U}_2 \end{bmatrix} \begin{bmatrix} \mathbf{S}_1 & \mathbf{0} \\ \mathbf{0} & \mathbf{0} \end{bmatrix} \begin{bmatrix} \mathbf{V}_1^{\mathrm{T}} \\ \mathbf{V}_2^{\mathrm{T}} \end{bmatrix} = \mathbf{U}_1\mathbf{S}_1\mathbf{V}_1^{\mathrm{T}}. \tag{3.25}$$

The number of non-zero SVs gives the rank of the decomposed matrix, which, in this case, coincides with n (assuming $n < lj_b$), the dimension of the state-space matrix $\mathbf{A}$. The comparison of Eqs. (3.24) and (3.25) shows that the observability and the controllability matrices can be calculated from the outputs of the SVD using the following partition of the singular values matrix:

$$\begin{aligned} \mathbf{O} &= \mathbf{U}_1\mathbf{S}_1^{1/2}, \\ \mathbf{\Gamma} &= \mathbf{S}_1^{1/2}\mathbf{V}_1^{\mathrm{T}}. \end{aligned} \tag{3.26}$$

Once the observability and controllability matrices are obtained, the identification of the state-space model matrices $\mathbf{A}$ and $\mathbf{C}$ is straightforward. On one hand, matrix $\mathbf{C}$ can be extracted from the first l lines of the observability matrix. On the other hand, the state matrix $\mathbf{A}$ can be computed according to different approaches. The developed software utilizes the Balanced Realization (BR) method which exploits the shift structure of the observability matrix, that is [126]:

$$\begin{bmatrix} \mathbf{C} \\ \mathbf{CA} \\ \dots \\ \mathbf{CA}^{j_b-2} \end{bmatrix} \mathbf{A} = \begin{bmatrix} \mathbf{CA} \\ \mathbf{CA}^2 \\ \dots \\ \mathbf{CA}^{j_b-1} \end{bmatrix} \Leftrightarrow \mathbf{A} = \begin{bmatrix} \mathbf{C} \\ \mathbf{CA} \\ \dots \\ \mathbf{CA}^{j_b-2} \end{bmatrix}^{\dagger} \begin{bmatrix} \mathbf{C} \\ \mathbf{CA}^2 \\ \dots \\ \mathbf{CA}^{j_b-1} \end{bmatrix} = \mathbf{O}^{to\dagger}\mathbf{O}^{bo}, \tag{3.27}$$

where $\mathbf{O}^{to}$ contains the first $l(j_b-1)$ lines of $\mathbf{O}$, and $\mathbf{O}^{bo}$ contains the last $l(j_b-1)$ lines of $\mathbf{O}_{j_b}$. The symbol $\dagger$ represents the Moore-Penrose pseudo-inverse.

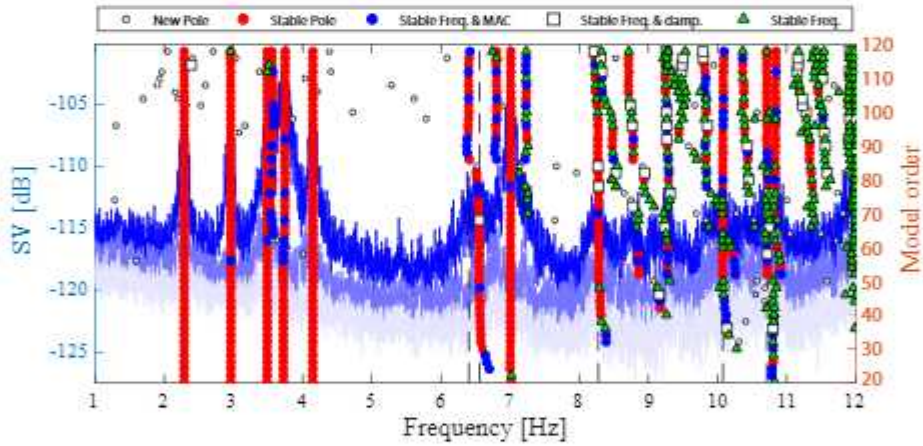

Fig. 3.5: Dynamic identification of the Consoli Palace using Cov-SSI in MOVA (stabilization diagram).

Figure 3.5 shows the stabilization diagram obtained using the Cov-SSI method for the ambient vibration data-set recorded during the AVT of the Consoli Palace. To do so, jb has been assumed as 70, resulting in a $70 \cdot 9 \times 70 \cdot 9$ Toeplitz matrix. Then, matrices $\mathbf{O}$, $\mathbf{\Gamma}$, $\mathbf{A}$ and $\mathbf{C}$ and then the modal parameters are estimated considering an odd number of singular values and vectors varying from 20 to 120. Similarly to the previous analyses, it is noted in Fig. 3.5 that six clear columns of stable poles are found at frequency values corresponding to the main natural frequencies of the Consoli Palace in the considered frequency range.

Data-SSI

Data-driven stochastic subspace identification (Data-SSI) is similar to Cov-SSI, but identifies the state sequence before the estimation of the state-space matrices. Data-driven SSI consists of the following steps: (a) construction of the block Hankel matrix of the measurements, H_i; (b) computation of the projection matrix, P_i; (c) estimation of the observability matrix, Γ_i; and (d) extraction of the modal parameters estimates from matrix Γ_i. The block Hankel matrix (sketched in Fig. 3.4) is defined as:

$$\mathbf{H}_i = \frac{1}{\sqrt{j}} \left[\begin{array}{cccc} \mathbf{y}(0) & \mathbf{y}(1) & \dots & \mathbf{y}(j-1) \\ \mathbf{y}(1) & \mathbf{y}(2) & \dots & \mathbf{y}(j) \\ \vdots & \vdots & \ddots & \vdots \\ \mathbf{y}(i-1) & \mathbf{y}(i) & \dots & \mathbf{y}(i+j-2) \\ \hline \mathbf{y}(i) & \mathbf{y}(i+1) & \dots & \mathbf{y}(i+j-1) \\ \mathbf{y}(i+1) & \mathbf{y}(i+2) & \dots & \mathbf{y}(i+j) \\ \vdots & \vdots & \ddots & \vdots \\ \mathbf{y}(2i-1) & \mathbf{y}(2i) & \dots & \mathbf{y}(2i+j-2) \end{array}\right] = \left[\begin{array}{c} \mathbf{Y}_{0|i-1} \\ \hline \mathbf{Y}_{i|2i-1} \end{array}\right] = \left[\begin{array}{c} \mathbf{Y}_p \\ \hline \mathbf{Y}_f \end{array}\right], \tag{3.28}$$

where $2i$ and j, with $j \leq s - 2i + 1$, are user-defined quantities representing the number of output block rows and the number of columns of matrix $\mathbf{H}_i$, respectively. The block Hankel matrix in Eq. (3.28) is subdivided into two sub-matrices, named as $\mathbf{Y}_p$ and $\mathbf{Y}_f$, which are usually referred to as past and future output block matrices. The identification of the Kalman filter state sequences and, as a consequence, of the state-space matrices is based on the orthogonal projection of the row space of the future outputs on the row space of the past outputs:

$$\mathbf{P}_i = \mathbf{Y}_f / \mathbf{Y}_p = \mathbf{Y}_f \mathbf{Y}_p^{\mathrm{T}} \left(\mathbf{Y}_p \mathbf{Y}_p^{\mathrm{T}}\right)^{\dagger} \mathbf{Y}_p, \tag{3.29}$$

which can be efficiently computed by the LQ factorization of the block Hankel matrix of the outputs. The main theorem of Data-SSI states that the projection matrix $\mathbf{P}_i$ can be factorized into the product of the observability matrix $\mathbf{O}_i$ and the Kalman filter state sequence $\hat{\mathbf{S}}_i$:

$$\mathbf{P}_i = \mathbf{O}_i \hat{\mathbf{S}}_i, \tag{3.30}$$

where $\hat{\mathbf{S}}_i$ is a matrix containing Kalman filter estimates of the state vector at different time steps. Similarly, the projection matrix $\mathbf{P}_{i-1}$ can be obtained as:

$$\left[\begin{array}{c} \mathbf{Y}_{0|i-1} \\ \mathbf{Y}_{i|i} \\ \hline \mathbf{Y}_{i+1|2i-1} \end{array}\right] = \left[\begin{array}{c} \mathbf{Y}_{0|i} \\ \hline \mathbf{Y}_{i+1|2i-1} \end{array}\right] = \left[\begin{array}{c} \mathbf{Y}_p^+ \\ \mathbf{Y}_f^- \end{array}\right] \Leftrightarrow \mathbf{P}_{i-1} = \mathbf{Y}_f^- / \mathbf{Y}_p^+, \tag{3.31}$$

where $\mathbf{Y}_p^+$ is the past output with one extra block row, while $\mathbf{Y}_f^-$ is the future output matrix without the first block row $\mathbf{Y}_{i|i}$. The observability matrix $\mathbf{O}_i$ can be estimated from the SVD of matrix $\mathbf{W}_1\mathbf{P}_i\mathbf{W}_2$:

$$\mathbf{W}_1\mathbf{P}_i\mathbf{W}_2 = \begin{bmatrix} \mathbf{U}_1 & \mathbf{U}_2 \end{bmatrix} \begin{bmatrix} \mathbf{\Sigma}_1 & \mathbf{0} \\ \mathbf{0} & \mathbf{0} \end{bmatrix} \begin{bmatrix} \mathbf{V}_1^{\mathrm{T}} \\ \mathbf{V}_2^{\mathrm{T}} \end{bmatrix} = \mathbf{U}_1\mathbf{\Sigma}_1\mathbf{U}_1^{\mathrm{T}} \tag{3.32}$$

According to the Canonical Variate Analysis (CVA) method, the weighting matrices $\mathbf{W}_1$ and $\mathbf{W}_2$ take the form $\mathbf{W}_1 = \left((1/j)\mathbf{Y}_f\mathbf{Y}_f^{\mathrm{T}}\right)^{-1/2}$ and $\mathbf{W}_2 = \mathbf{I}$. Then, the observability matrix $\mathbf{O}_i$ and the Kalman filter state sequence $\hat{\mathbf{S}}_i$ can be computed as:

$$\begin{aligned} \mathbf{O}_i &= \mathbf{U}_1\mathbf{\Sigma}_1^{1/2}, \\ \hat{\mathbf{S}}_i &= \mathbf{O}_i^{\dagger}\mathbf{P}_i. \end{aligned} \tag{3.33}$$

A similar factorization can be applied to $\mathbf{P}_{i-1}$:

$$\mathbf{P}_{i-1} = \mathbf{O}_i^{\uparrow}\hat{\mathbf{S}}_{i_1} \Leftrightarrow \hat{\mathbf{S}}_{i+1} = \left(\mathbf{O}_i^{\uparrow}\right)^{\dagger}\mathbf{P}_{i-1}, \tag{3.34}$$

where $\mathbf{O}_i^{\uparrow}$ can be directly obtained from $\mathbf{O}_i$ by deleting the last l rows. Finally, the state-space matrices $\mathbf{A}$ and $\mathbf{C}$ are obtained in a least squares sense as [101]:

$$\begin{bmatrix} \mathbf{A} \\ \mathbf{C} \end{bmatrix} = \begin{bmatrix} \hat{\mathbf{S}}_{i+1} \\ \mathbf{Y}_{i|i} \end{bmatrix} \hat{\mathbf{S}}_i^{\dagger}. \tag{3.35}$$

3.3.3. Comparison analysis

The identification results using all the previously reported methods are presented in Table 3.1. As reported earlier, six clear modes are identified in the frequency range from 0 to 12 Hz. These correspond to two global first bending modes in the $x-$ and $y-$directions, denoted as Fx1 and Fy1, respectively, one global torsional mode, T1, and three local modes related to the interaction between the palace and the bell-tower, denoted as L1, L2, and L3. The global mode shapes obtained using Cov-SSI are depicted in Fig. 3.6. It is noted that very similar resonant frequency estimates are obtained by all the different identification methods, while large differences are found in terms of damping ratios. The quality of damping estimates is highly dependent on the level of excitation of the structure, which is often quite low in CH structures in operational conditions. This is specially critical in this case study, where ambient accelerations in the palace did not exceed 1.5E-3 m/s^2, so substantial uncertainties are expected to arise in the determination of damping properties.

Table 3.1: Vibration-based system identification results of the Consoli Palace through the AVT conducted on May 4th 2017 using the EFDD, p-LSCF, Cov-SSI, and Data-SSI methods.

	Natural frequencies [Hz]				Damping ratios [%]			
Mode	EFDD	p-LSCF	Cov-SSI	Data-SSI	EFDD	p-LSCF	Cov-SSI	Data-SSI
Fx1	2.270	2.296	2.285	2.287	1.471	0.561	1.243	1.383
Fy1	2.953	2.970	2.958	2.961	0.361	0.166	0.926	1.017
L1	3.479	3.463	3.488	3.492	0.247	0.118	1.325	1.387
L2	3.740	3.723	3.729	3.717	0.352	1.767	2.542	2.824
T1	4.153	4.124	4.148	4.150	0.303	0.423	1.087	1.226
L3	6.986	7.016	7.010	7.008	0.138	0.549	1.134	1.121

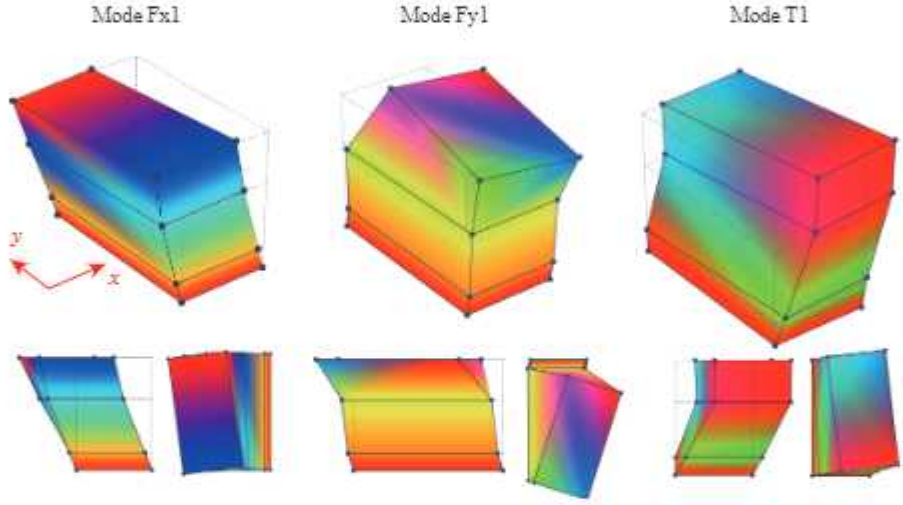

Fig. 3.6: Global mode shapes, first bending modes Fx1 and Fy1 and torsional mode T1, obtained from the AVT of the Consoli Palace using Cov-SSI.

3.4.Automated SSI

Given their trade-off between accuracy and computational demands, the automation efforts in this thesis have been devoted to SSI methods. In particular, two different algorithms have been implemented, depending whether the number of block rows in the Hankel/Toeplitz matrix are kept fixed in Section 3.4.1 or are varied within a certain interval in Section 3.4.2.

3.4.1.SSI with fixed time lag

The SSI algorithms are controlled by two user-defined parameters: (i) the model order n, and (ii) the time-lag parameter (j_b–Cov-SSI, i–Data-SSI). The considerations in these two methods is equivalent, so let us focus the discussion on Cov-SSI. In this case, the value of j_b defines number of block rows in the Toeplitz matrix and, therefore, determines the computational cost in the SVD in Eq. (3.25). Too small values of j_b may fail to identify low-frequency modes,

while too large values increase the number of spurious modes and raise the computational burden of the identification. The value of j_b may be chosen by the following rule of thumb [130]:

$$j_b \geq \frac{f_s}{2\, f_o}, \tag{3.36}$$

with f_o the expected fundamental frequency of the system. This condition ensures that the covariance series in $\mathbf{T}_{1|_{j_b}}$ contain a time window with a sufficiently large number of cycles of the lowest frequency of interest.

With regard to the model order, theoretically n can be defined by inspecting the number of non-zero singular values in the SVD of the Toeplitz matrix. Nevertheless, in practice, due to the presence of noise in the measurements and the circumstance that the system may not have a perfectly linear behavior, singular values that should be zero usually present certain residual values. As a result, it is common to specify the model order in a conservative way with the aim of identifying weakly-excited modes (at least larger than twice the number of physical modes of the system). Nonetheless, this leads to the introduction of numerical modes (also called spurious or noise modes) induced by over-modeling of the noise in the output measurements. The most popular approach to separate physical from spurious modes consists in conducting the identification for increasing model orders within a certain interval $[n_{min}, n_{max}]$ with steps Δn. Let us denote $H_n = (n_{max} - n_{min})/\Delta n$ the number of model orders to be identified. A initial cleansing of the modal poles can be conducted at this stage by means of hard criteria (HC) eliminating complex conjugate modes and poles violating certain feasibility constraints, e.g. physically meaningful damping ratios (ζ_{max}) or minimum modal phase collinearity (MPC) [131] values. Then, the retained modal parameter estimates are represented together conforming a stabilization diagram (See Fig. 3.7 (a)). On this basis, stable poles can be identified as those abiding certain soft criteria (SC) in terms of tolerances of modal estimates (resonant frequency, damping ratios and mode shapes) obtained between consecutive model orders. This allows to distinguish physical from spurious modes by looking for vertical alignments of stable poles in the stabilisation diagram, that is to say, modes that consistently appear in most of the identifications.

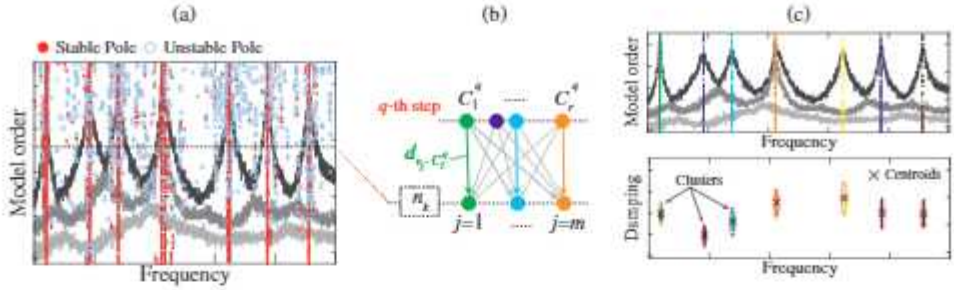

Fig. 3.7: Automated SSI: (a) stabilization diagrams, (b) modal distance, and (ccc) agglomerate hierarchical clustering.

While stabilisation diagrams provide a powerful tool to manually identify sets of physical modes, automated interpretation procedures are required for their use in continuous SHM. To this aim, agglomerate hierarchical clustering algorithms such as the one proposed in reference [116] are commonly adopted. The main goal is to group the previously identified stable modes into a set of homogeneous data clusters pertaining to the same structural mode. The algorithm starts by setting the first cluster seeds C_i^0, $i = 1, ..., r$ as the stable poles obtained for the maximum model order n_{max}, and initiating their cluster sizes as $cs_i = 1$. Afterward, the algorithm sequentially explores the similarities between the existing clusters C_i^q $(q = 1, \ldots, H_n)$ and the stable poles identified with model orders from $n_{max} - \Delta n$ to n_{min}. Let us focus on the construction of a generic cluster C_i. At a generic q-th step, cluster C_i^q is compared against the m stable poles v_j, $j \in [1, ..., m]$, identified at the corresponding model order n_k, $k = 1 - (2 - n_{max}) \frac{q - H_n}{1 - H_n}$ (see Fig. 3.7) (b). In order to compare mode v_j and cluster C_i^q, a similarity metric is defined as:

$$d_{v_j - C_i^q} = (1 - \eta) \frac{\left| f_{v_j} - \overline{f}_{C_i^q} \right|}{\overline{f}_{C_i^q}} + \eta \left(1 - MAC \left(\boldsymbol{\Theta}_{v_j}, \overline{\boldsymbol{\Theta}}_{C_i^q} \right) \right), \tag{3.37}$$

where $\overline{f}_{C_i^q}$ and $\overline{\boldsymbol{\Theta}}_{C_i^q}$ denote the mean values of the frequencies and mode shapes of the poles conforming cluster C_i^q, respectively, while f_{v_j} and $\boldsymbol{\Theta}_{v_j}$ are the frequency and the mode shape of the j-th pole, v_j, respectively. Term η denotes a weighting factor between the contributions of the similarities in terms of resonant frequencies and mode shapes. Then, the similarities between C_i^q and the m poles are arranged in a similarity vector $\mathbf{d}_q$ as:

$$\mathbf{d}_q = \left[d_{v_1 - C_i^q}, d_{v_2 - C_i^q}, \ldots, d_{v_m - C_i^q} \right]^{\mathrm{T}}, \tag{3.38}$$

and the following rule is applied:

$$\begin{cases} C_i^{q+1} = C_i^q \cup \{v_h\}\,,\ cs_h = cs_h + 1 & \text{if } d_{q,h} = \min(\mathbf{d}_q) \leq d_{max} \\ C_i^{q+1} = C_i^q & \text{otherwise} \end{cases} \tag{3.39}$$

meaning that the h-th mode v_h (which is the closest one in terms of frequency and mode shape) is assigned to cluster C_i^q if the similarity value $d_{q,h}$ is smaller than an user-defined threshold d_{max}. If assigned, the centroid of the current cluster is updated in the next step C_i^{q+1} as the average value of frequencies, damping ratios, and mode shapes of the poles pertaining to this cluster. At this stage, poorly populated clusters can be considered as spurious modes and disregarded by checking if their cluster sizes are below a certain user-defined threshold cs_{min}, i.e. $cs_i \leq cs_{min}$. The algorithm terminates with a set of $C_i^{H_n}$ clusters characterized by their centroids (average value of frequencies, damping ratios, and mode shapes) and cluster sizes cs_i (see Fig. 3.7 (c)).

3.4.2. Fully automated SSI

Instead of following a rule of thumb such as the one in Eq. (3.36), other authors propose the use of convergence analyses of the condition number of $\mathbf{T}_{1|_{j_b}}$ or certain modal estimates for increasing values of j_b to ascertain the optimal value of the time-lag parameter (see e.g. [132]). In this thesis, an alternative procedure first proposed by Ubertini *et al.* [47] and consisting of conducting iterative identifications affecting both the model order n and the time-lag parameter j_b has been adopted. This procedure comprises the following steps: (a) modal identification for different values of the number of rows and columns of the Toeplitz/Hankel matrices, respectively; (b) noise modes elimination; and (c) clustering analysis.

(a) Iterative modal identification

A total number of N SSI analyses are performed considering values of j_b varying within certain user-defined intervals $\left[j_{b,min}, j_{b,max}\right]$ and steps Δj_b. This procedure results in a set of M poles, whose modal information can be organized in matrix form as:

$$\begin{aligned} \mathbf{f} &= [f_1\, f_2\, \ldots\, f_M]^{\mathrm{T}}\,, \\ \boldsymbol{\zeta} &= [\zeta_1\, \zeta_2\, \ldots\, \zeta_M]^{\mathrm{T}}\,, \\ \boldsymbol{\Theta} &= [\boldsymbol{\Theta}_1\, \boldsymbol{\Theta}_2\, \ldots\, \boldsymbol{\Theta}_M]\,, \end{aligned} \tag{3.40}$$

where f_m, ζ_m, and $\boldsymbol{\Theta}_m$ denote the frequency, damping, and mode shape vector of an arbitrary m-th mode, $m = 1, 2, \ldots, M$.

(b) Noise modes elimination

Noise modes elimination is performed similarly to the previous procedure in Section 3.4.1, but accounting for variations of both j_b and i. To discern between noise modes and physical ones, a vector $\mathbf{c} = [c_1, c_2, \ldots, c_M]^{\mathrm{T}}$ is computed with components c_m, $m = 1, 2, \ldots, M$, given by:

$$c_m = \begin{cases} -1 + \sum_{l=1}^{M} \delta_{lm}, & \text{if} \quad \zeta_m \in [0, \zeta_{max}] \\ 0, & \text{if} \quad \zeta_m \notin [0, \zeta_{max}] \end{cases} \tag{3.41}$$

with

$$\delta_{lm} = \begin{cases} 1, & \text{if} \quad \Delta f_{lm} \leq \epsilon_f,\ \Delta\zeta_{lm} \leq \epsilon_\zeta,\ 1 - MAC_{lm} \leq \epsilon_{MAC} \\ 0, & \text{otherwise} \end{cases}$$
$$\Delta f_{lm} = \frac{|f_l - f_m|}{f_m},\ \Delta\zeta_{lm} = \frac{|\zeta_l - \zeta_m|}{\zeta_m},\ MAC_{lm} = MAC(\boldsymbol{\Theta}_l, \boldsymbol{\Theta}_m), \tag{3.42}$$

with ϵ_f, ϵ_ζ, and ϵ_{MAC} being the user-defined SC tolerances. An arbitrary component c_m represents the number of modes, among all the M identified ones, which have similar modal features to those of the m-th mode. Therefore, the m-th mode is said to be stable when it is similar in terms of frequency, damping, and mode shape to a minimum number N_{min} of other modes, i.e. $c_m \geq N_{min}$ (a value of $N_{min} = N/10$ is recommended in reference [47] as a compromise for eliminating most of the noise modes without canceling the physical ones). Then, the number of stable poles can be readily obtained computing a vector $\mathbf{S}$:

$$\mathbf{S} = [S_1\, S_2\, \ldots\, S_M]^{\mathrm{T}},$$
$$S_m = \begin{cases} 1, & \text{if} \quad c_m \geq N_{min} \\ 0, & \text{otherwise} \end{cases} \tag{3.43}$$

whose components assign 0 and 1 to unstable and stable modes, respectively. Hence, the total number of stable modes, P, simply reads $P = \sum_{l=1}^{M} S_l$. The vectors of stable frequencies $\mathbf{f}^s$ and damping ratios $\boldsymbol{\zeta}^s$, and the matrix of stable mode shapes $\boldsymbol{\Theta}^s$ can be extracted as:

$$\mathbf{f}^s = \mathbf{HE}\,\mathbf{f} = [f_1\, f_2\, \ldots\, f_P]^{\mathrm{T}},$$
$$\boldsymbol{\zeta}^s = \mathbf{HE}\,\boldsymbol{\zeta} = [\zeta_1\, \zeta_2\, \ldots\, \zeta_P]^{\mathrm{T}}, \tag{3.44}$$
$$\boldsymbol{\Theta}^s = \left(\mathbf{HE}\,\boldsymbol{\Theta}^{\mathrm{T}}\right)^{\mathrm{T}} = [\boldsymbol{\Theta}_1\, \boldsymbol{\Theta}_2\, \ldots\, \boldsymbol{\Theta}_P],$$

where **HE** is a $P \times M$ matrix whose non-zero components are $HE_{p,\pi_p} = 1$, $p = 1, 2, \ldots, P$, with $\pi_1, \pi_2, \ldots, \pi_p$ being the positions of the non-zero terms of vector **S**.

(c) Clustering analysis

An agglomerate hierarchical clustering algorithm is implemented to automate the interpretation of the SSI outputs from the previous steps. Such an analysis is aimed at grouping the P stable modes into a set of homogeneous data clusters pertaining to the same structural mode. The algorithm starts by generating a permutation vector $\mathbf{v} = [v_1, v_2, \ldots, v_P]^{\mathrm{T}}$, containing the elements of vector $\mathbf{p} = [1, 2, \ldots, P]^{\mathrm{T}}$ in a random order. There follows an iterative procedure composed of P steps sketched in Fig. 3.8. At the first step, the v_1-th mode is considered as the first cluster seed $C_1^1 = \{v_1\}$, where C_1^1 represents cluster C_1 evaluated at step number 1 (superscript 1). The next $P - 1$ steps work in a similar way. Let us focus on a generic q-th step, at which a certain number r of clusters will already exist. In order to compare the v_q-th mode and a cluster C_j, $j \in [1, ..., r]$, a similarity rule equivalent to the one in Eq. (3.37) is defined as:

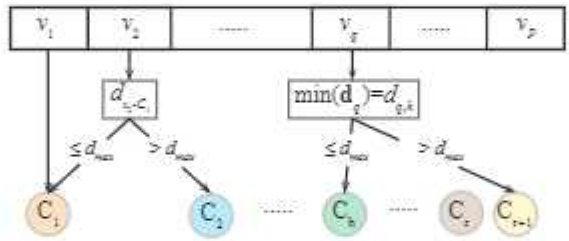

Fig. 3.8: Graphical sketch of the agglomerate hierarchical clustering approach.

$$d_{v_q-C_j} = \frac{\left| f_{v_q}^s - \overline{f}_{C_j} \right|}{\overline{f}_{C_j}} + 1 + MAC(\boldsymbol{\Theta}_{v_q}^s, \overline{\boldsymbol{\Theta}}_{C_j}), \tag{3.45}$$

where $\overline{f}_{C_j}$ and $\overline{\boldsymbol{\Theta}}_{C_j}$ denote the mean values of the frequencies and mode shapes of the poles composing cluster C_j, respectively, while $f_{v_q}^s$ and $\boldsymbol{\Theta}_{v_q}^s$ are the frequency and the mode shape of the v_q-th mode, respectively. Then, the similarities between the v_q-th mode and the r clusters are arranged in a similarity vector $\mathbf{d}_q$ as:

$$\mathbf{d}_q = \left[d_{v_q-C_1}, d_{v_q-C_2}, \ldots, d_{v_q-C_r} \right]^{\mathrm{T}}, \tag{3.46}$$

and the following rule is applied:

$$\begin{aligned} &\text{if } d_{q,h} = \min(\mathbf{d}_q) \leq d_{max} \Rightarrow C_h^q = C_h^{q-1} \cup \{v_q\}, \\ &\text{if } d_{q,h} = \min(\mathbf{d}_q) > d_{max} \Rightarrow C_h^q = C_h^{q-1}, C_{r+1}^1 = \{v_q\}, \end{aligned} \tag{3.47}$$

meaning that the v_q-th mode is assigned to cluster C_h (which is the closest one in terms of frequency and mode shape) if the similarity value $d_{q,h}$ is smaller than an user-defined threshold d_{max}; otherwise a new cluster C_{r+1} is created containing the v_q-th mode. Likewise in the previous procedure, the algorithm terminates with a certain number nc of clusters defined by their centroids and cluster sizes.

3.5.Modal Tracking

When implemented into a long-term ambient vibration-based SHM system, the previously introduced automated OMA procedures result in clusters of stable poles in time such as those shown in Fig. 3.9 (a) for the case of the Consoli Palace. In this figure, one can easily note that some of the identified clusters do not actually represent any real mode of the structure, some of them being clear outliers. This is a frequent situation in practice due to failures in the identification or the presence of nonstationary non-Gaussian excitations. Moreover, the identification may fail to identify some modes at times when these are weakly-excited (e.g. during night-time when excitations induced by traffic are usually low). To address these issues, it is necessary to implement a frequency tracking approach to extract time series of the modal signatures of the structure. A classical frequency tracking approach is to define a reference list or baseline modal properties extracted from a separate AVT [37]. Once defined, the time series of modal features are traced by exploiting similarities between the reference modes and all the identified sets of modal characteristics. This can be conducted by comparing the sets of poles continuously extracted by the automated OMA procedure against the reference baseline through a similarity metric equivalent to that in Eq. (3.37). To avoid misclassification, the comparison is only conducted for sets of poles abiding with certain user-defined tolerances in terms of resonant frequencies, damping ratios and MAC values. The modal tracking algorithm can be set up as static or dynamic whether the reference baseline is set fixed or variable. The latter procedure updates the reference modes as new poles are added to the time series, which allows to accommodate fast trends in the modal signatures induced by EOCs (e.g. freezing conditions). The outcome of modal tracking is the time series of resonant frequencies, damping ratios and mode shapes of the reference modes as shown in Fig. 3.9 (b).

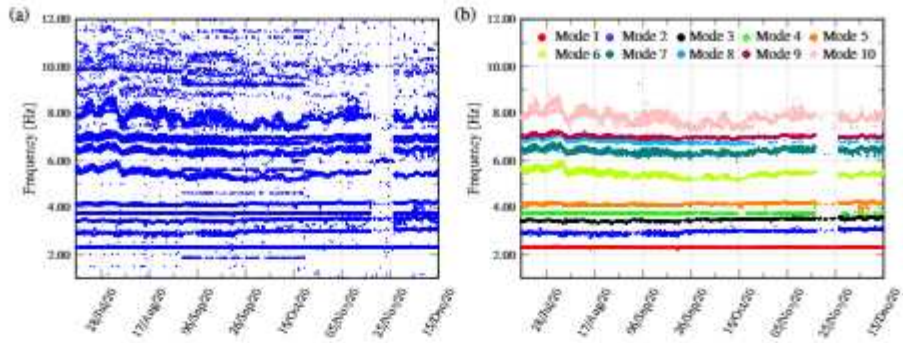

Fig. 3.9: Identified resonant frequencies by automated OMA of the Consoli Palace (a), and time series of meaningful resonant frequencies obtained by modal tracking (b).

With the aim of facilitating the frequency tracking process and avoiding the need for conducting an independent AVT, a novel density-based tracking procedure was proposed in reference [124] inspired by the work of Favarelli and Giorgetti [133]. The algorithm starts by automatically setting the reference baseline (starting phase) without no assumptions on the reference modal signatures or the number of modes to track. The idea is to analyze the probability distribution function (PDF) of the identified resonant frequencies in an initial period of N_t acquisitions collected in an observation vector $\mathbf{x}$ as shown in Fig. 3.10 (a) for the Z-24 Bridge ($N_t = 200$). In this case, the histogram of $\mathbf{x}$ in Fig. 3.10 (b) reveals seven areas of concentrated probability (modes of the PDF) corresponding to the first seven natural frequencies of the bridge in the broadband up to 21 Hz. To automatically identify these modes, a clustering procedure combining k-means and GMM is implemented. Firstly, k-means clustering [77] is used to partition the data into K clusters with maximum squared Euclidean distance between their centroids. To avoid the dependence on the initial seed of the k-means approach, the optimal clustering is selected as the best solution among 10 k-means repetitions with random centroid initialization. The best solution is then used as the initial classification for the GMM. Since the number of modes in the reference baseline is unknown, the previous procedure is conducted sequentially for increasing numbers of target clusters from $K = 1$ to K_{max}, with K_{max} being conservatively larger than the maximum number of expected modes. Once obtained, the optimal number of clusters and the corresponding baseline modes are obtained through the GMM with minimum BIC (refer to Section 2.4.4). In the case of the Z-24 Bridge, K_{max} was set to 12. It is noted in Fig. 3.10 (b) how the proposed procedure accurately identifies the seven natural modes of the bridge. On this basis, the reference baseline modes are defined according to the average values of the modal poles pertaining to the identified mixtures.

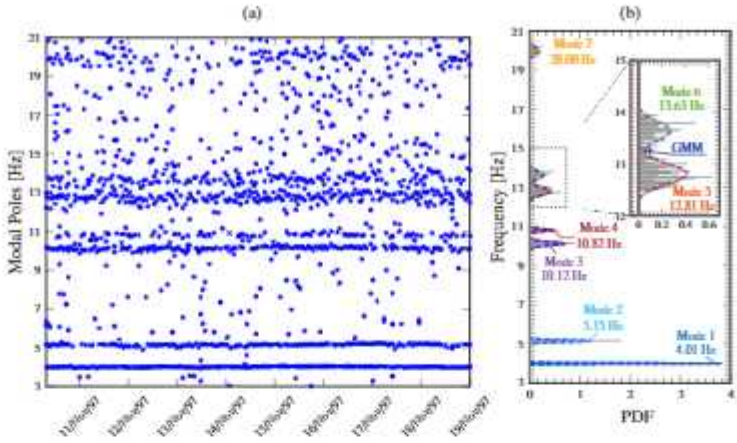

Fig. 3.10: Modal identification results of the first $N_t = 200$ acquisitions in the Z-24 Bridge (a), and automated identification of the reference modal baseline through parametric clustering (b).

Once the reference baseline is identified, it follows the online phase where the reference modes are tracked throughout the whole monitoring period. To do so, a Gaussian kernel is defined for all the reference resonant frequencies in the baseline as:

$$\mathcal{N}\left(\theta; f^{\text{ref}}, \sigma_r\right) = e^{-\frac{1}{2\sigma_r^2}\left(\theta - f^{\text{ref}}\right)^2}, \tag{3.48}$$

with f^{ref} and σ_r being the r-th reference resonant frequency and the associated standard deviation σ_r. Parameter σ_r controls the kernel width, and, as a rule of thumb, it can be selected as the standard deviations obtained by the mixtures identified in the previous GMM. Then, to compare the identified poles at a generic time instant q, the following distance metric is also defined:

$$dm = (1-\alpha)\frac{\left|f^p - f^{\text{ref}}\right|}{f^{\text{ref}}} + \alpha\left[1 - MAC\left(\boldsymbol{\Theta}^p, \boldsymbol{\Theta}^{\text{ref}}\right)\right], \tag{3.49}$$

with superscripts ref and p relating the corresponding magnitudes to the reference mode and a generic pole, and coefficient α being a weighting factor between the contribution of the resonant frequencies and mode shapes. At a generic step N_a in the tracking process, consider a number n_{ref} reference modes and n_p poles abiding certain under-defined tolerances with respect to the baseline modes. Then, the distances between the retained poles with respect to the baseline modes are computed and stored in a distance matrix $\mathbf{D} \in \mathbb{R}^{n_{\text{ref}} \times n_p}$. On this basis, the pole with minimum distance to every reference mode is selected

and stored in observation matrix **F** containing the time series of tracked modes:

$$\mathbf{F} = \begin{bmatrix} f_1^{(1)} & \dots & f_1^{(N_a)} \\ \dots & \dots & \dots \\ f_{n_{\text{ref}}}^{(1)} & \dots & f_{n_{\text{ref}}}^{(N_a)} \end{bmatrix}. \tag{3.50}$$

The previous tracking procedure can be also made dynamic by updating the reference resonant frequencies every time a new pole is collected in **F**. To do so, following the Bayes' rule and considering conjugate prior and posterior distributions, the mean values of the Gaussian kernels in Eq. (3.48) are updated as f_{up}^{ref}:

$$f_{up}^{\text{ref}} = \sigma_{up} \left(\frac{f^p}{\sigma_f^2} + \frac{f^{\text{ref}}}{\sigma_r^2} \right), \tag{3.51}$$

with

$$\sigma_{up} = \left(\frac{1}{\sigma_f^2} + \frac{1}{\sigma_r^2} \right)^{-1}, \tag{3.52}$$

and σ_f denoting the standard deviation of a zero-mean Gaussian likelihood function. Large values of σ_f decrease smoothness but allow capturing sudden changes of modal frequencies. The standard deviation of the Gaussian kernels in Eq. (3.48) are not updated throughout the tracking process to keep the kernel width constant.

3.6. Application case study: Z-24 Bridge

This section presents the combination of the previously introduced OMA tools with the statistical pattern recognition techniques previously introduced in Chapter 2 for the damage assessment of the Z-24 Bridge (Section 1.5.1). In particular, the acceleration records of this case study were subject to a filtering process including linear detrend, second-order Butterworth filtering with cut-off frequencies of 1 and 30 Hz, and signal down-sampling to 60 Hz. Then, the modal signatures of the bridge were identified following the previously introduced automated Cov-SSI procedure with identification parameters $j_b = 120$ (2 s), $d_{max} = 0.03$, $\zeta_{max} = 10\%$, and model orders ranging from 2 to 100 with steps of 2. The resulting set of modal clusters in time is furnished in Fig. 3.11 (blue dots). On this basis, the time series of physically representative modes of the bridge were extracted through the automated frequency tracking approach previously introduced in Section 3.5. To do so, the reference baseline obtained by a GMM and previously reported in Fig. 3.10 was used to trace the time series of the seven modal signatures of the bridge. In the analyses, the model parameters of the Guassian kernels used for the tracking were extracted from the GMM, and the standard deviation of the likelihood function used for the

updating of the reference resonant frequencies (mean values of the Guassian kernels) was set to $\sigma_f = 0.55$. Also, the tolerances for relative variations of resonant frequencies were set between 3% to 5%. It is noted in Fig. 3.11 that the proposed algorithm successfully traces the time series of resonant frequencies all throughout the monitoring period (average success rate of 75.77%).

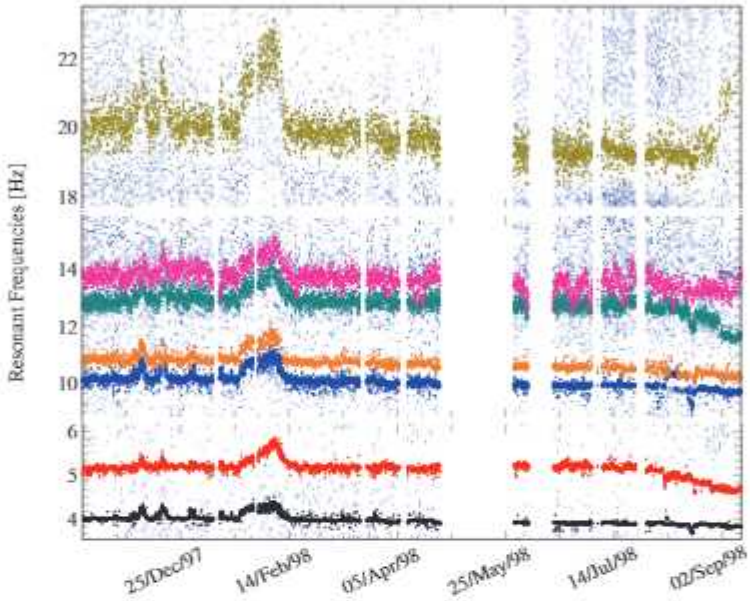

Fig. 3.11: Time series of resonant frequencies of the Z-24 Bridge identified by automated density-based frequency tracking.

The correlation between the fundamental frequency and the environmental air temperature is depicted in Fig. 3.12 (a). It is clear the existence of a non-linear biphasic correlation for temperatures below and above zero. This fact explains the presence of sudden shifts in the natural frequencies previously reported in Fig. 3.11 (see e.g. January 1998). As previously hypothesized by many other authors, this phenomenon is explained by the stiffening of the asphalt layer during freezing conditions. The results in Figs. 3.11 and 3.12 are clear examples of the need for identifying and eliminating the variance induced by EOCs before conducting damage identification. To do so, a cluster-wise non-linear MLR model has been trained considering the first four resonant frequencies of the bridge as estimators, and the recordings by 5 temperature sensors as predictors (air temperature, temperature in Web south, pavements, and soffit, see reference [134] for further details). The monitoring data have been trivially separated in two clusters containing temperatures below and above zero, and a MLR model has been constructed over a training period defined from November 10^{th} 1997 until July 14^{th} 1998 (4404 samples). Reasonably good fittings

were found between the predictions of the MLR model and the experimental data as shown in Fig. 3.12 (a) (coefficient of determination R^2=0.8 and root-mean-squared error (RMSE) of 4.3E-2). Once trained, the MLR model is used to reconstruct the time series of resonant frequencies throughout the damage assessment period as shown in Fig. 3.12.

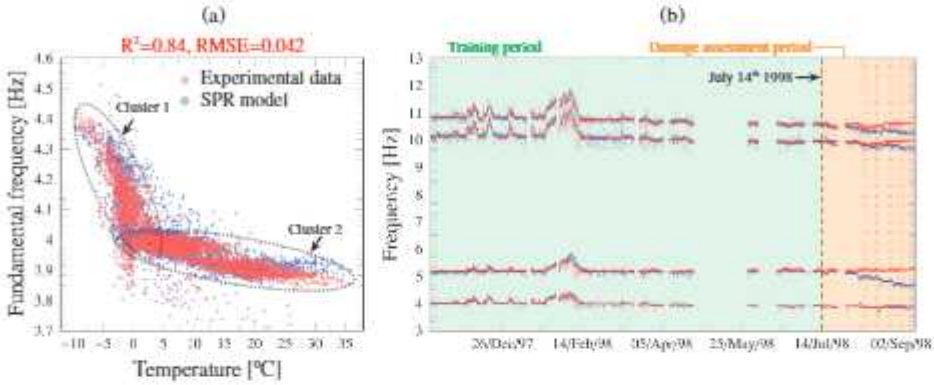

Fig. 3.12: Correlation between the fundamental frequency of the Z-24 Bridge and air temperature (over the training period from November 10$^{\text{th}}$ 1997 until July 14$^{\text{th}}$ 1998) (a). Predictions of the first four resonant frequencies of the Z-24 Bridge by MLR (b). Red dotted lines in (b) denote the dates when the artificial damage was induced in the bridge.

Finally, Fig. 3.13 shows the Hotelling's T^2 control chart of the residuals from Fig. 3.12. In this case, given the limited number of data-points in the damage assessment period, a subgroup size $r = 1$ has been defined in Eq. (2.27) for better illustration. The UCL has been set with a confidence level of 90% and estimated through the empirical analysis of the cumulative distribution of the data points in the training period. The appearance of the induced damage is clearly noted in Fig. 3.13 in the shape of a persistent accumulation of data points above the UCL. In particular, after the first damage scenario (August 10$^{\text{th}}$ 1998, (D1)-Lowering of pier of 20 mm), the number of data points violating the UCL raises to 67.5%. It is also noticeable in Fig. 3.13 (b) that persistent shifts are found in the data-points after some major damage events (indicated with inserts in the figure), which evidence the appearance of accumulated damage. To highlight this aspect, the moving median of the data points in the control chart (time window of 72 data points, 3 days) is included in Fig. 3.13. It can be observed that the moving median exhibits three major shifts (after D1, D3 and D5) followed by intermediate progressive raises as a result of intermediate pathologies. These results demonstrate the ability of the adopted SHM techniques to handle large databases of heterogeneous monitoring data and effectively detect damage and, to some extent, track its severity.

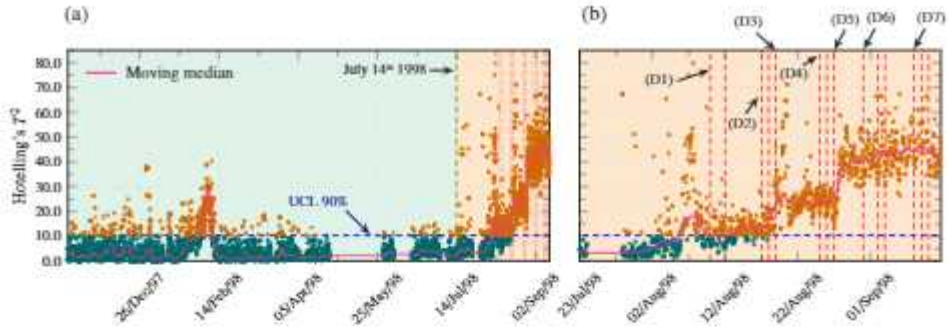

Fig. 3.13: Control chart for damage identification of the Z-24 Bridge (a) and zoom view of the damage assessment period (b). Red dashed lines indicate the dates when the artificial damage was induced in the bridge ((D1)-lowering of pier 20 mm, (D2)-lowering of pier 80 mm, (D3) - tilt of foundation, (D4) - spalling of concrete, (D5) - landslide at abutment, (D6) - failure of concrete hinge, (D7) - rupture of tendons).

4. Ambient Noise Deconvolution Interferometry

4.1. Introduction

The vibration-based SHM techniques overviewed in the previous chapter are highly effective for interrogating the global integrity of structures. This constitutes a remarkable advantage of dynamic testing, since sensors do not need to be deployed proximate to the pathology or in areas of difficult access to detect damage. Nonetheless, such techniques may be inefficient in detecting local pathologies with little influence on the global stiffness and, consequently, on the modal features of the monitored asset. Moreover, damage localization through the analysis of variations in the modal signatures is usually troublesome in large-scale civil engineering structures, where the identification of high-frequency modes is often challenging or impossible. Such limitations support the need for implementing aggregated SHM systems fusing the monitoring data from heterogeneous sensing solutions (e.g. dynamic, static, chemical) so to achieve both local and global damage identification.

In general, *data fusion* relates the integration of information from multiple sources into a new database to enhance the observability and identifiability of a system [41]. This new database is intended to be more informative, reducing uncertainties in the damage identification by increasing the information completeness and enhancing the decision making. In general, data fusion can be achieved in three levels, namely *data-level*, *feature-level*, and *decision-level* [135]. In data-level fusion, the raw measurements from multiple sensors are directly combined before further processing. Feature-level fusion directly operates on statistical features or signatures of heterogeneous nature. Finally,

in decision-level fusion, decision-making is performed by integrating the decisions achieved from different data sources through particular combination rules. Some common data fusion techniques are data registration, Bayesian probabilistic approaches, Dempster-Shafer (DS) evidential approach, fuzzy reasoning, state estimation, machine learning algorithms, and weighted combinations. For a comprehensive review on data fusion techniques applied to SHM, readers may consult reference [136]. Within the paradigm of SHM as a statistical pattern recognition problem, feature-level fusion represents a natural simple approach. Note that the statistical models presented in Chapter 2 work on arbitrary sets of estimators and predictors, irrespectively of the nature of the sensor system used for their extraction. Therefore, it is possible to use feature sets combining data of very diverse nature, and fuse them within the novelty analysis by constructing hybrid control charts. For instance, it is possible to use static data to eliminate the effect of EOC over dynamic features and vice versa. This approach has been implemented in the developed software tools as explained later in Chapter 6.

Seismic interferometric techniques represent another interesting approach for data fusion with an important synergy with OMA. Seismic interferometry conceives the response of a dynamic system as a superposition of propagating waves, and exploits the wave velocities between pairs of sensors as DSFs [137]. The fundamentals of this approach lie in the fact that scattering and attenuation of propagating pulses depend upon the constitutive properties of the medium and, therefore, the identification of wave velocities provides an indirect evaluation of the intrinsic stiffness of the system [138]. Given that wave velocities depend locally upon the stiffness of the structure, damage identification through seismic interferometry is local in essence [139]. Most interestingly, damage identification (detection, localization and, to some extent, quantification) can be performed in a fully data-driven way simply by peak-picking analysis of waveforms [140]. Moreover, the combination of seismic interferometry and OMA is trivial since both approaches exploit the same monitoring data and simply differ in the obtained DSFs, requiring no additional sensors if a sensor arrangement suitable for both techniques is properly designed.

The broad majority of research on the application of seismic interferometry to structural system identification has focused on reinforced-concrete (RC) buildings under seismic actions. In this regard, a noticeable contribution was made by Snieder and Şafak [141] who studied the wave propagation properties of the 9-storey RC Millikan Library in Pasadena (Los Angeles, US) during the Yorba Linda M_w 4.3 earthquake in 2002. Another noteworthy contribution was made by Todorovska and Trifunac [142] on the damage identification of the Van Nuys 7-story hotel under different earthquakes. Their results demonstrated considerable wave delays (decrease in stiffness) during the 1994 Northridge and 1971 San Fernando earthquakes, which agree well with the observed damage by separate inspections. Nonetheless, the number of works on the use of seismic

interferometry for the system identification of structures under ambient vibrations is considerably more scarce. Among them, a remarkable contribution is the one by Nakata and Snieder [143] who implemented the Ambient Noise Deconvolution Interferometry (ANDI) proposed by Prieto *et al.* [144] for the monitoring of an 8-storey building in Japan. Lacanna *et al.* [145] conducted a pioneering application of continuous OMA and ANDI for structural assessment of the Giotto's bell-tower in Florence, Italy. Despite reporting some limitations for the identification of environmental effects on the wave velocities due to insufficient sampling frequency and short monitoring time, their results evidenced the superior capabilities of SHM systems based on automated OMA/ANDI for damage detection, localization, and quantification.

In view of the promising coupling between OMA and ANDI as a cost-efficient solution to attain full damage identification, considerable research efforts in this line have been conducted in this thesis. This chapter summarizes the main scientific achievements, which span from fundamental research on the development of new theoretical formulations in reference [146] to field applications to diverse structures in references [147, 148, 149]. Firstly, Sections 4.2 and 4.3 present the fundamentals and signal processing of seismic interferometry, respectively. Section 4.4 reports the implementation of ANDI through time window stacking and, finally, Section 4.5 presents two exemplary application case studies: the Sciri Tower in Section 4.5.2 and the Chiaravalle bridge in Section 4.5.1.

4.2. Transfer Functions and Impulse Response Functions

Let us consider a mono-dimensional structure (e.g. a tower or a building) equipped with an array of sensors monitoring its response $u(z,t)$ along the height $0 \leq z \leq H$, where t is the time variable and H the total height of the structure as sketched in Fig. 4.1. Deconvolution interferometry allows getting insight into the propagation of shear waves between two arbitrary sensors, considering one sensor at level z_{ref} as reference input signal $u(z_{ref},t)$ and the other at level z as output signal $u(z,t)$. Assuming that the structure behaves as a LTI system, the reference and output signals can be related in the time domain t as [142]:

$$u(z,t) = u(z_{ref},t) * h(z,z_{ref},t) = \int_0^t u(z_{ref},s)\, h(z,z_{ref},t-s)\, \mathrm{d}s, \quad (4.1)$$

or, alternatively, in the frequency domain ω as:

$$\widehat{u}(z,\omega) = \widehat{u}(z_{ref},\omega)\, \widehat{h}(z,z_{ref},\omega), \quad (4.2)$$

where $*$ indicates convolution, and a hat indicates Fourier transform. Functions $\widehat{h}(z,z_{ref},\omega)$ and $h(z,z_{ref},t)$ denote the transfer function (TF) and the impulse

response function (IRF) between the output signal $u(z,t)$ and the input signal $u(z_{ref},t)$, respectively. The IRFs physically relate the responses of the system at different levels z to a virtual Dirac Delta impulse $\delta(t)$ at level z_{ref}. In other words, these functions represent the Green's functions of the system and characterize the propagation of an input pulse applied at z_{ref} among the receivers deployed in the structure [150]. The IRFs can be computed by taking the inverse Fourier transform of the corresponding TFs as follows:

$$h(z,z_{ref},t)=\mathscr{F}^{-1}\left\{\widehat{h}(z,z_{ref},\omega)\right\}=\mathscr{F}^{-1}\left\{\frac{\widehat{u}(z,\omega)}{\widehat{u}(z_{ref},\omega)}\right\}, \tag{4.3}$$

with $\mathscr{F}^{-1}$ denoting the inverse Fourier transform operator. Nonetheless, the IRFs can be only obtained in practice for a finite frequency band $|\omega|<\omega_{max}=(Fs/2)2\,\pi$, with Fs being the sampling frequency, that is:

$$h(z,z_{ref},t)=\frac{1}{2\pi}\int_{-\omega_{max}}^{+\omega_{max}}\hat{h}(z,z_{ref},\omega)e^{-\mathrm{i}\omega t}\,\mathrm{d}\omega. \tag{4.4}$$

In addition, a regularized version of the TFs in Eq. (4.3) is usually introduced to avoid numerical instability due to division by null numbers as:

$$h(z,z_{ref},t)\approx\mathscr{F}^{-1}\left\{\frac{\widehat{u}(z,\omega)\,\overline{\widehat{u}(z_{ref},\omega)}}{\left|\widehat{u}(z_{ref},\omega)\right|^2+\epsilon}\right\}, \tag{4.5}$$

where the bar indicates complex conjugate, and ϵ denotes a regularization parameter. In this work, we use $\epsilon=0.1\overline{P}$, with $\overline{P}$ being the average power spectrum of the reference input signal.

The velocity of the shear waves propagating in the structure can be computed by simple peak-picking analysis of the IRFs as illustrated in Fig. 4.1. Following the approximate Snell's law, ray paths between the monitoring stations are traced first. Then, the time-lag τ_i between the motion at level z_{i+1} and level z_i is obtained by peak-picking the maximum values of the IRFs $h(z_{i+1},z_{ref},t)$ and $h(z_i,z_{ref},t)$ along an identified ray path [151]. It can be proved that the time difference between the local maxima of $h(z_{i+1},z_{ref},t)$ and $h(z_i,z_{ref},t)$ maximizes the cross-correlation between $u(z_{i+1},t)$ and $u(z_i,t)$ [140]. Then, the velocity of the pulses traveling between the sensors can be computed as $v_i=l_i/\tau_i$, with $l_i=z_i-z_{i+1}$. The number of IRFs that can be computed in a bridge monitored at N different stations equals N and, therefore, the resolution of the identified wave velocity distribution is $N-1$. Finally, it is important to note that the response at any arbitrary level can be used as reference, usually termed as virtual source. Virtual sources are typically defined either at the base or the roof levels, and do not necessarily need to coincide with the physical source (e.g. the base accelerations induced by earthquakes).

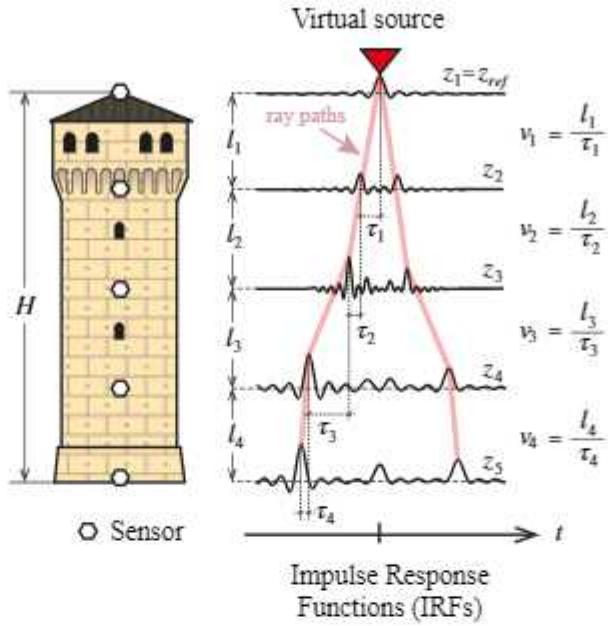

Fig. 4.1: Schematic of the peak-picking analysis of a waveform obtained by deconvolution interferometry considering a virtual source at the roof level.

Furthermore, although acceleration records are often used to describe the propagation of seismic waves, other physical measurements can be also used such as displacements, velocities or strains.

4.3.Low-pass and band-pass filtering of IRFs

It has been reported in the literature that high-rise buildings may exhibit a dispersive behavior [152]. This means that the wave-number k and velocity of the propagating waves are functions of the frequency ω according to a certain dispersion relation. More specifically, the traveling waveform can be defined by the phase and group velocities as $c^p = \omega/k$ and $c^g = \partial\omega/\partial k$, respectively. The phase velocity determines the velocity of propagation of the pulses, while the group velocity defines the velocity of propagation of the envelopes of the waveforms. When the system is not dispersive, the phase and group velocities coincide, i.e. $c^p = c^g$. For better comprehension, the reader may refer to Appendix A.1 where the theoretical formulation of the wave propagation problem in visco-elastic Timoshenko beams from reference [146] is summarized. In those derivations, the concepts of dispersion, group and phase velocities appear naturally when solving the dynamic equation of motion in the frequency domain under base ground harmonic accelerations.

In order to identify the wave velocities in a dispersive structure, it is usually

convenient to isolate the contribution of certain frequency bands to the computed waveforms. To do so, a band-pass filter $\widehat{S}$ can be applied to the TFs in the frequency domain as:

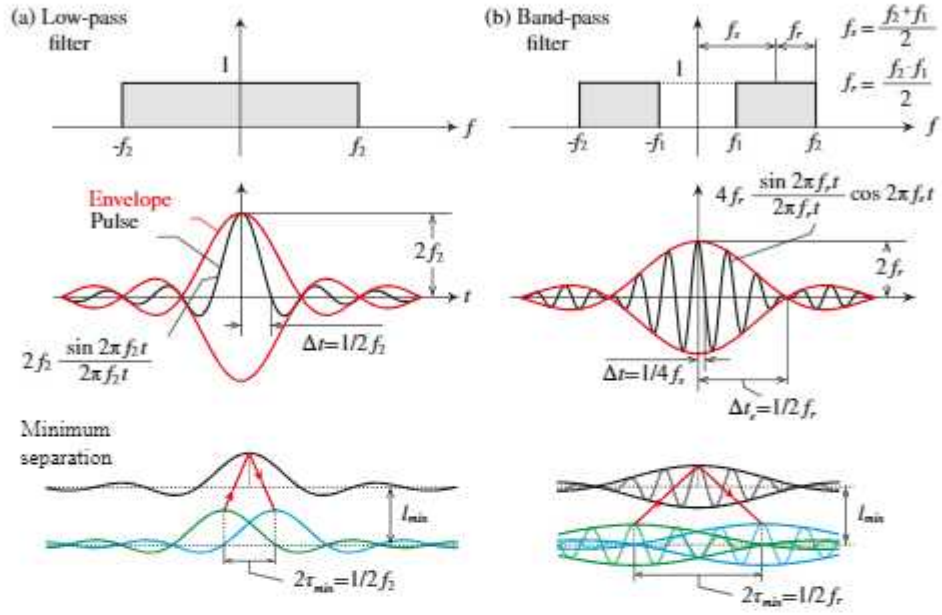

Fig. 4.2: Virtual source function in the frequency ($f = \omega/2\pi$) and time (t) domains, for a box function (low-pass filter) (a) and shifted box function (band-pass filter) (b).

$$h(z, z_{ref}, t) = \mathscr{F}^{-1}\left\{\widehat{h}(z, z_{ref}, \omega)\,\widehat{S}(\omega, \omega_1, \omega_2)\right\}, \tag{4.6}$$

with $\omega_2 > \omega_1$ denoting the cut-off frequencies. This filter can be defined as a shifted box function as follows:

$$\widehat{S}(\omega, \omega_1, \omega_2) = \begin{cases} 1 & \omega_1 \leq |\omega| \leq \omega_2 \\ 0 & \text{otherwise} \end{cases} \tag{4.7}$$

Note that the incorporation of $S(\omega)$ into Eq. (4.2) implies that, at the reference level z_{ref}, the TF corresponds to the band-pass filter, that is $\widehat{h}(z_{ref}, z_{ref}, \omega) = \widehat{S}(\omega)$ or, alternatively, the IRF $h(z_{ref}, z_{ref}, t) = S(t)$. Figure 4.2 shows $S(t)$ and $\widehat{S}(f)$ for both low-pass and band-pass filtering, where $f = \omega/2\pi$. It is noted that the low-pass filter $S(t)$ in the time domain corresponds to a sinc function, with half-width of the central lobe $\Delta t = 1/2f_2$. On the other hand, the band-pass filter $S(t)$ in the time domain is a harmonic function modulated by a sinc function. The half-widths of the central lobe of $S(t)$ and its envelope are $\Delta t = 1/2f_s$ and $\Delta t_e = 1/2f_r$, respectively, with $f_s = (f_2 + f_1)/2$ and

$f_r = (f_2 - f_1)/2$ the semi-sum and semi-difference of the cut-off frequencies. For clarity purposes, Figure 4.3 summarizes the calculation process of IRFs.

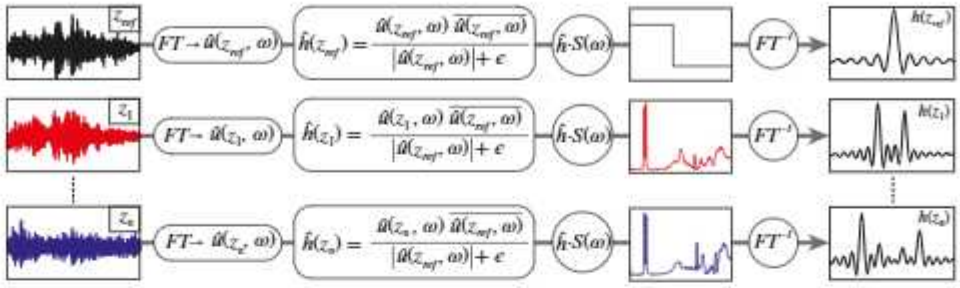

Fig. 4.3: Flowchart of the calculation of IRFs through ambient noise deconvolution interferometry.

The clear identification of propagating pulses within a waveform is a key aspect in the assessment of wave velocities through a peak-picking approach. To do so, some practical considerations must be taken into account, including:

- *Assessment of phase and group velocities*: The identification of group velocities is more robust than the identification of phase velocities due to the higher smoothness of the envelopes of the IRFs. Nevertheless, given that masonry structures are characterized by large stiffness and, as a result, large wave velocities and short propagation times, and considering that in dispersive structures $c^g > c^p$ (see e.g. [152]), the identification of group velocities is often impractical. Therefore, the use of inverse calibration of wave propagation models usually becomes imperative for the identification of group velocities.

- *Minimum separation between sensors*: Two different propagating pulses can only be distinguished if there exists a sufficient time shift between their arrival times. In order to address this issue, let us focus on the case of an upward pulse reflecting off a free surface and propagating downward as illustrated in the bottom part of Fig. 4.2. If the structure is dispersive, the travel time of the pulses τ_p will give the phase velocity c^p, while the travel time of the envelopes τ_g will give the group velocity c^g. For generality, let us consider a band-pass filter with cut-off frequencies f_1 and f_2 as shown in Fig. 4.2 (b). If there is one single propagating mode in the frequency band (f_1-f_2), and if we consider that the half-width of the central lobe of the pulse quantifies the uncertainty of its time localization, two pulses can be only distinguished as separate processes if shifted in time more than the width of the central lobe. Therefore, the minimum separations between sensors to resolve the incident and reflected pulses

l^p_{min} and propagating envelopes l^g_{min} read:

$$l^p_{min} = c^p/8f_s, \quad l^g_{min} = c^g/4f_r, \tag{4.8}$$

whereby c^p and c^g can only be measured if f_s and f_r are large enough, respectively.

- *Maximum frequency of analysis*: Ebrahimian and Todorovska [152] demonstrated through an equivalent Timoshenko beam model for wave propagation analysis in high-rise buildings the existence of a critical frequency $f_{cr} = c_s\sqrt{k_G}/r_g 2\pi$ (with c_s being the shear wave velocity in the material, k_G the shear correction factor of a Timoshenko beam equivalent to the building, and r_g the radius of gyration of the building). Above this critical frequency, a secondary wave propagation mode intervenes in the waveforms generating complex interference patters.

- *Minimum sampling frequency*: Considering a separation l between sensors, a traveling pulse can be only identified if the sampling frequency rate F_s satisfies the following condition:

$$F_s \geq c^{p,g}/l. \tag{4.9}$$

- *Minimum observable variations in wave velocities*: The suitability of a monitoring system for detecting damage-induced wave delays is highly conditioned by the sampling frequency. In particular, for a given wave velocity c and separation l between sensors, i.e. a wave lag $\tau = l/c$, a rough estimate of the relationship between the minimum observable reductions in the wave velocity δc and the sampling frequency F_s reads:

$$\delta c = -\frac{l}{F_s\tau^2 + \tau}. \tag{4.10}$$

4.4.ANDI through time window stacking

The extension of the previous formulation to the continuous monitoring of structures is of pivotal importance for the identification (detection, localization and quantification) of early-stage damages. To this aim, deconvolution interferometry can be applied to ambient-vibration records considering time windows of duration T, typically with a certain overlapping to minimize the variance of the estimates on the velocity of the traveling waves. Specifically, the deconvolved waveforms can be stacked (averaged) over N intervals of duration T as

follows:

$$h(z, z_{ref}, t) = \frac{1}{N}\sum_{n=1}^{N}\left[\mathscr{F}^{-1}\left\{\frac{\widehat{u}_n(z,\omega)}{\widehat{u}_n(z_{ref},\omega)}\right\}\right] \approx$$
$$\approx \frac{1}{N}\sum_{n=1}^{N}\left[\mathscr{F}^{-1}\left\{\frac{\widehat{u}(z,\omega)\,\overline{\widehat{u}(z_{ref},\omega)}}{\left|\widehat{u}(z_{ref},\omega)\right| + \epsilon}\right\}\right]. \tag{4.11}$$

4.5. Application case studies

From the literature review in Section 4.1, it is clear that research efforts devoted to the implementation of seismic interferometric techniques for SHM have focused on building-like structures, while the potential for other structural typologies remains virtually unexplored. In particular, long multi-span bridges may offer a fruitful application line. Let us consider a bridge structure instrumented with an array of accelerometers recording lateral ambient vibrations $a(x,t)$ along its length $0 \leq x \leq L$ as sketched in Fig. 4.4, with L being the total length of the bridge covered by the measuring chain. Assuming the bridge as a LTI system, the acceleration records of a reference sensor $a(x_{ref},t)$ and an arbitrary one $a(x,t)$ can be related following the exact same formulation as the one previously reported in Sections 4.2 and 4.4. In addition, it is often possible to locate accelerometers in these structures with considerable separation so that wave velocities can be assessed without requiring excessively high data acquisition rates. Furthermore, it has been reported in the literature the difficulties involved in the OMA of multi-span bridges with simply supported span configurations, since the local modes of the spans typically appear as closely-spaced clusters of poles in the stabilization diagram (see e.g [153]). Under these circumstances, ANDI may represent a complementary or alternative technique to conventional OMA. In this light, this thesis presented in reference [149], for the first time in the literature, the application of ANDI for the system identification of a long multi-span concrete viaduct, the Chiaravalle viaduct (Section 1.5.7). The main numerical results and discussion from these research works are reported below in Section 4.5.1. On the other hand, the incorporation of ANDI into long-term SHM schemes remains virtually unexplored. While the pioneering work by Lacanna *et al.* [145] reported the first coupled application of continuous ANDI and OMA, no efforts were conducted to embed these techniques within the statistical pattern recognition paradigm, that is the identification and removal of EOC. With the aim of addressing this gap in the literature, the experimental campaign in the Sciri Tower (Section 1.5.4) and published in reference [147] was specifically designed to conduct OMA and ANDI in parallel. The key results and conclusions extracted from those works are reported hereafter in Section 4.5.2.

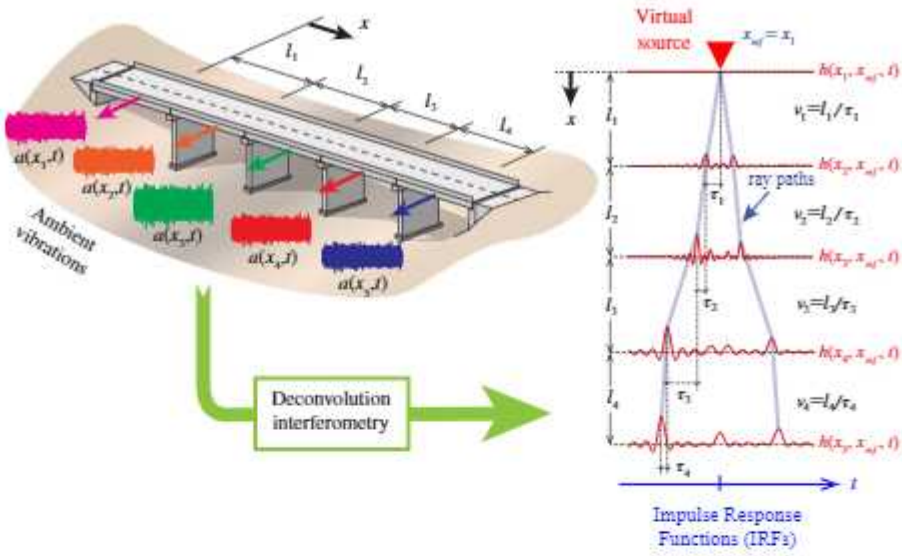

Fig. 4.4: Schematic of an ANDI-based SHM system for the identification of the lateral dynamic behavior of a long multi-span viaduct.

4.5.1. Chiaravalle viaduct

The acceleration records acquired in the AVT of the Chiaravalle viaduct (Section 1.5.7) on February 4$^{\text{th}}$ and 7$^{\text{th}}$ 2020 were processed through OMA and ANDI. The modal identification of the viaduct was performed using multi-setup automated Cov-SSI. To this aim, the acceleration records were thoroughly inspected, and the presence of anomalous spikes and spurious trends were eliminated through Hanning window filtering and moving average baseline correction, respectively. Then, the signals were filtered with a Butterworth band-pass filter with cut-off-frequencies of 1 and 30 Hz and, finally, the resulting signals were down-sampled at 100 Hz to decrease the computational cost in the subsequent modal identification. The parameters used in the identification included maximum and minimum numbers of block rows/columns in the Toeplitz matrix of covariances j_b of 300 and 400, respectively, with steps of 10, and model's orders running from 10 to 80 with steps of 2 for Set-ups 1 and 2, and from 140 to 300 with steps of 4 for Set-up 3. Figure 4.5 furnishes an example of the obtained stabilization diagrams, corresponding to the first asynchronous acquisition of Set-up 1. The mode shapes extracted from the considered set-ups were merged using the least squares approach proposed by Au [109]. Table 4.1 collects the resonant frequencies (f_i) and damping ratios (ζ_i) identified in the frequency range 0-10 Hz, and Fig. 4.6 plots the first eight mode shapes. For comparison purposes, the identification results from previous AVTs on the viaduct and reported in references [31, 32, 29, 33] are also included in Table 4.1. In comparison with the testing campaign carried out

right after the seismic upgrading of the viaduct in 2017 by Gara *et al.* [29], four new modes have been observed in the present survey, including one longitudinal and three transverse modes. Regarding the modes identified in both surveys, only small deviations are found in the resonant frequencies (with maximum relative differences below 3%), which are essentially attributable to differences in the environmental conditions of the tests. It is interesting to note that the natural frequencies identified in both campaigns for the transverse modes are significantly larger (on average by a factor of ≈ 2) than those identified in 2014 [31, 32, 33], that is before the seismic upgrading. These results confirm the effectiveness of the overall stiffening of the viaduct after the rehabilitation. Regarding the identified mode shapes in Fig. 4.6, it is noted that these do not seem to exhibit any relative rotations at the piers. This fact indicates that the pendulum isolators did not activate due to friction, which is ascribed to the low in-service loading conditions (wind and traffic) registered during the tests with ambient vibrations of the order of a few thousandths of g. Thence, the modal forms of the viaduct in the horizontal plane resembles the behavior of a continuous beam structure with elastic supports accounting for the stiffness/mass properties of the piers.

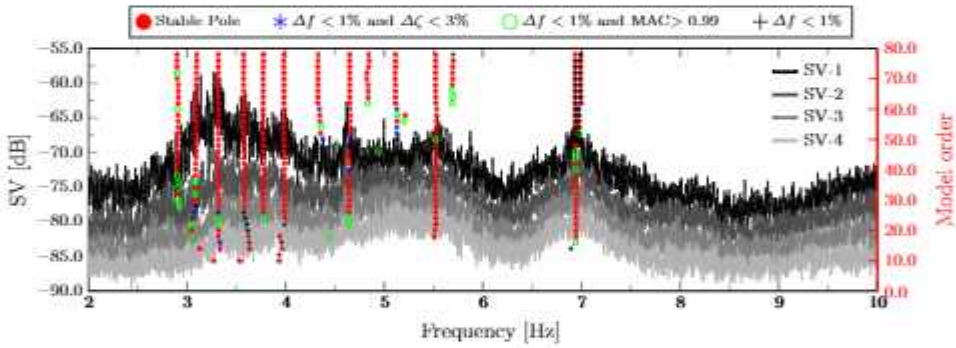

Fig. 4.5: Stabilization diagram of the first asynchronous test conducted for Set-up 1 ($j_b = 300$; Δf: difference in frequency; $\Delta\zeta$: difference in damping ratio; MAC: Modal Assurance Criterion between the poles obtained by two subsequent model orders).

Table 4.1: Experimentally identified natural frequencies, f_i, and damping ratios, ζ_i, of the Chiaravalle bridge using the Cov-SSI method in the frequency range 0-10 Hz, and comparison with the results from previous experimental campaigns.

		2014 Campaign [31, 32, 33]		2017 Campaign [29]		2020 Campaign	
Mode No.	Description	f_i [Hz]	ζ_i [%]	f_i [Hz]	ζ_i [%]	f_i [Hz]	ζ_i [%]
1	1st longitudinal	-	-	-	-	2.74	3.80
2	1st transverse	1.58	0.93	2.76	4.38	2.75	1.35
3	2nd transverse	1.61	0.57	3.01	3.42	3.00	1.52
4	3rd transverse	2.05	1.78	3.16	3.23	3.07	1.90
5	4th transverse	1.81	1.91	3.29	2.63	3.26	2.52
6	5th transverse	2.26	0.42	3.55	1.96	3.48	2.26
7	6th transverse	2.79	0.27	3.84	3.04	3.75	2.30
8	7th transverse	-	-	-	-	3.93	2.01
9	8th transverse	-	-	-	-	4.04	4.06
10	9th transverse	-	-	4.25	2.53	4.18	2.35
11	10th transverse	-	-	4.55	2.40	4.42	2.07
12	2nd longitudinal	-	-	4.97	1.96	4.90	3.14
13	11th transverse	-	-	5.25	2.76	5.18	2.66
14	12th transverse	-	-	-	-	6.05	2.60

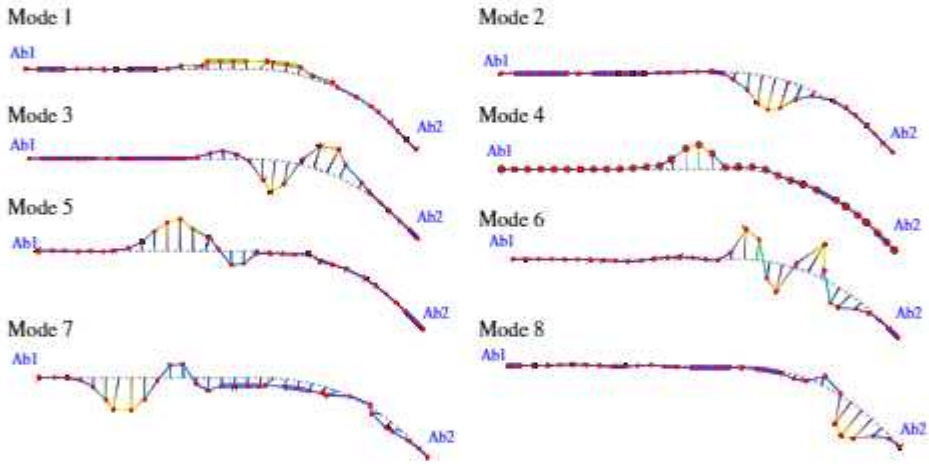

Fig. 4.6: First eight experimentally identified mode shapes of the Chiaravalle viaduct.

The ambient acceleration records were also processed through the ANDI approach previously introduced in Section 4.4. In this case, the IRFs were computed considering 10-min-long windows with 50% overlap and stacked (averaged) over every 30-min long vibration record. In these analyses, the ambient vibrations sampled at a sampling rate of $F_s = 1500$ Hz were used to accurately assess the wave propagation velocities. In addition, virtual sources (VSs) were considered at the most distant stations. Figures 4.7 (a,c) and (b,d) show the IRFs experimentally identified in KC1 in the transverse (Channels 1-14) and longitudinal (Channels 15-17) directions, respectively. In this first set-up, VSs have been considered at the first abutment ($x_{ref} = 0.0$ m) and at P13

(x_{ref} = 357.5 m). In order to cover the main resonant frequencies of the viaduct, the IRFs have been filtered in the broad-band frequency of 0.5-10 Hz according to Eq. (4.5). It is noted in these figures that two quasi-symmetric pulses can be clearly identified (with ray paths denoted by blue lines). This behavior coincides with the waveforms obtained by Nakata and Snieder [143] for building structures under ambient excitations. Those authors pointed out that, unlike buildings under seismic excitations where the physical source relates to a single base motion [141], ambient vibrations are characterized by multiple load sources inside and outside the structure (e.g. micro-tremors, wind loads or traffic), giving origin to both causal and acausal pulses. In general, waves propagate in three directions throughout the structure with multiple reflections from boundaries and nonhomogeneities. Nevertheless, the relative simplicity of the waveforms in Fig. 4.7 suggests the wave propagation is predominantly one-dimensional in KC1, thereby the wave velocities can be readily computed by peak-picking analysis. It is also interesting to note that the wave velocity is clearly larger in the longitudinal direction, which may be expected considering that the longitudinal and shear-wave velocities in an elastic material are defined as $c_L = \sqrt{E/\rho}$ and $c_s = \sqrt{G/\rho}$, respectively, with E, G and ρ being the Young's modulus, shear modulus, and mass density.

The IRFs experimentally identified in KC2 and KC3 are shown in Figs. 4.8 (a,c) and (b,d), respectively. As evidenced in these figures, no clear traveling pulses were identified in set-ups 2 and 3. The poor identification results in these testing set-ups is ascribed to two main causes. Firstly, the low ambient vibration levels registered on February 7th 2020, when the last two set-ups were conducted, led to low signal-to-noise ratios, hampering the identification of traveling pulses. Secondly, the curved geometry of the last three kinematic chains may result in complex reflection, scattering and diffraction patterns. Because of these difficulties in the identification of clear traveling pulses, ANDI analyses were restricted to the first straight kinematic chain of the viaduct.

In order to interpret the propagating waveforms reported in the subsequent section, a finite element model (FEM) of the Chiaravalle viaduct was modeled in SAP2000 as shown in Fig. 4.9. For the sake of clarity and ease in the interpretation of the results, a simplified 2D continuous multi-span beam model was developed. This choice is supported by the experimental evidence, where the identified mode shapes evidence the transverse continuity of the deck, being possible to conclude that the pendulum isolators behave as rigid deck-pier constraints. The material properties of the model were retrieved from the experimental data reported in reference [33], including the elastic moduli of the columns, columns bent, and beams of 25.80 GPa, 29.68 GPa and 33.52 GPa, respectively. Equivalent 2-nodes elastic Timoshenko beam elements were used to model the deck, accounting for the inertial/mass properties of the V-shaped (Fig. 1.17 (a)) and the adjacent box beam (Fig. 1.17 (b)) cross-sections. In order to tune the shear area values of the equivalent Timoshenko

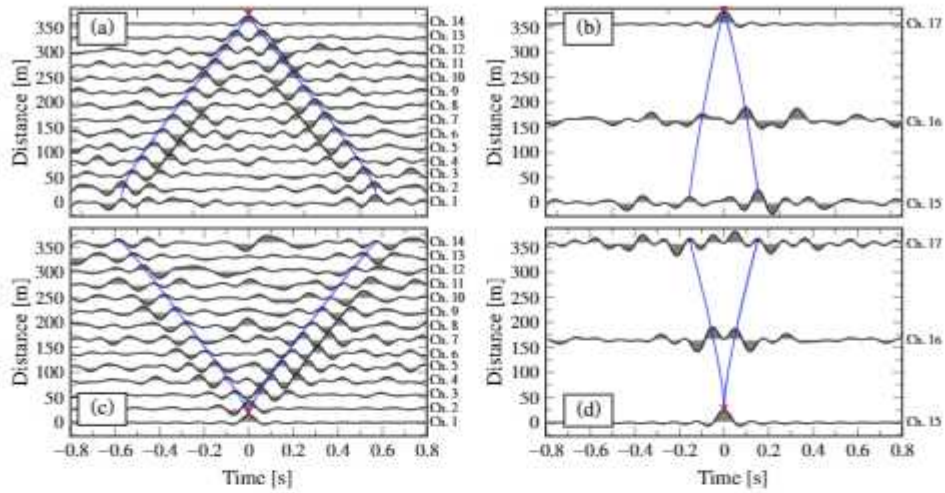

Fig. 4.7: Stacking waveforms over 10-min long IRFs of the Chiaravalle viaduct in the first set-up conducted on February 4$^{\text{th}}$ 2020 and filtered in the broad-band frequency of 0.5-10 Hz. Transverse (a,c) and longitudinal (b,d) directions, and VS (▼) at the first abutment ($x_{ref} = 0.0$ m) and P13 ($x_{ref} = 357.5$ m).

beams, two local FEMs of the bridge's cross-sections were developed separately using the commercial software ANSYS as shown in the inserts of Fig. 4.9 (a). For each model, a section of the bridge's deck was simulated in parallel using 3D 8-nodes SOLID185 elements and 2-nodes BEAM188 Timoshenko beam elements. Parametric analyses were performed considering clamped boundary conditions and increasing tip transverse displacements, so that the shear areas of the Timoshenko beams were sought to minimize the mismatch between the reaction forces of both modelings. The piers were modeled through elastic supports defined by three elastic springs with longitudinal k_l, transverse k_t, and rotational k_ϕ stiffness constants. The elastic constants of these supports were computed using local FEMs of the piers in ANSYS as shown in the inserts of Fig. 4.9 (a). Specifically, three different model types were developed, including the two-column bent piers, the wall pier (P17), and the single-column bent piers (P24 and P25). These local models were defined using BEAM188 elements, including rigid links to take into account the real position of the elements' centroids. For simplicity, and given the considerable increase in the foundation stiffness achieved by the seismic upgrading of the viaduct, the soil-foundation interaction was neglected and fixed base conditions were assumed. On this basis, the elastic constants (k_l, k_t, and k_ϕ) were extracted by sub-structuring analysis of the local pier models, condensing the stiffness/mass properties of the piers to a master node located at the deck's centroid. It is important to mention that the consideration of perfect bonding between the original columns and the concrete jacketing added in the seismic retrofit resulted in a too stiff model, with

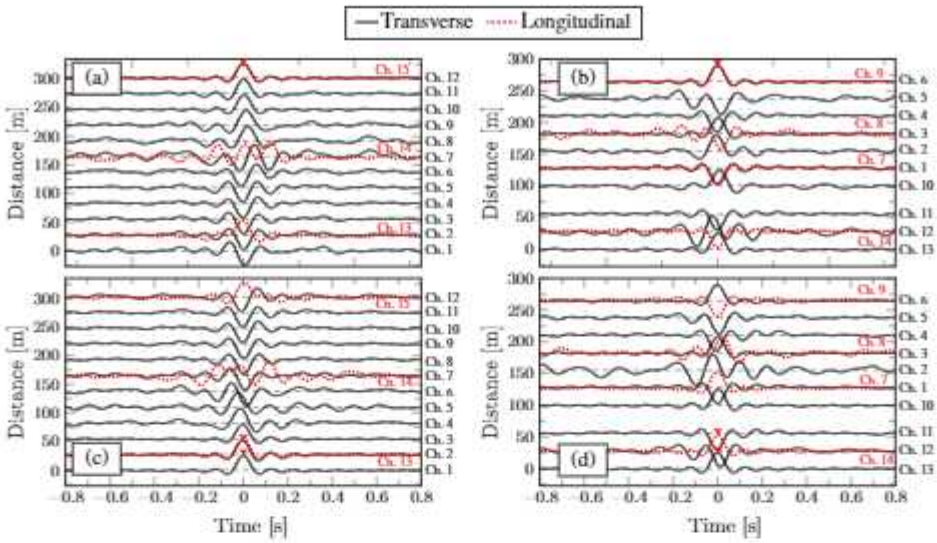

Fig. 4.8: Stacking waveforms over 10-min long IRFs of the Chiaravalle viaduct in the second (a,c) and third set-ups (b,d) conducted on February 7th 2020 and filtered in the broad-band frequency of 0.5-10 Hz. Virtual sources (▼) are defined at the most distant stations.

numerical resonant frequencies substantially exceeding the experimental ones. This fact indicates that, instead of performing as a solid section, the jacketing-column ensemble behaves as a composite section. In order to account for this effect, the formulation prescribed in the Eurocode 4 EN 1994-1-1 [154] for the design of composite steel and concrete structures was adopted. According to this formulation, the effective flexural stiffness $(EI)_{eff}$ of the composite section reads:

$$(EI)_{eff} = (EI)_c + k_c(EI)_j, \tag{4.12}$$

with $(EI)_c$ and $(EI)_j$ being the flexural stiffness of the original column and of the concrete jacketing, respectively, and k_c standing for an efficiency factor. Factor k_c was adjusted by manual tuning, achieving a reasonably good agreement between the experimental and numerical modal features for a value of $k_c = 0.55$. On this basis, the resulting longitudinal and transverse stiffness of the piers of the viaduct are furnished in Fig. 4.9 (b). The comparison between the first four experimental modal features and the predictions of the resulting FEM is presented in Table 4.2. Relatively good agreements are found in terms of natural frequencies and mode shapes, with mean relative differences in frequency and MAC values of 7.2% and 0.88, respectively.

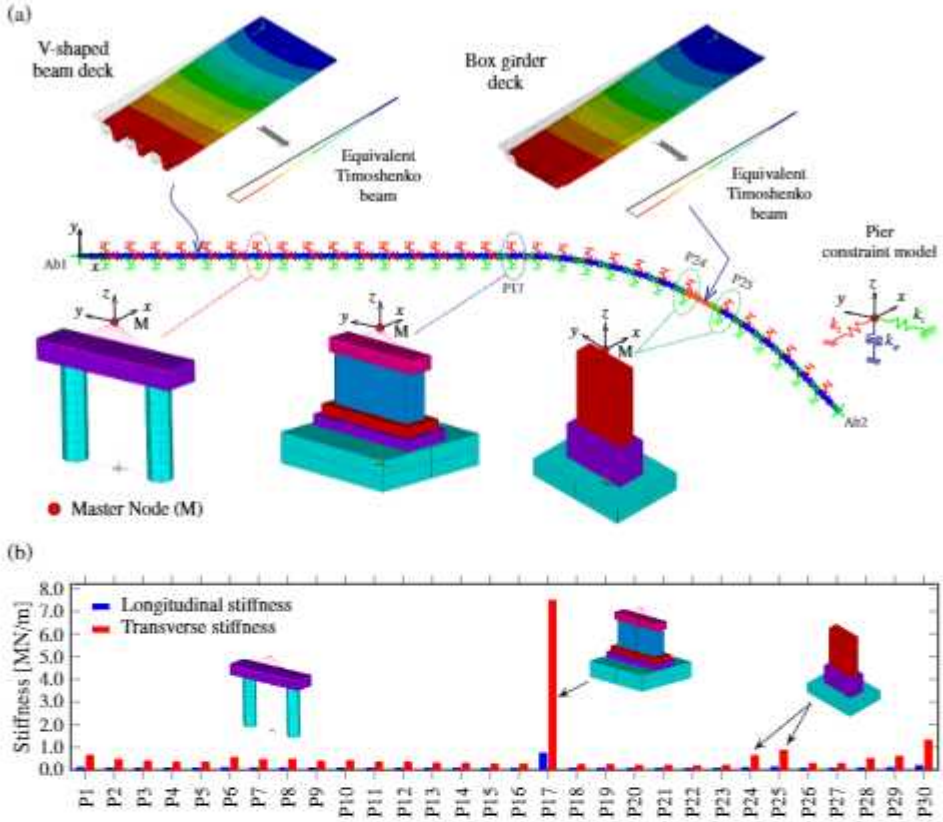

Fig. 4.9: Finite element modeling (a), and stiffness of the piers of the Chiaravalle viaduct obtained by substructuring analysis.

Table 4.2: Comparison between the experimental campaign and the FEM of the Chiaravalle viaduct in terms of resonant frequencies and mode shapes (terms f_{exp} and f_{FEM} denote the experimental and numerical resonant frequencies, respectively).

Mode No.	Description	f_{exp} [Hz]	f_{FEM} [Hz]	$100(f_{exp} - f_{FEM})/f_{exp}$	MAC
1	1st longitudinal	2.74	2.60	5.34	0.84
2	1st transverse	2.75	2.84	-3.13	0.96
3	2nd transverse	3.00	3.29	8.81	0.88
4	3rd transverse	3.07	3.46	-11.32	0.82

Numerical waveforms were also extracted by time-history analysis of the FEM of the viaduct. To do so, two different load cases were considered: one single random transverse point load applied at the first abutment (LC1) (Fig. 4.10), and random point loads applied at all the piers of the viaduct (LC2) (Fig. 4.11). The point loads were defined as Gaussian white noise processes, and the time-history analysis was conducted using the Hilbert-Hughes-Taylor linear direct integration method with a time step of 6.67E-4 s (i.e. 1500 Hz).

The Rayleigh damping model was adopted considering the resonant frequencies and damping ratios of modes 2 and 11 from Table 2.1 to compute the mass/stiffness proportionality coefficients. Ten seconds long acceleration response time series of the first abutment and 13 piers of KC1 were extracted and processed through ANDI. For the first load case, Figs. 4.10 (a) and (b) report the numerical transverse and longitudinal IRFs, respectively, considering the VS at $x_{ref} = 0.0$ m (coincident with the physical source in this particular load case). It is observed in this figure that, when one single physical source is considered, only causal traveling pulses (positive time values) are found, as well as some reflections from the piers in the transverse direction in Fig. 4.10 (a). Such a behavior resembles the waveforms in building structures under seismic excitations reported by previously published works (see e.g. [141, 155]), where only causal pulses are found alongside some reflections from the roof level when the virtual source coincides with the physical one. On the other hand, when random loads are located all throughout the viaduct, the numerical waveforms furnished in Fig. 4.11 approximate the experimental ones previously reported in Fig. 4.7. This supports the co-existence of multiple excitation sources as the driving mechanism of the experimentally observed causal and acausal traveling pulses. The numerical longitudinal waves in Figs. 4.10 (b) and 4.11 (b) also propagate at a considerably higher velocity likewise the experimental ones from Fig. 4.7 (b). These results thus evidence the potential of ANDI to achieve a meaningful representation of the physics underlying the dynamic response of bridge structures.

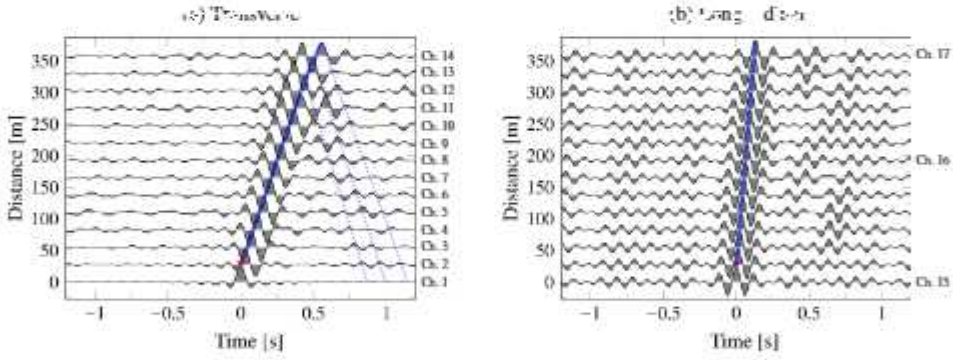

Fig. 4.10: Numerical transverse (a) and longitudinal (b) IRFs computed by time-history analysis of the FEM of the Chiaravalle viaduct in the broad-band frequency of 0.5-10 Hz considering a point random excitation at the first abutment (LC1, VS $x_{ref} = 0.0$ m).

The comparison of the experimental and numerical IRFs is further analyzed in Fig. 4.12 in terms of wave arrival times. In this figure, the arrival times obtained from the numerical IRFs considering the two aforementioned load cases (Figs. 4.10 and 4.11) are benchmarked against the experimental counter-

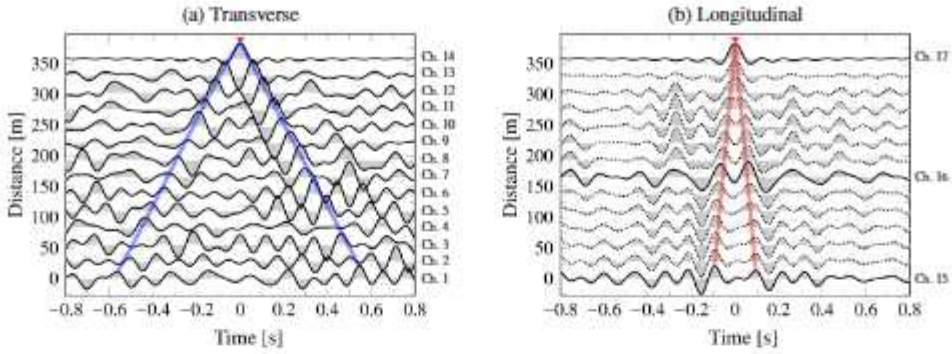

Fig. 4.11: Numerical transverse (a) and longitudinal (b) IRFs computed by time-history analysis of the FEM of the Chiaravalle viaduct in the broad-band frequency of 0.5-10 Hz considering random excitations at all the piers (LC2, VS at $x_{ref} = 357.5$ m).

parts from Fig. 4.7. The numerical results corresponding to LC1 were obtained by peak-picking analysis of the IRFs considering the VS coincident with the physical one ($x_{ref} = 0.0$ m), while the results for LC2 were estimated as the average arrival times between the causal and acausal pulses. Considerably good agreements are found between the numerical and experimental arrival times of transverse waves, while some discrepancies are observed for longitudinal waves. Specifically, the global waves velocities (traversing the whole kinematic chain) obtained from the numerical transverse waves are 661.3 m/s and 672.0 m/s for LC1 and LC2, respectively, while the experimental velocities for VSs at $x_{ref} = 0.0$ m and $x_{ref} = 357.5$ m are 606.7 m/s and 601.3 m/s, respectively. As mentioned earlier, the discrepancies are larger for longitudinal waves, with global wave velocities of 2837.6 m/s and 3025.23 m/s for LC1 and LC2, in contrast to the experimental results with 2242.8 m/s and 2381.22 m/s for VSs at $x_{ref} = 0.0$ m and $x_{ref} = 357.5$ m, respectively. These differences are ascribed to epistemic uncertainties in the modeling, as well as the effect of the dissipative devices installed during the upgrading works in the viaduct (namely concave friction pendulum isolators and viscous dampers [30]), which were disregarded in the modeling. Note that the effect of these uncertainties is magnified in the longitudinal direction, where waves travel faster and sampling errors due to a limited acquisition rate also increase.

In order to investigate the presence of dispersive effects in the ambient vibration response of the Chiaravalle viaduct, Fig. 4.13 depicts the experimental band-pass filtered IRFs obtained in KC1 considering increasing cut-off frequencies, namely 0.5-5 Hz, 0.5-15 Hz, and 0.5-30 Hz. In order to ease the interpretation of the results, inserts with the time distances between upward and downward pulses are included in Fig. 4.13. The effect of considering wider frequency bands can be readily noted in this figure in the shape of narrower

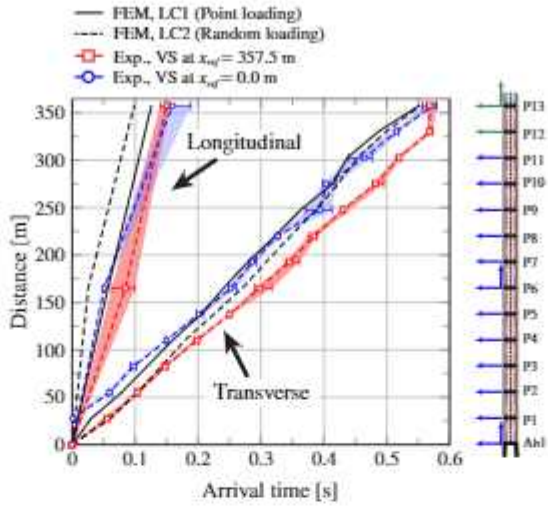

Fig. 4.12: Distance from the first abutment of the Chiaravalle viaduct versus wave arrival times [0.5-10 Hz]. Shaded areas represent the maximum/minimum values obtained in the 10-min long time windows used to stack the experimental IRFs.

propagating pulses. As previously discussed in Section 4.3, the pulse at the reference level is defined as a sinc function, whose width of the central lobe is inversely proportional to the width of the box filter in Eq. (4.5). Therefore, the use of wider frequency bands may facilitate the identification of separate traveling pulses, although high-frequency secondary propagation modes may arise hampering the identification. In this work, the use of cut-off frequencies above 40 Hz resulted in too complex waveforms, precluding the clear identification of traveling pulses. With regard to the wave velocities, it is noted in Fig. 4.13 (a) that transverse waves propagate at slightly faster velocities, whilst the opposite effect is observed for longitudinal waves in Fig. 4.13 (b). In this light, the degree of dispersion in the dynamic response of viaduct is further investigated in Fig. 4.14. In this figure, the dispersion relations for longitudinal (a,c) and transverse waves (b,d) are reported in the frequency band between 5 Hz and 40 Hz. To do so, the experimental waveforms were filtered to different frequency bands with increasing cut-off frequencies, namely 5 Hz, 10 Hz, 15 Hz, 20 Hz, 25 Hz, and 40 Hz, and the wave velocities were obtained through peak-picking analysis. The experimental dispersion curves in Figs. 4.14 (a,b) agree with the previous discussion regarding the results of Fig. 4.13. Note that the velocity of the longitudinal waves experiences fast decreases in the low-frequency range until it tends to an asymptotic value for cut-off frequencies above 15 Hz. Such a behavior agrees with the theoretical dispersion relation observed in axially loaded road-like structures [156]. On the other hand, the dispersion relation for transverse waves exhibits the opposite behavior, with increasing phase velocities for larger frequencies. Similar dispersion relations are also observed in

beam-like buildings as reported by Ebrahimian and Todorovska [152]. Those authors pinpointed the contribution of bending deformation as an essential factor in the dispersive propagation of shear waves through beam-like structures.

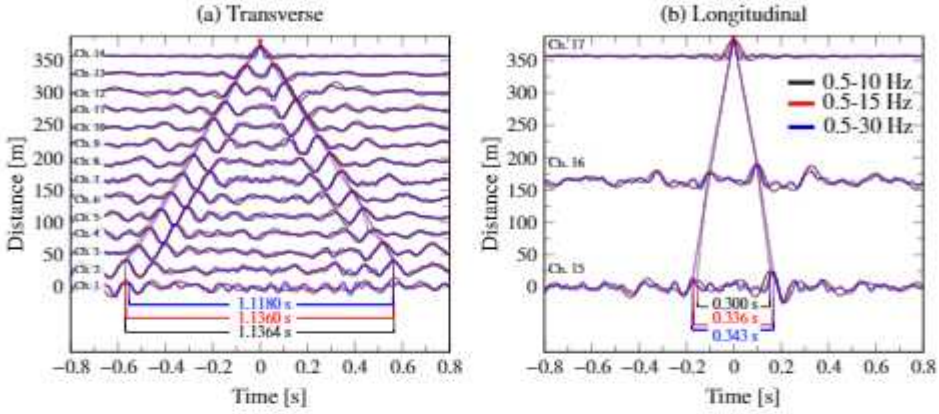

Fig. 4.13: Stacking waveforms over 10-min long IRFs in the first kinematic chain of the Chiaravalle viaduct and filtered in the broad-band frequencies of 0.5-10 Hz, 0.5-15 Hz, and 0.5-30 Hz.

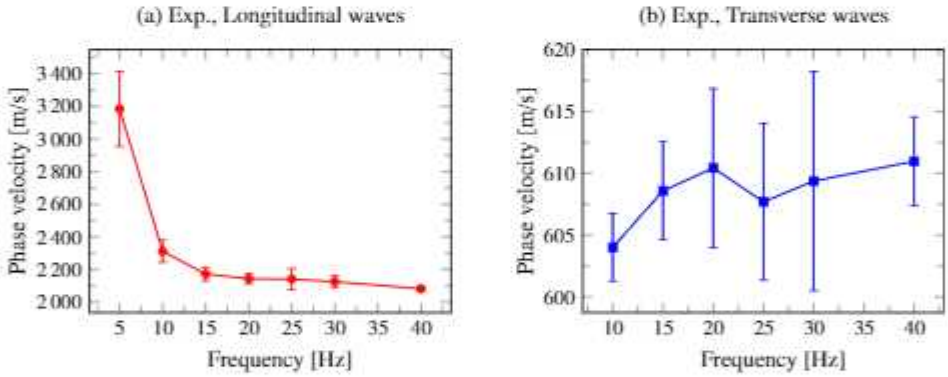

Fig. 4.14: Dispersion curves in the longitudinal (a) and transverse (b) directions of KC1 of the Chiaravalle viaduct obtained by peak-picking analysis of the ambient noise band-pass filtered IRFs. The error bars in (a,b) represent the minimum/maximum values of the computed wave velocities in the 10-min long stacking IRFs.

Research efforts were finally devoted to the appraisal of the potential application of ANDI for damage identification of the piers of the Chiaravalle viaduct. To this aim, the FEM of the viaduct was used to simulate different damage scenarios with increasing severity through stiffness reductions of the piers. Specifically, three different damage severities were considered, with stiffness reductions of $D = 15\%$, 25% and 35%. On this basis, nine different damage scenarios were defined by applying the three considered stiffness

reductions to piers P2, P6, and P11. With the aim of assessing local wave delays and so identify the damage (localization an quantification), the first kinematic chain was divided into three layers: L1 $x \in [0.0, 110.0]$ m (Ab1-P4); L2 $x \in [110.0, 220.0]$ m (P4-P8); and L3 $x \in [220.0, 357.5.0]$ m (P8-P13). The analysis was performed in terms of transverse waves considering one single random point load at the first abutment (LC1). Likewise previous analyses, 10 seconds long acceleration response time-series were computed with a sampling rate of 5000 Hz. Figure 4.15 furnishes the damage identification results for the nine considered damage scenarios in terms of local wave velocities v_i (a,b,c), and relative variations with respect to the undamaged condition Δv_i (d,e,f). In general terms, it is clearly noted that wave delays concentrate in the layers where the damaged pier is effectively localized. This is particularly evident when damage is localized in layers L1 and L2 (d,e), with reductions between 1 and 2%. Lower accuracy is found in the identification when damage localized in the third layer L3 for a stiffness reduction of 15% (see Figure 4.15 (f)), finding similar wave delays in L2. In this case, since L3 is longer than L1 and L2, the relative effect of the damaged pier upon the wave velocity is smaller. Thereby, errors in the peak-picking analysis of the IRFs due to the limited sampling rate gain importance, restraining the effectiveness of the damage identification. This highlights one of the key factors in the success of ANDI for damage identification: the need for high data acquisition rates (refer to Eq. (4.10)). Nevertheless, as the damage severity increases, the accuracy in the damage localization improves considerably highlighting the actual location of the damage. In all the cases, it is noted that the wave delays increase with the damage severity, which demonstrates the ability of ANDI not only for damage detection and localization, but also to some extent for quantification. It is important to mention that the decays of the resonant frequencies of the FEM of the viaduct achieved maximum values of 0.6% in the fourth resonant frequency, and less than 0.4% in the fundamental frequency. Such low frequency decays and small variations in the mode shapes are at the limit of what is actually detectable with long term OMA-based detection techniques. On the other hand, ANDI exhibits a higher sensitivity to local defects since it directly exploits features that are local in-nature, i.e. local wave delays. Additionally, note that ANDI operates on the analysis of the complete IRFs, while OMA typically uses ambient vibration records to identify a dynamic model (typically a state-space system) and extracts a reduced set of modal signatures. In this regard, it is important to pinpoint that modal features (resonant frequencies, damping ratios and mode shapes) can be also extracted from the IRFs as a particular case (see e.g. [157, 148]).

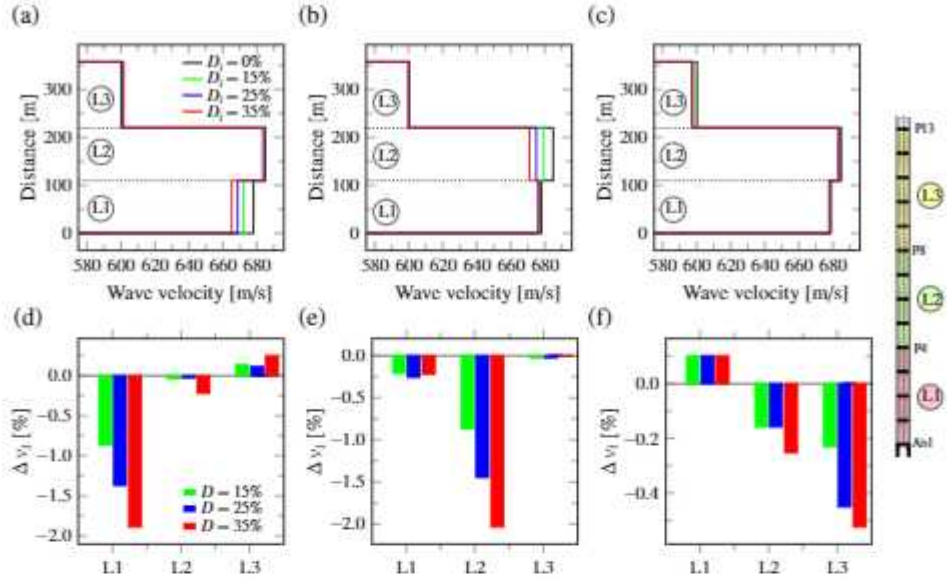

Fig. 4.15: Damage identification results of the Chiaravalle viaduct using numerical transverse IRFs filtered in the broad-band frequency of 0.5-10 Hz when damage is imposed in piers P2 (a,d), P6 (b,e), and P11 (c,f). The identification results are reported in terms on local wave velocities (a,b,c), and relative variations of local wave velocities Δv_i with respect to the undamaged condition (d,e,f) ($F_s = 5000$ Hz).

4.5.2.Sciri Tower

This last case study presents the implementation of OMA and ANDI for full structural assessment of the Sciri Tower (Section 1.5.4). During this experimental campaign, ambient vibration data were acquired continuously from February 13th until March 10th 2019 and processed with the purpose of extracting the modal and wave propagation characteristics of the tower. Figure 4.16 shows a flowchart of the automated OMA and ANDI system implemented in the Sciri Tower. It is important to remark that ambient vibrations were recorded at three different sampling frequencies to evaluate the robustness of the wave identification, including 200 Hz, 1000 Hz, and 5000 Hz.

The identification results using the Cov-SSI algorithm of the first 30-min long vibration records, taken on February 13th 2019 at 2:00 pm and down-sampled to 40 Hz, are presented in Fig. 4.17 and Table 2.1. The raw data were initially preprocessed by subtracting the temporal mean and applying time-domain Hanning filtering to eliminate undesired noise sources such as spikes related to electrical interferences. Seven vibration modes were identified in the frequency range between 0 and 12 Hz, including two flexural modes in the NE direction (Fx1 and Fx2), two flexural modes in the SE direction (Fy1 and Fy2), one torsional mode (Tz1), and two higher order flexural modes, (Fx3 and Fy3). These modes were continuously tracked by the automated OMA procedure previously introduced

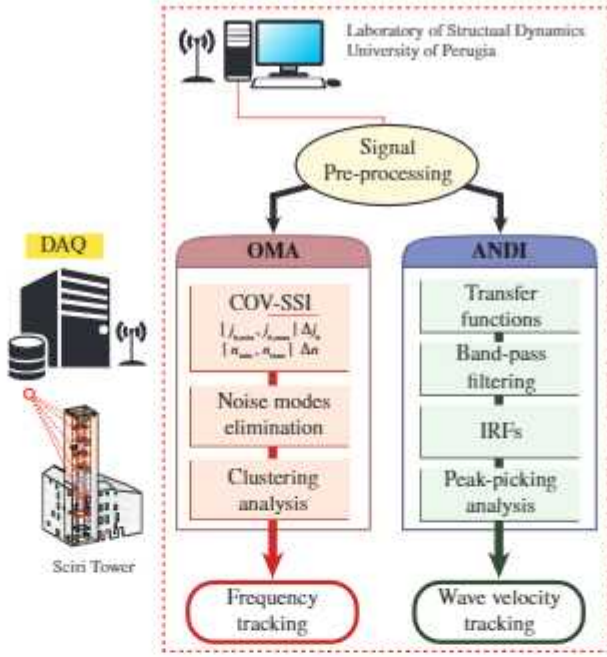

Fig. 4.16: Flowchart of the automated OMA and ANDI system implemented in the Sciri Tower.

in Chapter 3 all throughout the monitoring period as shown in Fig. 4.18. In this figure, the temperature time series recorded by the two thermocouples (indoor and outdoor) are also shown. Clear day-night oscillations can be found in all the natural frequencies, with increases during daytime and decreases during night-time. Figure 4.19 further investigates the effects of environmental temperature on the resonant frequencies of the tower. It is noted that there is a positive correlation of all the frequencies with temperature, that is, increasing temperatures yield increasing natural frequencies and vice versa as commonly found in historic structures. Note that the thermal sensitivity of the resonant frequencies, given by the slope of the linear fittings, is larger for higher-order modes.

The arrival times of the traveling pulses were automatically extracted from every 30-min ambient vibration record. To do so, the IRFs were computed considering 10-min-long windows with 50% overlap and staked (averaged) over every 30-min long vibration record. In addition, virtual sources were considered at the roof level (z_{ref} = 36.70 m), and the resulting waveforms were filtered to the frequency band 0.1-20 Hz. Figures 4.20 (a) and (b) show the IRFs in the SE (Channels 1, 4, 5, 7, 9, and 11) and NE (Channels 2, 6, 8, 10 and 12) directions (refer to Fig. 1.8), respectively, obtained for every 30-min-long ambient vibration recorded during the first 48 hours and sampled at F_s=200

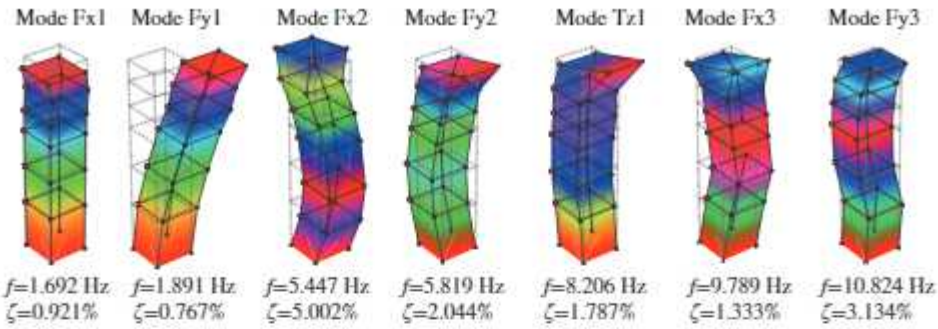

Fig. 4.17: Experimentally identified mode shapes estimated through Cov-SSI on February 13th 2019 at 14:00 UTC. (Identification parameters: $[n_{min}, n_{max}] = [40, 80]$, $\Delta n = 1$, $[j_{b,min}, j_{b,max}] = [140, 200]$, $\Delta j_b = 10$, $\zeta_{max} = 10\%$, $s = 5\%$, $\epsilon_f = 0.05$, $\epsilon_\zeta = 0.01$, and $\epsilon_{MAC} = 0.01$)

Hz. It is noted in these figures that two quasi-symmetric pulses can be clearly identified (with ray paths denoted by blue dashed lines), so that wave velocities were computed as the average of the upward and downward pulses. By means of the peak-picking analysis of these IRFs, Fig. 4.20 (c) depicts the computed wave travel times τ_i versus the distance D_i from the reference level $z_{ref} = 36.7$ m. In this light, Table 4.3 collects the mean $\overline{\tau_i}$ and standard deviation values σ_τ of the wave arrival times obtained by peak-picking analysis of the IRFs staked over 30-min intervals throughout the first 48 hours, considering sampling frequencies of $F_s = 200$ Hz, $F_s = 1000$ Hz, and $F_s = 5000$ Hz. Moreover, shear S-wave velocities in the heights of 24.3-36.70 m and 9.3-24.3 m computed by least squares fitting of the mean arrival times are also reported, representing the velocities of the free-standing portion of the tower and the section of the tower constrained by the adjoining building, respectively. Firstly, it is noted that the wave velocity is larger in all the cases in the bottom part of the tower because of the contribution of the building aggregate. Furthermore, the velocity of the bottom part is lower in the NE direction where one of the façades of the tower remains unrestrained (see Fig. 1.8). Conversely, the velocity of the uppermost part of the tower is always larger in the NE direction, where so is its inertia and thus its stiffness. Therefore, these results evidence the potential of ANDI to represent well the physics underlying the dynamic response of structures.

Figure 4.21 shows the time series of the identified wave arrival times in the NE and SE directions of the Sciri Tower considering sampling frequencies of 200 Hz (Feb. 13th - Feb. 25th 2019), 1000 Hz (Feb. 24th - Mar. 4th 2019), and 5000 Hz (Mar. 4th - Mar. 10th 2019). Error bars indicate the standard deviation of the arrival times obtained from every 10-min-long window stacked over every 30-min vibration record. It is first noted that, while some day-night fluctuations are effectively captured, a considerable scatter is found in the wave arrival times obtained with a sampling frequency of 200 Hz. This fact raises

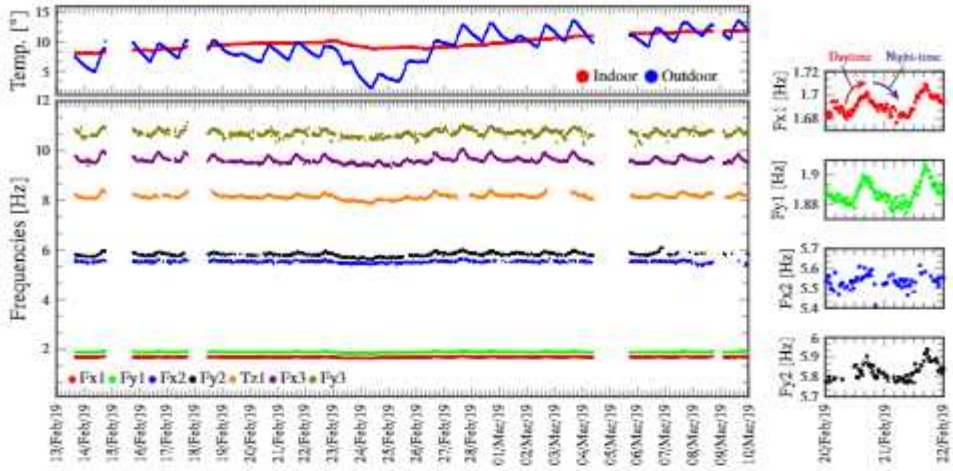

Fig. 4.18: Temperature time series and modal tracking in the Sciri Tower since February 13th until March 10th 2019.

one of the most challenging issues of this technology, that is the need for high sampling frequencies for an accurate assessment of the velocity of propagating waves. As evidenced by the results of Lacanna *et al.* [145], the high velocity of traveling pulses, along with the limited separation between sensors that is typically possible in historic buildings, make the detection of environmental effects require high sampling frequencies. In addition, the effects of early-stage damage are usually lower than environmental effects (see e.g. [83, 19]), thereby high-sampling frequencies are critical for early damage detection in ANDI-based SHM systems. From the relationship in Eq. (4.10), considering a wave velocity of 366.42 m/s, as obtained in Fig. 4.20 (c) in the SE direction, and a maximum sensor separation of 27.4 m, the maximum observable reduction in the wave velocity considering a sampling frequency of 200 Hz ($\Delta t = 5$ ms) is 23 m/s. On the other hand, the minimum observable velocity variations are 5 m/s and 1 m/s for sampling frequencies of 1000 Hz ($\Delta t = 1$ ms) and 5000 Hz ($\Delta t = 0.2$ ms), respectively. The resolution of the identified wave velocities is inversely proportional to the separation of the sensors as shown in Eq. (4.10), therefore the need for high sampling frequencies increases for the assessment of local wave velocities and their profile along the tower. In this regard, a clearer representation of day/night fluctuations can be noted for increasing sampling frequencies in Fig. 4.20. Specifically, it is observed in all the cases that wave arrival times decrease for increasing environmental temperature. Alternatively, wave velocities (i.e. stiffness) increase for increasing temperature. These results agree with the previously reported results on the day/night fluctuations of the resonant frequencies in Fig. 4.18 as a result of temperature-induced closure of cracks. With regard to the uncertainty in the tracking of the wave arrival times, it is noted in Fig. 4.21 that the standard deviations increase systematically

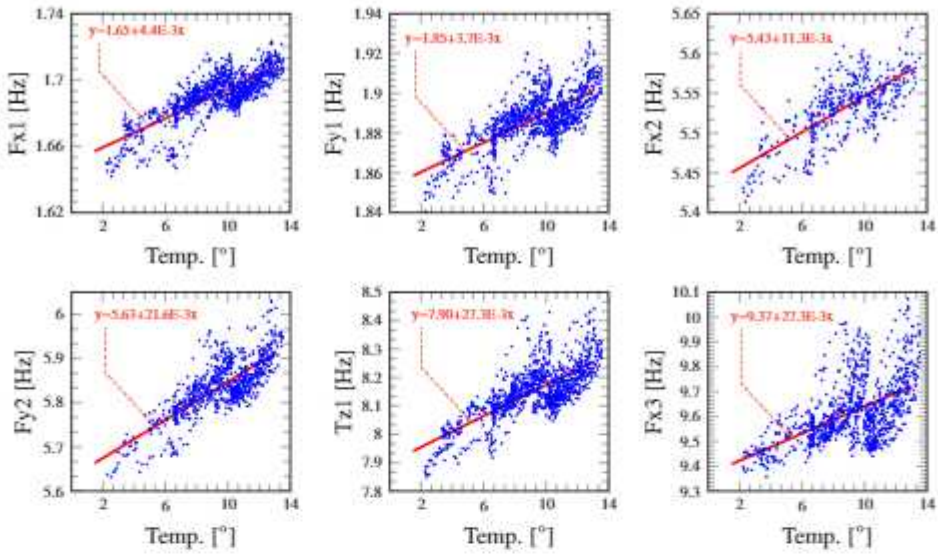

Fig. 4.19: Correlation analysis between the natural frequencies of the Sciri Tower versus outdoor temperature.

between 1:00 and 5:00 a.m. This fact indicates limitations in the identification stemming from low signal-to-noise ratio since ambient excitation due to traffic and human activities is minimum during this time lapse.

To further investigate the effects of environmental temperature upon the identified wave velocities, Figs. 4.22 and 4.23 depict the identified wave velocities in the SE and NE directions versus environmental temperature, respectively. Furthermore, in order to assess the potential of this approach for identifying local wave velocities, two different layers were considered, namely L1 (9.3 m$< z <$28.4 m), and L2 (28.4 m$< z <$36.7 m). In these analyses, only the results obtained for sampling frequencies of 1000 Hz and 5000 Hz are presented, since the accuracy of the identification performed with 200 Hz proved insufficient to capture temperature-induced daily fluctuations. In order to extract robust correlations between wave velocities and environmental temperature, the corrupted wave identification results during the early morning hours due to low excitation levels were filtered out using the MCD previously reported in Section 2.3. In the analyses, we sought a subset of $\approx 0.9n_p$ samples, with n_p being the number of data points in the time series of identified wave velocities. Then, the 10% of the samples in the time series of velocities with the largest Mahalanobis distances with respect to the previously defined sample subset were disregarded as outliers. In general, it can be concluded from Figs. 4.22 and 4.23 that the relation between wave velocities and environmental temperature can be approximately defined as linear. It is observed that the accuracy of the identification considerably improves with the sampling

Table 4.3: Mean $\overline{\tau_i}$ and standard deviation values of the wave arrival times obtained by peak-picking analysis of the IRFs staked over 30-min intervals throughout the first 48 hours (0.1-20 Hz, 10-min-long time windows with 50% overlap).

		Direction: SE (Channels 1, 4, 5, 7, 9, and 11)								
		F_s=200 Hz			F_s=1000 Hz			F_s=5000 Hz		
z [m]	D_i [m]	$\overline{\tau_i}$ [ms]	σ_τ [ms]	v [m/s]	$\overline{\tau_i}$ [ms]	σ_τ [ms]	v [m/s]	$\overline{\tau_i}$ [ms]	σ_τ [ms]	v [m/s]
36.70	0.00	0.500	0.000		1.502	0.000		0.100	0.000	
32.90	3.80	18.021	8.189		20.634	7.499		24.987	6.696	
28.40	8.30	31.608	3.416		32.151	2.239		32.600	1.534	
24.30	12.40	34.671	5.487	301.144	33.405	3.640	294.651	32.993	5.067	294.779
16.90	19.80	38.750	5.736		38.048	7.429		35.154	6.672	
9.30	27.40	76.634	5.138	388.785	73.419	3.788	404.363	73.974	3.305	405.171
		Direction: NE (Channels 2, 6, 8, 10 and 12)								
		F_s=200 Hz			F_s=1000 Hz			F_s=5000 Hz		
z [m]	D_i [m]	$\overline{\tau_i}$ [ms]	σ_τ [ms]	v [m/s]	$\overline{\tau_i}$ [ms]	σ_τ [ms]	v [m/s]	$\overline{\tau_i}$ [ms]	σ_τ [ms]	v [m/s]
36.70	0.00	0.500	0.000		1.502	0.000		0.100	0.000	
28.40	8.30	32.779	1.725		32.414	2.087		33.409	1.537	
24.30	12.40	33.877	2.737	311.442	33.420	2.159	314.978	33.953	2.021	307.762
16.90	19.80	39.420	5.611		39.534	6.551		38.936	5.983	
9.30	27.40	76.706	2.153	387.518	76.824	2.131	386.844	77.544	2.022	384.594

frequency of 5000 Hz, while many outliers are present in the results obtained for $F_s = 1000$ Hz due to poor sampling limitations in the peak-picking analysis. It is also interesting to note that, in both cases, wave velocities are larger in the bottom layer L1 where the contribution of the building aggregate is localized. With regard to the effects of environmental temperature, it is noted that global velocities exhibit positive correlations with temperature, and the sensitivity in the SE direction ($F_s = 5000$ Hz, 9.5 m/s/C°) is substantially larger than in the NE direction ($F_s = 5000$ Hz, 0.7 m/s/C°). Considering the plan distribution of the building ensemble, such a behavior is reasonable given that the horizontal constraint imposed by the aggregate is stronger in the SE direction. In terms of local velocities, some differences can be noted in the SE and NE directions. In the SE direction, a large positive correlation ($F_s = 5000$ Hz, 20.7 m/s/C°) between wave velocity and environmental temperature is found in the bottom layer L1. This behavior is ascribed to larger temperature-induced crack closure effects in the section of the tower constrained by the building aggregate, where thermal expansion is more constrained and the heterogeneity degree of the material is larger. Conversely, a small correlation ($F_s = 5000$ Hz, 0.5 m/s/C°) is found in the top section of the tower (L2) where thermal expansion is minimally constrained. In the NE direction, small temperature sensitivities are found in both layers, and with opposite sign to those obtained in the SE direction. These results evidence the key role of the building aggregate into the effects of environmental temperature on the stiffness distribution of the Sciri Tower.

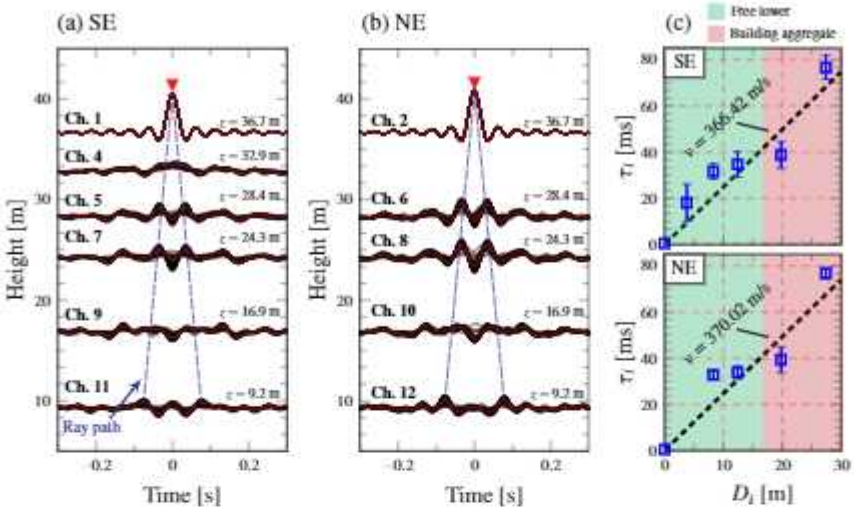

Fig. 4.20: Staking waveforms for the first 48 hours and filtered in the broad-band frequency of 0.1-20 Hz, (a) NE component, and (b) SE component. Red lines indicate the staked IRFs over the first 48 hours. (c) Travel times at different heights versus distance to the roof. Error bars denote the standard deviations of the travel times obtained for every 30-min long records, and the global velocity of the waves crossing the whole structure obtained by linear regression is denoted with black dashed lines (F_s—200 Hz).

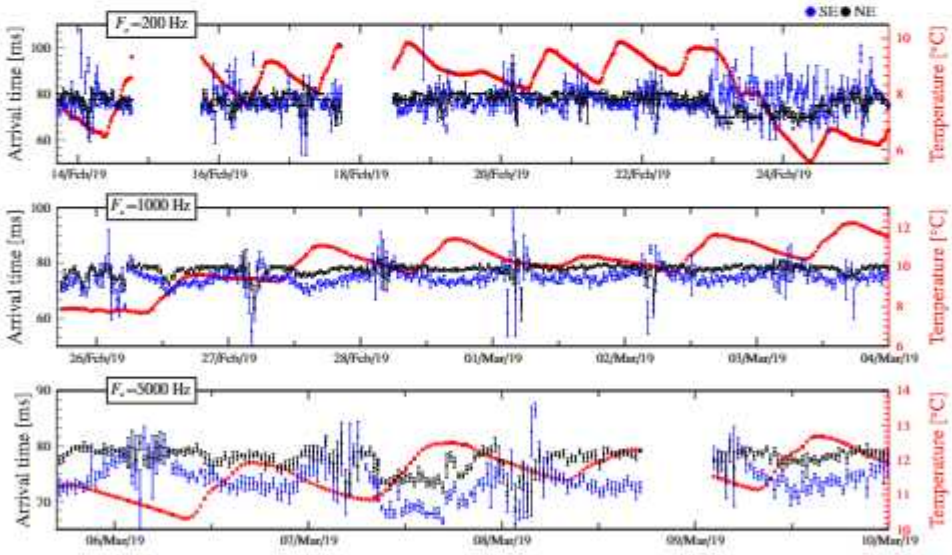

Fig. 4.21: Time series of wave arrival times in the NE and SE directions of the Sciri Tower since February 13$^{\text{th}}$ until March 10$^{\text{th}}$ 2019. Error bars indicate the standard deviation of the identified arrival times obtained by every 10-min-long windows stacked over every 30-min vibration record.

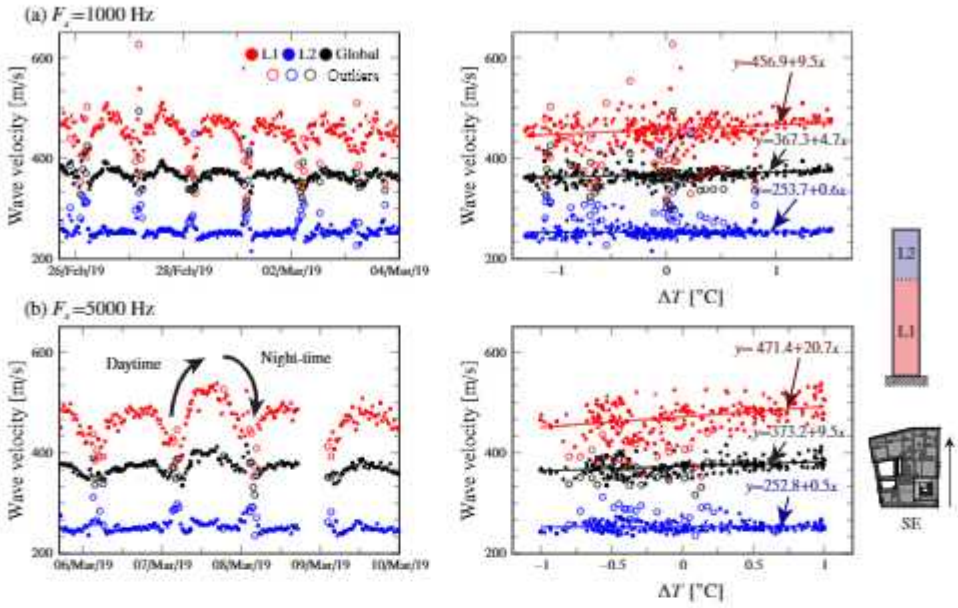

Fig. 4.22: Wave velocity tracking in the SE direction of the Sciri tower considering two layers, L1 (9.3 m< z <28.4 m), and L2 (28.4 m< z <36.7 m), and the whole tower (9.3 m< z <36.7 m), with sampling frequencies of F_s=1000 Hz and 5000 Hz.

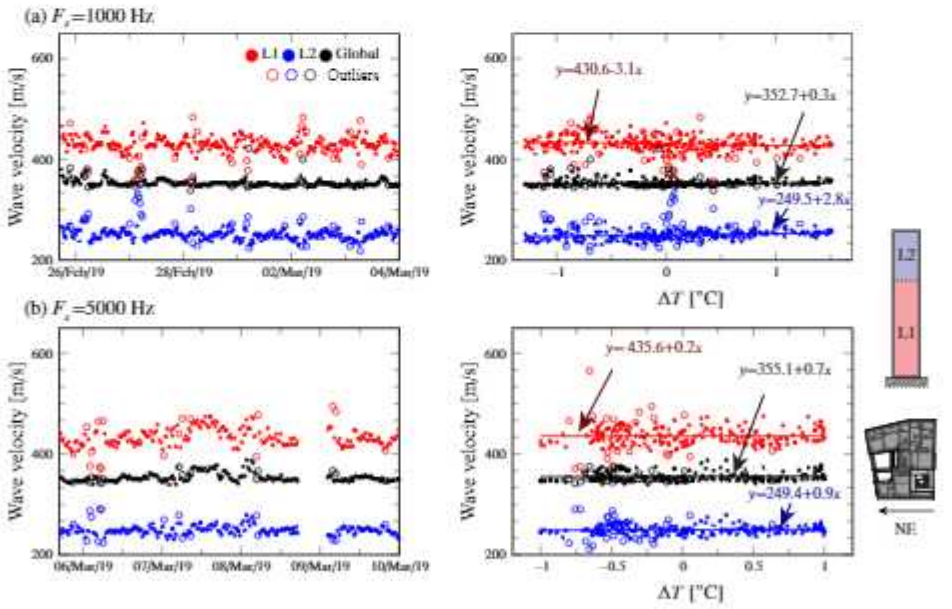

Fig. 4.23: Wave velocity tracking in the NE direction of the Sciri tower considering two layers, L1 (9.3 m< z <28.4 m), and L2 (28.4 m< z <36.7 m), and the whole tower (9.3 m< z <36.7 m), with sampling frequencies of F_s=1000 Hz and 5000 Hz.

5. Digital Twins for Damage Identification

5.1. Introduction

All the unsupervised SHM techniques presented so far are mainly proficient for damage detection, while information on the localization and severity of damage can be only inferred in some particular cases. For instance, whilst the seismic interferometry techniques previously overviewed in Chapter 4 effectively identifies the approximate location of damage (between pairs of sensors), damage quantification can be only assessed indirectly in terms of wave delays. Similarly, while the results in Chapter 2 demonstrated that damage quantification can be conducted by assessing damage-induced frequency decays, this information can hardly be translated into load bearing capacity losses. Similar limitations are also common in static monitoring (e.g. strain gauges or electrical resistivity measurements) which, despite assessing the local condition of the monitored structure, can only clearly localize and quantify damage if located proximate to the defect. Therefore, supervised learning techniques suffer from three major issues:

- **The location of defects can only be identified in approximate terms**. These include the identification of certain regions or group of elements that may be experiencing damage, although the identification of specific structural members affected by damage is extremely challenging. This represents a limiting factor in the definition of post-event detailed inspection plans with the subsequent economic inefficiencies.
- **Damage quantification can only be conducted indirectly**. Since

damage assessment is only inferred from the structural response, conclusions on the structural safety can be hardly extracted. This reduces considerably the ability of infrastructure owners to conduct data informed decision-making, specially when managing the maintenance of infrastructural systems since no sound information is available to establish prioritization rules.

- **Inability to conduct damage prognosis**. Since the information stock of damage progression in structural systems is very limited, the definition of data-based predictive models is generally unfeasible. Moreover, civil engineering structures differ considerably depending on site conditions, design standards used in the construction, climate conditions, and more factors which are also constantly subjected to variations (e.g. traffic intensity, climate change). Such limitations considerably hinder the labor of infrastructure managers when managing the periodicity of inspections and rehabilitation interventions.

To address the aforementioned limitations, it is critical to inject engineering knowledge into the processing of monitoring data through supervised learning techniques. These techniques, often referred to as Structural Identification (St-Id) or model updating, represent the most efficient solution to achieve complete damage identification capabilities. Model updating aims to bridge the gap between numerical models and real systems by tuning the model parameters in such a way that the mismatch amidst experimental and theoretical observations is minimal [158]. Overall, methods for model updating can be categorized into deterministic and probabilistic or uncertainty quantification (UQ) approaches [159]. Deterministic methods are relatively mature and a large number of successful applications can be found in the literature (see e.g. [158, 43]). These methods determine a unique solution by solving an optimization problem, which typically minimizes a non-linear objective function accounting for the discrepancies between theoretical models and experimental data. To address ill-conditioning and ill-posedness, regularisation and parametrisation are often adopted [160]. Common regularisation approaches are variations of the classical Tikhonov regularisation, which introduces an additive constraint to the objective function in the form of a model norm scaled by a Lagrange multiplier (see e.g. [161]). Despite deterministic St-Id methods are in general intuitive and require moderate computational efforts, a major limitation relates to their inability to handle uncertainties. This hinders their implementation into condition-based maintenance schemes, since no evidence on the reliability of the model nor the robustness of decisions made from its predictions can be obtained. Alternatively, UQ models not only allow assessing the effects of uncertainty on the updated model parameters, but also provide means to evaluate the uncertainties on derived quantities such as response predictions [162]. In this light, Bayesian model updating (BMU) methods are becoming especially

popular owing to their ability to address uncertainties, robustness to the presence of noise in the measurements, and efficiency to handle ill-conditioning limitations. The latter is achieved by specifying prior probability distribution functions (PDFs) over the uncertain parameters, which imposes a regularization to the inverse problem. Such excellent features have fostered their implementation to multiple structural systems (refer to [163, 164] for an extensive state-of-the-art review). The evaluation of the posterior PDFs requires solving a possibly high-dimensional integral which, except for some trivial cases, needs to be approximated numerically. Markov chain methods are usually implemented to extract series of samples to estimate the posterior PDFs, allowing to sample from a large class of high-dimensional distributions. Popular procedures for Markov Chain Monte Carlo (MCMC) sampling are the Metropolis-Hastings [165] and Gibbs algorithms [166], although a variety of more efficient sampling algorithms have been proposed in recent years [167], including Transitional MCMC (TMCMC) [168], BMU with Structural Reliability [169], Bayesian broad learning (BBL) [170], hybrid particle swarm MCMC [171], and Sparse Bayesian Learning [172], among others.

The progressive cheapening of sensor technologies [173] and the hasty development of machine learning (ML) and artificial intelligence(AI) [174] in recent years have enabled the incorporation of supervised learning approaches to the novel concept of Digital Twins (DTs) [175, 176]. In general, a DT represents a digital replica of a physical asset characterized by cyber-physical interaction [177]. In the context of SHM of civil engineering structures, a DT involves a physics-based or a machine learning model that continuously exploits monitoring data to infer and classify the health condition of the physical asset [178]. The concept of DTs in the realm of SHM is directly applicable by extending St-Id techniques to exploit continuous data streams of monitoring data. Nevertheless, despite the obvious potential of this approach, only a few attempts have been made in the literature and mostly using simplistic models or based on laboratory case studies. One of the major obstacles for the extensive implementation of DTs in engineering practice stems from the difficulties involved in the use of computationally intensive numerical models into automated long-term SHM systems. This is particularly critical in BMU methods, whose computational cost is commonly orders-of-magnitude higher than deterministic methods. To tackle such a challenge, recent advances in the development of high-fidelity surrogate models (SMs) have brought new horizons for real-time St-Id. Indeed, a broad variety of surrogate modeling methods have been successfully applied in the context of St-Id, including Response surface models (RSMs) [179], PCE [180], Support Vector Regression [181], and Kriging [182], as well as techniques from ML such as Gaussian process approximation [183], or Artificial Neural Networks [184]. For instance, Pepi *et al.* [185] developed a PCE SM of the modal properties of a cable-stayed footbridge in Terni (Italy), and implemented an MCMC BMU algorithm to identify the model parameters

of the bridge. Schneider *et al.* [186] proposed a BMU procedure using rational PCE meta-models of the response of dynamic systems in the frequency domain, and demonstrated its effectiveness for the St-Id of a cross-laminated timber plate. Nonetheless, most research works limit to St-Id applications using experimental measurements from isolated tests, while investigations coping with continuous SHM data are much more scarce. In this regard, a noteworthy contribution was made by Cabboi *et al.* [187], who reported the deterministic RSM-based damage identification of a stone-masonry tower exploiting continuous time series of resonant frequencies extracted by automated OMA.

It is evident from the literature review above that the development of DTs for SHM still remains in the early stages of development. With the aim of addressing this gap in the literature, considerable efforts have been devoted in this thesis for the development of continuous deterministic and probabilistic digital twinning techniques for real-time damage identification of large-scale in-operation structures. This chapter presents the theoretical formulation and main scientific achievements published in references [188, 147, 189, 190]. The chapter is organized as follows: Section 5.2 presents the theoretical basis of deterministic and probabilistic DTs within the context of SHM. Sections 5.3 outlines the fundamentals of surrogate modeling. Section 5.4 reports the definition of synthetic damage scenarios through non-linear numerical simulations to validate SL techniques and, finally, Section 5.5 reports two illustrative case studies.

5.2.Continuous St-Id

The general work-flow of an SHM system involving DT-based St-Id can be sketched as shown Fig. 5.1. In general, the monitoring system iteratively acquires experimental data from the physical asset. This information is used to feed the DT, which conducts St-Id by inverse calibration. Finally, damage assessment can be conducted by inspecting the appearance of anomalies both in the experimental time series and in the outputs of the DT. To attain quasi-real-time damage identification, it is of pivotal importance to guarantee that the total computational time involved in the signal processing, inverse calibration of the DT, and the damage assessment is lower than the acquisition time (often 30 minutes). If so, at any step $j+1$, the damage identification can be conducted in parallel with the previous acquisition j without accumulating time delays. In this thesis, all the analyses have been conducted on the basis of ambient vibration-based SHM systems, thus exploiting time series of modal signatures. Nonetheless, the framework in Fig. 5.1 is completely general, and most of the conclusions obtained hereafter can be easily extended to other monitoring systems. With this said, the procedure comprises four consecutive steps:

(A) *Automated OMA* – Ambient vibrations are periodically recorded by a

DAQ and stored in separate data files containing a certain time duration. Then, a set of modal signatures (resonant frequencies f_j, mode shapes φ_j, and damping ratios ζ_j) is extracted through automated OMA.

(B) *Removal of EOC* – The presence of benign fluctuations driven by EOC in the previously identified modal signatures is minimized through statistical pattern recognition. Note that this step can be directly applied to the time series of modal properties or after the St-Id. The second approach allows to explore the appearance of environmental effects upon the model parameters, although the model calibration becomes more challenging and time-consuming as shown hereafter in Section 5.5.

(C) *DT-based St-Id* – This step relates the St-Id of the asset through the model updating of the DT. This is accomplished by solving a certain optimization problem seeking the combination of certain damage-sensitive model parameters $\mathbf{x}$ that minimize the mismatch between the theoretical predictions of the model and the previously identified experimental modal signatures. As a result, the calibrated model parameters ($\hat{\mathbf{x}}$) are collected in an observation matrix $\hat{\mathbf{X}}$.

(D) *Damage identification* – Finally, the appearance of structural damage can be appraised by novelty analysis of the time series of modal signatures and model parameters contained in $\hat{\mathbf{X}}$. Since the model parameters are defined according to certain damage mechanisms or the condition of some structural members, the identification of permanent variations in their time series provides direct assessment of the location and severity of the damage.

5.2.1. Deterministic Identification

Deterministic St-Id approaches seek to minimize an objective function $J(\mathbf{x})$ accounting for the mismatch between the experimental data and the predictions of the numerical model of the structure. In the realm of vibration-based SHM, a common objective function including the relative differences between the l target modes of vibration reads [147, 149]:

$$J(\mathbf{x}) = \sum_{i=1}^{l} \left[\eta_{(1,i)} \varepsilon_i(\mathbf{x}) + \eta_{(2,i)} \delta_i(\mathbf{x}) \right] + \mathcal{R}(\mathbf{x}), \tag{5.1}$$

with

$$\varepsilon_i(\mathbf{x}) = \frac{\left| f_i^{\exp} - f_i^{\mathrm{DT}}(\mathbf{x}) \right|}{f_i^{\exp}}, \quad \delta_i(\mathbf{x}) = 1 - MAC\left(\varphi_i^{\exp}, \varphi_i^{\mathrm{DT}}(\mathbf{x}) \right), \tag{5.2}$$

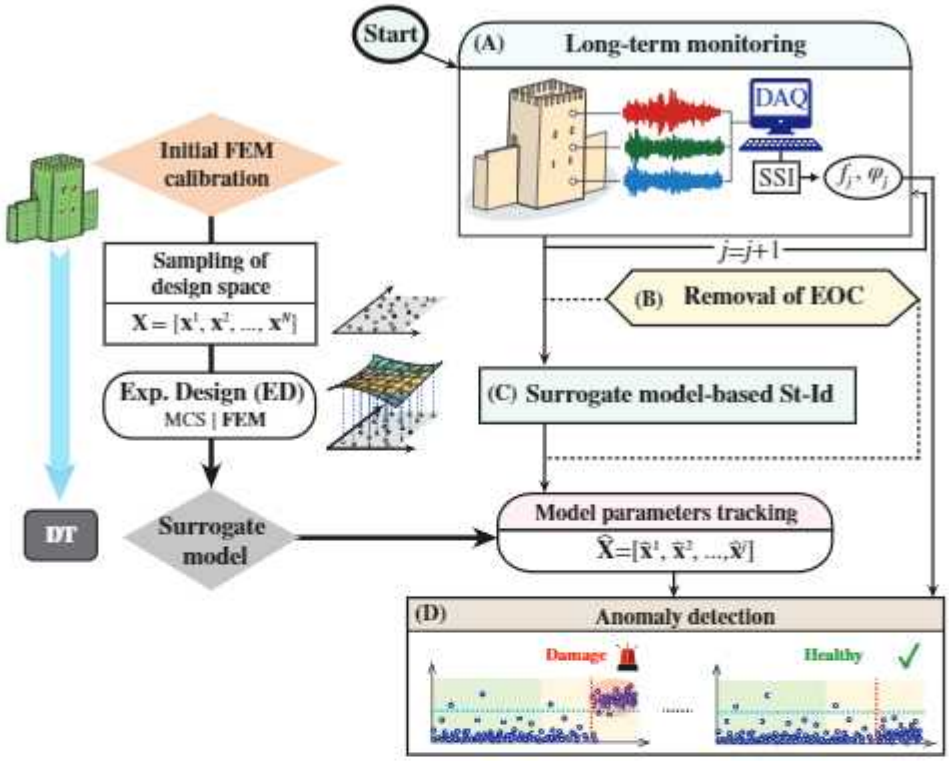

Fig. 5.1: Flowchart of a general DT-based continuous SHM system.

and $\eta_{(1,i)}$ and $\eta_{(2,i)}$ being weighting coefficients that scale the contribution of the first two terms of the objective function. Terms $f_i^{\exp}$ and $f_i^{DT}(\mathbf{x})$ denote the i-th resonant frequencies obtained by OMA and the DT, respectively, and terms $\varphi_i^{\exp}$ and $\varphi_i^{\mathrm{DT}}(\mathbf{x})$ stand for the corresponding mode shapes. On this basis, the St-Id procedure is given by the following constrained non-linear minimization problem:

$$\hat{\mathbf{x}} = \arg\min_{\mathbf{x}\in\mathbb{D}} J(\mathbf{x}) . \tag{5.3}$$

The last term in Eq. (5.1), $\mathcal{R}(\mathbf{x})$, stands for a regularization term used to mitigate ill-conditioning in the St-Id. The Tikhonov regularization represents a common approach given by:

$$\mathcal{R}(\mathbf{x}) = \frac{1}{m}\sum_{i=1}^{m} \eta_{(3,i)} \frac{\left(x_i - x_i^0\right)^2}{b_i - a_i}, \tag{5.4}$$

where terms a_i and b_i denote the limits of the allowed range of variation of model parameter x_i, i.e. $a_i \leq x_i \leq b_i$, and term $\eta_{(3,i)}$ represents a trade-off parameter used to weigh the intensity of the regularization for every model

parameter. The implemented regularization forces the solution to remain close to a reference vector of design variables $\mathbf{x}^0 = \left[x_1^0, ..., x_m^0\right]^{\mathrm{T}}$ denoting the undamaged condition. For small values of $\eta_{(3,i)}$, the design variable x_i remains almost unrestricted, while too large values may over-constrain the variation of x_i. Note that the aim of defining different trade-off parameters $\eta_{(3,i)}$ for each model parameter is to tackle the particular sensitivities of the modal features to variations in the model parameters. Finally, it is important to remark that the optimization problem in Eq. (5.3) is often non-convex, thereby global optimization algorithms are recommended to prevent the optimization from getting stuck at local minima.

5.2.2. Bayesian Identification

The Bayesian St-Id problem is formulated as the inference of certain model parameters $\mathbf{x}$ conditional on a set of experimentally identified modal properties $\mathbf{d}(t) \in \mathbb{R}^{m(1+N_o)}$. Let use denote with $\mathbf{d}(t)$ the periodically identified resonant frequencies $f_r(t)$ and mode shapes $\boldsymbol{\varphi}_r(t) \in \mathbb{R}^{N_o}$ at time instants t, with m and N_o being the number of identified modes and measured degrees of freedom (DOFs), respectively. The Bayes' theorem is used to estimate the posterior distribution $p\left(\mathbf{x}(t) \middle| \mathbf{d}(t)\right)$ of the model parameters $\mathbf{x}(t)$ at time instants t as:

$$p\left(\mathbf{x}(t) \middle| \mathbf{d}(t)\right) = \frac{p\left(\mathbf{d}(t) \middle| \mathbf{x}(t)\right) p\left(\mathbf{x}(t)\right)}{p\left(\mathbf{d}(t)\right)}, \tag{5.5}$$

where $p\left(\mathbf{x}(t)\right)$ is the prior distribution of the model parameters, $p\left(\mathbf{d}(t) \middle| \mathbf{x}(t)\right)$ denotes the likelihood function, and $p\left(\mathbf{d}(t)\right)$ stands for the evidence of the model class, selected so that $p\left(\mathbf{x}(t) \middle| \mathbf{d}(t)\right)$ integrates to one. For clarity of the notation, the dependence on time t is dropped in the following formulation.

The likelihood function $p\left(\mathbf{d} \middle| \mathbf{x}\right)$ represents the probability of observing the measured data $\mathbf{d}$ for model parameters equal to $\mathbf{x}$. Its definition is of pivotal importance in Bayesian inference, since it determines the probabilistic relation between the model predictions and experimental data including the unavoidable model and measurement errors. For modal frequencies, the most common approach to represent the likelihood function is the uncorrelated Gaussian error assumption for each identified modal frequency (see e.g. [185, 191]):

$$f_r = \hat{f}_r(\mathbf{x}) + \varepsilon_{f_r}, \tag{5.6}$$

where $\hat{f}_r(\mathbf{x})$ is the model prediction, while ε_{f_r} is the prediction error for the r-th modal frequency taken to be Gaussian with zero mean and standard deviation σ_{f_r}. Then, the likelihood term of the r-th resonant frequency reads:

$$p\left(f_r \middle| \mathbf{x}\right) = \frac{1}{\sigma_{f_r}\sqrt{2\pi}} \exp\left\{-\frac{1}{2}\frac{\left(f_r - \hat{f}_r(\mathbf{x})\right)^2}{\sigma_{f_r}^2}\right\}. \tag{5.7}$$

With regard to the mode shapes, an often-used formulation is to assume that the discrepancy vector between the measured mode shape vector and the model predicted one follows a zero-mean multivariate Gaussian distribution [192, 193]. The prediction error equation for the r-th mode shape is then:

$$\boldsymbol{\varphi}_r = \beta_r(\mathbf{x})\widehat{\boldsymbol{\varphi}}_r(\mathbf{x}) + \boldsymbol{\varepsilon}_{\varphi_r}, \tag{5.8}$$

where $\boldsymbol{\varepsilon}_{\varphi_r}$ is the prediction error vector for the r-th mode shape taken to be Gaussian with zero mean and covariance matrix $\sigma^2_{\varphi_r}\boldsymbol{\Sigma}_{\varphi_r}$, where matrix $\boldsymbol{\Sigma}_{\varphi_r}$ specifies the possible correlation between the components of the prediction error of the r-th mode shape. Term $\beta_r(\mathbf{x})$ is a normalization constant to accommodate the different normalizations of the experimental mode shapes $\boldsymbol{\varphi}_r$ (normalized to unit Euclidean norm) and the model predicted ones $\widehat{\boldsymbol{\varphi}}_r(\mathbf{x})$ (often mass-normalized). The scalar $\beta_r(\mathbf{x})$ is determined as the least squares solution of $\left\|\boldsymbol{\varphi}_r - \beta_r(\mathbf{x})\widehat{\boldsymbol{\varphi}}_r(\mathbf{x})\right\| = \mathbf{0}$, with $\|\cdot\|$ denoting Euclidean norm. This leads to:

$$\beta_r(\mathbf{x}) = \frac{\boldsymbol{\varphi}_r^{\mathrm{T}}\widehat{\boldsymbol{\varphi}}_r(\mathbf{x})}{\widehat{\boldsymbol{\varphi}}_r(\mathbf{x})^{\mathrm{T}}\widehat{\boldsymbol{\varphi}}_r(\mathbf{x})}. \tag{5.9}$$

The definition of the covariance matrix $\boldsymbol{\Sigma}_{\varphi_r}$ may be challenging in practice. For simplicity, the mode shape prediction error vectors are assumed uncorrelated in this work, whereby the covariance matrix simplifies to a diagonal matrix:

$$\boldsymbol{\Sigma}_{\varphi_r} = \frac{\boldsymbol{\varphi}_r^{\mathrm{T}}\boldsymbol{\varphi}_r}{N_0}\mathbf{I}_{N_0}, \tag{5.10}$$

with $\mathbf{I}_{N_0}$ being the $N_0 \times N_0$ identity matrix. In this way, the likelihood term of the r-th mode shape reads:

$$p\left(\boldsymbol{\varphi}_r \,|\, \mathbf{x}\right) = \frac{\exp\left\{-\frac{1}{2}\left[\boldsymbol{\varphi}_r - \beta_r(\mathbf{x})\boldsymbol{\varphi}_r(\mathbf{x})\right]^{\mathrm{T}}\boldsymbol{\Sigma}_{\varphi_r}^{-1}\left[\boldsymbol{\varphi}_r - \beta_r(\mathbf{x})\boldsymbol{\varphi}_r(\mathbf{x})\right]\right\}}{\sqrt{(2\pi)^{N_0}\det\left|\boldsymbol{\Sigma}_{\varphi_r}\right|}}. \tag{5.11}$$

In order to limit the number of parameters in the inference, a common approach in the literature consists of considering equal prediction errors σ_{f_r} and σ_{φ_r} for all the modes (see e.g. [194, 165, 192]) as a trade-off between computational burden and accuracy. Therefore, the dependence of prediction errors on r is dropped hereafter. Alternatively, the likelihood function can be also expressed using MAC values between the experimental and model predicted mode shapes. Taking the square root of (1-MAC) gives the fractional error between the measured and calculated mode shapes, i.e. $\varepsilon_{ms} = (1 - \mathrm{MAC}_r)^{1/2}$. Assuming the mode shape fractional error ε_{ms} follows a zero-mean Gaussian

distribution, the PDF of the mode shapes in terms of MAC values can be written as [195]:

$$p\left(\varphi_r \,|\, \mathbf{x}\right) = \frac{1}{\sqrt{2\pi\sigma_\varphi^2}} \exp\left\{-\frac{1}{2\sigma_\varphi^2}\left(1 - \mathrm{MAC}_r\right)\right\}. \tag{5.12}$$

On this basis, assuming the errors independence, the total likelihood function can be easily calculated as the product of the individual likelihoods. Considering that m modes of vibration have been identified, the total likelihood function reads:

$$p\left(\mathbf{d} \,|\, \boldsymbol{\theta}\right) = \prod_{r=1}^{m} p\left(f_r \,|\, \boldsymbol{\theta}\right) p\left(\varphi_r \,|\, \boldsymbol{\theta}\right), \tag{5.13}$$

where the parameter set $\boldsymbol{\theta}$ includes the model parameters $\mathbf{x}$ and the standard deviations σ_f and σ_φ. Note that the error uncertainties are unknown in reality, being necessary to make assumptions on their initial values. To do so, different methodologies have been proposed in the literature, including the posterior variance of the modal features estimated by Bayesian OMA, coefficients of variations of identified modal properties [193], or based on users' intuition and experience [194].

The evaluation in closed-form of the posterior PDF in Eq. (5.5) is infeasible in most applications, so adaptive MCMC sampling methods often become imperative. In reference [189], the DRAM MCMC algorithm proved particularly efficient for St-Id. The DRAM algorithm was firstly proposed by Haario *et al.* [196], and combines DR with an AM algorithm. Considering one delayed rejection step, the DRAM algorithm can be implemented according to the following steps:

1. Choose the length of the chain N_c and initialize the parameter set $\boldsymbol{\theta}_c = \boldsymbol{\theta}_0$, the error variances $\sigma_{f_0}^2$ and $\sigma_{\varphi_0}^2$, and the covariance of the proposal distribution $\Sigma_p = \Sigma_0$. Select the initial non-adaptation period n_a and set $i = 1$.

2. Propose a new parameter value $\boldsymbol{\theta}_{p,1}$ by sampling from a proposal Gaussian distribution $S(\boldsymbol{\theta}, \boldsymbol{\theta}_c)$ with mean at the current point $\boldsymbol{\theta}_c$ and covariance Σ_p, i.e. $\boldsymbol{\theta}_{p,1} = \boldsymbol{\theta}_c + \xi$, with $\xi \sim \mathcal{N}\left(\mathbf{0}, \Sigma_p\right)$.

3. Compute the acceptance probability:

$$\alpha_1\left(\boldsymbol{\theta}_c, \boldsymbol{\theta}_{p,1}\right) = \min\left(1, \frac{p\left(\boldsymbol{\theta}_{p,1} \,|\, \mathbf{d}\right) S(\boldsymbol{\theta}_{p,1}, \boldsymbol{\theta}_c)}{p\left(\boldsymbol{\theta}_c \,|\, \mathbf{d}\right) S(\boldsymbol{\theta}_c, \boldsymbol{\theta}_{p,1})}\right). \tag{5.14}$$

4. Generate a random number $\vartheta \sim \mathcal{U}(0,1)$. If $\alpha_1\left(\boldsymbol{\theta}_c, \boldsymbol{\theta}_{p,1}\right) > \vartheta$, accept the candidate sample $\boldsymbol{\theta}_i = \boldsymbol{\theta}_{p,1}$ and move to step (8). Otherwise, propose a second stage move in step (5).

5. Propose a second stage move $\boldsymbol{\theta}_{p,2}$ sampling from $S_2(\boldsymbol{\theta}, \boldsymbol{\theta}_{p,1}, \boldsymbol{\theta}_c)$. This second stage proposal is allowed to depend not only on the current position of the chain, but also on the candidate that has just been proposed and rejected. In this work, the covariance of the proposal in the second stage proposal is scaled by a factor γ as $\gamma\Sigma_p$.

6. Compute the acceptance probability

$$\alpha_2\left(\boldsymbol{\theta}_c, \boldsymbol{\theta}_{p,1}, \boldsymbol{\theta}_{p,2}\right) = \min\left\{1, \frac{p\left(\boldsymbol{\theta}_{p,2}|\mathbf{d}\right) S_1\left(\boldsymbol{\theta}_{p,2}, \boldsymbol{\theta}_{p,1}\right) S_2\left(\boldsymbol{\theta}_{p,2}, \boldsymbol{\theta}_{p,1}, \boldsymbol{\theta}_c\right)\left[1-\alpha_1\left(\boldsymbol{\theta}_{p,2}, \boldsymbol{\theta}_{p,1}\right)\right]}{p\left(\boldsymbol{\theta}_c|\mathbf{d}\right) S_1\left(\boldsymbol{\theta}_c, \boldsymbol{\theta}_{p,1}\right) S_2\left(\boldsymbol{\theta}_c, \boldsymbol{\theta}_{p,1}, \boldsymbol{\theta}_{p,1}\right)\left[1-\alpha_1\left(\boldsymbol{\theta}_c, \boldsymbol{\theta}_{p,1}\right)\right]}\right\}. \tag{5.15}$$

7. Accept of reject $\boldsymbol{\theta}_{p,2}$ by setting:

$$\boldsymbol{\theta}_i = \begin{cases} \boldsymbol{\theta}_{p,2}, & \text{with probability } \alpha_2\left(\boldsymbol{\theta}_c, \boldsymbol{\theta}_{p,1}, \boldsymbol{\theta}_{p,2}\right), \\ \boldsymbol{\theta}_c, & \text{with probability } 1-\alpha_2\left(\boldsymbol{\theta}_c, \boldsymbol{\theta}_{p,1}, \boldsymbol{\theta}_{p,2}\right), \end{cases} \tag{5.16}$$

8. Update the error variances $\sigma_{f_i}^2$ and $\sigma_{\varphi_i}^2$. Assuming an inverse Gamma $\left(\Gamma^{-1}\right)$ prior distribution for the error variances, the conjugate posterior also follows an inverse Gamma distribution and new samples can be drawn following a standard Gibbs sampling procedure [197]:

$$p\left(\sigma_f^2 \middle| \boldsymbol{\theta}_i, \mathbf{d}\right) \sim \Gamma^{-1}\left(\frac{n_{o,f}+m}{2}, \frac{n_{o,f}\, S_{o,f}^2 + SS_f\left(\boldsymbol{\theta}_i\right)}{2}\right), \tag{5.17}$$

$$p\left(\sigma_\varphi^2 \middle| \boldsymbol{\theta}_i, \mathbf{d}\right) \sim \Gamma^{-1}\left(\frac{n_{o,\varphi}+m}{2}, \frac{n_{o,\varphi}\, S_{o,\varphi}^2 + SS_\varphi\left(\boldsymbol{\theta}_i\right)}{2}\right), \tag{5.18}$$

where $n_{o,f}$, $n_{o,\varphi}$, $S_{o,f}$ and $S_{o,\varphi}$ are the input parameters of the prior distributions of σ_f^2 and σ_φ^2. In this work, the following values are chosen with the aim of making the priors uniformative: $n_{o,f} = n_{o,\varphi} = 1$ and $S_{o,f} = \sigma_{f_0}^2$, $S_{o,\varphi} = \sigma_{\varphi_0}^2$. Terms $SS_f\left(\boldsymbol{\theta}_i\right)$ and $SS_\varphi\left(\boldsymbol{\theta}_i\right)$ denote the sum of squared errors of resonant frequencies and mode shapes given by:

$$SS_f\left(\boldsymbol{\theta}_i\right) = \sum_{r=1}^{m}\left(f_r - f_r\left(\boldsymbol{\theta}_i\right)\right)^2, \tag{5.19}$$

$$SS_{\boldsymbol{\varphi}}(\boldsymbol{\theta}_i) = \sum_{r=1}^{m} \frac{N_0}{\boldsymbol{\varphi}_r^{\mathrm{T}} \boldsymbol{\varphi}_r} \left[\boldsymbol{\varphi}_r - \beta_r(\boldsymbol{\theta}_i)\boldsymbol{\varphi}_r(\boldsymbol{\theta}_i)\right]^{\mathrm{T}} \left[\boldsymbol{\varphi}_r - \beta_r(\boldsymbol{\theta}_i)\boldsymbol{\varphi}_r(\boldsymbol{\theta}_i)\right]. \tag{5.20}$$

9. Update the covariance matrix Σ_p as:

$$\Sigma_p = \begin{cases} \Sigma_0 & i \leq n_a \\ s_d \mathrm{cov}\left(\boldsymbol{\theta}_1, \ldots, \boldsymbol{\theta}_i\right) & i > n_a \end{cases} \tag{5.21}$$

   with $s_d = 2.4^2/d$ a scaling parameter, with d being the number of fitting parameters [196].

10. Set $i = i + 1$ and go to step 2 until the desired number of samples N_c is obtained.

Toy example: Truss structure

Let us introduce a simple toy example presented in reference [189] to illustrate the potentials of the previous MCMC approach for St-Id. The case study consists of a 31-bar planar truss structure used as a benchmark in many research works on FEM updating (e.g. [198]). The geometry and boundary conditions of the structure are shown in Fig. 5.2. It has been discretized in Matlab using planar 2-D truss elements with two translational DOFs per node, and the material has been considered as linear elastic with Young's modulus $E = 70$ GPa and mass density $\rho = 770$ kg/m^3. In this case study, the elastic moduli of the bars numbered with 31, 1, 28, 4, 18, 14, 7 and 22 are defined as the model updating parameters in $\boldsymbol{\theta}$. Specifically, i.i.d. stiffness multipliers θ_i, $i = 1, \ldots, 8$, uniformly distributed in $[0.7, 1.1]$, are defined as the unknown parameters. The first eight resonant frequencies and mode shapes are taken into account in the subsequent inference analysis. The mode shapes are discretized considering that seven sensors aligned in the vertical direction are located at nodes N2, N4, N6, N8, N10, N12 and N12 (indicated with red arrows in Fig. 5.2).

In the Bayesian inference analysis, the likelihood functions reported in Eqs. (5.9) and (5.11) are implemented. Considering that the prediction error parameters are the same for all the considered modes, the number of uncertain parameters to be included in the inference amount to 10, i.e. θ_i, $i = 1, \ldots, 8$, σ_f and $\sigma_{\boldsymbol{\varphi}}$. To illustrate the effectiveness of the implemented adaptive MCMC algorithm, a first analysis considering only θ_1 and θ_2 as the uncertain parameters is presented in Fig. 5.3. Defining the exact values of $\theta_1 = 0.8$ and $\theta_2 = 1.0$, the Bayesian inference results considering only the resonant frequencies and both the resonant frequencies and mode shapes are presented in Fig. 5.3 (a) and (b), respectively. The joint PDF of the uncertain parameters is obtained

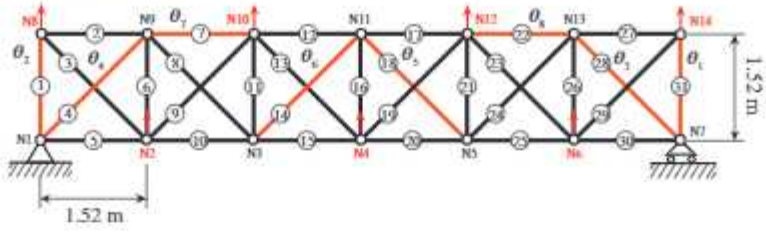

Fig. 5.2: Geometry, boundary conditions and parametrization of the benchmark 31-bar planar truss structure.

by drawing 8000 Markov chain samples with a burning time of 900 samples. The adaptive MCMC algorithm is activated after the first 1000 samples. The Gaussian proposal is initially defined as a diagonal covariance matrix of value 1E-2 and scaled by the factor $s_d = 2.4^2/d$. In the DR step, the covariance matrix of the proposal distribution is scaled down by a factor $\gamma = 0.1$. The initial location state θ_0 is defined by considering all the uncertain parameters equal to 1.0. To evaluate the effectiveness of the inference of the prediction errors according to Eqs. (5.17) and (5.18), large initial values are selected as $\sigma_f^2 = 3\%$ and $\sigma_\varphi^2 = 0.5\%$ (Eq. (5.11)). The selected hyperparameters led to an average acceptance rate of 67%, which is within the reasonable interval $[60\% - 70\%]$. Note that parameters θ_1 and θ_2 correspond to the stiffness multipliers of the symmetric vertical bars 31 and 1. Therefore, the problem becomes ill-posed when only the resonant frequencies are included in the inference, and two potential solutions arise, namely $(\theta_1, \theta_2) = (0.8, 1.0)$ and $(\theta_1, \theta_2) = (1.0, 0.8)$. It is observed in Fig. 5.3 that, indeed, the implemented DRAM algorithm is capable of finding the two solutions, leading to a bimodal PDF. It is evidenced in the Markov chain shown in Fig. 5.3 (a) how the adaptive MCMC algorithm allows exploring the two modes in the distribution, without getting stuck around as usual when implementing standard MCMC methods. Conversely, when both natural frequencies and mode shapes are included in the inference, the identification is well-posed and the resulting PDF becomes unimodal with one single mode at the true solution. In addition, it is observed that the marginal chains of the prediction errors rapidly achieve convergence, reaching low mean values and dispersion as expected given that the model has been used to generate the pseudo-experimental values.

5.3.Surrogate modeling

The primary goal of an SM in the context of St-Id is to provide a computationally light mathematical representation $\widehat{\mathcal{M}}$ of a resource-intensive numerical model of the monitored structure $\mathcal{M}$ (typically a FEM). Once constructed, the SM can be used as a black-box model in the optimization problem previously introduced in Section 5.3. Given the low computational demands of the SM,

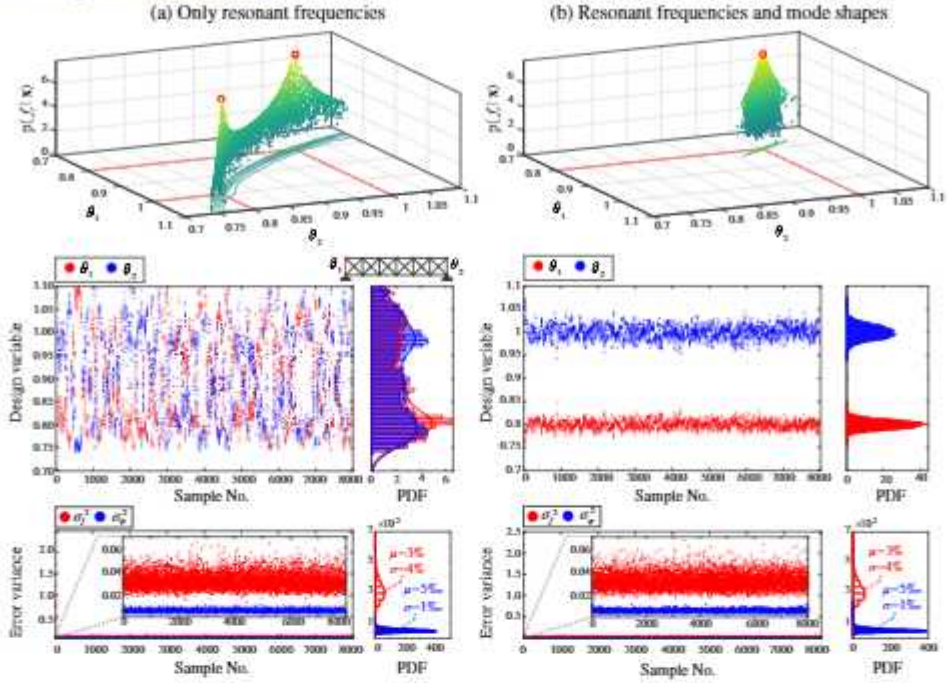

Fig. 5.3: Bayesian inference results of the stiffness multipliers θ_1 and θ_2 of the end verticals of the 31-bar truss structure and error variances considering: (a) resonant frequencies, (b) resonant frequencies and mode shapes. True solution: $(\theta_1, \theta_2) = (0.8, 1.0)$.

the St-Id becomes compatible with long-term SHM, in such a way that the SM can be understood as a DT of the monitoring asset. The construction of an SM generally comprises four consecutive steps as sketched in Fig. 5.4, including: (i) Selection of design variables or "parametrization"; (ii) Sampling of the design space, (iii) Generation of the training population, and (iv) Construction of the SM. The definition of the design space consists in selecting all those parameters and their variation ranges required to parametrize the original FEM. Let us consider m design variables $x_i \in \mathbb{R}, i = 1, \ldots, m$ allowed to vary only within a certain physically meaningful range $[a_i, b_i]$. Accordingly, the vector of design variables $\mathbf{x} = [x_1, \ldots, x_m]^{\mathrm{T}}$ spans the m-dimensional design space $\mathbb{D} = \{\mathbf{x} \in \mathbb{R}^m : a_i \leq x_i \leq b_i\}$. In this light, a SM provides a computationally efficient functional mapping between the selected damage-sensitive parameters $\mathbf{x}$ and the response $y = \mathcal{M}(\mathbf{x}) \in \mathbb{R}$ predicted by the numerical model of the structure, which constitutes the quantity of interest (QoI) in the St-Id. In the case of non-intrusive SMs, it is necessary to assemble a training population of N_s individuals mapping the output y and the design space $\mathbb{D}$, also referred to as the experimental design (ED). This is accomplished by drawing a set of samples uniformly over the input design space $\mathbb{D}$ and building a matrix of

design sites $\mathbf{X} = [\mathbf{x}^1, \ldots, \mathbf{x}^{N_s}] \in \mathbb{R}^{(m \times N_s)}$. Then, the corresponding outputs y^i are obtained by direct Monte Carlo simulations (MCS) using the main FEM and collected in an observation vector $\mathbf{Y} = \left[y^1, \ldots, y^{N_s}\right]^{\mathrm{T}}$. In this thesis, the modal properties extracted from a linear modal analysis of the FEM are assumed as outputs. Therefore, different SMs must be constructed for each natural frequency and modal amplitude of all the vibration modes involved in the analysis. Specifically, if l modes of vibration are selected and n_{DOF} degrees of freedom are used to characterize the mode shapes, a total of $l\,(1 + n_{DOF})$ SMs must be constructed.

In the remainder of this section, the different stages in the construction of a SM are concisely overviewed. Given that structural models in civil engineering are mostly developed through specialized commercial software where access to the core scripts is not granted, all the efforts in this thesis have been devoted to the development of non-intrusive meta-modeling techniques requiring no fundamental modifications in the formulation of the parent numerical model.

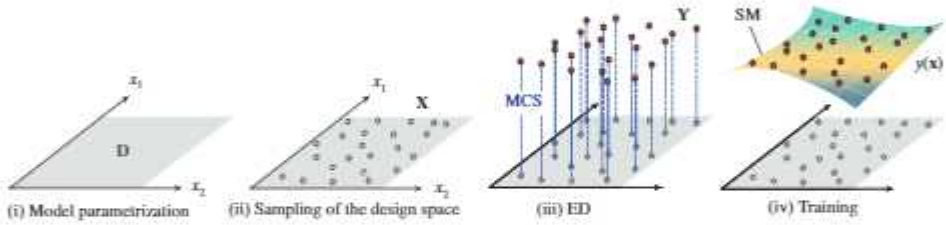

Fig. 5.4: Schematic representation of the construction of a non-intrusive SM.

5.3.1. Model Parametrization

The first step in model updating regards the definition of the model parameters to be updated. In general terms, it is critical to choose those parameters whose perturbation leads to the largest variations in the QoI. Sensitivity analysis constitutes the simplest and most intuitive approach [199], although more sophisticated parametrization methods can be found in the literature such as variance-based global sensitivity analysis [200], sensitivity-based parameter clustering [201], and more. In the context of St-Id for damage identification, the model parametrization becomes a formidable problem. On one hand, it is clear that the regions or members affected by a certain structural pathology are not strictly related to the sensitivity of the QoI obtained from the undamaged configuration of the structure, but the intrinsic characteristics of the associated damage mechanism (e.g. loading configuration, variation of boundary conditions). This implies that, if a classical sensitivity-based parametrization approach is adopted, elements with limited contribution to the sensitivity of the undamaged configuration will be omitted in the St-Id irrespectively of their proneness to be affected by a certain damage mechanism. For instance,

this is the case of the upper floors of buildings or towers, whose contribution to the global modal properties is very limited. As a result, sensitivity-based parametrization approaches will tend to omit these elements from the St-Id, making impossible the damage identification of these areas. On the other hand, the consideration of model parameters with marked differences in sensitivity induces ill-conditioning limitations in the optimization, which may compromise the reliability of the St-Id.

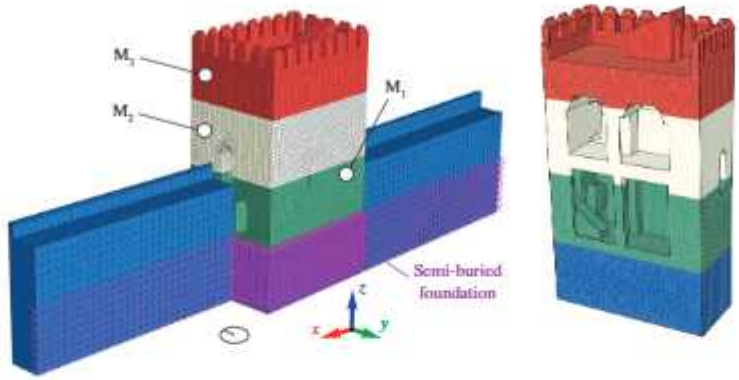

Fig. 5.5: Partitioning of the FEM of the Muhammad Tower.

From the previous discussion, it is clear that the model parametrization for damage identification should be designed according to the expected damage pathology and accommodating the potential appearance of distinct model sensitivities. In this thesis, three different parametrization strategies have been explored: (i) model parametrization according to engineering judgment (ii) sensitivity-based parameter clustering, and (iii) pathology-based parametrization. In the remainder, several application case examples are reported to illustrate these three approaches.

Figure 5.5 shows the 3D FEM of the Muhammad Tower (Section 1.5.6) built in ABAQUS environment [202] and reported in reference [190]. The selection of uncertain model parameters in this sort of massive systems is particularly challenging given that defects do not typically concentrate in a discrete set of structural members but diffusely across the structure. In these cases, a common approach consists in grouping certain parts of the structure forming macro-elements. In this particular case study, a simple parametrization was defined by partitioning the tower into three macro-elements M_l (M_1 in $z \in [0.0, 7.8]$, M_2 in $z \in [7.8, 11.8]$, and M_3 in $z \in [11.8, 15.9]$) as shown in Fig. 5.5. Then, the model parameters to be updated in the St-Id can be defined as stiffness multipliers affecting the elastic moduli of these macro-elements. The aim of such a partitioning was to provide a flexible parametrization capable of identifying a variety of damage pathologies affecting the bending stiffness of

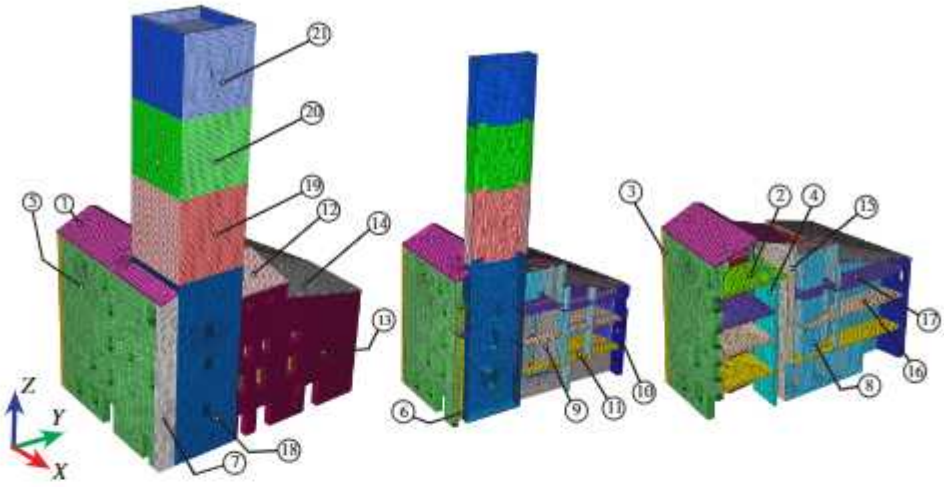

Fig. 5.6: Partitioning of the FEM of the Sciri Tower into 21 macro-elements.

the tower.

A similar parametrization into macro-elements was also defined for the Sciri Tower in references [188, 45, 189]. In this case, the FEM of the tower was first densely divided into a large set of 21 sections as sketched in Fig. 5.6, including ten masonry walls, four floors, three parts of the roof of the building aggregate, and four portions of the tower. The latter was divided into four portions located between heights of 0-18.9 m (18), 18.9-26.8 m (19), 26.8-33.8 m (20), and 33.8-41.0 m (21). In this light, a sensitivity-based clustering approach was adopted to form a reduced set of clusters (macro-elements) of model parameters with similar modal sensitivities. The sensitivities $\overline{S}_{ij}$ were obtained numerically by finite differences using the FEM. In this particular case study, $m = 7$ natural modes were considered with $N_o = 12$ measured DOFs, leading to a sensitivity matrix of dimension 21×91. In this light, the cosine distance can be used to compute the proximity between sensitivities pairs of sensitivities $(\boldsymbol{\alpha}, \boldsymbol{\beta})$ as:

$$\text{cosine distance}\,(\boldsymbol{\alpha}, \boldsymbol{\beta}) = 1 - \frac{\boldsymbol{\alpha}^{\mathrm{T}}\boldsymbol{\beta}}{\boldsymbol{\alpha}^{\mathrm{T}}\boldsymbol{\alpha}\boldsymbol{\beta}^{\mathrm{T}}\boldsymbol{\beta}}. \tag{5.22}$$

Note, however, that the cosine distance as defined in Eq. (5.22) is susceptible to become a skewed metric when combining both frequency and mode shape sensitivities. It is thus necessary to scale the residual sensitivity vectors to accommodate both quantities. Following the work by Bartilson *et al.* [203], a

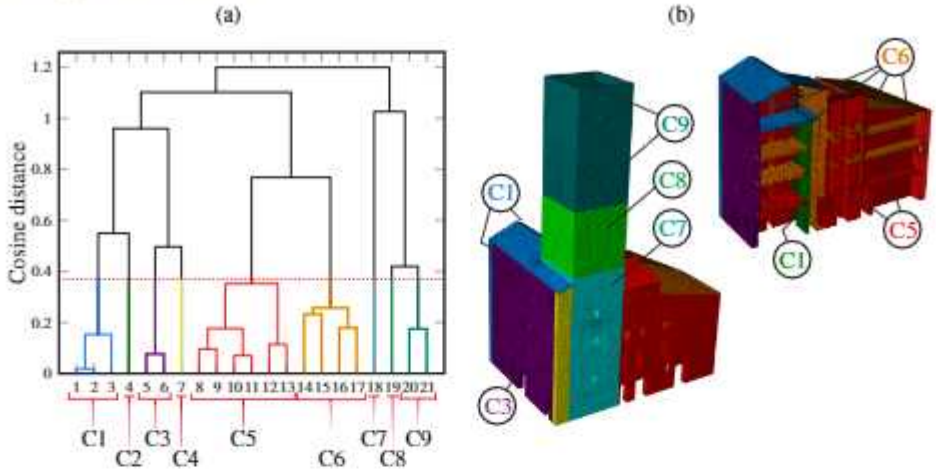

Fig. 5.7: Hierarchical binary tree of sensitivities to the Young's moduli of the 21 sections of the Sciri Tower (a) and resulting macro-element clusters (b).

general scaling rule for $\overline{S}_{ij}$ can be defined as:

$$\overline{S}_j = \begin{bmatrix} \mathbf{W}_f & \mathbf{0} \\ \mathbf{0} & \mathbf{W}_\varphi \end{bmatrix} \begin{bmatrix} r_f/\Delta\theta_j \\ r_\varphi/\Delta\theta_j \end{bmatrix}, \tag{5.23}$$

where r_f and r_φ concentrate the variations in terms of resonant frequencies and mode shapes induced by a perturbation in model parameter θ_j, respectively, and $\mathbf{W}_f$ and $\mathbf{W}_\varphi$ are residual weighting matrices reflecting the relative contribution of resonant frequencies and mode shapes to the sensitivities. As reported in reference [203], $\mathbf{W}_f$ and $\mathbf{W}_\varphi$ can be estimated as the inverse of the measurement covariance matrices of resonant frequencies and mode shapes, respectively. Alternatively, the weighting matrices can be defined in a simplified manner as $\mathbf{W}_f = \alpha\mathbf{I}$ and $\mathbf{W}_\varphi = \beta\mathbf{I}$, with parameters α and β standing for trade-off parameters weighing the relevance of the contribution of resonant frequencies and mode shapes to the sensitivity matrix, respectively. On this basis, an hierarchical clustering approach with the Unweighed Pair Group Method with Arithmetic Mean (UPGMA) [204] as the linkage method was applied to the 21-parameters FEM of the Sciri Tower. With the aim of keeping at least three macro-elements between partitions 18 to 21 in Fig. 5.6 to discretize the tower, a β/α ratio of 12 was found suitable after some manual tuning. The resulting hierarchical binary tree is shown in Fig. 5.7 (a). The tree was cut at a distance of 0.39, forming 9 clusters labeled with C1 to C9. The corresponding macro-elements are depicted in Fig. 5.7 (b). Note that the resulting discretization of the tower only includes three macro-elements, merging the previously defined top two elements (20,21) in Fig. 5.6 into C9. The resulting sensitivities grouped by macro-elements C1 to C9 are presented as 3-D bar plots in Figs. 5.8

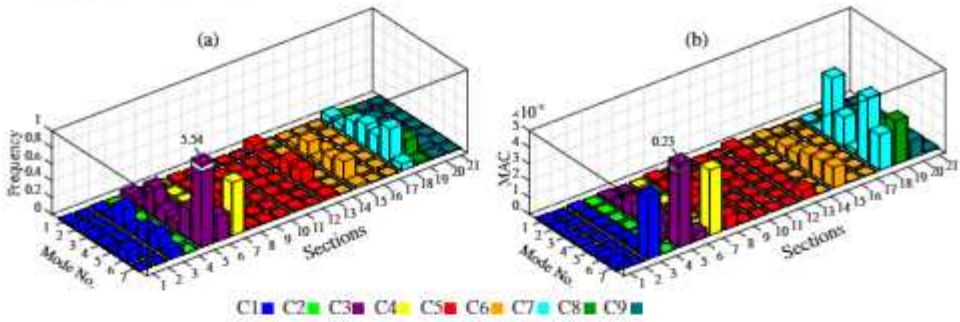

Fig. 5.8: Frequency (a) and mode shape sensitivities (b) of the 21 sections of the Sciri Tower organized into 9 macro-elements (The cosine distance utilized the complete set of mode shape sensitivities (5 modes with 12 DOFs per mode), but the results in (b) are represented by MAC sensitivities for clarity.)

(a) and (b) in terms of resonant frequencies and mode shapes, respectively.

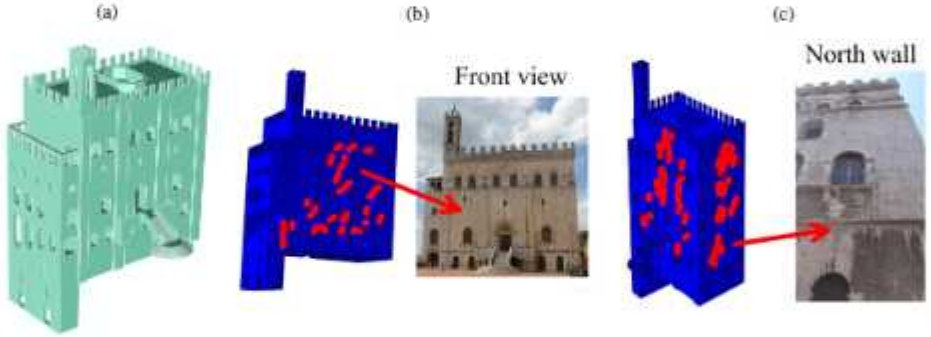

Fig. 5.9: FEM of the Consoli Palace (a) and model parametrization obtained from pushover analysis along the E-W (b) and N-S directions (c).

Finally, Fig. 5.9 illustrates the pathology-based parametrization designed for the Consoli Palace in reference [193]. With the aim of identifying sets of elements potentially affected by the seismic sequence occurred on May 15th 2021 (Section 1.5.5), non-linear pushover analyses along the two main directions of the building were conducted. The non-linear behavior of masonry was modeled using the classic Concrete Damage Plasticity (CDP) constitutive model [202] has been used. This approach, proposed by Lubliner *et al.* [205] and then modified by Lee and Fenves [206], is well-suited for the modeling of brittle masonry under cyclic loading considering cracking in tension and crushing in compression. This approach allows to determine damage-prone regions as those elements experiencing damage-induced stiffness degradation. In this case study, the non-linear analyses allowed us to determine two damage-prone regions as shown in Figs. 5.9 (b) and (c) representing the crack patterns resulting from pushover analyses along the E-W and N-S directions, respectively. Interest-

ingly, some of the identified crack patterns coincide with some cracks already existing in the palace, indicating that some of the damaging mechanisms are already activated. For instance, the parametrization in Fig. 5.9 (b) coincides with the existing crack pattern along the North wall and the internal horizontal vaults. In this light, model parameters can be set up as stiffness multiplier of the identified damage-prone elements.

5.3.2. Experimental Design

As anticipated above, non-intrusive SMs are trained by exploiting a set of realizations of parameters of interest of the model, called the ED, and the corresponding model evaluations, also called QoI. Therefore, the accuracy of such models is highly determined by the dimensions of the design space and the number and distribution of the training samples in the ED [207]. In engineering practice, obtaining the ED constitutes the most time-consuming part since it requires the evaluation of the computationally intensive forward model at each sample point. Choosing high-quality EDs is thus critical to achieve high accuracy in the SM construction with the least possible number of training samples. Sampling approaches can generally be divided into static (one-shot) and sequential methods. One-shot sampling generates the training sample points in one single step, and common approaches include fractional designs and orthogonal arrays [208]. While these techniques offer easy implementation and minimal computational cost, the determination of the optimal sample size may be troublesome when the behavior of the forward model is unknown. To minimize such difficulties, a number of sequential sampling strategies have been introduced, including adaptive and space-filling sequential methods [209]. On one hand, space-filling sequential designs such as Latin Hypercube Sampling (LHS), Sobol, Hammersley and Halton sampling [210] generate samples iteratively to attain good coverage of the parametric domain. On the other hand, adaptive sampling techniques iteratively draw new samples in regions of the parametric space with large prediction errors, enabling to account for local refinements in the ED (refer to references [211, 209] for a thorough state-of-the-art review).

In this thesis, LHS and Sobol sampling techniques have been implemented with excellent results in all the investigated case studies. To define the size of the ED, convergence analyses are conducted over a set of training data-sets with increasing number of samples. Let us illustrate this with the parametrization of the FEM of the Sciri Tower reported in reference [188] as shown in Fig. 5.10 (a). In this case, similarly two the parametrization previously shown in Fig. 5.6, the FEM of the tower was partitioned into four macro-elements M_i, $i = 1, \ldots, 4$. Then, the model parameters were defined as stiffness coefficients k_i, $i = 1, ..., 4$ affecting the elastic moduli of macro-elements M_i. Note in this case that, unlike the parametrization in Fig. 5.6, stiffness multiplier k_1 affects simultaneously the base of the tower and the building aggregate. On this basis, the upper/lower limits of k_i were set to $\pm 15\%$, in such a way that the design space $\mathbb{D}$ takes the

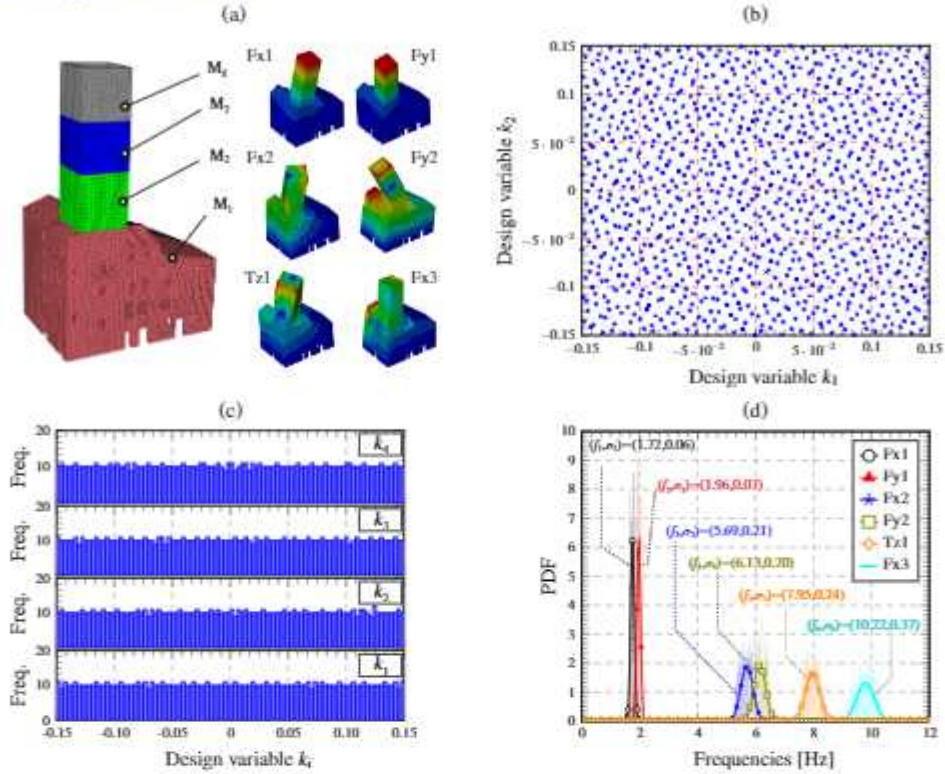

Fig. 5.10: (a) Partitioning of the FEM of the Sciri Tower and first six mode shapes. (b) Sampled data points of the design variables k_1 and k_2. (c) Histograms of the data samples k_i, $i = 1, ..., 4$. (d) Probability density functions (PDF) and Gaussian approximations of the first six natural frequencies (reference population of 1024 samples).

form:

$$\mathbb{D} = \left\{ \mathbf{x} \in \mathbb{R}^4 : -0.15 \leq k_i \leq 0.15 \right\}. \tag{5.24}$$

Then, random samples must be uniformly drawn over $\mathbb{D}$ to train the SM. Note that the proper size of the ED is not known beforehand since it is highly dependent on the smoothness of the investigated QoI and the variation range of the model parameters. Therefore, to select the size of the ED, convergence analyses with increasing EDs ought to be conducted assessing the accuracy of the corresponding SMs through certain quality metrics over a validation set (VS). In this particular case study, four different sample sizes were selected, including $N = 64$, 128, 256, and 512, as well as a VS of 1024 individuals. In practical terms, this implies the evaluation of the FEM for all the individuals of the considered populations, representing the most time-consuming stage of the process. Once obtained, convergence analyses should cover the stability of the QoI as well as the accuracy of the SMs constructed from each of the

considered EDs. Figures 5.10 (b) and (c) present the sampled data points by the quasi-random sequence of Sobol of the design variables k_1 and k_2 and the histograms of the data samples k_i for the VS, respectively. In all the cases, the histograms are almost flat, which proves the uniformity of the data sampling. On this basis, the first six natural frequencies and mode shapes were obtained for all the training population sizes by the FEM of the Sciri Tower. Figure 5.10 (c) depicts the PDF of the target natural frequencies for the VS.

Once the training populations are obtained, the accuracy of the corresponding SMs can be assessed by using the error metrics like those collected in Table 5.1. In this table, $\bar{\boldsymbol{y}}$ and $\sigma_{\boldsymbol{y}} = \sqrt{\left(\sum_{i=1}^{K}\left(\bar{\boldsymbol{y}} - y^{(i)}\right)^2\right)/(K-1)}$ denote the arithmetic mean and the quasi standard deviation of $\boldsymbol{\Upsilon}$, respectively. Term $\sigma_{\boldsymbol{y}\hat{\boldsymbol{y}}}$ represents the covariance of $(\boldsymbol{y}, \hat{\boldsymbol{y}})$, and $\sigma_{\boldsymbol{y}}^2$ and $\sigma_{\hat{\boldsymbol{y}}}^2$ indicate the variance of $\boldsymbol{y}$ and $\hat{\boldsymbol{y}}$, respectively. A special error metric $J_{MAC,r}$ in terms of mode shapes is also reported in Table 5.1.

Table 5.1: Error metrics for the accuracy assessment of surrogate models over a validation set (VS) of size N (Hatted terms denote the predictions of the SM).

Mean-squared error (MSE)	Mean absolute error (MAE)
$MSE = \sum_{i=1}^{N}\left(\hat{y}^{(i)} - y^{(i)}\right)^2 \Big/ \sum_{i=1}^{N}\left(\bar{y} - y^{(i)}\right)^2$	$MAE = (N\sigma_y)^{-1}\sum_{i=1}^{N}\left\lvert\hat{y}^{(i)} - y^{(i)}\right\rvert$
Coefficient of Determination (R^2)	**Maximum absolute error (MAE)**
$R^2 = \sigma_{y\hat{y}}^2\left(\sigma_y^2\sigma_{\hat{y}}^2\right)^{-1}$	$MAE = (N\sigma_y)^{-1}\max_{i=1}^{N}\left\lvert\hat{y}^{(i)} - y^{(i)}\right\rvert$
Mode shape errors	
$J_{MAC,r} = \mathrm{med}\left[1 - MAC\left(\varphi_r, \hat{\varphi}_r\right)\right]$	

The convergence analyses reported in reference [188] showed that a Kriging SM trained with 512 individuals represented a conservatively accurate solution to bypass the 3D FEM of the Sciri Tower. Scatter plots such as those reported in Fig. 5.11 (a) plotting the predictions of the SM versus the estimates of the forward model constitute a common tool to summarize the quality of the SM. It is noted in this figure how the low scatter of the data points around the diagonal line corroborates that the SM was formed with accuracy, with coefficients of determination R^2 very close to 1. In order to illustrate the importance of conducting the aforementioned convergence analyses, Fig. 5.11 (b) shows the scatter plot of a Kriging SM trained with 512 individuals but for a larger variation range in the design parameters of $\pm 100\%$. In this case, the notable scatter around the diagonal line indicates the existence of considerable discrepancies between the models, indicating the need for accounting for a denser ED.

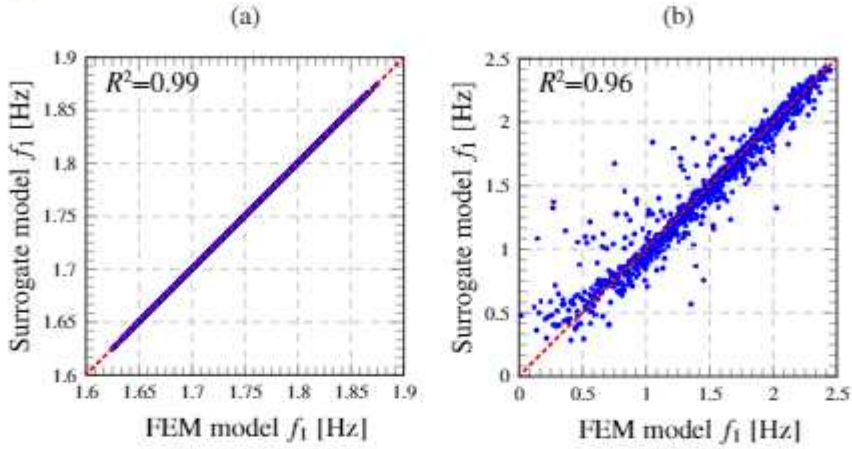

Fig. 5.11: Scatter plot of Kriging SMs with respect to the 3D FEM of the Sciri Tower for the first natural frequency (f_1) (training population of 512 samples and reference population of 1024 samples).

5.3.3. Non-intrusive meta-modeling techniques

In this section, the theoretical formulation of the non-intrusive meta-modeling techniques adopted throughout the course of the thesis is concisely overviewed, namely RSM, Kriging and PCE.

Response Surface Methods

The RSM is a collection of statistical techniques used for fitting empirical models and so reduce the computational effort in iterative processes [212]. In the context of vibration-based SHM, RMS models can be understood as Taylor expansions of the modal predictions of the FEM with respect to the selected modal parameters. For instance, a second-order quadratic RSM is given by [213]:

$$y(\mathbf{x}) = \alpha_0 + \sum_{j=1}^{m} \alpha_j x_j + \sum_{j=1}^{m} \alpha_{jj} x_j^2 + \sum_{j=1}^{m} \sum_{i \geq j}^{m} \alpha_{ji} x_j x_i + \epsilon, \tag{5.25}$$

with coefficients α_0, α_j, α_{jj} and α_{ji} being the intercept, linear, quadratic, and interaction coefficients, respectively. The term ϵ accounts for all those variability sources not included in the fitting, such as measurement error in the response, background noise, non-considered variables, etc. The model in terms of the observations included in the training population of N individuals can be written in matrix notation as:

$$\mathbf{Y} = \hat{\mathbf{X}}\mathbf{A} + \boldsymbol{\epsilon}, \tag{5.26}$$

where $\hat{\mathbf{X}}$ is a $N \times (m+1)(m+2)/2$ matrix collecting components $[1, x_j, x_j^2, x_j x_i]$ for each individual in the training population, $\mathbf{A}$ is the $(m+1)(m+2)/2$ vector of coefficients α_0, α_j, α_{jj} and α_{ji}, and ϵ is a $(m+1)(m+2)/2$ vector of random errors. The meta-model is thus determined when the coefficients vector $\mathbf{A}$ is known. Assuming ϵ as a normally distributed zero mean error, the coefficients vector $\mathbf{A}$ can be obtained by its least squares estimator as [214]:

$$\mathbf{A} = \left(\hat{\mathbf{X}}^{\mathrm{T}}\hat{\mathbf{X}}\right)^{-1}\hat{\mathbf{X}}^{\mathrm{T}}\mathbf{Y}, \tag{5.27}$$

and the corresponding model predictions read:

$$\hat{\mathcal{M}}(\mathbf{X}) = \hat{\mathbf{X}}\mathbf{A}. \tag{5.28}$$

Kriging model

The Kriging model, with origin in Geostatistics [215], is a commonly used technique of interpolation for spatial data. The The universal Kriging model approximates the response of a computational model as a realization of a Gaussian random process as [216]:

$$\hat{\mathcal{M}}(\mathbf{x}) = \mathcal{F}(\mathbf{x}) + \mathcal{Z}(\mathbf{x}), \tag{5.29}$$

where $\mathcal{F}(\mathbf{x})$ is a regression model, also called trend, and $\mathcal{Z}(\mathbf{x})$ is a zero-mean stochastic process. The latter is fully determined by its covariance function:

$$\mathrm{Cov}\left(\mathcal{Z}(\mathbf{x}), \mathcal{Z}(\mathbf{x}')\right) = \mathbb{E}\left[\mathcal{Z}(\mathbf{x})\mathcal{Z}(\mathbf{x}')\right] = \sigma^2 R\left(\left|\mathbf{x}-\mathbf{x}'\right|;\boldsymbol{\theta}\right), \tag{5.30}$$

with σ^2 being the Gaussian process variance, and $R\left(\left|\mathbf{x}-\mathbf{x}'\right|;\boldsymbol{\theta}\right)$ an auto-correlation function between two arbitrary input sample points $\mathbf{x}$ and $\mathbf{x}'$ and dependent upon certain hyper-parameters $\boldsymbol{\theta}$. The trend term of the universal Kriging model in Eq. (5.29) approximates the global behavior of $\mathcal{M}$, while the local variability is captured by the stochastic term. The trend term is commonly defined as a linear combination of $\psi(\mathbf{x})$ functions as:

$$\hat{\mathcal{M}}(\mathbf{x}) = \mathbf{a}^{\mathrm{T}}\psi(\mathbf{x}) + \mathcal{Z}(\mathbf{x}). \tag{5.31}$$

with $\mathbf{a}^{\mathrm{T}}$ standing for linear combination coefficients. Common $\psi(\mathbf{x})$ include constant, linear and quadratic polynomials (see [217]). On this basis, the construction of the Kriging meta-model in Eq. (5.31) consists in the determination of the coefficients of the PC expansion, $\mathbf{a}$, the process variance, σ^2, and the hyper-parameters of the auto-correlation function, $\boldsymbol{\theta}$. Common choices for the auto-correlation function include exponential, Gaussian, linear, spherical, cubic and cubic spline functions [217]. Gaussian auto-correlation functions have been considered in all the works of this thesis as one of the most commonly

adopted. These functions can be defined as the product of one-dimensional Gaussian correlations in the form [218]:

$$R\left(\mathbf{x}_i, \mathbf{x}_j, \boldsymbol{\theta}\right) = \prod_{k=1}^{M} \exp\left[-\theta_k \left(x_i^{(k)} - x_j^{(k)}\right)^2\right]. \tag{5.32}$$

Hyper-parameters θ_k in Eq. (5.32) determine the shape of the correlation function, with larger values of θ_k leading to faster decreases along the k-th dimension of input vector $\mathbf{x}$. This definition allows one to accommodate anisotropic auto-correlations (i.e. different correlations in different directions). Nevertheless, for the sake of simplicity, in this thesis correlations have been assumed isotropic with equal hyper-parameters θ_k across the dimensions of x, i.e. $\theta_k = \theta \quad \forall 1 \leq k \leq M$.

Given the values of the auto-correlation hyper-parameters $\hat{\boldsymbol{\theta}}$, the calibration of the trend model parameters $\left\{\mathbf{a}\left(\hat{\boldsymbol{\theta}}\right), \sigma^2\left(\hat{\boldsymbol{\theta}}\right)\right\}$ may be computed using an empirical best linear unbiased estimator (BLUE). The optimization yields analytical solutions as functions of $\hat{\boldsymbol{\theta}}$ [216]:

$$\mathbf{a}\left(\hat{\boldsymbol{\theta}}\right) = \left(\mathbf{F}^{\mathrm{T}}\mathbf{R}^{-1}\mathbf{F}\right)^{-1}\mathbf{F}\mathbf{R}^{-1}\mathbf{Y}, \tag{5.33}$$

$$\sigma^2\left(\hat{\boldsymbol{\theta}}\right) = \frac{1}{N}\left(\mathbf{Y} - \mathbf{F}\mathbf{a}\right)^{\mathrm{T}}\mathbf{R}^{-1}\left(\mathbf{Y} - \mathbf{F}\mathbf{a}\right), \tag{5.34}$$

where $\mathbf{R}_{ij} = R\left(\left|\mathbf{x}^{(i)} - \mathbf{x}^{(i)}\right|; \hat{\boldsymbol{\theta}}\right)$ and $\mathbf{F}_{ij} = \psi_j\left(\mathbf{x}^{(i)}\right)$ are the autocorrelation and the information matrices, respectively, evaluated at all the samples of the ED.

The optimal correlation parameters $\hat{\boldsymbol{\theta}}$ are typically determined by either the maximum-likelihood-estimated (labeled with ML) or by the leave-one-out cross validation (labeled with CV) [219], which lead to the following minimization problems:

$$\hat{\boldsymbol{\theta}}_{ML} = \arg\min_{\boldsymbol{\theta}}\left[\frac{1}{N}\left(\mathbf{Y} - \mathbf{F}\mathbf{a}\right)^{\mathrm{T}}\mathbf{R}^{-1}\left(\mathbf{Y} - \mathbf{F}\mathbf{a}\right)\left(\det\mathbf{R}\right)^{1/N}\right], \tag{5.35}$$

$$\hat{\boldsymbol{\theta}}_{CV} = \arg\min_{\boldsymbol{\theta}}\left[\mathbf{Y}^{\mathrm{T}}\mathbf{R}^{-1}\mathrm{diag}\left(\mathbf{R}^{-1}\right)^{-2}\mathbf{R}^{-1}\mathbf{Y}\right]. \tag{5.36}$$

Determining the optimal correlation parameters in Eqs. (5.35) and (5.36) is a complex multi-dimensional minimization problem. This problem is commonly solved through gradient-based iterative techniques such as the pattern search optimization algorithm proposed by Lophaven and co-authors [217]. Nevertheless, given that the optimization problem is usually non-convex, such an

approach may get stuck at local minima. In order to prevent the solution from depending upon initial guesses on the hyper-parameters, global optimization approaches such as genetic algorithms offer more robust solutions.

Once the optimal model parameters are determined, the prediction of a new point $\mathbf{x}$ is given by a Gaussian random variable with mean $\mu(\mathbf{x})$ and variance $\sigma^2(\mathbf{x})$:

$$\hat{\mathcal{M}}(\mathbf{x}) = \mu(\mathbf{x}) = \mathbf{a}^{\mathrm{T}}\boldsymbol{\psi}(\mathbf{x}) + \mathbf{r}(\mathbf{x})^{\mathrm{T}}\mathbf{R}^{-1}(\mathbf{Y} - \mathbf{F}\mathbf{a}), \tag{5.37}$$

$$\sigma^2(\mathbf{x}) = \sigma^2\left(1 - \left\langle \boldsymbol{\psi}(\mathbf{x})^{\mathrm{T}}\mathbf{r}(\mathbf{x})^{\mathrm{T}} \right\rangle \begin{bmatrix} \mathbf{0} & \mathbf{F}^{\mathrm{T}} \\ \mathbf{F} & \mathbf{R} \end{bmatrix} \begin{bmatrix} \boldsymbol{\psi}(\mathbf{x}) \\ \mathbf{r}(\mathbf{x}) \end{bmatrix}\right), \tag{5.38}$$

where $r_i(\mathbf{x}) = R\left(\left|\mathbf{x} - \mathbf{x}^{(i)}\right|; \boldsymbol{\theta}\right)$ is the correlation between the new sample $\mathbf{x}$ and the sample $\mathbf{x}^{(i)}$ of the ED. The prediction error mean is used as the surrogate to the original model $\mathcal{M}$, whereas the variance gives a local error indicator about the precision. It is important to note that the Kriging model perfectly interpolates the data of the ED, i. e. $\hat{\mathcal{M}}(\mathbf{x}^{(i)}) = \mathcal{M}(\mathbf{x}^{(i)}), \forall \mathbf{x}^{(i)} \in \mathbf{X}$.

Polynomial Chaos Expansion

Polynomial Chaos Expansion methods assume the components of $\mathbf{x}$ as independent random variables and the represent the output response as an expansion of y onto an orthogonal multivariate polynomial basis as [220, 219]:

$$y = \mathcal{M}(\mathbf{x}) = \sum_{\boldsymbol{\alpha} \in \mathbb{N}^M} a_{\boldsymbol{\alpha}} \psi_{\boldsymbol{\alpha}}(\mathbf{x}), \tag{5.39}$$

where $a_{\boldsymbol{\alpha}}$ are unknown deterministic coefficients, and $\psi_{\boldsymbol{\alpha}}$ are multivariate polynomials. Given the statistical independence of the input random variables, the input joint PDF may be cast as:

$$f_{\mathbf{X}}(\mathbf{x}) = \prod_{i=1}^{M} f_{X_i}(x_i), \tag{5.40}$$

where $f_{X_i}(x_i)$ denotes the marginal PDF of x_i. A family of univariate polynomials $\left\{\psi_j^{(i)}, j \in \mathbb{N}\right\}$ orthogonal with respect to f_{X_i} is adopted, that is:

$$\mathbb{E}\left[\psi_j^{(i)}(x_i)\,\psi_k^{(i)}(x_i)\right] = \int \psi_j^{(i)}(u)\,\psi_k^{(i)}(u) f_{X_i}(u)\,\mathrm{d}u = \delta_{jk}, \tag{5.41}$$

with δ_{jk} being the Kronecker delta operator. A variety of families of orthogonal polynomials have been proposed in the literature (see e.g. [221]), being the Legendre and Hermite polynomials the most commonly used ones for uniformly and normally distributed input variables x_i, respectively. Based upon

the resulting M families of univariate polynomials, the basis of multivariate polynomials $\left\{\psi_{\boldsymbol{\alpha}},\, \boldsymbol{\alpha} \in \mathbb{N}^M\right\}$ is defined as:

$$\psi_{\boldsymbol{\alpha}}(\mathbf{x}) = \prod_{i=1}^{M} \psi_{\alpha_i}^{(i)}(x_i), \tag{5.42}$$

where the multidimensional index notation $\boldsymbol{\alpha} = [\alpha_1, \ldots, \alpha_M]$ has been adopted. Such a construction guarantees the orthogonality property of the multivariate polynomials, i.e. $\mathbb{E}\left[\psi_{\boldsymbol{\alpha}}(\mathbf{x})\, \psi_{\boldsymbol{\beta}}(\mathbf{x})\right] = \delta_{\boldsymbol{\alpha}\boldsymbol{\beta}}$. In computational applications, the PC expansion in Eq. (5.39) must be truncated after P terms. A classical approach consists in retaining all those polynomials $\psi_{\boldsymbol{\alpha}}$ with total degree up to p, that is $0 \leq |\boldsymbol{\alpha}| \leq p$, with $|\boldsymbol{\alpha}| = \sum_{i=1}^{M} \alpha_i$. On this basis, the truncated PCE can be written in matrix form as:

$$\mathcal{M}_p(\mathbf{x}) = \sum_{0 \leq |\boldsymbol{\alpha}| \leq p} a_{\boldsymbol{\alpha}} \psi_{\boldsymbol{\alpha}}(\mathbf{x}) = \mathbf{a}^{\mathrm{T}} \boldsymbol{\psi}(\mathbf{x}), \tag{5.43}$$

where $\mathbf{a}$ and $\boldsymbol{\psi}$ are vectors containing the coefficients $\left\{a_{\boldsymbol{\alpha}}, 0 \leq |\boldsymbol{\alpha}| \leq p\right\}$ and the corresponding basis polynomials $\left\{\psi_{\boldsymbol{\alpha}}, 0 \leq |\boldsymbol{\alpha}| \leq p\right\}$. The PC coefficients can be estimated by least squares regression. To do so, a set of N realizations $\mathbf{X} = \left[\mathbf{x}^{(1)}, \ldots, \mathbf{x}^{(N)}\right]$ of the input random variables are selected in order to cover the design space, also referred to as the experimental design (ED) or training dataset. Accordingly, a set of model realizations/evaluations $\mathbf{Y} = \left[y^{(1)}, \ldots, y^{(N)}\right]^{\mathrm{T}}$ is obtained by Monte Carlo simulations (MCS) of the forward model, i.e. $y^{(i)} = \mathcal{M}\left(\mathbf{x}^{(i)}\right)$. Then, the least squares estimate of $\mathbf{a}$ reads:

$$\hat{\mathbf{a}} = \left(\boldsymbol{\Psi}^{\mathrm{T}} \boldsymbol{\Psi}\right)^{-1} \boldsymbol{\Psi}^{\mathrm{T}} \mathbf{Y}, \tag{5.44}$$

where the components of the data matrix $\boldsymbol{\Psi}$ are defined as $\boldsymbol{\Psi}_{ij} = \psi_{\boldsymbol{\alpha}_j}\left(\mathbf{x}^{(i)}\right), i = 1, \ldots, N, j = 0, \ldots, P-1$. The truncation scheme in Eq. (5.43) leads to a total number of terms in the expansion $\mathcal{A}^{M,p} = \left\{\boldsymbol{\alpha} \in \mathbb{N}^M : 0 \leq |\boldsymbol{\alpha}| \leq p\right\}$:

$$\mathrm{card}\mathcal{A}^{M,p} = \binom{M+p}{p} = \frac{(M+p)!}{M!p!}. \tag{5.45}$$

In general, any truncation scheme corresponds to a specific choice of a non empty finite set $\mathcal{A}$ of indices $\boldsymbol{\alpha}$. On this basis, it is possible to use the ED to estimate the coefficients of the associated PCE by least squares fitting following Eq. (5.44), leading to:

$$\hat{\mathcal{M}}_{\mathcal{A}} = \sum_{\boldsymbol{\alpha} \in \mathcal{A}} \hat{a}_{\boldsymbol{\alpha}} \psi_{\boldsymbol{\alpha}}(\mathbf{x}) = \hat{\mathbf{a}}^{\mathrm{T}} \boldsymbol{\psi}(\mathbf{x}). \tag{5.46}$$

The quality of the fitted PCE can be assessed through several error measurements. A common error quantity is the empirical generalization error E_{rr} defined as the mean squared value of the residuals, that is the differences between the model evaluations and the predicted values by the fitted PCE:

$$E_{rr} = \frac{1}{N}\sum_{i=1}^{N}\left[\mathcal{M}(\mathbf{x}) - \hat{\mathcal{M}}_{\mathcal{A}}(\mathbf{x}^{(i)})\right]^2. \tag{5.47}$$

A key limitation of E_{rr} in Eq. (5.47) regards its sensitivity to overfitting, which typically leads to underestimates of the generalization error. Indeed, it is clear that E_{rr} systematically decreases as the complexity of the PC expansion in Eq. (5.43) increases. A better metric for cross-validation applications with less sensitivity to overfitting is the so-called leave-one-out error Err_{LOO} [222]. Let us denote by $\hat{\mathcal{M}}_{\mathcal{A}}^{(-i)}$ the meta-model that has been built from the ED but removing the i-th observation. Then, the predicted residual is defined as the difference between the model evaluation at $\mathbf{x}^{(i)}$ and its prediction by $\hat{\mathcal{M}}_{\mathcal{A}}^{(-i)}$:

$$\Delta^{(i)} = \mathcal{M}(\mathbf{x}^{(i)}) - \hat{\mathcal{M}}_{\mathcal{A}}^{(-i)}(\mathbf{x}^{(i)}), \tag{5.48}$$

and the leave-one-out error is estimated as:

$$Err_{LOO} = \frac{1}{N}\sum_{i=1}^{N}\left(\Delta^{(i)}\right)^2. \tag{5.49}$$

The definition in Eq. (5.49) involves multiple PCE fittings and model evaluations, although within the context of linearly parametrized regression, it is possible to calculate Err_{LOO} analytically [223]:

$$Err_{LOO} = \frac{1}{N}\sum_{i=1}^{N}\left(\frac{\mathcal{M}(x^{(i)}) - \hat{\mathcal{M}}_{\mathcal{A}}(x^{(i)})}{1-h_i}\right)^2, \tag{5.50}$$

where

$$h_i = \psi_{A^{(k)}}\left(\psi_{A^{(k)}}^{\mathrm{T}}\psi_{A^{(k)}}\right)^{-1}\psi_{A^{(k)}}^{\mathrm{T}}. \tag{5.51}$$

The computational cost involved in the fitting of the PCE using the truncation scheme in Eq. (5.43) may be very high if the number of input variables M or the polynomial degree p are considerably large. Note that, as a rule of thumb, the number of realizations in the ED to uniformly cover the input design space is usually defined as two or three times the cardinality of the expansion, i.e. $\mathrm{card}\mathcal{A}^{M,p}$. An alternative hyperbolic truncation scheme was

proposed by Blatman and Sudret [222] to alleviate the computational cost in the PCE. Those authors defined a q-norm, $0 < q < 1$, as:

$$\|\boldsymbol{\alpha}\|_q = \left(\sum_{i=1}^{M} \alpha_i^q \right)^{1/q}, \tag{5.52}$$

in such a way that a truncated PCE can be obtained by selecting a finite set of indices $\boldsymbol{\alpha}$ with q-norm less than or equal to p:

$$\mathcal{A}^{M,p,q} = \left\{ \boldsymbol{\alpha} \in \mathbb{N}^M : \|\alpha\|_q \leq p \right\}. \tag{5.53}$$

The previous approach reduces the number of terms in the PCE by penalizing high-rank indices and favouring low-order interactions. Nonetheless, the resulting expansion may remain too costly when large-dimensional and highly non-linear problems are to be addressed. In such cases, it is often found that the non-zero coefficients in the expansion form a sparse subset of $\mathcal{A}^{M,p,q}$. This motivates the use of sparse linear regression methods to further reduce the number of basis polynomials $\psi_{\boldsymbol{\alpha}}$ in the expansion. In particular, the LAR algorithm previously presented to conduct sparse MLR in Section 2.4.3 can be used to this aim. In the context of PCE, LAR provides a collection of PC expansions incorporating an increasing number of basis polynomials, from 1 to $P = \text{card}\mathcal{A}^{M,p,q}$. The resulting sequence of index sets $\mathcal{A}^{(k)}$, $k = 0, \ldots, \min(P, N-1)$, is used to construct different PC expansions $\mathcal{M}_{\mathcal{A}^{(k)}}$ and, finally, a cross validation procedure is implemented for selecting the best meta-model. The definition of the optimum PCE using the LAR algorithm involves the following steps [222]:

1. Run the LAR procedure for given degree p and norm q.
   (a) Initialize to zero the polynomial coefficients, i.e. $a_{\boldsymbol{\alpha}0}, \ldots, a_{\boldsymbol{\alpha}p-1} = 0$. Set the initial residual equal to the vector of observations $\mathbf{Y}$.
   (b) Find the vector $\boldsymbol{\psi}_{\boldsymbol{\alpha}j}$, which is most correlated with the current residual.
   (c) Move $a_{\boldsymbol{\alpha}j}$ from 0 towards the least-square coefficient of the current residual on $\boldsymbol{\psi}_{\boldsymbol{\alpha}j}$, until some other predictor $\boldsymbol{\psi}_{\boldsymbol{\alpha}k}$ has as much correlation with the current residual. Such a move corresponds to the approximation of the active coefficients towards their least-square value, that is $\hat{\mathbf{a}}^{(k+1)} = \hat{\mathbf{a}}^{(k)} + \gamma^{(k)}\tilde{\mathbf{w}}^{(k)}$. Vector $\tilde{\mathbf{w}}^{(k)}$ and coefficient $\gamma^{(k)}$ are referred to as the LAR descent direction and step, respectively. Both quantities may be derived algebraically as shown in [74].
   (d) Continue the procedure until $m = \min(P, N-1)$ basis polynomials have been entered.

2. Recompute the coefficients of each produced sparse meta-model by least-squares regression.

3. Estimate the leave-one-out-error Err_{LOO} in Eq. (5.50) associated to each meta-model and retain the one with the lowest error estimate.

Note the LAR algorithm is very efficient since it only requires $\mathcal{O}\left(NP^2 + P^3\right)$ computations (i.e. the computational cost of ordinary least-square regression on P predictors) for producing a set of m meta-models. Additionally, in order to select the optimal degree p, the previous LAR approach can be performed for a series of potential degree values within certain interval $p \in [p_{min}, p_{max}]$. After every step in the analysis, the best PC expansion is stored and certain error/quality measurement is computed. Once complete, the optimal PC expansion is chosen as the meta-model with the minimum error/quality measurement. As the quality measurement, a corrected error estimate of the leave-one-out error in Eq. (5.50) accounting for the number of terms in the PC approximation P and the number of realizations in the ED N is used in this work as:

$$Err^{*}_{LOO} = Err_{LOO}\, T(P, N), \tag{5.54}$$

with $T(P, N)$ a correcting factor derived in [224] as:

$$T(P, N) = \frac{N}{N - P}\left[1 + \frac{\mathrm{tr}\left(\mathbf{C}^{-1}_{emp}\right)}{N}\right], \tag{5.55}$$

where

$$\mathbf{C}_{emp} = \frac{1}{N}\mathbf{\Psi}^{\mathrm{T}}\mathbf{\Psi}. \tag{5.56}$$

An extension of this SM was reported in reference [189] combining PCE with Kriging modeling. Given the general Kriging expansion in Eq. (5.29), the trend term can be readily defined the truncated PC expansion using the LAR procedure as:

$$\hat{\mathcal{M}}(\mathbf{x}) = \sum_{\boldsymbol{\alpha}\in\mathcal{A}} \hat{a}_{\boldsymbol{\alpha}}\psi_{\boldsymbol{\alpha}}(\mathbf{x}) + \mathcal{Z}(\mathbf{x}) = \mathbf{a}^{\mathrm{T}}\boldsymbol{\psi}(\mathbf{x}) + \mathcal{Z}(\mathbf{x}). \tag{5.57}$$

As reported in reference [189], the combination of these two techniques provide the resulting SM with both local and global modeling capabilities. On one hand, the PCE handles the global behavior of the model, while, on the other hand, Kriging can accurately reproduce local variations.

5.4.Synthetic damage scenarios through non-linear simulations

Given the circumstance that experimental data from civil engineering structures experiencing damage are not usually available, it is convenient to generate realistic synthetic damage scenarios to appraise the effectiveness of SM-based St-Id approaches. In this thesis, a systematic three-step approach has been adopted. Firstly, the structure is subjected to gravity loading and a loading condition inducing damage (e.g. a pushover or time-history analysis under seismic actions). Afterward, the imposed loading conditions in the model are released and, finally, the eigenvalue/eigenvector analysis related to modal analysis is performed considering the tangent stiffness matrix of the FEM through a linear perturbation analysis.

Table 5.2: Mechanical parameters utilized in the CDP model for masonry.

Elasto-plastic behaviour		**Tensile behaviour**		
K_c[a]	0.667	Tensile stress σ_t [kN/m^2]	Cracking strain $\tilde{\varepsilon}_t^{ck}$ [-]	Tensile damage parameter d_t [-]
Eccentricity	0.10	160	0.00E-00	0.00
Viscosity parameter[b]	0.003	120	1.74E-04	0.55
Dilation angle [°]	21	84	3.77E-04	0.80
		16	7.59E-04	0.90

[a] K_c is the ratio of the second stress invariant on the tensile meridian.
[b] The viscosity parameter is used for the viscoplastic regularization of the constitutive equations.
* Compressive strength $\sigma_c = 3500$ kN/m^2

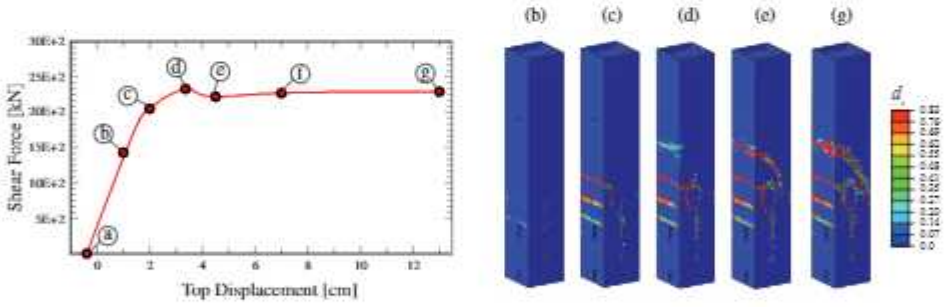

Fig. 5.12: Base shear force versus top displacement curve obtained by displacement-controlled pushover analysis of the Sciri Tower and simulated crack patterns in the tower.

As an illustrative example, Fig. 5.12 furnishes the synthetic damage scenarios generated in reference [45] for the Sciri Tower. In order to reproduce the non-linear mechanical behavior of the masonry, a CDP model with the mechanical properties reported in Table 5.2 was adopted. In this case, a displacement-controlled static-nonlinear pushover analysis was conduced by imposing increasing lateral displacements along the NW direction at the topmost floor of the tower. During the analysis, the shear base forces, top displacements, and tensile damage parameters d_t were monitored. The tensile damage parameter d_t

denotes the material degradation, and spans from 0 (undamaged material) to 1 (total loss of strength). Seven different damage scenarios, labeled from (a) to (g) in Fig. 5.12, were defined with increasing top displacements of 0.0 cm, 1.0 cm, 2 cm, 3.36 cm, 4.5 cm, 7 cm and 13 cm, respectively. The damage patterns in terms of contour maps of damage parameters d_t are represented in the right hand side of Fig. 5.12. The main failure mechanism consists of a major shear crack originating at approximately the mid height of the SE façade when the upper part of the tower reaches a maximum displacement of 3.36 cm (damage scenario (d)). This diagonal crack propagates downward until it reaches the NW façade, completely losing its bearing capacity and causing its subsequent collapse. This occurs when the maximum top displacement reaches a value of 13 cm (g), when convergence issues impede the continuation of the FEM simulation. Some other secondary cracking patterns can be observed in the intermediate damage scenarios (c), (c) and (e) as a result of stress concentrations at openings and the loss of connection with the adjoining building in the SE façade of the tower.

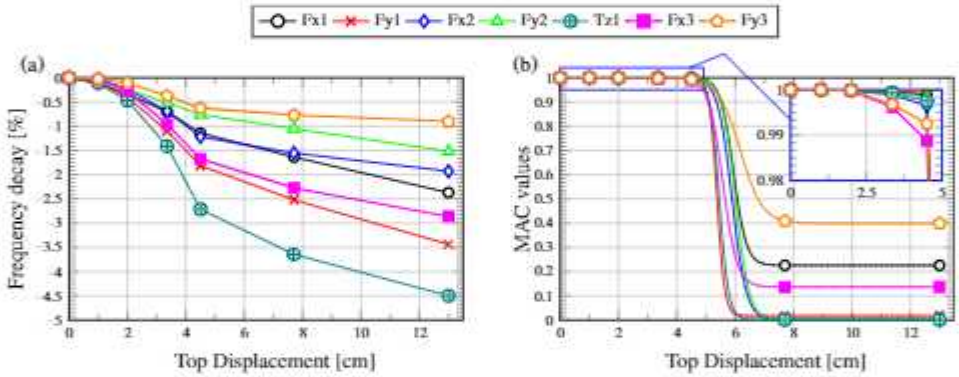

Fig. 5.13: Frequency decays (a) and MAC values (b) of the first seven modes of vibration obtained by the displacement-controlled pushover analysis of the FEM of the Sciri Tower. The continuous lines in (b) are obtained by fitting sigmoid functions through non-linear least squares.

In order to include the previous damage scenarios into the time series of modal features (resonant frequencies and mode shapes) extracted during the vibration testing campaign, every damage stage in Fig. 5.12 (from (a) to (g)) was characterized through a non-linear modal analysis. This led to the results reported in Fig. 5.13 where the frequency decays and MAC values of the first seven modes of vibration are plotted against top displacement. In this light, the frequency decays can be simply superimposed to the experimental time series of resonant frequencies. Instead, since mode shapes are commonly poorly affected by environmental conditions, the modes of vibration in the experimental time series can be simply replaced by the simulated ones.

5.5.Investigated case studies

This section finally presents two case studies illustrating the previously overviewed formulation for SM-based St-Id. Specifically, some of the numerical results and discussion reported in references [45, 189, 190] for the case studies of the Muhammad Tower (Section 1.5.6) and the Sciri Tower (1.5.4) are presented in Sections 5.5.1, 5.5.2 and 5.5.3. The differences between normalizing the time series of modal signatures before and after the St-Id are discussed in Sections 5.5.1 and 5.5.3.

5.5.1.Long-term deterministic St-Id: Muhammad Tower

This first case study presents the development of a DT of the Muhammad Tower in the Alhambra fortress for real-time deterministic damage identification. Following the general work-flow previously introduced in Fig. 5.1, the resulting SHM systems conducts damage identification (detection, localization, and quantification) by assessing the appearance of anomalies in the quasi-real-time series of modal signatures and model parameters reflecting the local stiffness of certain parts of the structure.

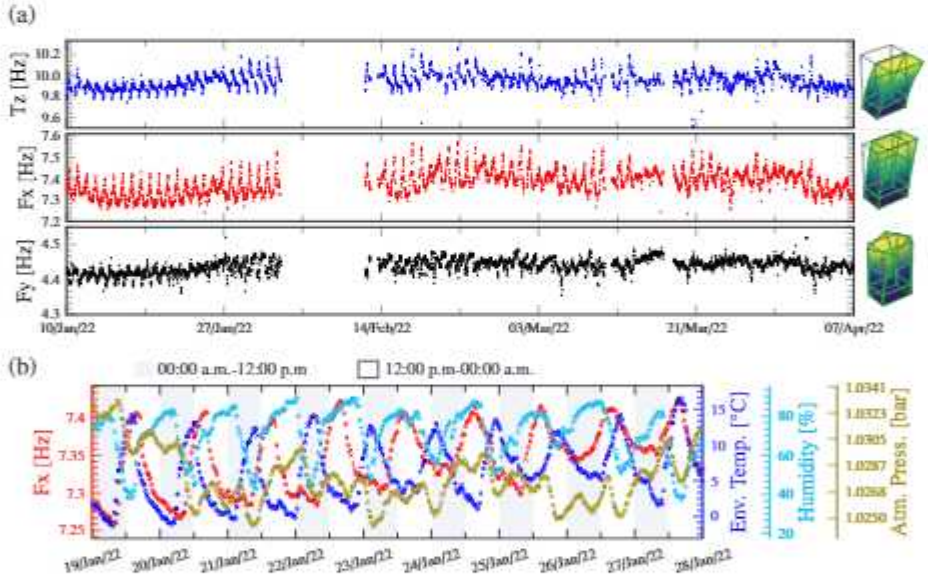

Fig. 5.14: Tracking of the resonant frequencies of the Muhammad Tower from January 10th until March 31st 2022 (a), and time series of Mode 2 and environmental data (January 19th until January 28th 2020) (b).

All the 30 min-long acceleration records acquired in the Muhammad Tower from January 10th until March 31st 2022 (3233 acceleration records) were processed following a filtering sequence comprising: (i) elimination of linear trends, (ii) removal of anomalous spikes through Hanning window filtering, and (iii) second order high-pass Butterworth filtering with a cut-off frequency

of 2 Hz. Once cleansed, the acceleration time signals were used to extract the modal signatures of the tower following the automated Cov-SSI procedure previously introduced in Section 3.4. To do so, the time-lag parameter j_b was assumed as 193 (corresponding to a time lag of 3.2 s), and the model orders varied from 20 to 120 with steps of 2. For the identification of stable poles, the maximum allowable damping ratio ζ_{max} and the MPC and MPD limit values were set to 10%, 80%, and 50%, respectively. The modal tolerances in the SC were defined as $\Delta f \leq 1\%$, $\Delta \xi \leq 3\%$, and $MAC \geq 0.99$. Finally, the weighing factor η (Eq. (3.37)) was set to 0, and the minimum size was chosen as 3% the number of stable poles obtained after the application of SC. Three modes in the frequency broadband up to 10 Hz were consistently identified as shown in Fig. 5.14 (a). Specifically, modes Fy and Fx are first-order bending modes along the N-S and W-E directions of the tower, respectively, while Tz is the first torsional mode of the tower. All the reference modes could be consistently tracked throughout the monitoring period with success ratios above 68%. To illustrate the effects of EOC, the time series of the resonant frequency of Mode 2, environmental temperature ET, humidity H and air pressure AP are furnished in Fig. 5.14 (b). It is noted in this figure that the daily oscillations in the resonant frequency are particularly well correlated with temperature and humidity, exhibiting certain in-phase and opposite-phase trends, respectively. The positive correlation with temperature is ascribed to the closure of micro- and macro-cracks induced by thermal expansion of the RE, while the negative correlation with the relative humidity indicates the softening of the material as the relative humidity increases. This leads to increases in the resonant frequency during day-times and decreases during night-times. In this case study, the effects of EOC in the time series of resonant frequencies were removed before conducting the St-Id. This was carried out by a MLR model with predictor variables given by ET, H, ET^2, H^2 as well as two derived quantities obtained as the moving averages of ET with time windows of 48 (1 day) and 1344 (1 month) data points.

For the construction of the DT, a 3D FEM of the Muhammad Tower was constructed and used to train a Kriging SM (Section 5.3.3). The design variables were defined as stiffness multipliers k_i, $i = 1, \ldots, 3$, affecting the elastic moduli of macro-elements M_i previously reported in Fig. 5.5. The stiffness multipliers were assumed to be uniformly distributed within the variation domain $[0.7, 1.2]$. Note that such a variation range is considerably large, with 0.7 meaning a reduction of 30% of the elastic modulus of the affected macro-element. In this light, random samples were drawn uniformly over $\mathbb{D} = \left\{\mathbf{k} \in \mathbb{R}^3 : 0.7 \leq k_i \leq 1.2\right\}$ using the quasi-random sequence of Sobol. It is important to remark that, since the first three modes of the tower were considered in the analysis, a total of 27 SMs (3 resonant frequencies plus 8×3 modal displacements) were built. From a set of convergence analyses as reported in Section 5.3.2, a training population of 160 individuals was selected to

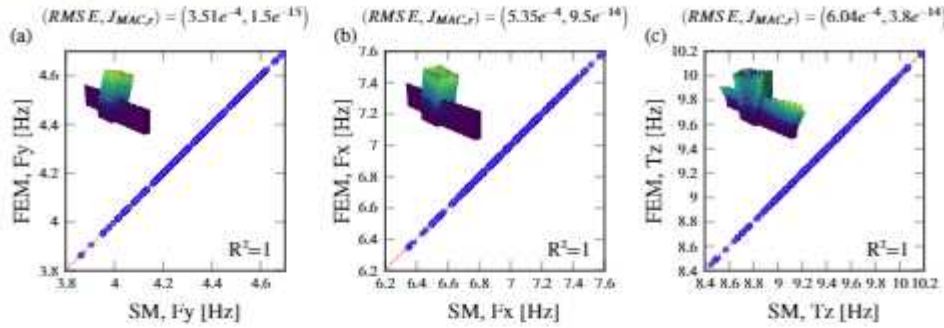

Fig. 5.15: Scatter plot of the predictions by the Kriging SM (160 training samples) versus the forward evaluations of the 3D FEM of the Muhammad Tower: (a) Fy, (b) Fx, (c) Tz.

train the SMs as a conservatively accurate solution (VS of 200 samples). The comparison between the predictions of the resulting SM and the forward FEM is shown in Fig. 5.15. The low scatter of the data points around the diagonal line corroborates that the SMs are formed with accuracy, with coefficients of determination R^2 very close to 1 and maximum RMSEs of 3.8E-4 Hz. Note in Fig. 5.15 that very low $J_{(MAC,r)}$ values are obtained for all the considered mode shapes, which demonstrates the high accuracy of the SMs to reproduce the modal displacements. An essential aspect of the SM regards its computational cost. It is important to remark that one linear modal analysis of the FEM of the Tower approximately takes 5 minutes in a standard PC (64-bit, 16.0 GB RAM, Intel(R) Core(TM) i7-8750H processor, 2.20 GHz CPU). Instead, the evaluation of the SM only takes 0.02 s, achieving a reduction of 99.998% with respect to the forward model.

Following a similar approach to the one presented above in Section 5.4, ten different damage scenarios (labeled from DS1 to DS10) were defined after a pushover analysis. In this case, the tower was subjected to gravity loading and increasing lateral displacements along the NS direction following a parabolic profile, obtaining the base shear versus top displacement curve reported in Fig. 5.16 (a). Samples of the damage patterns for DS1, DS4, DS6, DS8, DS9 and DS10 are represented in Fig. 5.16 (b) in terms of contour maps of the tensile damage parameter d_t. The main failure mechanism consists of a major horizontal crack originating from the door opening in the first level of the tower until crossing completely the north façade (DS1, DS2). Another major diagonal crack propagates upward from the door opening in the second level (DS1), although it does not cross the north façade until DS3. Some other secondary cracking patterns can be also observed as a result of stress concentrations in the remaining openings all throughout the tower. The structure loses completely its load bearing capacity when the main horizontal crack crosses entirely the

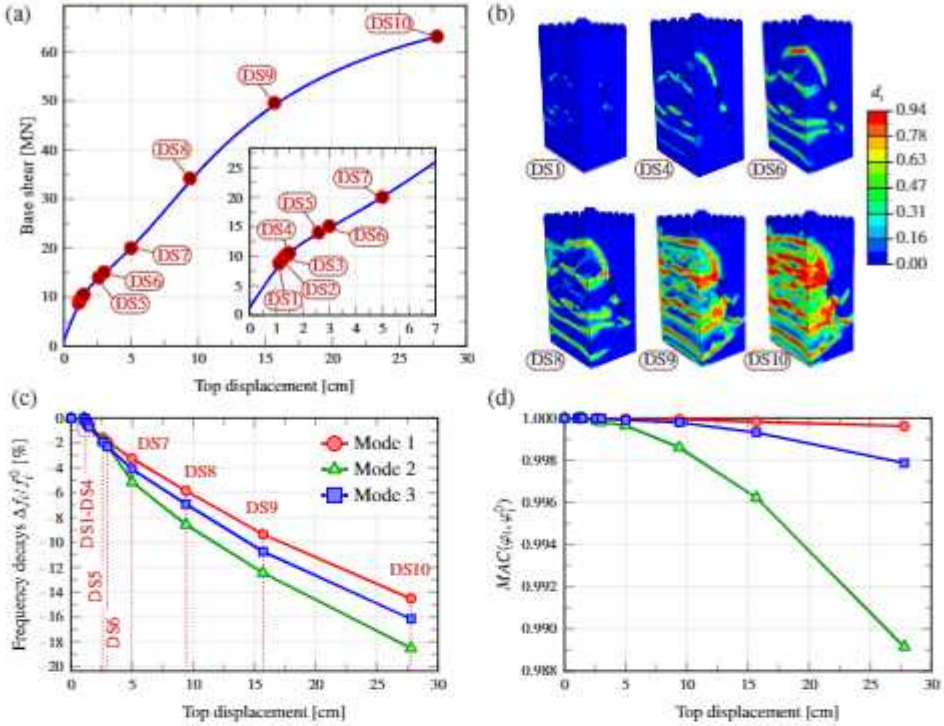

Fig. 5.16: Base shear force versus top displacement curve obtained by displacement-controlled pushover analysis of the Muhammad Tower (a), simulated crack patterns (b), damage-induced frequency decays (c) and MAC values (d) of the first three modes of vibration.

cross-section of the tower for a maximum top displacement of 27.8 cm (DS10). On this basis, the frequency decays and variations in the mode shapes related to the previously defined damage conditions are reported in Fig. 5.16 (d). The frequency decays start to increase when the top displacement overpasses a value of about 1.25 cm, that is when the major failure mechanism in the tower activates (drift ratios of 1.45‰ and 0.78‰ with respect to the height of the free-standing portion of the total height of the tower, respectively). Damage-induced effects primarily concentrate in terms of resonant frequencies, achieving maximum decays of up to about 14-18% for DS10, while only slight variations are observed in the mode shapes.

Finally, the deterministic St-Id approach previously introduced in Section 5.2.1 was applied sequentially to each set of identified modal data (30 min) over the testing period from January 10$^{\text{th}}$ until March 31$^{\text{st}}$ 2022. To this aim, the non-linear minimization problem in Eq. (5.3) was solved using a Particle Swarm optimization algorithm (40 particles and error tolerance 1E-5). In the regularization term $\mathcal{R}(\mathbf{x})$, a reference vector of design variables $\mathbf{k}^0 = [1, 1, 1]^{\mathrm{T}}$ was considered (i.e. $\mathbf{k}^0$ represents the situation when macro-elements M_i possess undamaged

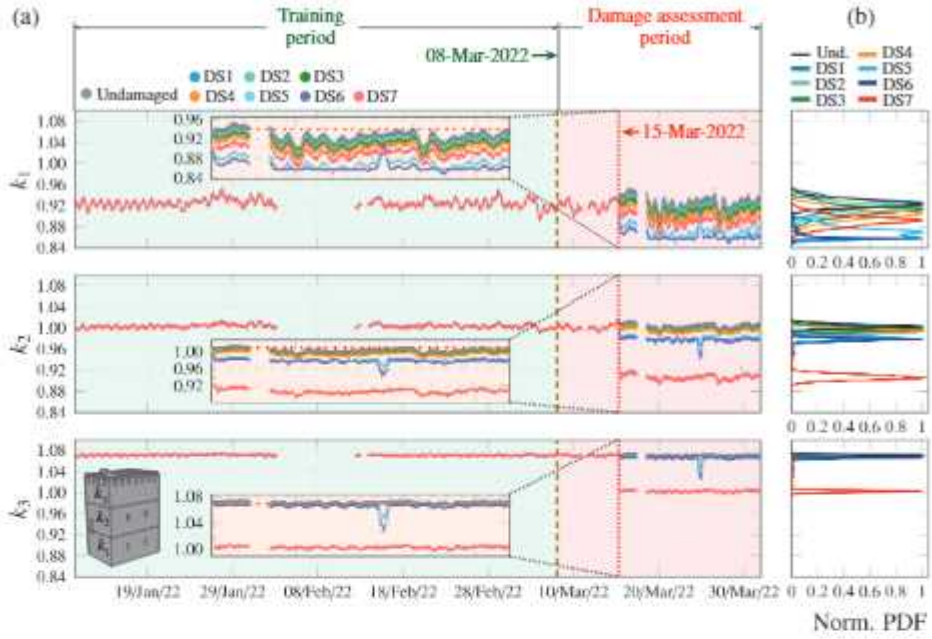

Fig. 5.17: Time series of identified stiffness multipliers k_i of macro-elements M_i, $i = 1, \ldots, 3$, of the Muhammad Tower (a) and PDFs of data-points in the damaged period for synthetic damage scenarios DS1 to DS7 (b).

nominal Young's moduli). The weighting parameters $\eta_{(1,i)}$ and $\eta_{(2,i)}$ in the cost function were defined after some manual tuning as $\eta_{(1,1)} = \eta_{(1,2)} = 1.0$, $\eta_{(1,3)} = 0.3$ and $\eta_{(2,1)} = \eta_{(2,2)} = \eta_{(2,3)} = 0.5$. Note that the weight given to the third resonant frequency (Tz) was lower than those assigned to the first two modes due to the limitations of the MLR model to remove the effects of EOC from this frequency. With regard to the trade-off parameters $\eta_{(3,i)}$, good identification results were obtained when assuming $\eta_{(3,1)} = 0.30$, $\eta_{(3,2)} = 0.72$, $\eta_{(3,3)} = 1.2$. These values were defined after inspecting the sensitivity of the model response with respect to variations in the design variables k_i. In this particular case study, the low sensitivity of the modal features of the tower to variations in k_3 considerably hinders the location of damage in M_3 (top macro-element), thereby a larger regularization parameters $\eta_{(3,i)}$ was assigned to this macro-element.

The considered damage scenarios were incorporated in the time series of modal features from March 15$^{\text{th}}$ 2022. Given the minimal impact of the considered damage scenarios upon the mode shapes of the tower, the time series of experimental modal displacements were maintained unaffected. In this light, the outcomes of the continuous DT-based St-Id are presented in Figs. 5.17 and 5.18. Figures 5.17 (a) and (b) depict the time series of identified stiff-

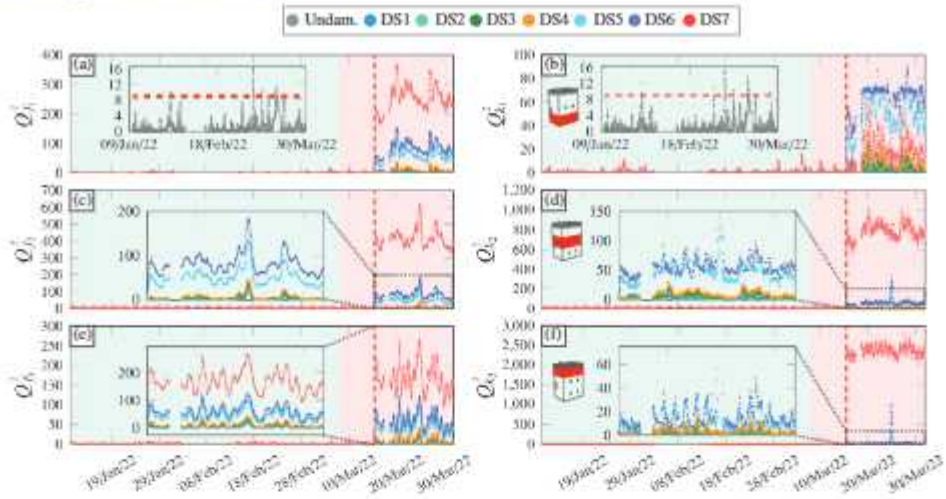

Fig. 5.18: Mahalanobis distances with respect to the in-operation training period in terms of the first three fundamental frequencies of the Muhammad Tower (a,c,e) and the identified stiffness multipliers k_i (b,d,f) for synthetic damage scenarios DS1 to DS7. Red dashed lines stand for the 99% confidence level of the considered features empirically estimated for the training period.

ness multipliers k_i and the corresponding histograms after the application of damage, respectively. In addition, Fig. 5.18 presents the squared Mahalanobis distances with respect to the training period as a novelty analysis metric in terms of resonant frequencies and stiffness multipliers. It is clear in these figures that all the considered damage scenarios except for DS1 can be detected in the shape of sudden drops in the time series of k_i after the damage condition is imposed. Although some slight decreases are noticeable for DS1 in k_1 with respect to the undamaged condition (see the zoom insert in Fig. 5.17 (a)), the frequency decay associated with this damage scenario is lower than the residual variance in the normalized time series of resonant frequencies and, therefore, goes unnoticed. Instead, the damage-induced frequency decays of the remaining scenarios overpass the residual variances and, therefore, appear as clear anomalies in the time series of the stiffness parameters. Furthermore, these results evidence the localization and quantification ability of the proposed approach, allowing to effectively track the evolution of damage in the tower. Specifically, note in Fig. 5.17 that scenarios DS1 to DS4 primarily affect the stiffness of macro-element M_1 with increasing severity. Moreover, some slight decreases can be also observed in k_2, while almost no effects are noticeable in k_3. These results coincide with the damage patterns previously furnished in Fig. 5.16 (b), which reported the initiation and propagation of the major horizontal crack (affecting M_1) from DS1 until DS4. Afterward, new diagonal cracks affecting macro-elements M_2 and M_3 originate, which agrees with the

anomalies observed in Figs. 5.17 and 5.18 for DS5, DS6 and DS7. In particular, note that no significant degradation is found in k_3 until DS7, when the diagonal crack originating at the upper corner of the opening in the second floor crosses the North façade of the tower (see Fig. 5.16 (b)). Interestingly, it is noted in Fig. 5.17 (a) that the stiffness degradation for DS7 in k_1 decreases with respect to the values obtained for DS5 and DS6. This circumstance has no physical justification and evidences some limitations in the St-Id. On one hand, this may be due to the natural limitation of any model parametrization that does not explicitly represent the damage mechanism under analysis, as it is the case in the present work since the model does not count on any particular parameter accounting for the specific crack pattern observed in Fig. 5.16 (b). On the other hand, despite the implementation of the regularization function $\mathcal{R}$, the circumstance that only three modes are consistently identified in the experimental campaign represents an observability limitation. These aspects certainly give origin to important sources of ill-conditioning, which may explain the aforementioned inconsistency in the damage identification. Nonetheless, given that DS7 represents an extremely severe damage condition, it can be concluded that the developed DT-based St-Id is proficient for damage identification of early-stage and moderate damage pathologies. It is noticeable in Fig. 5.18 that the damage-induced anomalies are more easily detectable in terms of stiffness multipliers, which furthers justify the use of the proposed methodology as a complementary approach to traditional OMA-based SHM. Finally, it is important to remark that the computational time to perform the St-Id is only around 7.4 s, which guarantees the compatibility of the proposed approach with long-term SHM applications.

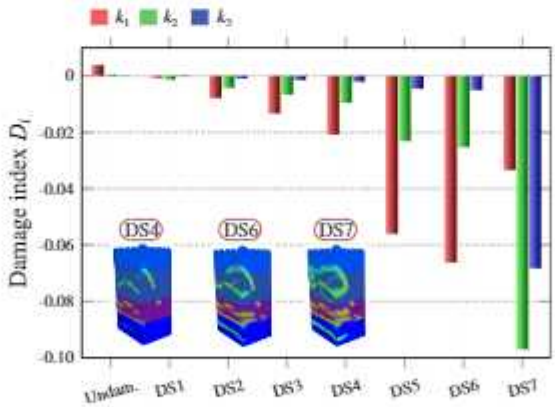

Fig. 5.19: Damage indexes D_i in the three macro-elements M_i defined in the Muhammad Tower obtained for synthetic damage scenarios DS1 to DS7.

Finally, a comprehensive damage index D_i is depicted in Fig. 5.19 to summarize the previous damage identification results. The damage index is simply

defined as the relative variation of the medians of the time series of stiffness multipliers k_i in the damaged period with respect to the healthy baseline. It is noted in this figure that increasing damage indexes are obtained as the damage condition progresses, strengthening the discussion above on the ability of the proposed approach to localize and quantify damage. Moreover, these results highlight the impossibility of properly identifying DS1 and DS2 as a consequence of the afore-mentioned limitations in the statistical pattern recognition and the inverse model calibration, respectively.

5.5.2. Long-term deterministic St-Id: Sciri Tower

This second case study regards the application of deterministic and Bayesian SM-based St-Id for damage identification of the Sciri Tower. All the analyses were conducted on the basis of the vibration testing results previously reported in Fig. 4.18. For the St-Id, second order quadratic RSM model was adopted and trained with an ED of 512 individuals. The deterministic St-Id problem from Eq. (5.3) was solved using a Particle Swarm optimization algorithm for each set of identified modal data (30 min) over the testing period since February 13$^{\text{th}}$ until March 10$^{\text{th}}$ 2019. A reference vector of design variables $\mathbf{x}^0 = [0, 0, 0, 0]^{\mathrm{T}}$ has been considered (i.e. $\mathbf{x}^0$ represents the situation when macro-elements M_i possess nominal values of Young's modulus), along with a parameter variation range of $-0.15 \leq k_i \leq 0.15$. The mode shapes of modes Fx2 and Fy2 were excluded from the optimisation because of their high modal complexity (refer to reference [188] for further details). The weighting coefficients in the objective function were set as $\eta_{(1,i)} = 1$ and $\eta_{(2,i)} = 0.5$. The trade-off parameters in the regularization term were defined after sensitivity analysis as $\eta_{(3,1)} = 1$, $\eta_{(3,2)} = 0.5$, $\eta_{(3,3)} = 0.25$, and $\eta_{(3,4)} = 0.15$. One essential aspect regards the computational times required to perform the St-Id. While the 3D FEM takes on average a CPU time of 10 min to complete one single linear modal analysis in a standard PC (64-bit, 64 GB RAM, Intel Xeon processor E3-1225 v5, 3.30 GHz CPU), the St-Id of the Sciri Tower using the RSM only requires 0.02 s (i.e. a reduction of 99.998%). Such a low evaluation time allows to perform the St-Id in about 0.3 s, making the proposed approach fully compatible with real-time SHM applications.

The outcome of the continuous surrogate model-based St-Id is presented in Fig. 5.20. In this case, the time series of E_2, E_3, and E_4 are sorted in decreasing order, indicating that the stiffness of the tower decreases in height, which is consistent with the architectural configuration of the tower. It is interesting to note in Fig. 5.20 that the proposed approach can capture daily fluctuations in the intrinsic stiffness of the tower. Specifically, increasing and decreasing trends of E_i can be observed during daytime and night-time, respectively. At this stage, it is essential to filter out the effects of EOC from the time series of identified model parameters. Figure 5.21 shows the time series of identified elastic moduli E_i along with the predicted ones adopting a MLR model with

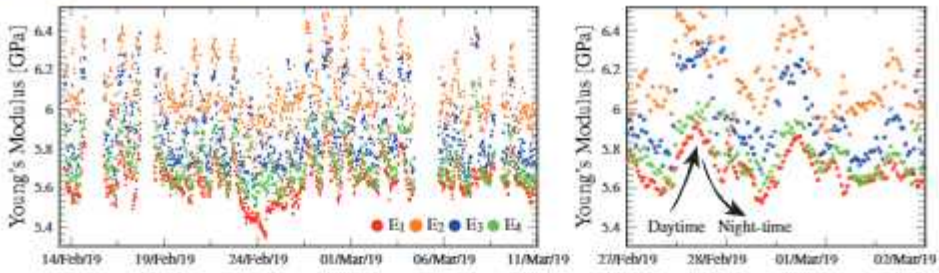

Fig. 5.20: Time series of fitted Young's moduli of macro-elements M_i, $i = 1, ..., 4$, enabled by the online surrogate model-based St-Id of the Sciri Tower.

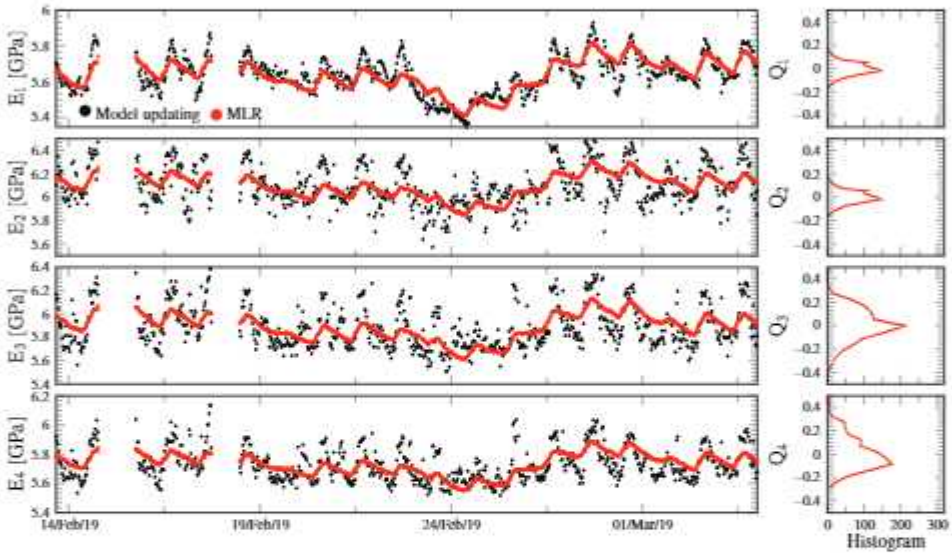

Fig. 5.21: Identified elastic moduli E_i of the Sciri Tower and predicted time series using MLR along with the histograms of their residuals.

environmental temperature (indoor and outdoor) as predictor variable (training period of two weeks and a half (800 data points)). Additionally, Fig. 5.21 also depicts the histograms of the residuals Q_i between the identified moduli E_i and the predicted ones $\hat{E}_i$, i.e. $Q_i = E_i - \hat{E}_i$. In this light, any of the novelty analysis techniques previously introduced in Chapter 2 can be applied herein. Since the model parameters directly refer to specific regions of the tower, the detection of anomalies in the time series of k_i provides direct assessment of the location and severity of damage.

To evaluate the effectiveness of the developed SM-based St-Id approach, the synthetic damage scenarios previously reported in Section 5.4 were incorporated in terms of frequency decays and damaged mode shapes in the time series of experimental modal signatures of the Sciri Tower after the training

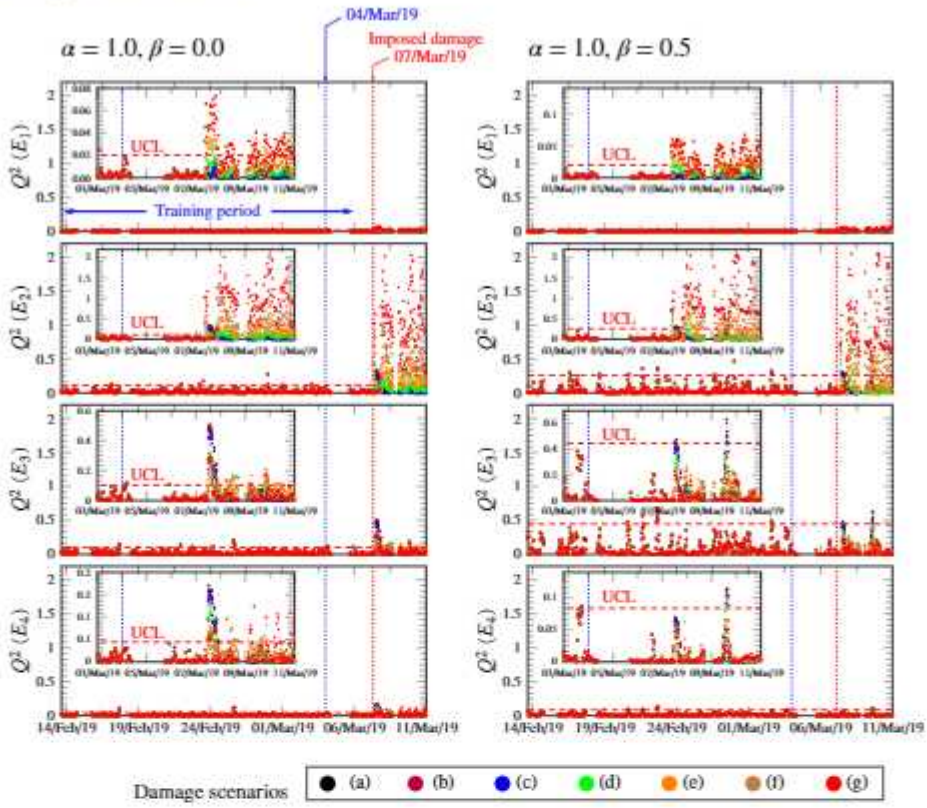

Fig. 5.22: Results of surrogate model-based damage identification of the Sciri Tower when subjected to simulated damage scenarios with increasing severity (training population = 800 individuals, $\mathrm{UCL}_i = 4\sigma_i^p$).

period from the 7th March 2019. Fig. 5.22 depicts the squared values of the residuals of the elastic moduli of macro-elements M_i throughout the monitoring period. Moreover, UCLs are indicated with red dashed horizontal lines to ease the identification of permanent variations in the statistical distributions of the residuals. These UCLs have been defined as four times the standard deviation of the residuals within the training period ($\mathrm{UCL}_i = 4\sigma_i^p$). From these results, it is quite evident that outliers concentrate in macro-element M_2, which agrees well with the damage patterns previously discussed in Fig. 5.12. Additionally, some outliers can be also recognized in macro-element M_1, while almost no outliers are noted in the last two macro-elements M_3 and M_4. In order to devise suitable metrics for determining whether the structure may experience damage, Fig. 5.23 (a) reports the analysis of outliers in the time series from Fig. 5.22. In this case, increases in the number of outliers are concentrated in macro-elements M_1 and M_2, which agrees with the simulated damage patterns. Moreover, almost no variations are observed in the number of outliers

for macro-elements M_3 and M_4 where no damage is expected. Interestingly, when mode shapes are not included in the optimization, no significant increases in the number of outliers are detected until the damage scenario (d), that is when the major diagonal crack in the tower takes place. These results demonstrate the usefulness of including mode shapes into the surrogate model-based St-Id to minimize ill-conditioning limitations and enable early-stage damage localization. Considerably worse results are obtained with the two other statistical models, where a considerable amount of outliers is also found for macro-elements M_3 and M_4 which are known to remain healthy. The reason for this poor performance is ascribed to the limited number of data samples in the training period, hence larger databases would be required to further appraise their effectiveness. These analyses are completed with the results furnished in Fig. 5.23 (b), where deviations in the distributions of outliers are studied. For this purpose, a damage index is defined as the the ratio between the average values of the squared residuals outside and inside the training period. It is noted that the best damage identification results are again those obtained using the MLR model and including mode shapes in the St-Id ($\beta = 0.5$). In this case, the proposed damage index exhibits a monotonically increasing behaviour with the damage severity, outputting largest values for the macro-element M_2, followed by the macro-element M_1, and constant values close to zero in the case of macro-elements M_3 and M_4 where no damage is expected. These results demonstrate the ability of the proposed surrogate model-based approach for damage identification, being capable of localizing structural pathologies and quantifying their severity through novelty analysis of the time series of tracked model parameters.

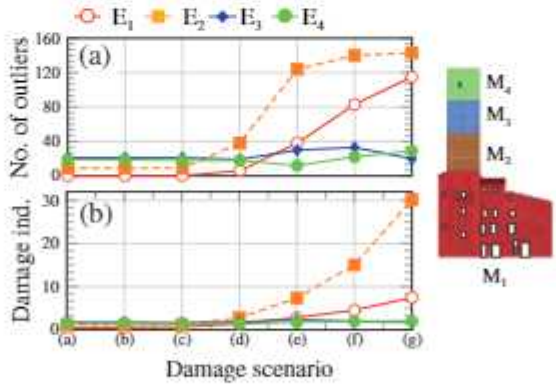

Fig. 5.23: Damage identification results in the Sciri Tower through outlier analysis of residuals between identified Young's moduli and statistical predictions. The damage index is defined as the ratio between the average values of the squared residuals outside and within the training period (training population = 800 individuals).

5.5.3. Long-term probabilistic St-Id: Sciri Tower

This last case study presents the SM-based BMU of the Sciri Tower reported in reference [189]. In this case, the St-Id is not deterministic but stochastic following the theoretical formulation previously presented in Section 5.2.2. The adopted model parametrization is the one reported in Fig. 5.7. In this light, the model updating parameters θ_i, $i = 1, \ldots, 9$, to be identified in the subsequent Bayesian inference are defined as linear proportionality coefficients of the elastic moduli E_i of the corresponding macro-elements, i.e. $E_i = \theta_i \cdot E_{i,0}$, with $E_{i,0}$ being the nominal (undamaged) value of the Young's modulus of the i-th macro-element. Given the large number of forward model evaluations involved in BMU, the motivation for developing a computationally efficient SM is particularly evident herein. To this aim, a SM combining PCE and Kriging modeling was developed following the theoretical basis overviewed above in Sections 5.3.3 and 5.3.3. For the construction of the surrogate models, the design variables θ_i were assumed to be uniformly distributed in a considerably large interval $[0.7, 1.3]$. In the PCE expansion, Legendre polynomials of orders ranging from 2 to 6 were selected with a q-norm of 0.6, and the leave-one-out error in Eq. (5.50) was used to select the optimal expansions. Once constructed, the PCE expansion was used as the trend term in the Kriging model. Considering Gaussian correlations, the fitting parameters and the hyper-parameters of the Kriging model were determined by solving the maximum-likelihood-estimator in Eq. (5.35) with a genetic algorithm. The first seven resonant frequencies and mode shapes of the Sciri Tower are taken into account, which amounts to a total of 91 uni-dimensional meta-models.

To determine the optimal dimension of the design space, a convergence analysis was conducted considering different design spaces sampled by LHS with increasing sizes of $N = 50$, 100, 200, 500, 1000 and 2000, and a VS of 3000 samples was defined. From a convergence analysis, an ED of $N = 500$ samples was selected. The resulting scatter plots of the resonant frequencies obtained by the FEM and the predictions by the surrogate model are shown in Fig. 5.24. The low scatter of the points around the diagonal line ($R^2 \approx 1$) and maximum RMSEs of 5E-2 corroborate that the SMs were formed with accuracy. In addition, very close fittings of the mode shapes were also obtained, with maximum J_{MAC} (see Table 5.1) metric values of the order of E-3. It is important to mention that every linear modal analysis of the 3D FEM took around 5 minutes on a 4-core Intel Xeon CPU 3.30 GHz (64 GB RAM) computer. Instead, the the computational time required to evaluate the SM only took about 0.5 ms, ensuring its applicability in the following continuous BMU.

In this case study, the effects of EOC upon the modal signatures of the tower were filtered out before conducting the St-Id. To do so, a data normalization approach combining MLR and PCA was implemented. Firstly, the modal signatures until May 3rd (800 samples) were selected as the training period. The time series of environmental temperature (indoor and outdoor)

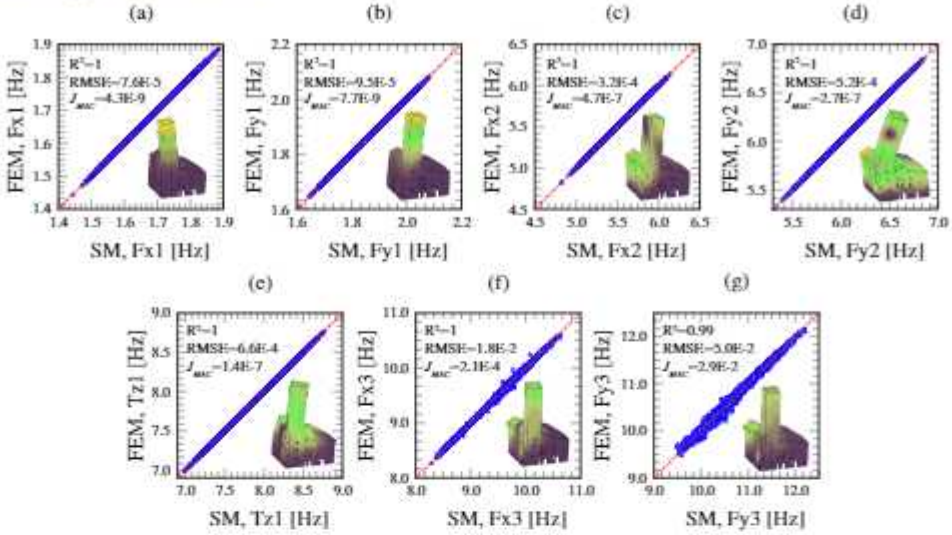

Fig. 5.24: Scatter plot of the PCE-Kriging meta-model (500 training samples) with respect to the FEM of the Sciri Tower for the first seven natural modes (validation set of 3000 samples, RMSE = Root Mean Squared Error).

were used as predictors in the MLR model. Then, the residual variances in the resonant frequencies due to unmodeled operational factors were further minimized using PCA with one single PC (explaining more than 90% of the total variance). Then, an initial SM-based BMU was carried out considering the whole normalized training period as reported in Fig. 5.25. Since mode shape displacements were only obtained in the tower and no information was acquired in the building aggregate, the inference limited to the identification of parameters θ_9, θ_8 and θ_7, corresponding to the macro-elements pertaining to the tower. Moreover, given the relatively low number of measured modal displacements, the likelihood function formulated in terms of MAC values in Eq. (2.1) was implemented herein. Gaussian prior distributions with a mean value of 1 and a standard deviation of 0.1 were defined for all the fitting parameters. During the analyses, a total number of 3000 samples with a burning time of 900 samples were drawn by the DRAM MCMC approach previously overviewed in Section 5.2.2. The Gaussian proposal was initially defined as a diagonal covariance matrix of value 1E-2 and scaled by the factor $s_d = 2.4^2/d$. In the DR step, the covariance matrix of the proposal distribution was scaled down by a factor $\gamma = 0.1$. The initial location state θ_0 was defined by considering all the uncertain parameters equal to 1.0, and the initial prediction errors were estimated from the statistical analysis of the time series of identified modal signatures as $\sigma_f^2 = 3.0\%$ and $\sigma_\varphi^2 = 0.9\%$ (Eq. (5.12)). All things considered, the selected hyper-parameters led to an average acceptance rate of 67%. Figure 5.25 (a) presents a three-dimensional scatter plot of the Markov

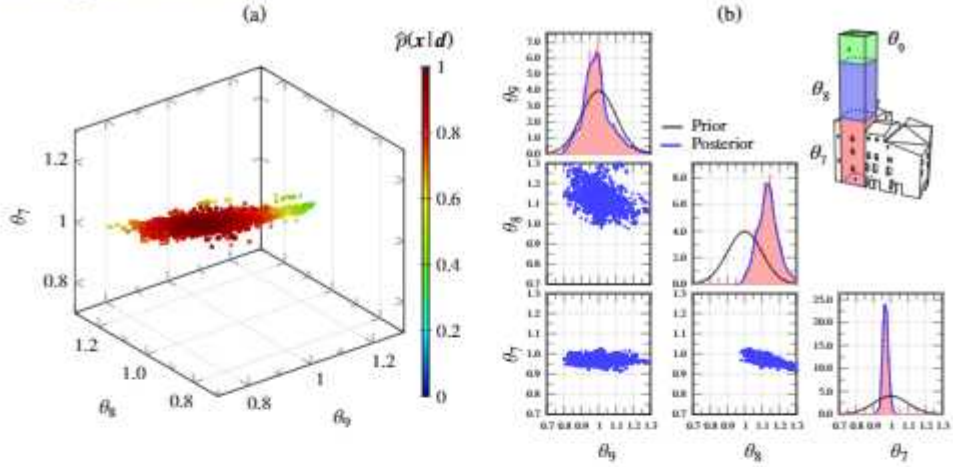

Fig. 5.25: Bayesian identification results of the stiffness coefficients θ_9, θ_8 and θ_7 of the Sciri Tower considering the modal signatures during the training period (800 samples, from February 13^{th} to May 3^{rd}, 2019). Three-dimensional scatter plot of the obtained Markov chain (a), and correlation analysis (b).

chain on a colour scale representing the normal kernel smoothed probability values of the samples ($\hat{p}\left(\mathbf{x}|\,\mathbf{d}\right)$, normalized between 0 and 1). The statistical analysis of the marginal chains is reported in Fig. 5.25 (b). It is clearly noted that, in accordance with the sensitivity analysis previously reported in Fig. 5.8, the dispersion of the PDFs of the fitting parameters increases in height. Lastly, it is important to highlight that the total computational time to obtain the Markov chains amounts to about 20 min, which enables the integration of the proposed approach into a continuous SHM scheme, given that OMA is carried out every 30 minutes of data recording.

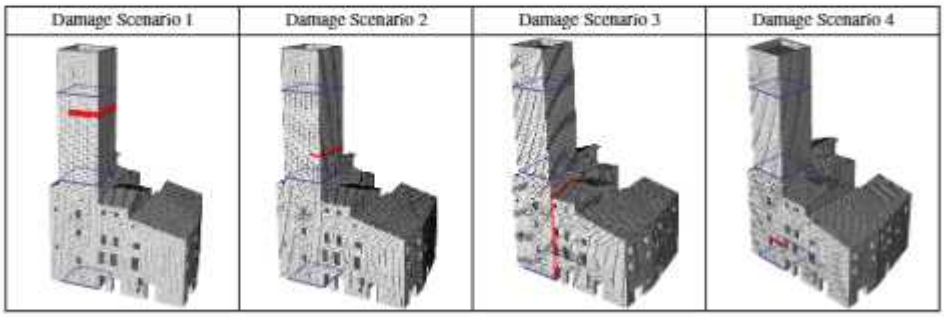

Fig. 5.26: Synthetic damage scenarios defined using the 3D FEM of the Sciri Tower.

In order to assess the effectiveness of the St-Id, four different synthetic damage scenarios were created on the basis of the 3D FEM of the Sciri Tower as shown in Fig. 5.26. The scenarios were defined by eliminating the stiffness of

certain parts of the FEM to simulate crack-like defects. In particular, Damage Scenarios 1, 2, and 4 include damage in the macro-elements C9, C8 and C7, respectively, while Damage Scenario 3 simulates the detachment between the east façade of the tower and the building aggregate. The corresponding modal signatures were obtained by linear modal analysis of the 3D FEM, and the resulting damage-induced frequency decays with respect to the undamaged condition are reported in Table 5.3. These frequency decays were incorporated in the time series of resonant frequencies in the shape of constant mean shifts. On the other hand, the mode shapes corresponding to the damage conditions were directly used in the damage assessment period. Note that the adopted parametrization does not account for model parameters strictly related to the affected elements in the damage scenarios in Fig. 5.26. Instead, the selected parametrization was designed to offer a general model to identify structural defects conceivable as global stiffness reductions in horizontal sections of the tower.

Table 5.3: Damage-induced decays in the resonant frequencies of the Sciri Tower under Damage Scenarios 1 to 4.

	Frequency decays [%]						
Case scenario	Mode 1	Mode 2	Mode 3	Mode 4	Mode 5	Mode 6	Mode 7
Damage Scenario 1	-0.01	-0.02	-0.05	-0.05	-0.02	-0.12	-0.02
Damage Scenario 2	-0.49	-0.58	-1.00	-1.51	-1.55	-3.29	-0.35
Damage Scenario 3	-1.62	-1.70	-1.20	-2.69	-2.70	-3.81	-0.27
Damage Scenario 4	-6.24	-3.36	-1.95	-1.12	-9.11	-1.30	-0.85

To alleviate the computational burden, the modal data were split into data-sets containing 48 hours of measurements with 24 hours overlap, which amounts to a total of 20 model identifications. Nevertheless, as already mentioned the computational time involved in the MCMC sampling amounts to about 20 minutes, being possible to reduce the time resolution in the St-Id if needed. The covariance matrix of the proposal distribution was taken as the covariance matrix of the Markov chains obtained by the previous BMU in Fig. 5.25, as well as the initial prediction errors, while the rest of the identification parameters were kept constant. The obtained marginal PDFs for the four damage scenarios are furnished in Fig. 5.27. It is observed that no clear variations can be found for Damage Scenario 1, while reasonably good identification results were obtained for the rest of the damage scenarios. The damage identification limitations in Section C9 are attributable to the low sensitivity of the modal signatures of the tower to variations in the stiffness of the upper part of the tower as previously shown in Fig. 5.8. In order to provide a comprehensive metric for damage identification, a damage index D_i is presented in Fig. 5.28 as the relative percent differences of the medians of the Markov chains with respect to the initial one obtained in the training period. The results in this

figure confirm the previous discussion, being possible to clearly identify damage in Scenarios 2 to 4. Damage Scenario 2 is characterized by marked stiffness reductions in macro-elements C8 and C9 (see Fig. 5.27 (b)). Although this damage condition does not explicitly affect the stiffness of C9, the reductions in this macro-element are ascribed to ill-conditioning limitations given the low modal sensitivity related to the stiffness of the top section of the tower. This circumstance may be also explained by the inherent limitations of the adopted parametrization, since no model parameter accounting for the local stiffness reduction in the elements affected by the crack in Damage Scenario 2 are considered. This aspect may facilitate the obtained solution affecting C8 and C9 to appear more likely from a Bayesian perspective than the solution only affecting C8 (where the crack is truly located). Finally, it is noted that damage-induced variations in Damage Scenario 3 concentrate in macro-element C8 (θ_8) with some decreases in C7 (θ_7). This indicates that given the defined parametrization, the implemented BMU approach finds as the most probable solution for the given observations the one with concentrated stiffness reductions in the middle section and with only moderate decreases in the bottom part of the tower. Despite Section C8 is directly in contact with the building aggregate, note that the detachment of the tower from the building aggregate in Damage Scenario 3 cannot be easily modeled by affecting the stiffness of the defined macro-elements. This circumstance evidences a natural limitation of any model parametrization that does not explicitly represent a certain damage mechanism, as it is in this case since there is no particular parameter accounting for the connection with the building aggregate. In fact, observe that Damage Scenario 4, which effectively affects the stiffness of C7, does concentrate reductions in the PDF of θ_8. In this case, some spurious increases in the stiffness of C8 are found, which are ascribed to observability limitations related to the defined parametrization.

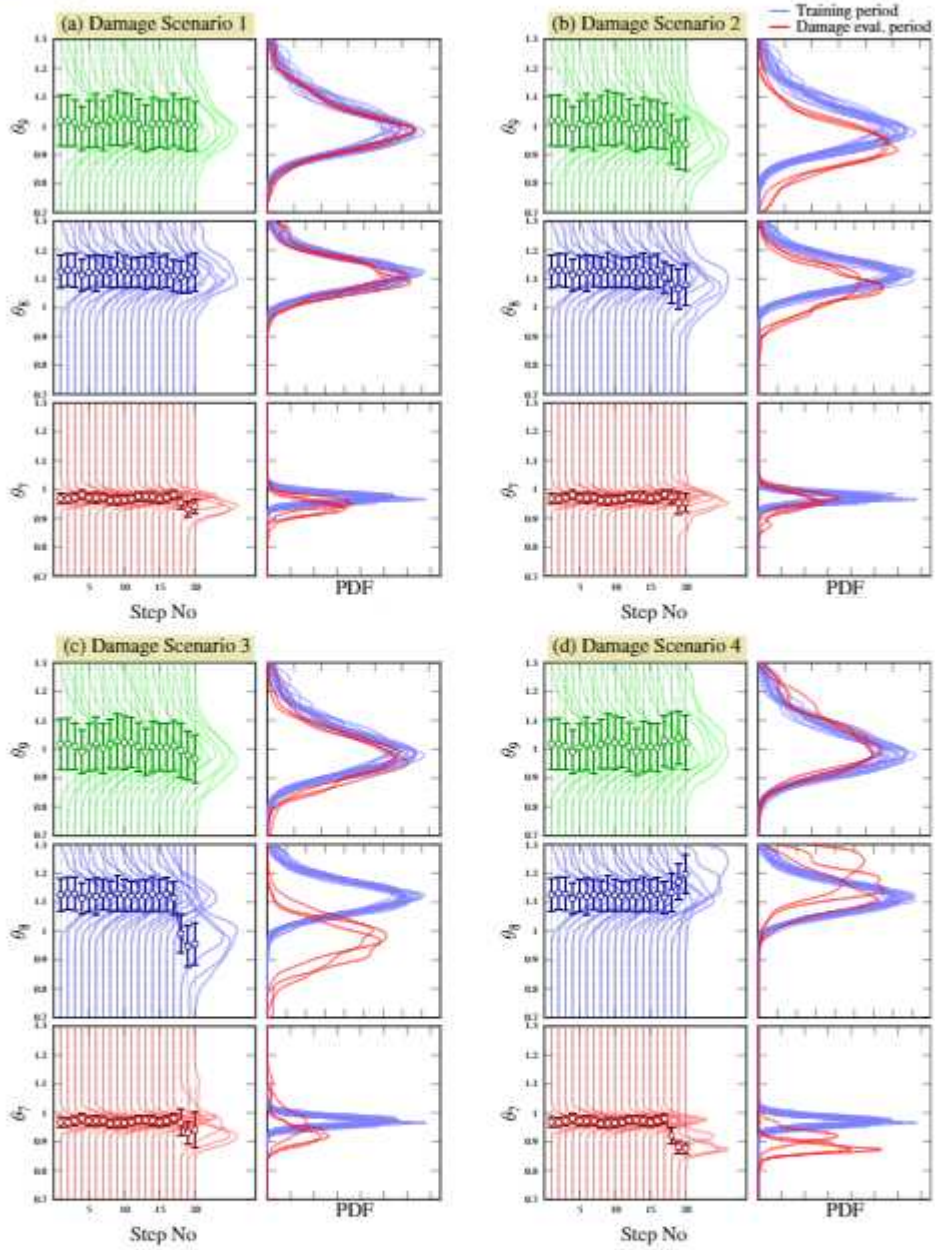

Fig. 5.27: Bayesian damage identification results of the Sciri Tower throughout all the monitoring period from February 13^{th} until March 10^{th} 2019 considering four synthetic damage scenarios (a to d). Error bars indicate standard deviation values.

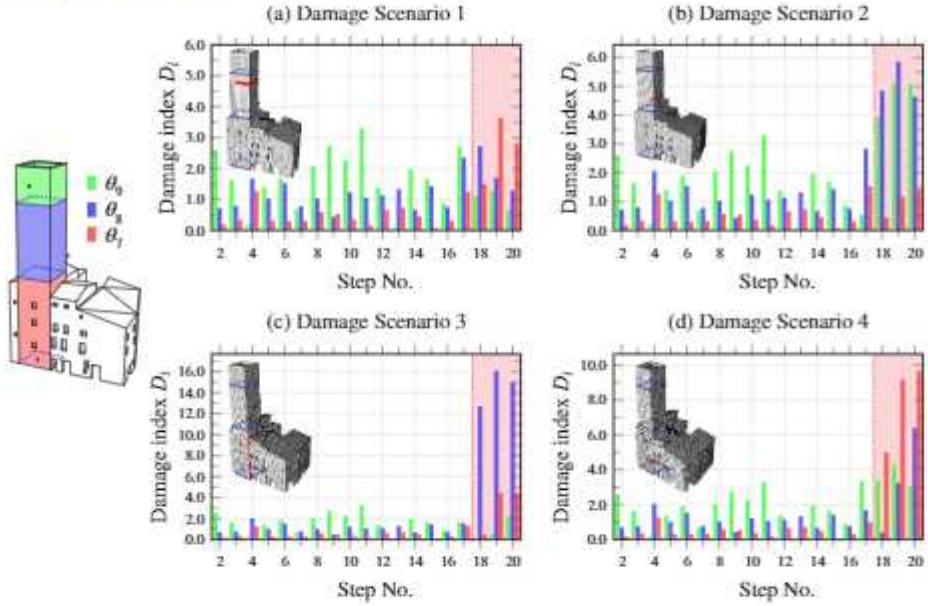

Fig. 5.28: Damage indices D_i obtained as the relative percent differences of the medians of the Markov chains of parameters θ_9, θ_8 and θ_7 of the Sciri Tower with respect to the initial chain obtained in the training period for Damage Scenarios 1 to 4 (a to d).

6. Software Implementation: MOVA/MOSS and P3P

6.1. Introduction

A clear evidence of the low technological transfer of SHM to engineering routine practice is the limited number of software solutions available in the market. Among the few existing software solutions, the majority are devoted to OMA. The most popular software programs for vibration-based SHM of structures are MACEC, LMS Test.Lab, and ARTeMIS. MACEC [225] is a MATLAB toolbox for OMA of structures developed by the Structural Mechanics Section of KU Leuven. This offers an extensive gallery of system identification methods for AVT of structures, including, among others, FDD, data-based and Cov-SSI, and p-LSCF. Nonetheless, this software does not allow performing continuous OMA and, therefore, cannot be directly applied to long-term vibration-based SHM. The LMS Test.Lab Modal Analysis software [226] implements a very robust version of the p-LSCF method under the commercial name of PolyMAX although, alike MACEC, this software does not permit the implementation of long-term SHM systems. ARTeMIS [227] was developed by the company Structural Vibration Solutions A/S, funded in 1999 as a spin-off from Aalborg University in Denmark. This software is particularly well-suited for AVT of structures and, unlike the previous software programs, the most recent versions include a Damage Detection Plug-in with automated SSI and Hotelling's control charts. Nevertheless, ARTeMIS lacks the possibility of using statistical pattern recognition methods to filter out environmental effects and, therefore, it may be difficult to detect early-stage damage using this tool. In any case, there is not a software program of general use allowing the management of

aggregated SHM systems within the statistical pattern recognition paradigm.

As an effort to contribute to the technological transfer of SHM, all the theoretical developments of this thesis have been systematically incorporated into two software suits, called MOVA and MOSS, Italian acronyms of "MOnitoraggio delle Vibrazioni Ambientali" (AVT) and "MOnitoraggio dello Stato di Salute" (SHM), respectively. MOVA focuses on AVT, while MOSS is dedicated to the autonomous management of long-term aggregated SHM systems. The latter includes automated OMA, frequency tracking, filtering of environmental effects, fusion of heterogeneous sensor data, and supervised St-Id. The data fusion capability of MOSS specifically lies in the possibility of performing pattern recognition using arbitrary combinations of predictors and estimators, including vibration and non-vibration data. In this way, once set up, the user has online access to a number of control charts assessing the performance of all those desired damage-sensitive features, and the system triggers an alarm (visual, sound, and/or by e-mail) when an anomaly is detected in any of them. The initial releases of the codes were reported in reference [25], although new algorithms and tools have been constantly incorporated ever since.

Inspired by the potential of MOVA/MOSS, a second software tool specific for the SHM of highway bridges was also developed within a research project funded by Anas S.p.A. as reported in reference [124]. The software code, named P3P, was developed in collaboration with researchers from Politecnico di Milano and the University of Padova. P3P constitutes an user-friendly and updated version of MOVA/MOSS with specific functionalities addressing the prescriptions by the Italian guidelines of the monitoring of viaducts [5]. The software program includes automated OMA, frequency tracking, filtering of environmental effects, and damage detection through novelty analysis, as well as two modules specific for processing and analysis of seismic events and structural reliability analysis of bridges.

In the remainder of this chapter, a concise overview of the main functionalities of MOVA/MOSS and P3P are reported in Sections 6.2 and 6.3, respectively.

6.2.MOVA/MOSS: Ambient Vibration Testing and Integrated SHM

The overarching purpose of MOSS is the fully autonomous management of permanent integrated SHM systems. Typically, the work-flow of an SHM system using MOSS is sketched in Fig. 6.1. The monitoring system consists of an integrated sensor network deployed on the structure of interest, and of an in-place DAQ system that permanently collects the monitoring data. Subsequently, computer files containing monitoring records of certain time duration are sent through the internet or another data transmission system to a server or to the cloud where the data are stored.

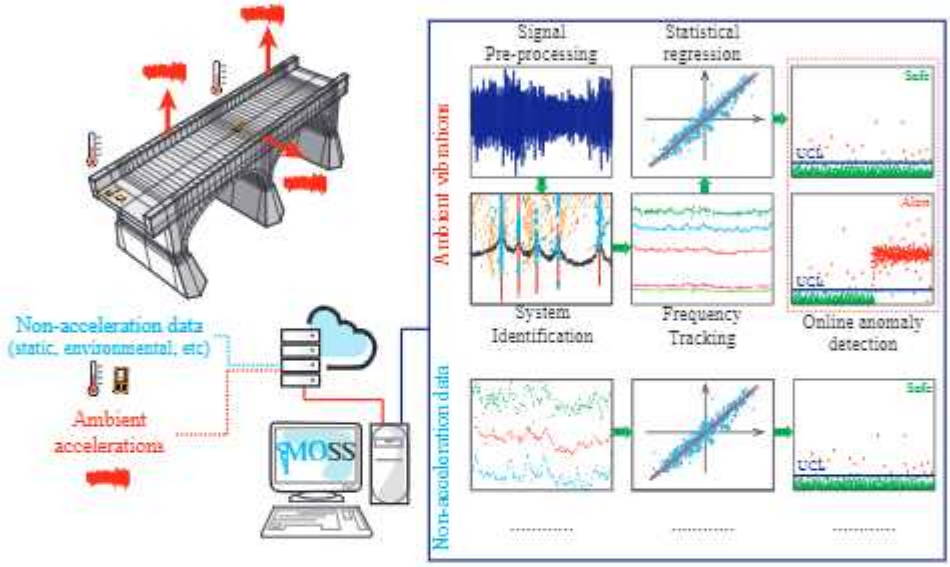

Fig. 6.1: Schematic of a permanent SHM system using MOSS.

MOSS automatically processes all the monitoring records and updates user-defined control charts. To do so, it distinguishes between dynamic measurements and measurement data of different nature (e.g. temperature sensors, strain gauges, or inclinometers). On one hand, MOSS performs automated OMA using the ambient vibration records according to the methodologies previously introduced in Chapter 3. This process comprises five sequential steps, namely (i) pre-processing of measurement records according to certain user-defined filtering process; (ii) automated OMA; (iii) frequency tracking; (iv) elimination of environmental effects through pattern recognition techniques; and (v) control charts and online anomaly detection. In parallel, MOSS processes the rest of measurement data and performs data fusion. Specifically, the user can freely decide to use these extra monitoring data as predictors and/or estimators. That is to say, non-dynamic monitoring data can be used to filter out the environmental effects over the resonant frequencies or, alternatively,

they can be used as damage-sensitive features. In the latter case, anomalies in their time series are investigated likewise vibration data through control charts. Therefore, MOSS permits the definition of multiple control charts and performs simultaneous online damage detection of diverse damage-sensitive features. Additionally, the user can introduce a DT of the structure along with an objective function involving some of the previously defined estimators so that MOSS can conduct online St-Id following the theoretical formulation previously outlined in Chapter 5. Once set up, MOSS manages automatically the data stream from the monitoring system and signal an alarm when an anomaly is detected in any of the constructed control charts.

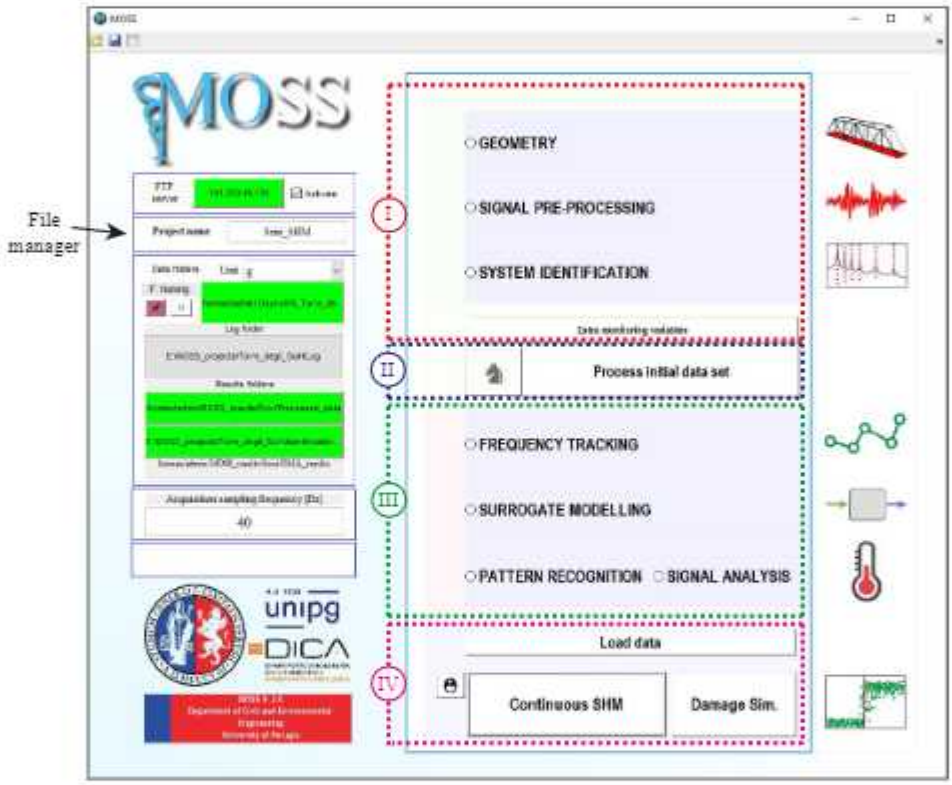

Fig. 6.2: MOSS main GUI.

Originally developed using MATLAB environment, MOVA and MOSS have been implemented in C++ providing a compact graphical user interface (GUI). The main GUI of MOSS is shown in Fig. 6.2. The interface is organized in four consecutive steps:

I **System Identification**: This step encompasses the main capabilities of MOVA for AVT, and has the purpose of defining the geometry of the structure and the signal processing procedure used for all the measure-

ment records. This includes the following sub-sections: *GEOMETRY*, *SIGNAL PRE-PROCESSING*, *SYSTEM IDENTIFICATION*, and *Extra monitoring variables*. The latter allows the user to introduce as many non-dynamic sensors (e.g. static or environmental) as desired by providing a reference tag, the measurement unit, naming protocol, and the computer folder that contains the record files.

II **Process of initial data set**: This step includes the sub-section named *Process initial data set* and generates an initial data population of modal features to be used in the subsequent steps. The initial data-set of measurements (preferably those corresponding to the training period) along with the results folders (including the processed signals and the identification results) are introduced through the file manager located in the left part of the interface.

III **Frequency tracking and elimination of environmental effects**: This comprises the sub-sections named *FREQUENCY TRACKING* and *MULTIVARIATE STAT. ANAL. (MSA)*, and it is devoted to defining the parameters for automated frequency tracking and the statistical models used for pattern recognition. Additionally, a module named *SURROGATE MODEL* is also available for performing SM-based St-Id.

IV **Damage detection**: This last step constitutes the core of MOSS, and performs the online damage detection of the previously defined damage-sensitive features. It includes the sub-sections indicated as *Continuous SHM* and *Damage simulation*. The latter allows the user to explore the effects of artificial damage upon the constructed control models.

Project configuration: This section of the GUI manages the definition of the monitoring data-base, general characteristics of the project (name, date), log folder, naming protocols, outputs settings, and file configuration properties (extension, header lines, decimal separator and text delimiter). MOVA/MOSS accept most file formats (.txt, .csv, .raw, .xlsx, .tdms) and allow the definition of arbitrary naming protocols to indicate the acquisition dates of the monitoring data. The archive where monitoring data are continuously stored can be local or accessible via FTP. The definition of the latter is conducted through the FTP manager shown in Fig. 6.3. After introducing the IP address of the repository, this manager allows the user to navigate through the archive and identify the directories containing the monitoring database.

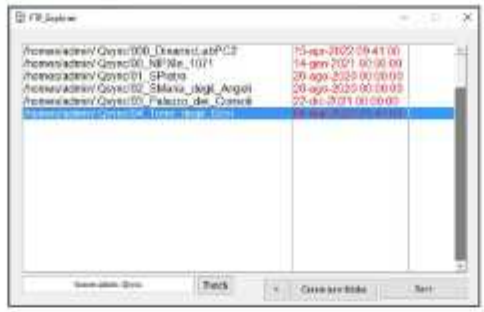

Fig. 6.3: FTP manager in MOVA/MOSS showing the monitoring archive of the Laboratory of Structural Dynamics of the University of Perugia.

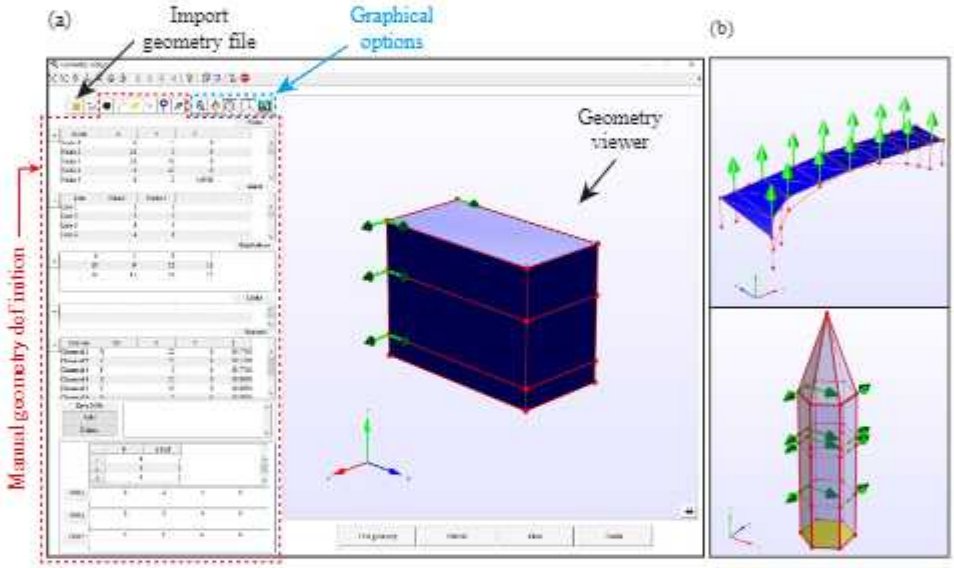

Fig. 6.4: Screenshot of the geometry module: (a) Consoli Palace, (b) reinforced-concrete bridge and masonry tower.

Geometry module: This interface allows the definition of a geometrical model and the accelerometer layout for the representation of the mode shapes. Three-dimensional models can be constructed using nodes, lines, and planes, as well as kinematic conditions between active and slave nodes. Every active node is defined at least by a measurement channel and the corresponding direction/orientation ($\pm x$, $\pm y$, or $\pm z$). Kinematic conditions include rigid-plane diaphragms and link conditions between slave and active nodes. Additionally, the interface incorporates a formula editor allowing for inserting general symbolic constraints between sets of nodes. The whole process can be carried out graphically using the mouse, manually by typing the information directly in the

edit tables, or by loading a geometry file in ASCII format. Figure 6.4 (a) shows the geometrical model built for the AVT of the Consoli Palace. The model includes 9 acceleration channels and rigid-plane diaphragms at each floor of the building. For illustrative purposes, Fig. 6.4 (b) shows two sample geometries defined for a bridge structure and a tower.

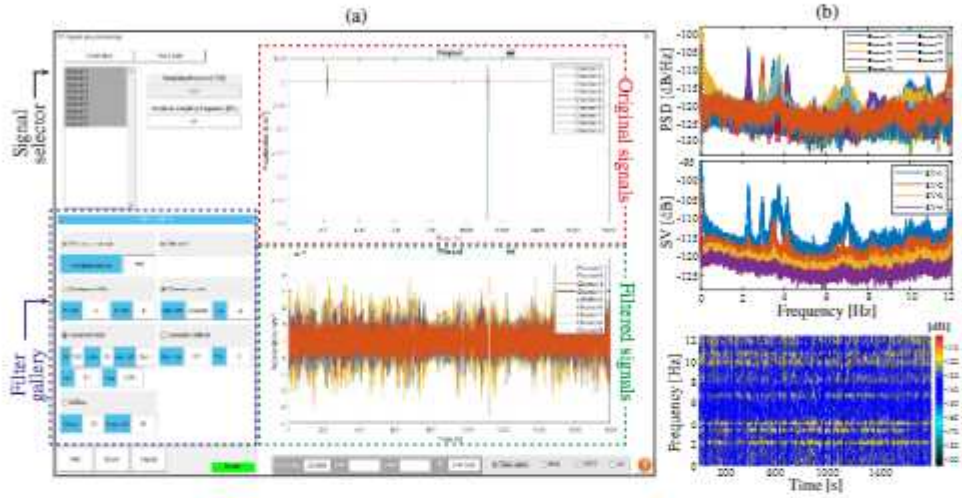

Fig. 6.5: Screenshot of the signal pre-processing module (a), and analyses of the filtered signals (b).

Signal pre-processing module: This module, shown in Fig. 6.5 (a), permits the definition of signal processing sequences to minimize the effects of noise and the presence of abnormal events. Specifically, the software interface includes: signal downsampling, moving average/median filtering, linear detrend, band-pass filtering, Hanning window filtering of signal spikes, Hanning window filtering of non-stationary excitations produced by swinging bells (common in CH structures), and a robust Multichannel Singular Spectrum Analysis (MSSA) denoising approach [228]. The software accounts for the application order of the selected filtering techniques, and the graphical representation of the filtered signals against the raw ones enables users to check the effectiveness of the implemented signal processing sequence. The comparison can be performed in the time domain, through PSDs, time-frequency analysis (short Fourier Transform, Choi Williams and Wigner-Ville distributions), and SVs of the PSDs (see Fig. 6.5 (b)). Specifically, Fig. 6.5 presents the pre-processing of the accelerations recorded during the AVT of the Consoli Palace conducted on May 4th 2017. In this case, ambient vibration data were collected during 30 min at a sampling frequency of 1652 Hz. The raw signals evidence the strong effect of the swinging bells located in the bell-tower of the palace, which ring regularly every 15 minutes. In order to minimize these effects and improve the system

identification, the selected signal processing sequence includes: downsampling to 40 Hz, linear de-trend, moving average filtering with time window length of 200 s, and Hanning window filtering to eliminate the effect of swinging bells and signal spikes. Note that the swinging of bells induces a significant violation of the white noise assumption and must be filtered out before conducting the system identification. The implemented time-domain Hanning window filter suppress those parts of the signals affected by swinging bells, in such a way that the resulting signals do comply with the white noise assumptions.

System identification module: This interface manages the vibration-based identification of the structure. Here the user can select any of the identification techniques previously introduced in Chapter 3. The identification results are presented in the shape of tabulated data, stabilization diagrams (SSI and p-LSCF), or SVs of the PSDs (EFDD), exportable reports, and the histogram representation of the MAC matrix. Moreover, this interface counts on a specific section for mode shape representation, including the animation of complex modes, complexity plots, and display of quality factors such as the Mode Complexity Factor (MCF), Mode Phase Collinearity (MPC), and Mean Phase Deviation (MPD). As an example, Fig. 6.6 (a) shows a screenshot of this module with the identification results obtained with the AVT of the Consoli Palace using COV-SSI, and Fig. 6.6 (b) shows a screenshot of the mode shape representation interface with the analysis of the first vibration mode.

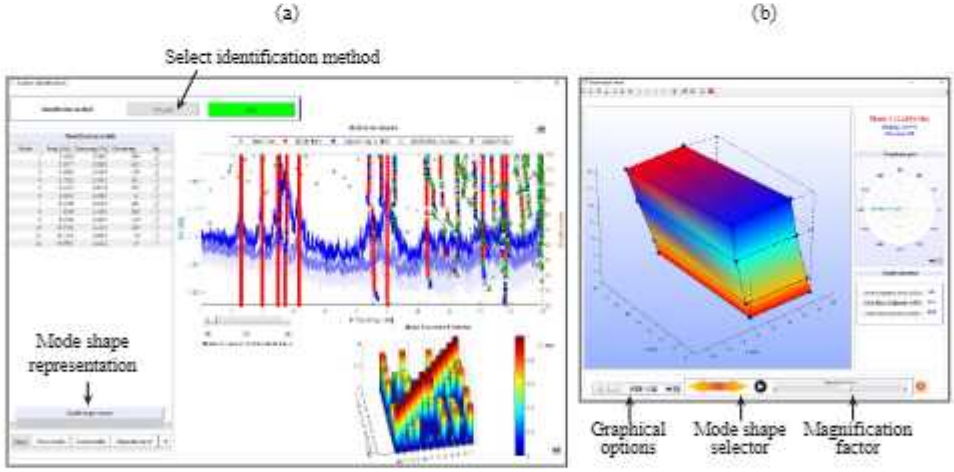

Fig. 6.6: Screenshots of the system identification module (a) and mode shape viewer (b).

Frequency tracking module: Once the initial data population has been processed, this module allows to extract the time series of resonant frequencies, damping ratios, and mode shapes of the structure. To do so, the user must

introduce a reference set of frequencies (typically retrieved from an AVT using a relatively large set of sensors) and a set of tolerances on allowable maximum relative frequency variations and minimum MAC values. Alternatively, the automated identification procedure introduced in Section 3.5 can be also used to define the modal baseline if a separate AVT is not available.

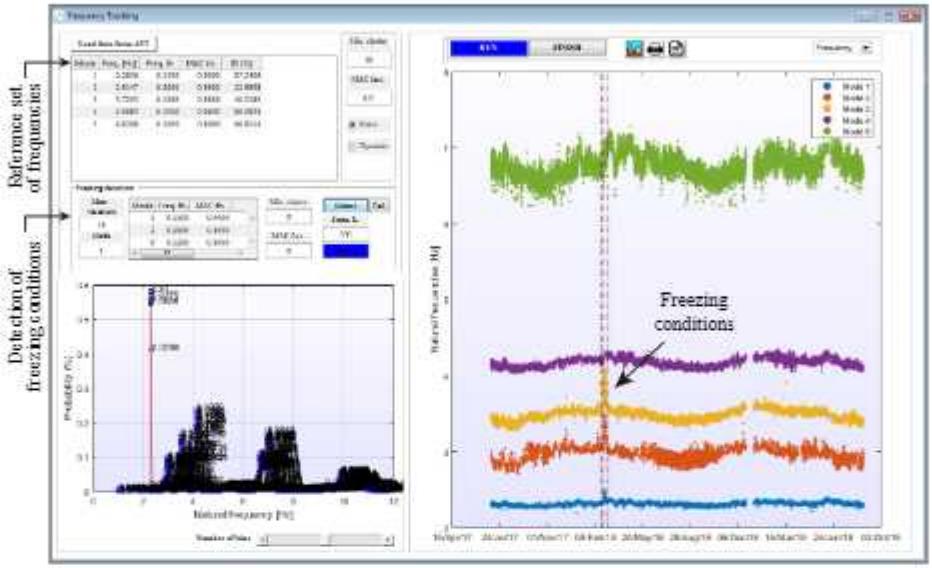

Fig. 6.7: Screenshot of the frequency tracking module with identification results of the permanent SHM system installed in the Consoli Palace.

Figure 6.7 shows a screenshot of this interface with the results obtained from the long-term monitoring of the Consoli Palace. The vibration-based identification of the palace was conducted using Cov-SSI according to the automation procedure previously presented in Section 3.4.2. In this case, only five modes corresponding to Fx1, Fy1, L1, T1, and L3 were tracked, while Mode L2 was disregarded because of difficulties in its separation from modes L1 and T1. This is due to the reduced number of sensors used in the monitoring (only 3), what hinders the discrimination of very closely spaced modes by means of MAC comparison. Special attention must be also devoted to the potential occurrence of freezing conditions. Specifically, freezing conditions are clearly visible in the time series of the resonant frequencies of the Consoli Palace in Fig. 6.7 during the time period from February 25th to March 1st 2017. In order to automatically detect such conditions, the frequency tracking interface counts on a specific section for that purpose. This section incorporates a gradient-based detection algorithm that allows to identify data regions of certain time length (336 h in the example of Fig. 6.7 and marked with black dashed lines) with sudden increases in the resonant frequencies. Once detected, the user can introduce new tolerance values for performing local frequency tracking over these

regions. Afterward, freezing conditions can be tackled in two different ways: using clustering analysis and setting different statistical regression techniques as illustrated later, or directly dismissing the identification results corresponding to the detected regions. The latter approach is acceptable when freezing conditions only occur during short periods of time. Finally, the module also allows to set up different modal baselines for different periods of time in cases the structure experience considerable variations (e.g. rehabilitation interventions).

Surrogate modeling module: This module comprises all the necessary steps to conduct SM-based St-Id as reported in Chapter 5. These include: (i) Construction of the ED using LHS and Sobol sampling; (ii) SM training (Kriging and RSM); (iii) Definition of St-Id algorithm (deterministic or probabilistic). The user can also introduce a general SM trained independently in the shape of a MATLAB (.mat) function. Once defined, the outputs of the St-Id are considered as general estimators susceptible for statistical pattern recognition and novelty analys in the following modules.

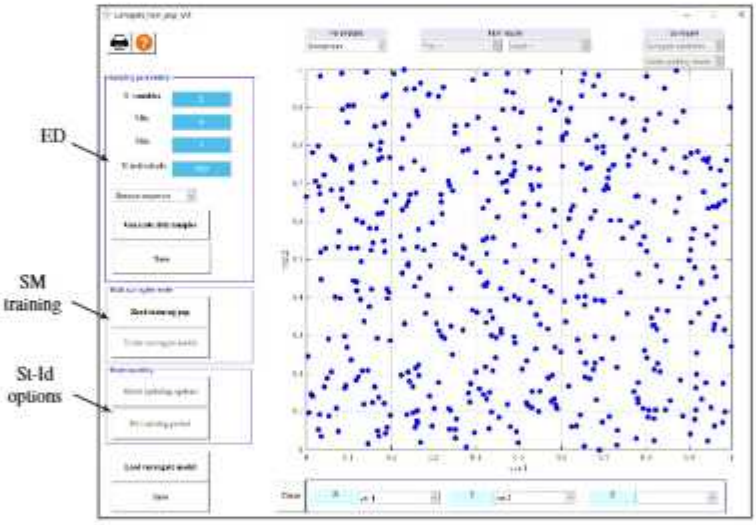

Fig. 6.8: Screenshot of the surrogate modeling module in MOSS.

Multivariate statistical analysis module: This module, shown in Fig. 6.10, permits the definition of different statistical models accounting for distinct damage-sensitive features. Every model, identified by an user-defined label name, is assessed through statistical pattern recognition in the subsequent damage identification module. Specifically, this interface includes the following features:

- **Outliers elimination**: Outliers represent anomalous data points arising

as a result of identification and/or tracking errors. Their presence in the time series of damage-sensitive features may drastically reduce the effectiveness of regression models for the elimination of environmental effects, and it can grossly distort the computation of the mean and covariance matrices used later for statistical process control. With the aim of reducing the number of outliers in the training period, this interface includes the MCD procedure previously reported in Section 2.3.

- **Filling of missing data**: A very common situation in SHM concerns the appearance of missing data due to faulty sensors, identification errors, electrical shutdowns or battery issues. To solve this issue, a specific imputation module is included in MOSS as shown in Fig. 6.9. The module counts on a large variety of imputation methods, including linear interpolation, autoregressive modeling, shallow/deep neural networks, and several PCA-based imputation algorithms (refer to [229]).

- **Clustering analysis**: The interface incorporates a GMM for detection of freezing conditions. In particular, the algorithm classifies the damage-sensitive features into two separate groups of dissimilar variance. Then, different regression methods can be built for each data cluster and so remove the environmental effects in a more effective manner.

- **Estimators/Predictors definition**: Every statistical model is defined by a set of estimators (independent variables) and predictors (dependent variables). The user can freely select as estimators and/or predictors the resonant frequencies, damping ratios, max/min acceleration values, and acceleration root-mean-squares (RMS), as well as the mean, max/min, and standard deviation values of the non-dynamic measurements. Additionally, the interface incorporates a *variable calculator* that allows to define new estimators/predictors by typing general mathematical expressions involving different variables. This includes the possibility of adding time delays in certain parameters to build dynamic regression models, that is to say, models accounting for past observations of certain predictors to account for thermal capacitance effects (e.g. the dynamics of heating up and cooling down processes).

- **Build of statistical models**: The user can select among eight different regression models, including output-only (PCA, FA, co-integration and AANN) and input-only models (MLR, SMLR, ARX, and MLR/PCA).

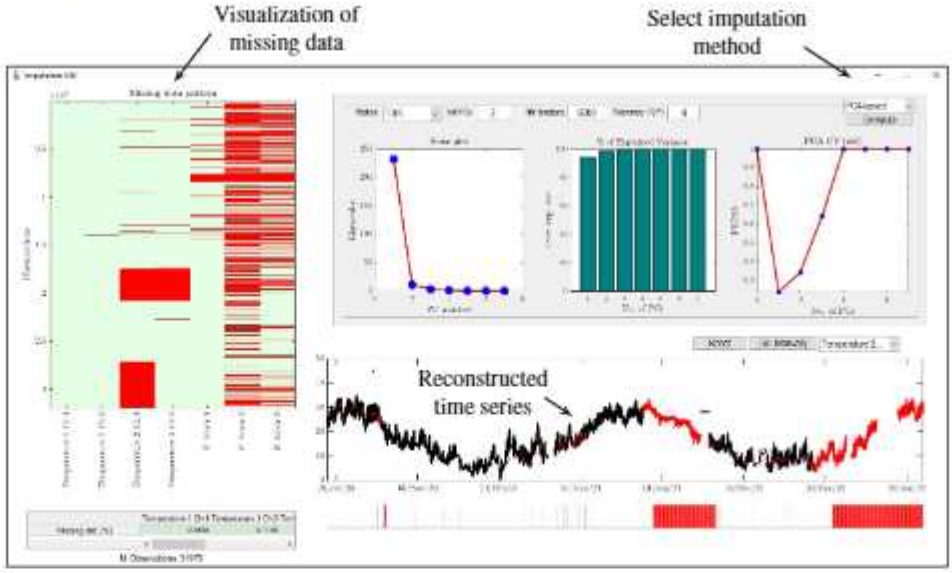

Fig. 6.9: Screenshot of the GUI for filling missing data in MOSS with the imputation results of the temperature time series acquired in the Consoli Palace using the PCA-based trimmed scores regression (TSR) method.

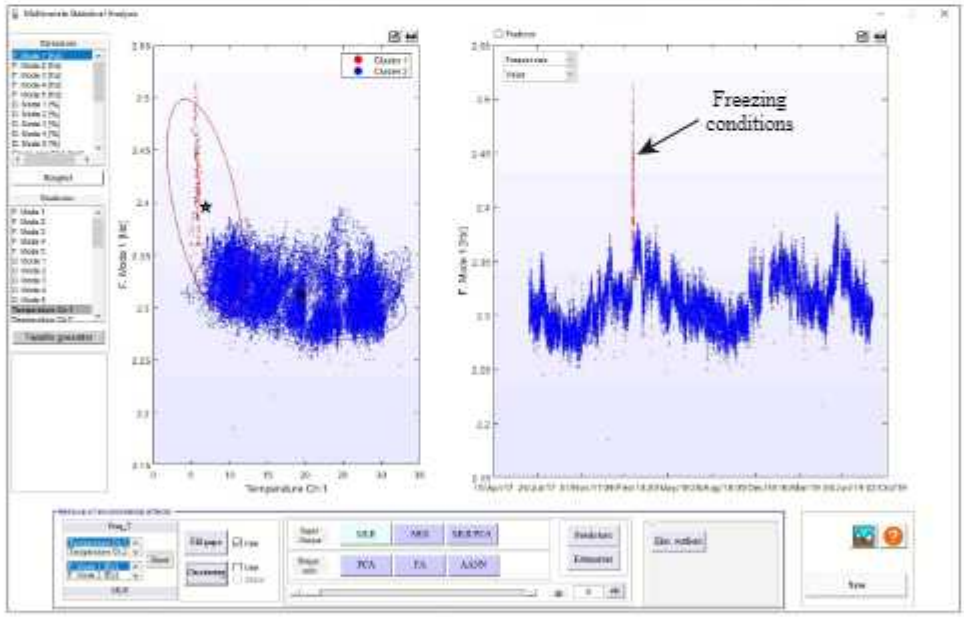

Fig. 6.10: Screenshot of the multivariate statistical analysis module with the clustering results of the resonant frequencies of the Consoli Palace identified during the first year of monitoring.

The results in Fig. 6.10 show the application of GMM clustering for identifi-

cation of freezing conditions in the case study of the Consoli Palace. It is noted that the sudden increase of natural frequencies induced by freezing conditions can be accurately detected by the model. Then, different statistical models can be applied to eliminate the environmental effects in each of the identified clusters. Nevertheless, for the sake of simplicity, and given that freezing conditions were only observed once during the whole monitoring period, the data-set corresponding to freezing conditions have been dismissed when using the *frequency tracking* module. On this basis, Fig. 6.11 analyses the correlation between the mean temperature and crack amplitudes assessed by LVDT-1 (C1) against the resonant frequencies of global modes Fx1, Fy1, and T1 of the Consoli Palace during the one-year training period.

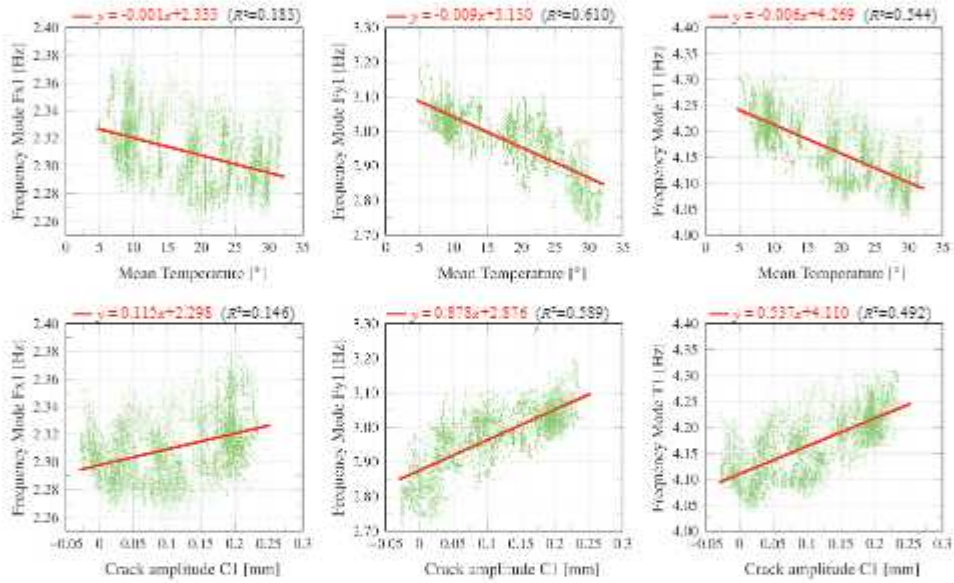

Fig. 6.11: Correlation between mean temperature and crack amplitudes assessed by LDVT-1 and the resonant frequencies of global modes Fx1, Fy1, and T1 of the Consoli Palace during the one-year training period.

In light of the previous analyses, three different statistical models are defined in the *Multivariate statistical analysis* module, labeled as MLR-F, PCA-F and ARX-C. Models MLR-F and PCA-F define the resonant frequencies as estimators, while ARX-C considers for this purpose the crack amplitude C1. The aim of these models is to perform a local/global damage assessment of the Consoli Palace. On one hand, the first two models evaluate the presence of damage affecting the overall stiffness of the structure, while the second one accounts for local damage inducing behavioral variations in the amplitudes of crack C1. In the PCA-F model, only two principal components (PCs) sufficed to explain more than 90% of the variance of the estimators. The characteristics of these statistical models are as follows:

- MLR-F: Estimators → {Fx1, Fy1, L1, T1, L3}; Predictors → {T1, T2, C1, C2}; Regression model → MLR.
- PCA-F: Estimators → {Fx1, Fy1, L1, T1, L3}; Regression model → PCA (retained PCs: 2).
- ARX-C: Estimators → {C1}; Predictors → {T1, T2}; Regression model → ARX.

Figure 6.12 depicts the statistical predictions obtained for all the defined models and the corresponding Hotelling's T-square control charts. For clarity purposes, only the time series of the frequencies of mode Fx1 and crack amplitudes C1 are plotted in the figure during the one-year training period. With regard to the statistical predictions obtained by models MLR-F and PCA-F, it is noted that better fittings of the natural frequency of Fx1 are obtained using PCA. Conversely, larger differences between experimental and statistical predictions are observed in the MLR-F model. In this case, it is noted that although the use of temperature and crack amplitude measurements allows the modeling of the daily and, to some extent, seasonal variations in the resonant frequencies, there are still some seasonal fluctuations that cannot be accurately reproduced. This may be ascribed to the specific sensor locations, which may fail at characterizing the temperature distribution throughout the building. On the other hand, it is noted in the ARX-C model that the use of temperature measurements as exogenous variables can well reproduce both the seasonal and daily fluctuations in the time series of crack amplitudes C1. However, it is important to remark that the statistical predictions using a MLR model instead of an autoregressive model led to large residuals. Specifically, while seasonal fluctuations could be captured sufficiently well using only temperature measurements as predictors, daily fluctuations could be not accurately reproduced. This fact may indicate the correlation of crack amplitudes with the temperature distribution in different locations of the building (recall that the temperature sensors are located right aside the LVDTs). The graphs in the right hand side of Fig. 6.12 reports the time series of T^2 distances along with the UCL corresponding to a confidence level of 99%. Here, it is noted that the number of outliers after the training period is slightly larger in the MLR-F model (6.03%) compared to the PCA-F (2.85%), which confirms the better fitting of the experimental data using PCA.

Damage detection and simulation modules: The damage detection module, shown in Fig. 6.13, allows to manage permanent SHM systems in real-time and in a completely autonomous way. The interface includes real-time graphs of the time series of the estimators, predictors, and measurement data, a web cam of the monitored asset, as well as the corresponding control charts. Every time a new data file is found, the interface graphs are updated and the software

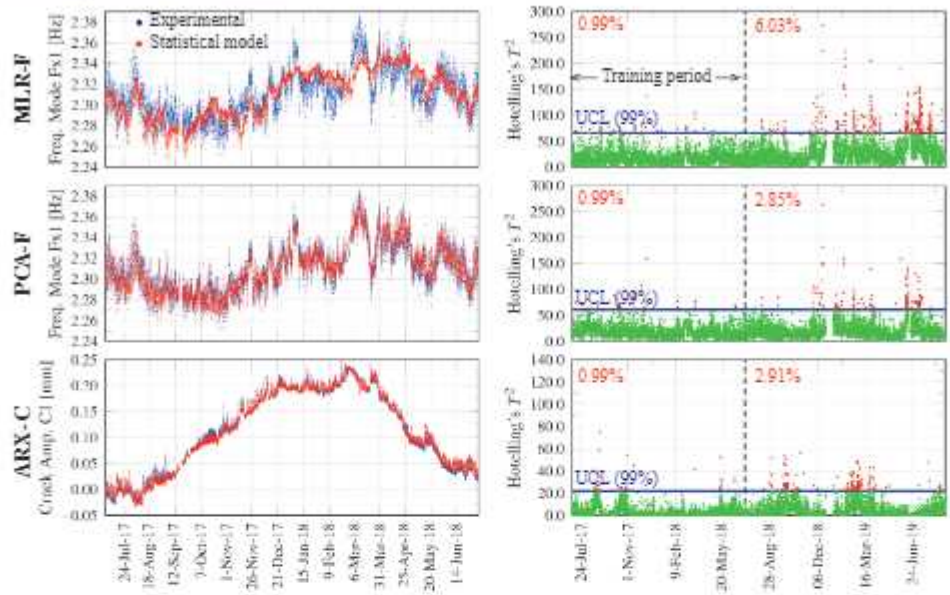

Fig. 6.12: Plots of time histories of the natural frequency of mode Fx1 and crack amplitude C1 obtained by statistical models MLR-F, PCA-F, and ARX-C, and corresponding Hotelling's T-square control charts.

performs damage detection based on all the previously defined statistical models. If an anomaly is found in any of the models, the software triggers an alert and notifies the user with a sound-alert, an alert message in the console of the interface, and (if desired) an e-mail with an attached screenshot of the control chart with the detected anomaly. In this way, the user can check whether a system notification may be a false alarm or, conversely, an in-situ inspection ought to be planned. The work-flow of this interface comprises the following steps: (a) automatic detection of new data files, signal pre-processing, system identification, and frequency tracking; (b) St-Id (if defined), construction of statistical models, elimination of environmental effects, and updating of control charts; and (c) automatic damage detection. The progress of each step is notified in the console of the interface. Moreover, if no files are found in a maximum period of time prescribed by the user, the software sends a warning notification of unintended system shutdown. Additionally, an extra module dedicated to the analysis of all the processed acceleration time histories is also included as shown in Fig. 6.14. In the case a sudden anomaly is detected, this module allows the user to inspect in detail the corresponding time series of accelerations to verify whether the anomaly may be due to problems in the monitoring system or to an extreme event such as an earthquake.

Note that a damage detection algorithm based upon the detection of outliers in the control charts would lead to a large number of false alarms. In

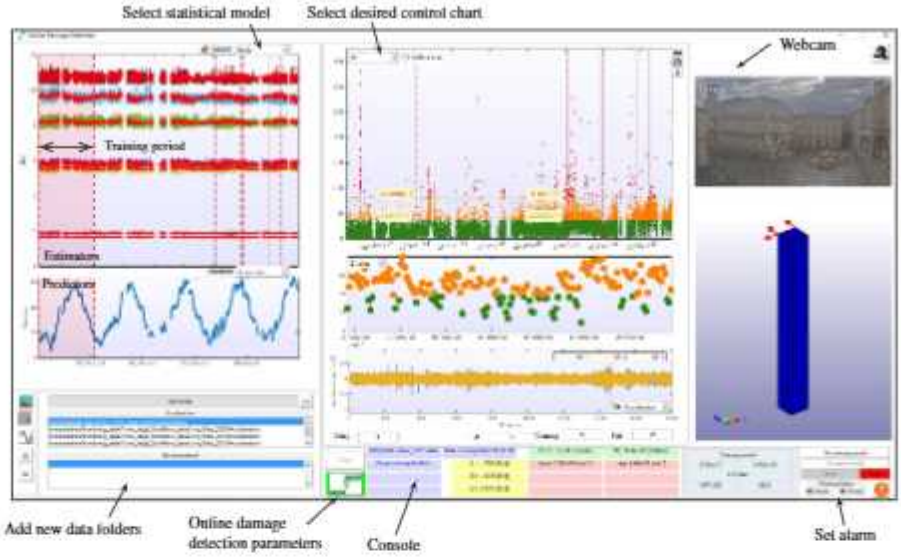

Fig. 6.13: Screenshot of the damage identification module.

particular, considering a subgroup size of 4 and a UPC of 99%, this would result in $(365 \cdot 24 \cdot 2/4)/100 = 43.8$ alarm notifications per year on average, even when the structure remains in healthy conditions. To minimize the rate of false alarms, MOSS includes the automated damage detection method in Section 2.6. Moreover, in order to tune the convergence parameter cp_{max} and assess the effectiveness of a statistical model for damage detection, the software also counts on a *Damage Simulator* module available in the last section of the main GUI in Fig. 6.2. This allows the user to introduce artificial damage scenarios in terms of mean shifts in the estimators from a given date forward. As an example, Fig. 6.15 shows the control charts obtained for the previously defined statistical models (MLR-F, PCA-F, and ARX-C) when artificial damage is introduced from August 20st 2018. In particular, frequency decays of $\Delta f_1 = -3.44$E-2 Hz $(-1.5\%\overline{\text{Fx1}})$ and $\Delta f_1 = -2.53$E-2 Hz $(-1.0\%\overline{\text{Fx1}})$ are introduced in the time series of the resonant frequency of mode Fx1 for MLR-F and PCA-F models, respectively. It is important to remark that, given the inferior fitting performance of the MLR-F model formerly reported in Fig. 6.12, a larger frequency decay value was necessary in this case to successfully detect the imposed damage. In the case of the ARX-C model, a mean shift of 1.10E-2 mm $(10\%\overline{\text{C1}})$ is included in the time series of crack amplitudes C1. A convergence parameter value of $cp_{max} = 96$ is assumed, that is to say, the same anomaly must be detected in 96 consecutive steps (48 hours since every file is 30-min long) to be considered as a potential fault.

Note that in Fig. 6.15 the imposed damage scenarios were successfully detected by all the statistical models. Additionally, a total of 15, 17, and 14 false

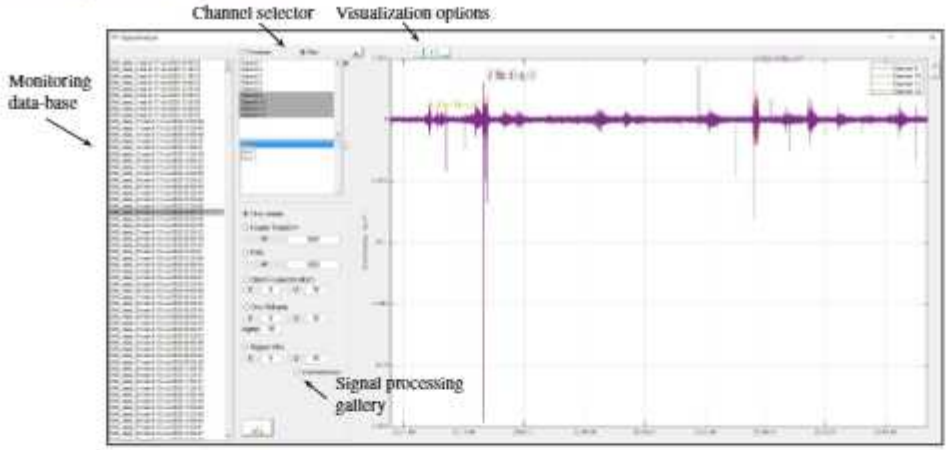

Fig. 6.14: Screenshot of the signal analyzer module in MOSS.

positives are detected for the MLR-F, PCA-F, and ARX-C models, respectively. These are indeed related to noticeable shifts in the corresponding residuals and arise even when no damage is introduced. This circumstance evidences limitations of the statistical models to reproduce certain in-control operational and/or environmental effects. It is thus concluded that the fitting efficiency of the selected statistical models within the training period determines the minimum detectable damage and the appearance rate of false alarms. In the particular case of the Consoli Palace, a denser monitoring of the temperature distribution in the building, as well as of other environmental factors such as the humidity in the masonry, may reduce the minimum detectable anomalies and the false alarm rate.

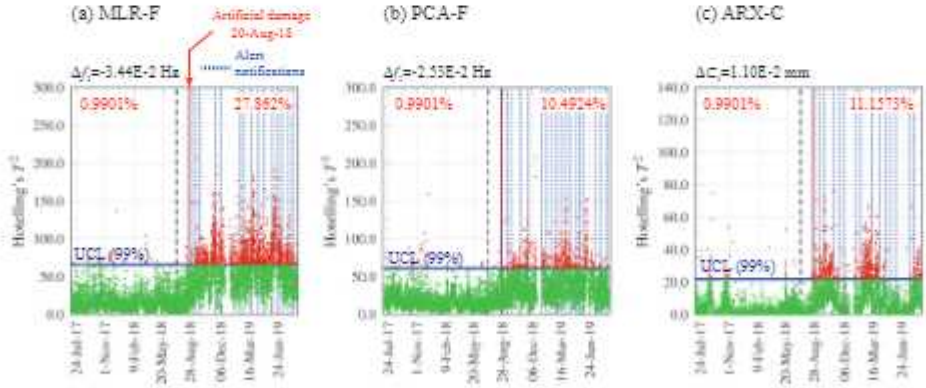

Fig. 6.15: Automatic detection of simulated damage scenarios applied to the monitoring time series of the Consoli Palace considering different statistical models: (a) MLR-F, (b) PCA-F, and (c) ARX-C.

Finally, MOSS allows to live stream the identification results of the SHM system on a website. In particular, Fig. 6.16 shows the SHM section in the website of the Laboratory of Structural Health Monitoring and Earthquake Engineering (https://shmlab.weebly.com) with the tracking of the resonant frequencies of the Sciri Tower. In addition, the time series of identified elastic moduli of the macro-elements reported in Section 5.5.2 and continuously identified through deterministic St-Id of a RSM meta-model are also shown. These results demonstrate the feasibility of automating the SHM problem within the statistical pattern recognition paradigm and represent one of the first realistic applications of digital twinning within the realm of civil engineering. Furthermore, the commitment of this thesis for freely disseminating the SHM results among the scientific community and the general public is envisaged to accelerate the technological transfer of SHM to engineering routine practice.

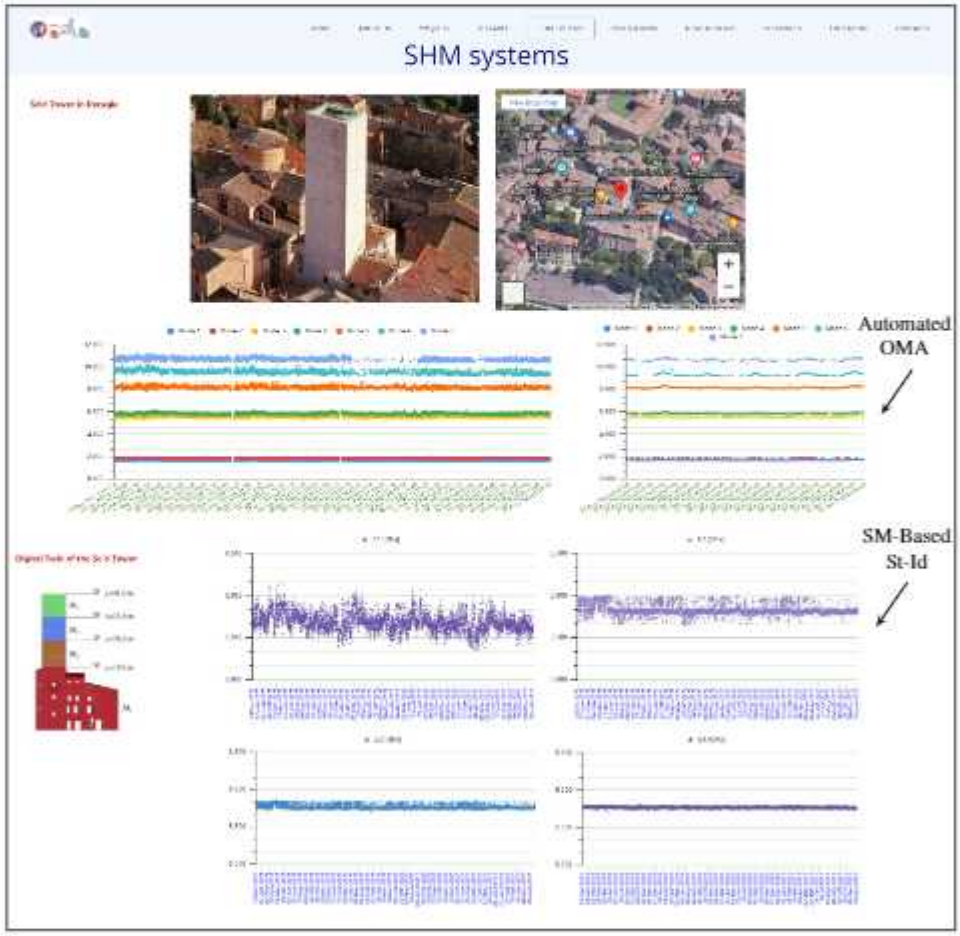

Fig. 6.16: SHM section in the website of the Laboratory of Structural Health Monitoring and Earthquake Engineering of the University of Perugia showing the identification results of the Sciri Tower.

6.3.P3P: SHM of highway bridges

Similarly to MOSS, the general work-flow of P3P is sketched in Fig. 6.17 and involves (i) signal pre-processing; (ii) data normalization and (iii) anomaly detection. The outcome of this process is the generation and automated updating of multiple control charts assessing the desired sets of damage-sensitive features.

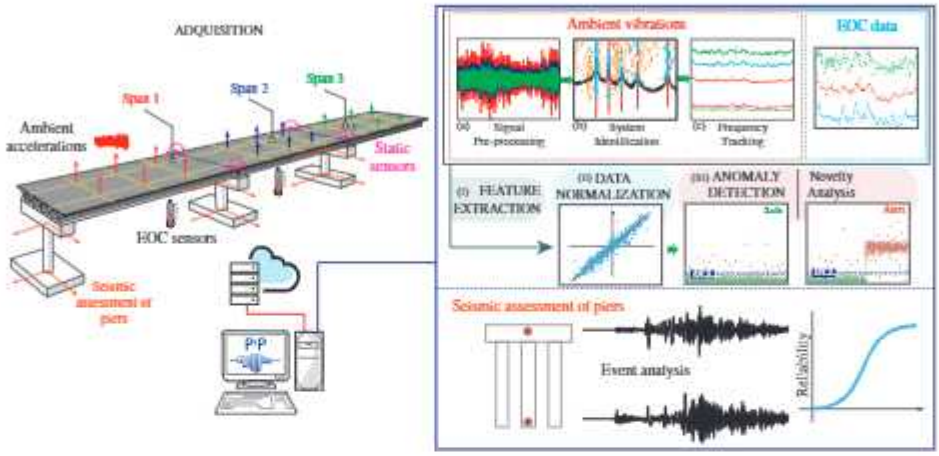

Fig. 6.17: Schematic of a permanent SHM system installed in a bridge structure using P3P.

The main GUI of P3P, shown Fig. 6.18, comprises 10 main modules, namely (i) *Project configuration*; (ii) *Modal Geometry*; (iii) *Signal pre-processing*; *System Identification - OMA*; (iv) *Definition of static/environmental data*; (v) *Modal tracking*; (vi) *Statistical Pattern Recognition*; (vii) *Continuous SHM*; (viii) *Seismic analysis*; and (ix) *Reliability analysis*.

Unlike MOVA/MOSS, the geometry module in P3P allows to identify sets of channels belonging to different spans in multi-span bridges. Finally, the user can also set certain channels dedicated to seismic analysis (typically at the base and top of piers). Moreover, the seismic and reliability analysis modules are exclusive of P3P. The seismic reliability module allows to identify seismic events as acceleration signals overpassing a certain user-defined acceleration threshold. Then, the user can conduct the analysis of the registered seismic event, including its comparison with the design spectra prescribed by the Italian seismic code (NTC 2008), and the computation of meaningful engineering parameters such as Arias intensity, cumulative absolute velocity (CAV), response spectra, as well as the displacement drifts between the base and top of the piers. On the other hand, the reliability analysis module allows to compute the reliability index of the bridge under study by introducing its geometrical properties (dimensions, number of girders, typology and loading conditions), material parameters (concrete and steel classes), and the cross-section of the

girders (dimensions and position of reinforcements).

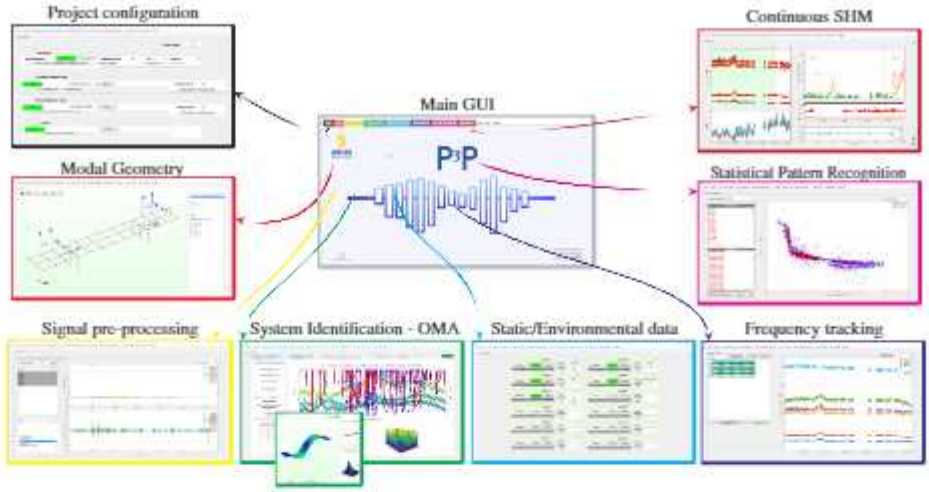

Fig. 6.18: Software architecture of P3P.

Let us illustrate the potential of P3P with the identification results of the Trigno V bridge (Section 1.5.8). Note that the OMA of long multi-span bridges with simply supported span configuration represents a formidable problem. In particular, it is well-known in the literature that repetitive or quasi-periodic structures exhibit clustered modes with closely spaced natural frequencies and modes with similar wavelengths [153], which hampers considerably the discrimination of physical poles from stabilization diagrams. To avoid such difficulties, the modal identification was conducted at the span level by grouping the accelerometers deployed in each span as separate subgroups. Ambient vibrations were processed including a linear detrend, second-order Butterworth band-pass filter with cut-off frequencies of 1 Hz and 15 Hz, and down-sampling to 30 Hz. An example of the processed acceleration time series and the corresponding PSD curves for the second span of the Trigno Bridge are furnished in Figs. 6.19 (a) and (b). Then, the automated Cov-SSI procedure previously introduced in Section 3.4.1 was applied to identify the modal signatures of all the spans. In this light, Fig. 6.20 (a) shows the stabilization diagram obtained from the second span of the Trigno Bridge using the processed time signals from Fig. 6.19. The modal identification in all the spans was conducted with time lag parameters j_b ranging from 24 (0.8 s) to 44 (1.45 s), and model orders between 2 and 120 with steps of 2. For the elimination of spurious poles, HC include maximum damping ratios of $\zeta_{max} = 10\%$ and minimum MPC values of 80%. Besides, a minimum cluster size of 20 and a maximum distance $d_{max} = 0.07$ were set for the clustering of stable poles. The identification results in Fig. 6.20 (a) reveal the existence of five alignments of stable poles. Is is observed in Fig. 6.20 (b) that the automated OMA procedure succeeds at identifying five clusters

of stable poles. Note that the two first clusters (with frequencies of 3.88 and 4.16 Hz) correspond to two clear peaks clearly observable in both the SVs of the spectral matrix (inserted in the background of Fig. 6.20 (b) for clarity purposes) and the PSD curves from Fig. 6.19 (b). Indeed, these clusters are highly populated with stable poles identified at most of the considered model orders. Conversely, the remaining poles in the frequency broadband between 8 and 14 Hz are noticeably less populated, with a considerable number of misclassification at several model orders. This fact agrees with the inspection of the PSD curves or the SVs, which, despite exhibiting energy concentrations at frequencies neighboring the identified clusters, do not present clear resonant peaks. Since the traffic was considerably intense during the acquisitions, this is conceivably ascribed to the interaction with the passing vehicles, which may be masking the structural vibrations in this frequency range.

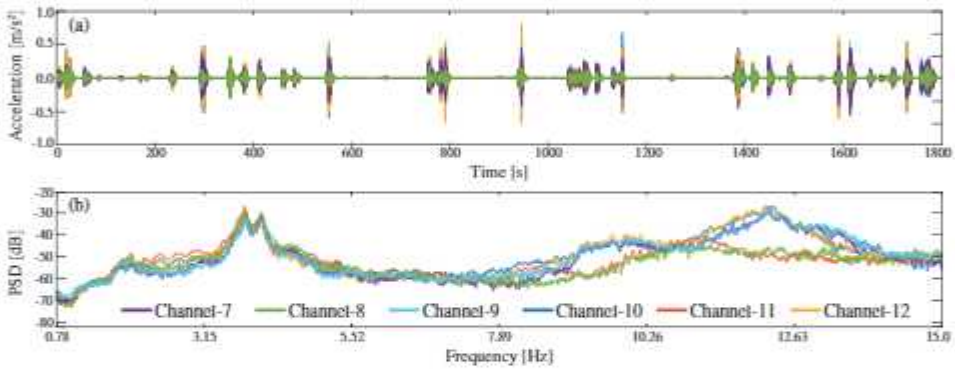

Fig. 6.19: Ambient vibrations recorded in the second span of the Trigno Bridge (a), and corresponding PSD curves (4096 data points, frequency resolution of 7.32E-3 Hz, 11:00 p.m., October 13th) (b).

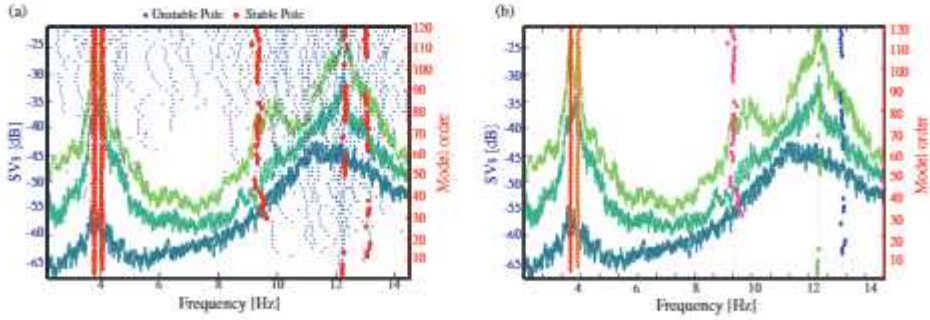

Fig. 6.20: Modal Identification of the second span of the Trigno Bridge (11:00 p.m., October 13th 2021): (a) Stabilization diagram, and (b) clusters of identified physical modes.

Following the previous procedure and after interpretation of the natural mode shapes, four vibration modes were consistently found in all the spans of the bridge as illustrated in Fig. 6.21. The identification results averaged over all the acquisitions are reported in Table 6.1, and the resonant frequencies of all the spans of the Trigno Bridge are also illustrated in Fig. 6.22 for easy interpretation of the results. These include two closely spaced modes, namely a first-order flexural mode (3.8-3.9 Hz) and a first-order torsional mode (4.0-4.2 Hz), a second-order torsional mode (9.3-12.3 Hz), and a second-order flexural mode (12.0-13.2 Hz). Note in Table 6.1 that, indeed, all the spans exhibit very close resonant frequencies (especially the first two modes) and mode shapes with very similar wavelengths (Fig. 6.21), which justifies the use of span-wise identification. Finally, note that low variability was found between the resonant frequencies identified over all the acquisitions (average variability of 0.4%). Conversely, the identification of structural damping is considerably more uncertain, with large variability ranges as common in OMA of moderately rigid civil engineering structures.

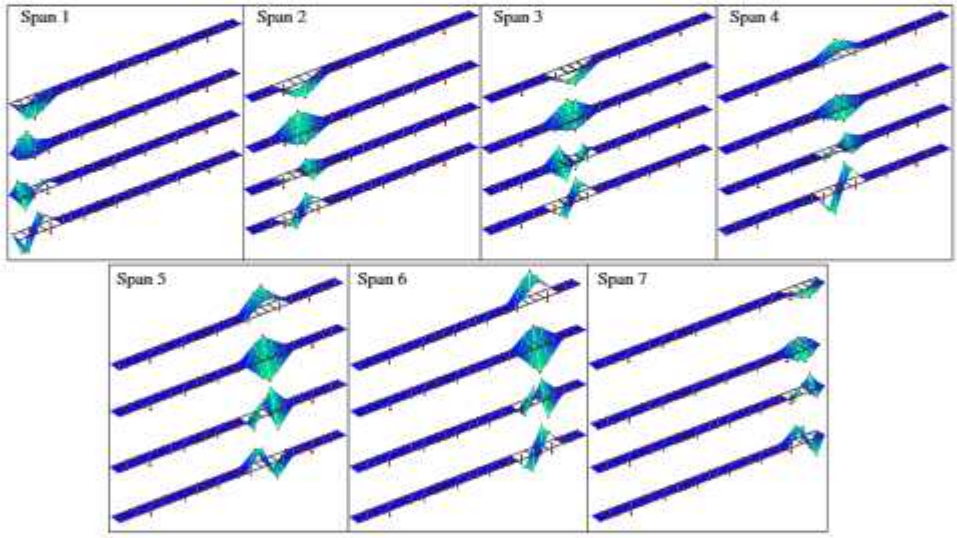

Fig. 6.21: Natural mode shapes of the Trigno Bridge (11:00 p.m., October 13th 2021).

Table 6.1: Modal identification results of the Trigno V Bridge (October 13th).

	Mode No.	f_i [Hz]	ζ_i [%]		Mode No.	f_i [Hz]	ζ_i [%]
Span 1	1	3.87 ± 3.4E-01%	1.62 ± 7.8%	Span 5	1	3.85 ± 1.9E-01%	1.72 ± 23.9%
	2	4.16 ± 7.3E-02%	2.57 ± 10.1%		2	4.13 ± 8.4E-01%	2.57 ± 22.2%
	3	10.06 ± 8.2E-01%	2.62 ± 57.4%		3	9.74 ± 3.2E-01%	2.09 ± 13.2%
	4	13.05 ± 9.5E-02%	1.34 ± 25.9%		4	12.76 ± 5.8E-01%	1.85 ± 16.5%
Span 2	1	3.79 ± 3.6E-02%	1.36 ± 6.6%	Span 6	1	3.82 ± 1.8E-01%	1.47 ± 9.9%
	2	4.06 ± 4.6E-01%	2.39 ± 49.0%		2	3.98 ± 4.1E-01%	3.49 ± 7.7%
	3	9.31 ± 8.2E-01%	3.25 ± 10.0%		3	9.84 ± 1.9E+00%	4.84 ± 15.4%
	4	12.20 ± 2.6E-01%	1.39 ± 7.9%		4	12.49 ± 7.8E-01%	1.53 ± 25.2%
Span 3	1	3.85 ± 2.5E-01%	1.24 ± 25.8%	Span 7	1	3.89 ± 3.7E-01%	1.88 ± 42.8%
	2	4.11 ± 2.9E-01%	1.60 ± 45.5%		2	4.13 ± 6.0E-01%	1.95 ± 17.9%
	3	9.32 ± 2.7E-01%	2.14 ± 27.8%		3	12.26 ± 9.7E-02%	1.91 ± 45.2%
	4	12.04 ± 2.5E-01%	1.61 ± 30.3%		4	13.15 ± 2.5E-01%	2.18 ± 12.1%
Span 4	1	3.84 ± 2.3E-01%	1.61 ± 16.8%				
	2	4.09 ± 8.8E-01%	4.25 ± 17.8%				
	3	11.19 ± 2.1E-01%	1.61 ± 36.7%				
	4	12.09 ± 3.6E-01%	1.33 ± 25.0%				

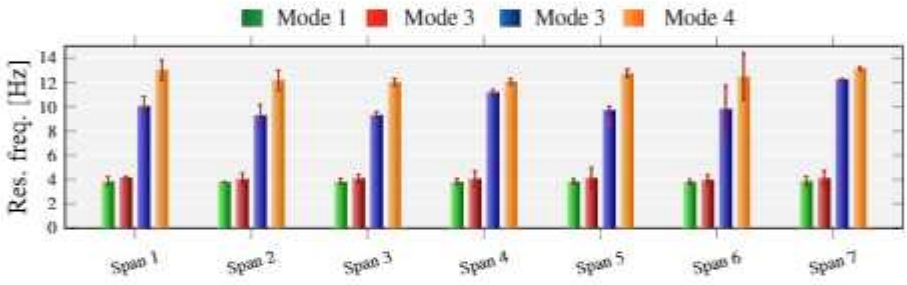

Fig. 6.22: Resonant frequencies of the first four resonant frequencies of the spans of the Trigno Bridge (error bars indicate the uncertainty in the identifications [%]).

7. Conclusion

7.1. Conclusions

This thesis has presented a comprehensive approach for *autonomous aggregated SHM* systems. Such systems combine the processing of heterogeneous sensing data with digital twining techniques to achieve complete damage identification capabilities (global/local damage detection, localization, and quantification). The final outcome materializes in multiple quality control charts assessing the appearance of anomalies in arbitrary combinations of features, possibly including modal data, static features, or model parameters from the continuous inverse calibration of a digital twin. Fostered by an application-oriented philosophy and with the aim of achieving maximum technological transfer to large-scale civil engineering structures, this thesis has rendered a number of fundamental developments across diverse areas of the paradigm of SHM as a statistical pattern recognition. These include: (i) development of automated OMA and modal tracking techniques; (ii) advanced statistical pattern recognition techniques to identify varying environmental regimes and unknown sets of optimal predictors; (iii) automated ANDI techniques for damage localization and quantification; and (iv) supervised damage identification through SM-based deterministic and Bayesian probabilistic St-Id. All the developed techniques have been tested and validated with real monitoring data from in-operation large civil engineering structures, providing clear evidence of their accuracy and effectiveness. In addition, their implementation into a comprehensive software platform provides further evidence of the potential of the presented developments to achieve an effective technological transfer of SHM to engineering routine practice. Specific conclusions on the diverse topics addressed during the course of this thesis can be listed as follows:

- The use of sparse pattern recognition techniques offers a powerful solution to filter out the effects of EOC from civil engineering structures with complex correlations with environmental factors. This is particularly critical in massive historic constructions, where thermal capacitance effects play a leading role. In these cases, sparse techniques combining large sets of predictors may unveil such effects with minimal expert judgment and with the subsequent enhancements in the accuracy of the damage identification. In addition, a practical use of such techniques may be the identification of EOC sensors not contributing to the variability of the structural behavior, so allowing to subtracting or relocating them.

- Seismic interferometric techniques offer a complementary approach to provide OMA with enhanced local damage identification capabilities. ANDI exhibits a higher sensitivity to local defects since it directly exploits features that are local in-nature, i.e. local wave delays. The local nature of these techniques stems from the characterization of wave delays between every two pair of sensors recording the motion along the monitored structure, thus providing a spatial discretization of damage according to the sensors layout. Additionally, ANDI operates on the analysis of complete IRFs, while OMA typically uses ambient vibration records to identify a dynamic model (typically a state-space system) and extracts a reduced set of modal signatures. In this regard, it is important to pinpoint that modal features (resonant frequencies, damping ratios and mode shapes) can be also extracted from the IRFs as a particular case (see e.g. [157, 148]). A final discussion on the advantages and disadvantages of OMA and ANDI is presented in Fig. 7.1.

- Non-parametric clustering techniques (no predefined number of clusters) represent a powerful tool to identify varying environmental regimes and to automate modal tracking procedures. These techniques are particularly useful for structures experiencing temperatures below zero, where the formation of ice crystals in the porosity or micro-cracks in the material originates sudden increases in the resonant frequencies. On this basis, clustering techniques allow to extend classical pattern recognition techniques to reproduce non-linear correlations with EOC. Additionally, a novel modal tracking technique based on a combination of k-means and GMMs has been proposed to automate the definition of modal reference baselines in vibration-based SHM systems.

- The use of SMs represents a feasible solution for the supervised damage identification problem. Such techniques allow to inject engineering knowledge in the identification problem by keeping the high-fidelity nature of detailed numerical models but with computational times in the St-Id compatible with long-term real-time SHM. Numerical results and

SHM Method	Advantages	Disadvantages/Limitations
OMA	• Global damage detection capability. • Considerable freedom to locate the sensors. • Noise effects can be minimized by adopting stochastic system identification approaches. • Relatively easy automation. • High flexibility in its application to diverse structural typologies.	• The excitations must be stationary. • Low sensitivity to local defects. • Damage localization/quantification usually requires the inverse calibration of a numerical model, which is often computationally intensive in the realm of civil engineering structures. • Damping estimates, while highly sensitive to damage, are usually subjected to high levels of uncertainty.
ANDI	• No model assumptions are required. • Excitations may be non-stationary. • Intrinsic damage localization and quantification capabilities. • Relatively simple signal processing. • Moderate sensitivity to local defects. • Offers a natural way for separating structural responses from soil structural interaction effects in high-rise structures.	• High sampling frequencies are required. • Wave propagation patterns must be easily identifiable, which limits its applicability to structures with dominant single-mode wave propagation behaviour (e.g. high-rise buildings, long straight bridges). • Separation between sensors must be long enough to capture wave delays with accuracy. • The sensors layout must be designed according to the expected wave propagation patterns.

Fig. 7.1: Advantages and disadvantages of OMA and ANDI.

discussion on a number of real large-scale civil engineering structures have demonstrated the feasibility of SM-based deterministic and probabilistic St-Id, which represents a step beyond the concept of DTs in civil engineering.

7.2. Original contributions

In pursue of the objectives of this thesis, a number of novel contributions have been rendered across several disciplines in the realm of SHM. The main contributions have been organized below into major disruptive contributions in Section 7.2.1, and minor or methodological advances in Section 7.2.2.

7.2.1. Major original contributions

The main novel contributions of this thesis can be listed as follows:

- Development of MOVA/MOSS and P3P as cutting-edge software solutions involving all the necessary functionalities to enable the autonomous management of aggregated SHM systems.
- First application of automated ANDI combined with continuous OMA for full structural identification of large-scale civil engineering structures.
- First implementation in the literature of ANDI for structural identification of bridge structures.
- Pioneering implementation of Bayesian digital twinning techniques for real-time damage identification of large-scale structures.

Last but not least, it is important to strengthen that all the fundamental developments in this thesis have been applied to real in-operation full-scale civil engineering structures. These evidences embody per se an important contribution in the field of SHM, where the lack of compelling real-world implementations represents one of the primary causes of its slow technological transfer.

7.2.2. Minor advances

The most remarkable methodological contributions of this thesis, presented chapter-wise, comprise:

☐ Chapter 2: *SHM as a statistical pattern recognition problem.*

- Sparse MLR (SMLR) for automated elimination of environmental effects from continuous monitoring data streams.
- Cluster-wise statistical pattern recognition through GMM for elimination of EOC.
- Automated anomaly detection in quality control charts using a PELT algorithm.

☐ Chapter 3: *OMA.*

- Implementation of fully automated SSI techniques into a compact software suite.
- Density-based automated modal tracking through GMM clustering.

☐ Chapter 4: *ANDI.*

- Novel Timoshenko beam formulation for propagation analysis of normal strain waves.
- Incorporation of wave velocities into the FEM updating problem.

☐ Chapter 5: *DTs for damage identification.*

- Implementation of PCE-Kriging meta-modeling for modal-based FEM updating.
- Use of pattern recognition techniques for elimination of EOC from time series of model fitting parameters.

7.3. Future Research

The experience acquired during the course of this thesis suggests four strategic lines of development, namely (i) SHM of infrastructural networks; (ii) implementation of transfer learning approaches; (iii) fusion of SHM data with non-destructive evaluation (NDE) tests and field inspections; and (iv) development of techniques for St-Id of families of DTs. These research lines can be further motivated and described as follows:

- The natural extension of the developed SHM techniques in this thesis is their implementation for the management of complete infrastructural systems, such as bridge networks or cities. A first approximation may be the implementation of certain decision-making techniques to prioritize interventions on the basis of a dense database of control charts assessing the condition of all the assets in the network. Nonetheless, this approach may be impractical since installing dense monitoring systems in all the assets of the network may be simply unfeasible. In this light, some ongoing works are exploring the use of Bayesian Networks to infer the condition of unmonitored assets in a infrastructural network by exploiting monitoring data from a reduced set of monitored structures.

- The previous line of development overlaps with the concept of transfer learning from the field of AI. This innovative concept is particularly attractive for highway bridges, which are numerous in number and there are important similarities between short- and medium-span typologies. Feeding damage classification techniques with the experience from the monitoring of a reduced number of bridges may lead to decisive tools for infrastructure owners and policy makers to optimally design the management of bridge infrastructures at a regional or national level.

- Currently there is a weak link between the outcomes of visual inspections, NDE and SHM. In this regard, Bayesian St-Id techniques offer an ideal environment for data fusion. On one hand, it is possible to exploit the outcomes of NDE and visual inspections to refine the definition of the prior PDFs of the model parameters. On the other hand, NDE and visual inspections may be also used to further constrain the likelihood function in the St-Id, hence minimizing the uncertainty due to ill-conditioning. This may be possible by constraining the variation of certain parameters affecting regions where damage is certainly not present, so focusing the St-Id on regions where damage may potentially develop.

- As evidenced by the reported experience in this thesis on SL, the parametrization of the numerical model highly determines the accuracy in the St-Id. In this light, the parametrization should be designed according to the expected damage pathology, which is in general unknown beforehand. Moreover, given that model parameter inference in civil engineering is always an ill-conditioned problem (the uniqueness of the solution cannot be guaranteed), the damage assessment from the St-Id will always suffer from considerable uncertainty. It is thus clear the need for developing SL-based St-Id techniques capable of handling populations of DTs representing the different structural pathologies that the asset may experience during its lifespan. In this way, after the detection of an anomaly in the monitoring data, model selection techniques could be adopted to evalu-

ate the likelihood of the different DTs to explain the identified anomaly. In this line, ongoing research works are addressing the use of Bayesian model selection techniques based on nested sampling techniques.

A. Appendix

A.1. Propagation of elastic waves in visco-elastic Timoshenko beams

This section presents the theoretical formulation of the wave propagation of elastic waves through non-uniform viscoelastic Timoshenko beams proposed by Ebrahimian and Todorovska [152, 230] and extended in this thesis in reference [146] for the propagation of strain waves. Specifically, Section A.1.1 first outlines the theoretical formulation of wave dispersion in uniform Timoshenko beams. Secondly, Section A.1.2 extends this formulation with a propagator matrix approach for multi-layered Timoshenko beams and, finally, Section A.1.3 details the calculation of acceleration and strain IRFs.

A.1.1. Visco-elastic Timoshenko beam model

Firstly, the masonry tower is modelled as a cantilever uniform visco-elastic Timoshenko Beam (TB) subjected to seismic base motion u_g as sketched in Fig. A.1. The beam has a cross-section A, second moment of inertia I, shear correction factor κ, width W, and height H. The material is defined as elastic isotropic with Young's modulus E, shear modulus G, and mass density ρ. The longitudinal and shear wave velocities in the material are defined as $c_L = \sqrt{E/\rho}$ and $c_S = \sqrt{G/\rho}$, respectively [152].

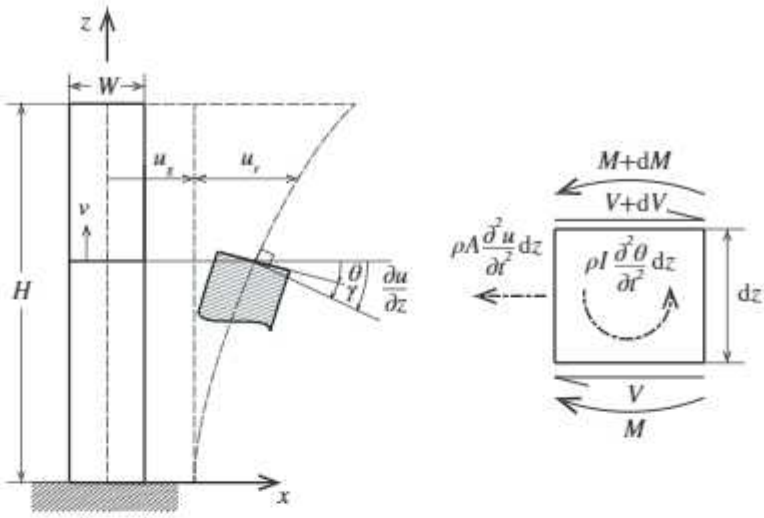

Fig. A.1: Uniform cantilever Timoshenko beam model.

The Timoshenko beam theory takes into account both shear deformation and rotational bending effects. To this aim, this theory distinguishes $\theta(z,t)$ and $\gamma(z,t)$ as the angles representing the rotations of an infinitesimal beam element located at height z due to bending and shear effects, respectively. Let us denote $u(z,t) = u_g(t) + u_r(z,t)$ the absolute horizontal displacement of the centre of gravity of the element with respect to the origin, where $u_r(z,t)$ stands for relative displacement. In addition, let us define $v(x,z,t)$ as the longitudinal displacement of the beam. Assuming small deformations, one can write the following kinematic conditions:

$$\frac{\partial u}{\partial z} = \theta + \gamma, \quad v = -x\,\theta, \tag{A.1}$$

and the shear forces V and bending moments M can be expressed in terms of rotations as:

$$V = \kappa A G \gamma, \quad M = -EI\frac{\partial \theta}{\partial z}. \tag{A.2}$$

Damping is included in this work by using the Kelvin-Voigt material damping model. According to this model, dissipative damping forces are taken into account by defining bending and shear stresses, σ_x and τ_{xy}, as linear functions of the strain velocity through two constants c_σ and c_τ, what leads to the following stress-strain relations:

$$\sigma_x = \sigma_x^e + \sigma_x^d = E\varepsilon_x + c_\sigma \frac{\partial \varepsilon_x}{\partial t}, \tag{A.3}$$

$$\tau_{xy} = \tau_{xy}^e + \tau_{xy}^d = G\gamma_{xy} + c_\tau \frac{\partial \gamma_{xy}}{\partial t}, \tag{A.4}$$

where superscripts "e" and "d" denote elastic and damping stresses, respectively. If we further decompose the damping constants c_σ and c_τ as $c_\sigma = \mu_\sigma E$ and $c_\tau = \mu_\tau G$, and we assume the same viscosity constant for both types of deformation, $\mu_b = \mu_s = \mu$, the Kelvin-Voigt damping model can be readily introduced by replacing E and G by $E\left[1+\mu\left(\partial/\partial t\right)\right]$ and $G\left[1+\mu\left(\partial/\partial t\right)\right]$, respectively.

The equations of motion of the TB can be obtained by applying the Hamilton's Principle to the Lagrangian $\mathscr{L}$ and the Rayleigh dissipation function $\mathscr{R}$ of the system:

$$\delta \int \left(\mathscr{L} - \mathscr{R}\right) \mathrm{d}t = \delta \int \left(T - U - \mathscr{R}\right) \mathrm{d}t = 0, \tag{A.5}$$

with T being the total kinematic energy of the beam (including the rotary inertia effect), and U the potential energy due to bending and shear deformations. After some manipulations, Eq. (A.5) results in the following coupled system of equations:

$$\rho A \ddot{u} - \kappa G A \left(1 - \mu \frac{\partial}{\partial t}\right)\left(u'' - \theta'\right) = 0, \tag{A.6}$$

$$\rho I \ddot{\theta} - EI \left(1 - \mu \frac{\partial}{\partial t}\right)\theta'' - \kappa G A \left(1 - \mu \frac{\partial}{\partial t}\right)\left(u' - \theta\right) = 0, \tag{A.7}$$

where dots and commas stand for time and spatial derivatives, respectively. If we denote $D = [u, \theta]^{\mathrm{T}}$, Eqs. (A.6) and (A.7) can be rewritten in a decoupled system of fourth-order differential equations as:

$$\begin{aligned} &EI\ddot{D}'''' + \rho A \ddot{D} + \frac{\rho^2}{\kappa G}\ddot{\ddot{D}} - \rho I \left(1 + \frac{E}{\kappa G}\right)\ddot{D}'' + \\ &+ \mu G I \dot{D}'''' - \frac{\rho \mu I}{\kappa}\ddot{\ddot{D}}'' + \mu\left(-\rho I \ddot{\ddot{D}}'' + EI\dot{D}'''' + \mu G I \ddot{D}'''' + \rho A \ddot{\ddot{D}}\right) = 0, \end{aligned} \tag{A.8}$$

or in a more compact way as:

$$\begin{aligned} &c_L^2 c_S^2 \kappa \left(1 + \mu\frac{\partial}{\partial t}\right)^2 \frac{\partial^4 D}{\partial z^4} - \left(c_L^2 + \kappa c_S^2\right)\left(1 + \mu\frac{\partial}{\partial t}\right)\frac{\partial^4 D}{\partial z^2 \partial t^2} + \\ &+ \frac{\kappa c_S^2}{r_g^2}\left(1 + \mu\frac{\partial}{\partial t}\right)\frac{\partial^2 D}{\partial t^2} + \frac{\partial^4 D}{\partial t^4} = 0, \end{aligned} \tag{A.9}$$

with r_g being the radius of gyration $r_g = \sqrt{I/A}$. The solutions of Eq. (A.9) satisfy the following boundary conditions:

$$\theta(0,t) = 0, u(0,t) = u_g(t) \quad \text{at} \quad z = 0, \tag{A.10}$$

$$V(H,t) = M(H,t) = 0 \quad \text{at} \quad z = H. \tag{A.11}$$

Assuming harmonic excitations, the solutions for transverse displacements and rotations can be defined as one-dimensional waves as $u(z,t) = e^{\mathrm{i}(kz-\omega t)} = U(z)e^{-\mathrm{i}\omega t}$ and $\theta(z,t) = e^{\mathrm{i}(lz-\omega t)} = \Theta(z)e^{-\mathrm{i}\omega t}$, respectively, where ω stands for angular frequency and i is the imaginary unit. Upon substitution of these solutions into Eq. (A.9), the equation for transverse displacements u can be rewritten as:

$$c_L^2 c_S^2 \kappa \left(1 - \mathrm{i}\omega\mu\right)^2 k^4 - \left(c_L^2 + \kappa c_S^2\right)\left(1 - \mathrm{i}\omega\mu\right) k^2\omega^2 - \omega^2 \frac{\kappa c_S^2}{r g^2}\left(1 - \mathrm{i}\omega\mu\right) + \omega^4 = 0. \tag{A.12}$$

Note that Eq. (A.12) establishes a relationship between the wavenumbers k and the frequency ω, also called a dispersion relation. Thence, the velocities of the waves are functions of the frequency. More specifically, the travelling waveform can be defined by the phase and group velocities as $c^p = \omega/k$ and $c^g = \partial\omega/\partial k$, respectively. Furthermore, note that the dispersion relation for rotations is identical to Eq. (A.12) and, therefore, so are their wavenumbers ($l = k$), phase and group velocities. In order to non-dimensionalize the equations for further analysis, a dimensionless frequency, Ω, a moduli ratio, R, and a dimensionless damping constant, M, are introduced as follows [152]:

$$\Omega = \frac{\omega r_g}{c_S}, \quad R = \frac{G}{E} = \frac{c_S^2}{c_L^2}, \quad M = \frac{\mu c_S}{r_g}. \tag{A.13}$$

In terms of these dimensionless parameters, the four roots of Eq. (A.12) yield the following dimensionless wavenumbers:

$$K_{1,2} = \pm k_1 r_g = \pm\sqrt{\left(\frac{1}{\alpha}\right)\left(\frac{1}{\kappa} + R\right) + \sqrt{\left(\frac{1}{\alpha^2}\right)\left(\frac{1}{\kappa} - R\right)^2 + \frac{4R}{\alpha\Omega^2}}}, \tag{A.14}$$

$$K_{3,4} = \pm k_2 r_g = \pm\sqrt{\left(\frac{1}{\alpha}\right)\left(\frac{1}{\kappa} + R\right) - \sqrt{\left(\frac{1}{\alpha^2}\right)\left(\frac{1}{\kappa} - R\right)^2 + \frac{4R}{\alpha\Omega^2}}}, \tag{A.15}$$

with $\alpha = 1 - \mathrm{i}\omega M$. Hence, the solutions of the lateral displacements $U(z)$ and rotations $\Theta(z)$ in the frequency domain read:

$$U(z) = C_1 e^{\mathrm{i}k_1 z} + C_2 e^{-\mathrm{i}k_1 z} + C_3 e^{\mathrm{i}k_2 z} + C_4 e^{-\mathrm{i}k_2 z}, \tag{A.16}$$

$$\Theta(z) = B_1 e^{\mathrm{i}k_1 z} + B_2 e^{-\mathrm{i}k_1 z} + B_3 e^{\mathrm{i}k_2 z} + B_4 e^{-\mathrm{i}k_2 z}, \tag{A.17}$$

where C_i, B_i, $i = 1, \ldots, 4$ are constants determined by the boundary conditions in Eqs. (A.10) and (A.11). Substitution of Eqs. (A.16) and (A.17) into the coupled differential equations in Eqs. (A.6) and (A.7) leads to the following relations:

$$\frac{B1}{C1} = -\frac{B2}{C2} = -\frac{\mathrm{i}}{rg}\left(\frac{\Omega^2}{K_1 \kappa \alpha} - K_1\right), \tag{A.18}$$

$$\frac{B3}{C3} = -\frac{B4}{C4} = -\frac{\mathrm{i}}{rg}\left(\frac{\Omega^2}{K_2 \kappa \alpha} - K_2\right), \tag{A.19}$$

and the boundary conditions in Eqs. (A.10) and (A.11) imply:

$$\begin{bmatrix} C_1 \\ C_2 \\ C_3 \\ C_4 \end{bmatrix} = \mathbf{A}^{-1} \begin{bmatrix} u_g(t) \\ 0 \\ 0 \\ 0 \end{bmatrix}, \tag{A.20}$$

with:

$$\mathbf{A} = \begin{bmatrix} 1 & 1 & 1 & 1 \\ -\left(\frac{\Omega^2}{\alpha\kappa K_1} - K_1\right) & \left(\frac{\Omega^2}{\alpha\kappa K_1} - K_1\right) & -\left(\frac{\Omega^2}{\alpha\kappa K_2} - K_2\right) & \left(\frac{\Omega^2}{\alpha\kappa K_2} - K_2\right) \\ \left(\frac{\Omega^2}{\alpha\kappa} - K_1^2\right) e^{\mathrm{i}K_1(H/rg)} & \left(\frac{\Omega^2}{\alpha\kappa} - K_1^2\right) e^{-\mathrm{i}K_1(H/rg)} & \left(\frac{\Omega^2}{\alpha\kappa} - K_2^2\right) e^{\mathrm{i}K_2(H/rg)} & \left(\frac{\Omega^2}{\alpha\kappa} - K_2^2\right) e^{-\mathrm{i}K_2(H/rg)} \\ -(1/K_1) e^{\mathrm{i}K_1(H/rg)} & (1/K_1) e^{-\mathrm{i}K_1(H/rg)} & -(1/K_2) e^{\mathrm{i}K_2(H/rg)} & (1/K_2) e^{-\mathrm{i}K_2(H/rg)} \end{bmatrix}. \tag{A.21}$$

Finally, the bending-induced normal strain at a beam depth x can be directly obtained by the kinematic condition in Eq. (A.1) as $\varepsilon(x, z, t) = \partial v / \partial z = -x\, \partial 0(z, t)/\partial z = \Upsilon(z)\, e^{\mathrm{i}\omega t}$. The strain in the frequency domain $\Upsilon(z)$ is extracted from Eq. (A.17) as:

$$\Upsilon(z) = -\mathrm{i}k_1 B_1 e^{\mathrm{i}k_1 z} + \mathrm{i}k_1 B_2 e^{-\mathrm{i}k_1 z} - \mathrm{i}k_2 B_3 e^{\mathrm{i}k_2 z} + \mathrm{i}k_4 B_4 e^{-\mathrm{i}k_2 z}, \tag{A.22}$$

whereby it is concluded that the velocities of the waveforms arising from the strain field are identical to those obtained by monitoring lateral displacements in Eq. (A.16) or, alternatively, velocities or accelerations. Let us remark that, unlike acceleration-based wave propagation approaches, the position of strain transducers must be adequately tailored to maximize the bending-induced strains (typically $x = W/2$).

A.1.2. Visco-elastic layered Timoshenko beam model

In order to include non-uniform stiffness distributions and damage-induced variations, the tower is herein modelled as a visco-elastic TB with piecewise continuous properties as shown in Fig. A.2. In particular, n layers are numbered from bottom to top, and are characterized by their height $l^i = z^i - z^{i-1}$, longitudinal and shear wave velocities c_L^i and c_S^i, mass density ρ^i, and viscosity constants μ^i, $i = 1, \ldots, n$. It is important to note that such a modelling framework allows the representation of damage in the shape of local reductions in the layers' Young's modulus and/or shear modulus or, alternatively, local increases in the wavenumbers of the propagating pulses in virtue of Eqs. (A.14) and (A.15). Similar assumptions are common in damage identification techniques via computational model updating, being suitable for early-stage damage where the structure can be hypothesized to remain elastic. The layering of the model allows the definition of multiple flaws located at different heights of the tower, being the number of sensors deployed in the structure the only limiting factor in the spatial resolution of the damage localization. Moreover, the inverse calibration of this model makes it possible to quantify damage in terms of local reductions in the layers' elastic properties.

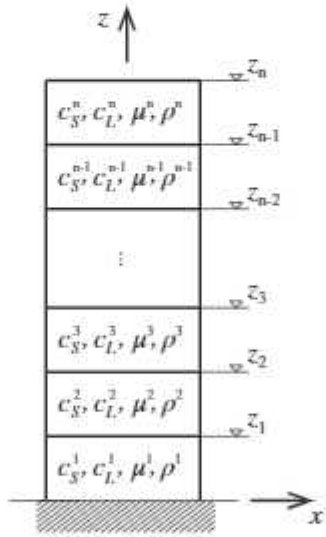

Fig. A.2: Cantilever layered Timoshenko beam model representing a masonry tower.

In a similar way to the uniform TB, harmonic excitations are assumed in such a way that $u(z,t)$, $\theta(z,t)$, $M(z,t)$ and $V(z,t)$ can be written as:

$$\begin{aligned} u(z,t) &= U(z)\, e^{i\omega t}, \quad \theta(z,t) = \Theta(z)\, e^{i\omega t}, \\ M(z,t) &= \mathscr{M}(z)\, e^{i\omega t}, \quad V(z,t) = \mathscr{V}(z)\, e^{i\omega t}. \end{aligned} \tag{A.23}$$

Considering the equilibrium of a differential beam element (see Fig. A.1), the state of every layer can be described by the following matrix equation:

$$\frac{\partial \mathbf{f}(z)}{\partial z} = \mathbf{B}\,\mathbf{f}(z), \tag{A.24}$$

where $\mathbf{f}(z) = \left[U(z), \Theta(z), \mathscr{M}(z), \mathscr{V}(z)\right]^{\mathrm{T}}$ denotes the stress-displacement vector or state vector, and matrix $\mathbf{B}$ takes the form [230]:

$$\mathbf{B} = \begin{bmatrix} 0 & 1 & 0 & \frac{1}{\kappa G A(1-\mathrm{i}\omega\mu)} \\ 0 & 0 & -\frac{1}{EI(1-\mathrm{i}\omega\mu)} & 0 \\ 0 & \rho I\omega^2 & 0 & 1 \\ -\rho A\omega^2 & 0 & 0 & 0 \end{bmatrix}. \tag{A.25}$$

According to the propagator matrix theory [231], it can be proved that if matrix $\mathbf{B}$ is a continuous function of z, as it is the case within each layer of the TB, the state vector $\mathbf{f}(z)$ at a given point z_o in a certain layer can be propagated throughout the layer as $\mathbf{f}(z) = \mathbf{P}(z, z_o)\,\mathbf{f}(z_o)$, where $\mathbf{P}(z, z_o)$ is the so-called propagator matrix from z_o. Solving the ordinary differential equation (A.24), $\mathbf{P}(z, z_o)$ can be written as:

$$\mathbf{P}(z, z_o) = e^{\mathbf{B}(z-z_o)}. \tag{A.26}$$

The propagator can be further decomposed using a Taylor series expansion to compute the exponential in Eq. (A.26). Nevertheless, it is more convenient to diagonalize the matrix $\mathbf{B}$ by a similarity transformation as $\mathbf{B} = \mathbf{S}\boldsymbol{\Lambda}\mathbf{S}^{-1}$, where $\boldsymbol{\Lambda}$ is the diagonal matrix of the eigenvalues of $\mathbf{B}$, and $\mathbf{S}$ contains the corresponding eigenvectors by columns. It can be seen that the eigenvalues of $\mathbf{B}$ correspond to $\pm ik_1$ and $\pm ik_2$ [230], with the wave-numbers k_1 and k_2 given by Eqs. (A.14) and (A.15). In this way, Eq. (A.26) can be decomposed as [230]:

$$\mathbf{P}(z, z_o) = \mathbf{S}e^{\boldsymbol{\Lambda}(z-z_o)}\mathbf{S}^{-1}, \tag{A.27}$$

where the exponential of a diagonal matrix is directly given by the exponential of the diagonal elements, that is:

$$e^{\boldsymbol{\Lambda}(z-z_o)} = \mathrm{diag}\left(e^{\mathrm{i}k_1(z-z_o)}, e^{-\mathrm{i}k_1(z-z_o)}, e^{\mathrm{i}k_2(z-z_o)}, e^{-\mathrm{i}k_2(z-z_o)}\right). \tag{A.28}$$

Given that $\mathbf{f}(z)$ must be continuous at the layer interfaces, the solution at an arbitrary interface z_k can be obtained as:

$$\mathbf{f}(z_k) = \prod_{i=0}^{k-1} \mathbf{P}(z_{i+1}, z_i)\,\mathbf{f}(z_o). \tag{A.29}$$

In view of the boundary conditions previously shown in Eqs. (A.10) and (A.11), the state vector is constrained at $z = 0$ and $z = H$ as:

$$\mathbf{f}(0) = \begin{bmatrix} U_g \\ 0 \\ M_g \\ V_g \end{bmatrix}, \quad \mathbf{f}(H) = \begin{bmatrix} U_r \\ \Theta_r \\ 0 \\ 0 \end{bmatrix}. \tag{A.30}$$

Assuming that the base motion U_g is prescribed, the base bending moment M_g and shear V_g, as well as the top displacement U_r and rotation Θ_r, remain unknown. Their values are obtained by solving the determined linear system of four equations formed by the solution at the base and its propagation to the roof. Thereafter, the state vector of the system can be obtained at any height z by the propagator matrix approach in Eq. (A.29). Finally, once the bending moment $\mathscr{M}(z)$ is known, the bending-induced normal strain in the frequency domain $\Upsilon(z)$ can be obtained as:

$$\Upsilon(z) = \frac{\mathscr{M}(z)}{EI\,(1 - \mathrm{i}\omega\mu)}. \tag{A.31}$$

A.1.3. Transfer Functions and Impulse Response Functions

Assume the TB as a linear system with ground motion U_g (or ground acceleration, $-\omega^2 U_g$) as input, and transverse displacements $U(z)$ and strains $\Upsilon(z)$ as outputs. In this light, the TFs can be obtained as $U(z)/U_g$ and $\Upsilon(z)/U_g$, respectively. More generally, the TFs can be defined between the motion of the structure at height z with respect to a reference level z_{ref}, that is to say, considering a virtual source at z_{ref} that does not necessarily coincide with the actual physical source. Let $\hat{h}_u$ and $\hat{h}_\varepsilon$ denote the TFs in terms of displacements and strains, respectively, as follows:

$$\hat{h}_u(z, z_{ref}, \omega) = \frac{\hat{u}(z,\omega)}{\hat{u}(z_{ref},\omega)} = \frac{U(z,\omega)}{U(z_{ref},\omega)}, \tag{A.32}$$

$$\hat{h}_\varepsilon(z, z_{ref}, \omega) = \frac{\hat{\varepsilon}(z,\omega)}{\hat{u}(z_{ref},\omega)} = \frac{\Upsilon(z,\omega)}{U(z_{ref},\omega)}. \tag{A.33}$$

In order to avoid numerical instability due to division by null numbers, TFs are often regularized as:

$$\hat{h}_u(z, z_{ref}, \omega) \approx \frac{U(z,\omega)\,\overline{U(z_{ref},\omega)}}{\left|U(z_{ref},\omega)\right|^2 + \eta}, \tag{A.34}$$

$$\hat{h}_\varepsilon(z, z_{ref}, \omega) \approx \frac{\Upsilon(z,\omega)\,\overline{U(z_{ref},\omega)}}{\left|U(z_{ref},\omega)\right|^2 + \eta}, \tag{A.35}$$

where the bar indicates complex conjugate, and η denotes a regularization parameter to avoid numerical instability. In this work, we use $\eta = 0.1\overline{P}$ with $\overline{P}$ being the average power of the reference input. The corresponding IRFs, $h_u(z, z_{ref}, t)$ and $h_\varepsilon(z, z_{ref}, t)$, are defined in the time domain and can be computed as the inverse Fourier transform of the TFs as $h_u(z, z_{ref}, t) = \mathscr{F}^{-1}\left\{\hat{h}_u(z, z_{ref}, \omega)\right\}$ and $h_\varepsilon(z, z_{ref}, t) = \mathscr{F}^{-1}\left\{\hat{h}_\varepsilon(z, z_{ref}, \omega)\right\}$. Typically, IRFs can be only obtained for a finite frequency band $|\omega| < \omega_{max}$, that is:

$$h_u(z, z_{ref}, t) = \frac{1}{2\pi}\int_{-\omega_{max}}^{\omega_{max}} \hat{h}_u(z, z_{ref}, \omega) e^{-\mathrm{i}\omega t}\mathrm{d}\omega, \tag{A.36}$$

$$h_\varepsilon(z, z_{ref}, t) = \frac{1}{2\pi}\int_{-\omega_{max}}^{\omega_{max}} \hat{h}_\varepsilon(z, z_{ref}, \omega) e^{-\mathrm{i}\omega t}\mathrm{d}\omega. \tag{A.37}$$

References

[1] ASCE. 2021 Report Card for America's Infrastructure. Technical report, American Society of Civil Engineers, 2021.

[2] R. Woodward, D. W. Cullington, A. F. Daly, P. R. Vassie, P. Haardt, R. Kashner, R. Astudillo, C. Velando, B. Godart, and C. Cremona. Bridge management in Europe (BRIME)–Deliverable D14–Final Report. Technical report, Transport Research and Innovation Monitoring and Information System, 2001.

[3] Fernando Moreu, Xiaomeng Li, Shunlong Li, and Dongyu Zhang. Technical specifications of structural health monitoring for highway bridges: New Chinese structural health monitoring code. *Frontiers in Built Environment*, 4:10, 2018.

[4] ISIS Canada. *Guidelines for Structural Health Monitoring*, 2001.

[5] Ministero delle Infrastrutture e dei Trasporti Consiglio Superiore dei Lavori Pubblici. *Linee guida per la classificazione e gestione del rischio, la valutazione della sicurezza ed il monitoraggio dei ponti esistenti*, 2020.

[6] Mark Moore, Brent M. Phares, Benjamin Graybeal, Dennis Rolander, Glenn Washer, and Janney Wiss. Reliability of visual inspection for highway bridges, volume I. Technical report, U.S. Department of Transportation, 2001.

[7] National Transportation Safety Board and United States Board. Collapse of I-35W Highway Bridge, Minneapolis, Minnesota, August 1, 2007. Technical report, National Transportation Safety, 2008.

[8] H. P. Chen. *Structural health monitoring of large civil engineering structures*. John Wiley & Sons, 2018.

[9] Rune Brincker and Carlos Ventura. *Introduction to operational modal analysis*. John Wiley & Sons, 2015.

[10] Filipe Magalhães, Álvaro Cunha, and Elsa Caetano. Vibration based structural health monitoring of an arch bridge: From automated OMA to damage detection. *Mechanical Systems and signal processing*, 28:212–228, 2012.

[11] Sérgio Pereira, Filipe Magalhães, Jorge Gomes, Álvaro Cunha, and José V Lemos. Installation and results from the first 6 months of operation of the dynamic monitoring system of Baixo Sabor arch dam. *Procedia engineering*, 199:2166–2171, 2017.

[12] Panida Kaewniam, Maosen Cao, Nizar Faisal Alkayem, Dayang Li, and Emil Manoach. Recent advances in damage detection of wind turbine blades: A state-of-the-art review. *Renewable and Sustainable Energy Reviews*, 167:112723, 2022.

[13] Filippo Ubertini, Gabriele Comanducci, and Nicola Cavalagli. Vibration-based structural health monitoring of a historic bell-tower using output-only measurements and multivariate statistical analysis. *Structural Health Monitoring*, 15(4):438–457, 2016.

[14] M. Z. Naser. Bridge failures/collapses, 2019. Mendeley Data.

[15] K Gkoumas, FL Marques Dos Santos, M Van Balen, A Tsakalidis, A Ortega Hortelano, M Grosso, G Haq, and F Pekár. Research and innovation in bridge maintenance, inspection and monitoring. *Publications Office of the European Union*, 2019.

[16] Bart Peeters and Guido De Roeck. One-year monitoring of the Z24-Bridge: environmental effects versus damage events. *Earthquake engineering & structural dynamics*, 30(2):149–171, 2001.

[17] Johan Maeck and Guido De Roeck. Description of Z24 benchmark. *Mechanical Systems and Signal Processing*, 17(1):127–131, 2003.

[18] Gunther Steenackers and Patrick Guillaume. Structural health monitoring of the Z24 Bridge in presence of environmental changes using modal analysis. In *Proceedings of IMAC*, volume 23, 2005.

[19] Filippo Ubertini, Nicola Cavalagli, Alban Kita, and Gabriele Comanducci. Assessment of a monumental masonry bell-tower after 2016 Central Italy seismic sequence by long-term SHM. *Bulletin of Earthquake Engineering*, 16(2):775–801, 2018.

[20] Nicola Cavalagli, Gabriele Comanducci, and Filippo Ubertini. Earthquake–induced damage detection in a monumental masonry bell-tower using long-term dynamic monitoring data. *Journal of Earthquake Engineering*, 22(sup1):96–119, 2018.

[21] Nicola Cavalagli and Vittorio Gusella. Dome of the Basilica of Santa Maria Degli Angeli in Assisi: static and dynamic assessment. *International Journal of Architectural Heritage*, 9(2):157–175, 2015.

[22] N. Cavalagli, A. Kita, S. Falco, F. Trillo, M. Costantini, and F. Ubertini. Satellite radar interferometry and in-situ measurements for static monitoring of historical monuments: The case of Gubbio, Italy. *Remote Sensing of Environment*, 235:111453, 2019.

[23] N. Cavalagli, A. Kita, V. L. Castaldo, A. L. Pisello, and F. Ubertini. Hierarchical environmental risk mapping of material degradation in historic masonry buildings: An integrated approach considering climate change and structural damage. *Construction and Building Materials*, 215:998–1014, 2019.

[24] A. Kita, N. Cavalagli, and F. Ubertini. Temperature effects on static and dynamic behavior of Consoli Palace in Gubbio, Italy. *Mechanical Systems and Signal Processing*, 120:180–202, apr 2019.

[25] Enrique García-Macías and Filippo Ubertini. MOVA/MOSS: Two integrated software solutions for comprehensive Structural Health Monitoring of structures. *Mechanical Systems and Signal Processing*, 143:106830, 2020.

[26] F. Mirabella, M. G. Ciaccio, M. R. Barchi, and S. Merlini. The Gubbio normal fault (Central Italy): geometry, displacement distribution and tectonic evolution. *Journal of Structural Geology*, 26(12):2233–2249, 2004.

[27] Paolo Balocchi and Giulio Riga. Considerations on the Seismotectonics and Seismogenesis of Tiberina-Gubbio Valley Extensional System (Central Italy). *Atti della Societa dei Naturalisti e Matematici di Modena*, 148:65–82, 2017.

[28] Luisa Valoroso, Lauro Chiaraluce, Raffaele Di Stefano, and Giancarlo Monachesi. Mixed-mode slip behavior of the Altotiberina low-angle normal fault system (Northern Apennines, Italy) through high-resolution earthquake locations and repeating events. *Journal of Geophysical Research: Solid Earth*, 122(12):10–220, 2017.

[29] Fabrizio Gara, Marco Regni, and Davide Roia. Caratterizzazione dinamica del Viadotto "Chiaravalle" per il controllo e monitoraggio ante operam e post operam. Technical report, Relazione Tecnica per ANAS S.p.A. – Compartimento per la viabilità per le Marche, 2017.

[30] L. Dezi, M. Merlino, and C. Sturbini. Seismic Upgrading of Chiaravalle Viaduct along the SS 76 - Falconara Airport Link Road. In *Italian Concrete Days*, 2018.

[31] Davide Roia, Marco Regni, Fabrizio Gara, Sandro Carbonari, and Francesca Dezi. Current state of the dynamic monitoring of the "Chiaravalle viaduct". In *2016 IEEE Workshop on Environmental, Energy, and Structural Monitoring Systems (EESMS)*, pages 1–6. IEEE, 2016.

[32] Marco Regni, Fabrizio Gara, Francesca Dezi, Davide Roia, and Sandro Carbonari. Soil-Foundation Compliance Evidence of the "Chiaravalle Viaduct". In *International Conference on Experimental Vibration Analysis for Civil Engineering Structures*, pages 871–881. Springer, 2017.

[33] Fabrizio Gara, Marco Regni, Davide Roia, Sandro Carbonari, and Francesca Dezi. Evidence of coupled soil-structure interaction and site response in continuous viaducts from ambient vibration tests. *Soil Dynamics and Earthquake Engineering*, 120:408–422, 2019.

[34] R. Fuentes, E. J. Cross, P. A. Gardner, L. A. Bull, T. J. Rogers, R. J. Barthorpe, H. Shi, N. Dervilis, C. R. Farrar, and K. Worden. Structural Health Monitoring and Damage Identification. *Handbook of Experimental Structural Dynamics*, pages 1–72, 2020.

[35] L. F. Ramos, L. Marques, P. B. Lourenço, G. De Roeck, A. C. C., and J. Roque. Monitoring historical masonry structures with operational modal analysis: Two case studies. *Mechanical Systems and Signal Processing*, 24(5):1291–1305, 2010.

[36] Federica Ottoni and Carlo Blasi. Results of a 60-year monitoring system for Santa Maria del Fiore Dome in Florence. *International Journal of Architectural Heritage*, 9(1):7–24, 2015.

[37] Enrique García-Macías and Filippo Ubertini. *Integrated SHM Systems: Damage Detection Through Unsupervised Learning and Data Fusion*. Springer, 2022.

[38] Charles R. Farrar, Scott W. Doebling, and David A. Nix. Vibration-based structural damage identification. *Philosophical Transactions of the Royal Society of London. Series A: Mathematical, Physical and Engineering Sciences*, 359(1778):131–149, 2001.

[39] Anders Rytter. *Vibrational based inspection of civil engineering structures*. PhD thesis, Dept. of Building Technology and Structural Engineering, Aalborg University, 1993.

[40] Alireza Entezami, Hassan Sarmadi, Behshid Behkamal, and Stefano Mariani. Big data analytics and structural health monitoring: a statistical pattern recognition-based approach. *Sensors*, 20(8):2328, 2020.

[41] Charles R. Farrar and Keith Worden. *Structural health monitoring: a machine learning perspective*. John Wiley & Sons, 2012.

[42] Keith Worden, Charles R. Farrar, Graeme Manson, and Gyuhae Park. The fundamental axioms of structural health monitoring. *Proceedings of the Royal Society A: Mathematical, Physical and Engineering Sciences*, 463(2082):1639–1664, 2007.

[43] Rongrong Hou and Yong Xia. Review on the new development of vibration-based damage identification for civil engineering structures: 2010-2019. *Journal of Sound and Vibration*, 491:115741, 2021.

[44] Onur Avci, Osama Abdeljaber, Serkan Kiranyaz, Mohammed Hussein, Moncef Gabbouj, and Daniel J. Inman. A review of vibration-based damage detection in civil structures: From traditional methods to Machine Learning and Deep Learning applications. *Mechanical systems and signal processing*, 147:107077, 2021.

[45] Enrique García-Macías, Ilaria Venanzi, and Filippo Ubertini. Metamodel-based pattern recognition approach for real-time identification of earthquake-induced damage in historic masonry structures. *Automation in Construction*, 120:103389, 2020.

[46] Spilios D. Fassois and John S. Sakellariou. Time-series methods for fault detection and identification in vibrating structures. *Philosophical Transactions of the Royal Society A: Mathematical, Physical and Engineering Sciences*, 365(1851):411–448, 2007.

[47] Filippo Ubertini, Carmelo Gentile, and Annibale Luigi Materazzi. Automated modal identification in operational conditions and its application to bridges. *Engineering Structures*, 46:264–278, 2013.

[48] Edwin Reynders, Jeroen Houbrechts, and Guido De Roeck. Fully automated (operational) modal analysis. *Mechanical systems and signal processing*, 29:228–250, 2012.

[49] Miroslav Pastor, Michal Binda, and Tomáš Harčarik. Modal assurance criterion. *Procedia Engineering*, 48:543–548, 2012.

[50] Mia Hubert, Michiel Debruyne, and Peter J. Rousseeuw. Minimum covariance determinant and extensions. *Wiley Interdisciplinary Reviews: Computational Statistics*, 10(3):e1421, 2018.

[51] Peter J. Rousseeuw. Least median of squares regression. *Journal of the American statistical association*, 79(388):871–880, 1984.

[52] Peter J. Rousseeuw and Katrien Van Driessen. A fast algorithm for the minimum covariance determinant estimator. *Technometrics*, 41(3):212–223, 1999.

[53] Peter J. Rousseeuw and Annick M. Leroy. *Robust regression and outlier detection*, volume 589. John Wiley & Sons, 2005.

[54] Mia Hubert, Peter J. Rousseeuw, and Stefan Van Aelst. Multivariate outlier detection and robustness. *Handbook of Statistics*, 24:263–302, 2005.

[55] Enrique García-Macías and Filippo Ubertini. Least Angle Regression for early-stage identification of earthquake-induced damage in a monumental masonry palace: Palazzo dei Consoli. *Engineering Structures*, 259:114119, 2022.

[56] N. Cavalagli, L. Botticelli, M. Gioffrè, V. Gusella, and F. Ubertini. Dynamic monitoring and nonlinear analysis of the dome of the basilica of S.Maria degli Angeli in Assisi . In *XI COMPDYN 2017*, volume 1, pages 2542–2553, 2017.

[57] Carmelo Gentile, Antonello Ruccolo, and Francesco Canali. Long-term monitoring for the condition-based structural maintenance of the Milan Cathedral. *Construction and Building Materials*, 228:117101, 2019.

[58] E. M. Tronci, M. De Angelis, R. Betti, and V. Altomare. Vibration-based structural health monitoring of a RC-masonry tower equipped with non-conventional TMD. *Engineering Structures*, 224:111212, 2020.

[59] Yong Xia, Bo Chen, Shun Weng, . Q. Ni, and Y. L. Xu. Temperature effect on vibration properties of civil structures: a literature review and case studies. *Journal of civil structural health monitoring*, 2(1):29–46, 2012.

[60] Bart Peeters. *System identification and damage detection in civil engineering*. PhD thesis, KU Leuven, 2000.

[61] Filipe de Magalhães. *Operational modal analysis for testing and monitoring of bridges and special structures*. PhD thesis, University of Porto, 2010.

[62] F. Ubertini, G. Comanducci, N. Cavalagli, A. L. Pisello, A. L. Materazzi, and F. Cotana. Environmental effects on natural frequencies of the San Pietro bell tower in Perugia, Italy, and their removal for structural performance assessment. *Mechanical Systems and Signal Processing*, 82:307–322, 2017.

[63] Hoon Sohn, Keith Worden, and Charles R. Farrar. Statistical damage classification under changing environmental and operational conditions. *Journal of intelligent material systems and structures*, 13(9):561–574, 2002.

[64] Ian Flood and Nabil Kartam. Neural networks in civil engineering. II: Systems and application. *Journal of computing in civil engineering*, 8(2):149–162, 1994.

[65] Rolands Kromanis and Prakash Kripakaran. Support vector regression for anomaly detection from measurement histories. *Advanced Engineering Informatics*, 27(4):486–495, 2013.

[66] Khaoula Ghoulem, Tarek Kormi, and Nizar Bel Hadj Ali. Damage detection in nonlinear civil structures using kernel principal component analysis. *Advances in Structural Engineering*, 23(11):2414–2430, 2020.

[67] Arnaud Deraemaeker and Keith Worden. A comparison of linear approaches to filter out environmental effects in structural health monitoring. *Mechanical systems and signal processing*, 105:1–15, 2018.

[68] H. F. Zhou, Y. Q. Ni, and J. M. Ko. Eliminating temperature effect in vibration-based structural damage detection. *Journal of Engineering Mechanics*, 137(12):785–796, 2011.

[69] Eloi Figueiredo, Joaquim Figueiras, Gyuhae Park, Charles R. Farrar, and Keith Worden. Influence of the autoregressive model order on damage detection. *Computer-Aided Civil and Infrastructure Engineering*, 26(3):225–238, 2011.

[70] Emanuel Sousa Tomé, Mário Pimentel, and Joaquim Figueiras. Damage detection under environmental and operational effects using cointegration analysis-application to experimental data from a cable-stayed bridge. *Mechanical Systems and Signal Processing*, 135:106386, 2020.

[71] Enrique García-Macías and Filippo Ubertini. Statistical process control procedures for online damage detection of a monumental masonry palace: the Consoli Palace in Gubbio, Italy. In *XI International Conference on Structural Dynamics EURODYN 2020*, 2020.

[72] Valentina Giglioni, Enrique García-Macías, Ilaria Venanzi, Laura Ierimonti, and Filippo Ubertini. The use of receiver operating characteristic curves and precision-versus-recall curves as performance metrics in unsupervised structural damage classification under changing environment. *Engineering Structures*, 246:113029, 2021.

[73] Trevor Hastie, Robert Tibshirani, and Martin Wainwright. *Statistical learning with sparsity: the lasso and generalizations*. Chapman and Hall/CRC, 2019.

[74] Bradley Efron, Trevor Hastie, Iain Johnstone, and Robert Tibshirani. Least angle regression. *Annals of statistics*, 32(2):407–499, 2004.

[75] Gideon Schwarz. Estimating the dimension of a model. *The annals of statistics*, pages 461–464, 1978.

[76] Hirotugu Akaike. On entropy maximization principle, Applications of Statistics. In *Proceedings of the Symposium held at Wright State University*, pages 27–41. North-Holland Publishing Company, 1977.

[77] Christopher M. Bishop. *Pattern recognition and machine learning*. springer, 2006.

[78] H. Hotteling. Multivariate quality control, illustrated by the air testing of sample bombsights. *Techniques of statistical analysis*, pages 111–184, 1947.

[79] Ronald B. Crosier. Multivariate generalizations of cumulative sum quality-control schemes. *Technometrics*, 30(3):291–303, 1988.

[80] Cynthia A. Lowry, William H. Woodall, Charles W. Champ, and Steven E. Rigdon. A multivariate exponentially weighted moving average control chart. *Technometrics*, 34(1):46–53, 1992.

[81] Rebecca Killick, Paul Fearnhead, and Idris A. Eckley. Optimal detection of changepoints with a linear computational cost. *Journal of the American Statistical Association*, 107(500):1590–1598, 2012.

[82] Claus Peter Fritzen. Vibration–based structural health monitoring–concepts and applications. In *Key Engineering Materials*, volume 293, pages 3–20. Trans Tech Publ, 2005.

[83] Filipe Magalhães and Álvaro Cunha. Explaining operational modal analysis with data from an arch bridge. *Mechanical Systems and Signal Processing*, 25(5):1431–1450, 2011.

[84] William Soo Lon Wah, Y. T. Chen, Gethin Wyn Roberts, and Ahmed Elamin. Separating damage from environmental effects affecting civil structures for near real-time damage detection. *Structural Health Monitoring*, 17(4):850–868, 2018.

[85] Qian Sun, W. J. Yan, W. X. Ren, and L. L. Liu. Application of transmissibility measurements to operational modal analysis of railway, highway, and pedestrian cable-stayed bridges. *Measurement*, 148:106880, 2019.

[86] Sergio Pereira, Filipe Magalhães, Jorge P Gomes, Álvaro Cunha, and José V Lemos. Dynamic monitoring of a concrete arch dam during the first filling of the reservoir. *Engineering Structures*, 174:548–560, 2018.

[87] Hyo Seon Park and Byung Kwan Oh. Real-time structural health monitoring of a supertall building under construction based on visual modal identification strategy. *Automation in Construction*, 85:273–289, 2018.

[88] Sandro Diord, Filipe Magalhães, Álvaro Cunha, and Elsa Caetano. High spatial resolution modal identification of a stadium suspension roof: Assessment of the estimates uncertainty and of modal contributions. *Engineering Structures*, 135:117–135, 2017.

[89] K. Soal, Y. Govers, J. Bienert, and A. Bekker. System identification and tracking using a statistical model and a kalman filter. *Mechanical Systems and Signal Processing*, 133:106127, 2019.

[90] Daiju Uehara and Jayant Sirohi. Full-field optical deformation measurement and operational modal analysis of a flexible rotor blade. *Mechanical Systems and Signal Processing*, 133:106265, 2019.

[91] Bruno J. A. Costa, Filipe Magalhães, Álvaro Cunha, and Joaquim Figueiras. Rehabilitation assessment of a centenary steel bridge based on modal analysis. *Engineering Structures*, 56:260–272, 2013.

[92] Pablo Pachón, Rafael Castro, Enrique García-Macías, Víctor Compan, and Esther Puertas. E. Torroja's bridge: Tailored experimental setup for SHM of a historical bridge with a reduced number of sensors. *Engineering Structures*, 162:11–21, 2018.

[93] Salvador Ivorra, Dora Foti, Valentina Gallo, Vitantonio Vacca, and David Bru. Bell's dynamic interaction on a reinforced concrete bell tower. *Engineering Structures*, 183:965–975, 2019.

[94] Luis F Ramos, Rafael Aguilar, and Paulo B Lourenço. Operational modal analysis of historical constructions using commercial wireless platforms. *Structural Health Monitoring*, 10(5):511–521, 2011.

[95] David L. Brown, Randall J. Allemang, Ray Zimmerman, and Mq Mergeay. Parameter estimation techniques for modal analysis. *SAE transactions*, pages 828–846, 1979.

[96] Samir R. Ibrahim and E. C. Mikulcik. A method for the direct identification of vibration parameters from the free response. *The Shock and Vibration Inform. Ctr. Shock and Vibration Bull. Part. 4: Sep. 1977*, 1977.

[97] Harvard Vold, John Kundrat, G. Thomas Rocklin, and Richard Russell. A multi-input modal estimation algorithm for mini-computers. *SAE Transactions*, pages 815–821, 1982.

[98] Jer-Nan Juang and Richard S. Pappa. An eigensystem realization algorithm for modal parameter identification and model reduction. *Journal of guidance, control, and dynamics*, 8(5):620–627, 1985.

[99] Palle Andersen. *Identification of civil engineering structures using vector ARMA models*. PhD thesis, Andersen1997, 1997.

[100] S. R. Ibrahim. Random decrement technique for modal identification of structures. *Journal of Spacecraft and Rockets*, 14(11):696–700, 1977.

[101] Peter Van Overschee and BL0888 De Moor. *Subspace identification for linear systems: Theory–Implementation–Applications*. Springer Science & Business Media, 2012.

[102] Sun-Yuan Kung. A new identification and model reduction algorithm via singular value decomposition. In *Proc. 12th Asilomar Conference on Circuits, Systems and Computers, Pacific Grove*, 1978.

[103] Fariba Abazarsa, Fariborz Nateghi, S. Farid Ghahari, and Ertugrul Taciroglu. Blind modal identification of non-classically damped systems from free or ambient vibration records. *Earthquake Spectra*, 29(4):1137–1157, 2013.

[104] Ka-Veng Yuen and Lambros S. Katafygiotis. Bayesian time-domain approach for modal updating using ambient data. *Probabilistic Engineering Mechanics*, 16(3):219–231, 2001.

[105] Julius S. Bendat and Allan G. Piersol. *Engineering applications of correlation and spectral analysis*. John Wiley & Sons, 1980.

[106] Rune Brincker, Lingmi Zhang, and Palle Andersen. Modal identification from ambient responses using frequency domain decomposition. In *18th international modal analysis conference (IMAC)*, volume 1, pages 625–630. San Antonio, TX, USA, 2000.

[107] Rune Brincker, Carlos E. Ventura, and Palle Andersen. Damping estimation by frequency domain decomposition. In *IMAC 19: A Conference on Structural Dynamic*, pages 698–703. Society for Experimental Mechanics, 2001.

[108] Bart Peeters and Herman Van der Auweraer. PolyMAX: a revolution in operational modal analysis. In *Proceedings of the 1st International Operational Modal Analysis Conference, Copenhagen, Denmark*, pages 26–27, 2005.

[109] Siu-Kui Au. Fast Bayesian FFT method for ambient modal identification with separated modes. *Journal of Engineering Mechanics*, 137(3):214–226, 2011.

[110] Morteza Ghalishooyan and Ahmad Shooshtari. Operational modal analysis techniques and their theoretical and practical aspects: a comprehensive review and introduction. In *6th International Operatiional Modal Analysis Conference IOMAC*, 2015.

[111] Fahad Bin Zahid, Zhi Chao Ong, and Shin Yee Khoo. A review of operational modal analysis techniques for in-service modal identification. *Journal of the Brazilian Society of Mechanical Sciences and Engineering*, 42(8):1–18, 2020.

[112] Wei Guan, L. L. Dong, J. M. Zhou, Yi Han, and J. Zhou. Data-driven methods for operational modal parameters identification: A comparison and application. *Measurement*, 132:238–251, 2019.

[113] S. K. Au, F. L. Zhang, and Y. C. Ni. Bayesian operational modal analysis: theory, computation, practice. *Computers & Structures*, 126:3–14, 2013.

[114] Carlo Rainieri and Giovanni Fabbrocino. Automated output-only dynamic identification of civil engineering structures. *Mechanical Systems and Signal Processing*, 24(3):678–695, 2010.

[115] Filipe Magalhães, Álvaro Cunha, and Elsa Caetano. Online automatic identification of the modal parameters of a long span arch bridge. *Mechanical Systems and Signal Processing*, 23(2):316–329, 2009.

[116] Giacomo Zini, Michele Betti, and Gianni Bartoli. A quality-based automated procedure for operational modal analysis. *Mechanical Systems and Signal Processing*, 164:108173, 2022.

[117] P. É. Charbonnel. Fuzzy-driven strategy for fully automated modal analysis: Application to the SMART2013 shaking-table test campaign. *Mechanical Systems and Signal Processing*, 152:107388, 2021.

[118] P. Cheema, M. Makki Alamdari, G. A. Vio, F. L. Zhang, and C. W. Kim. Infinite mixture models for operational modal analysis: An automated and principled approach. *Journal of Sound and Vibration*, 491:115757, 2021.

[119] Yi He, Judy P. Yang, and X. F. Li. A three-stage automated modal identification framework for bridge parameters based on frequency uncertainty and density clustering. *Engineering Structures*, 255:113891, 2022.

[120] E. M. Tronci, M. De Angelis, R. Betti, and V. Altomare. Multi-stage semi-automated methodology for modal parameters estimation adopting parametric system identification algorithms. *Mechanical Systems and Signal Processing*, 165:108317, 2022.

[121] Jyrki Kullaa. Damage detection of the Z24 bridge using control charts. *Mechanical Systems and Signal Processing*, 17(1):163–170, 2003.

[122] A. M. Yan, Gaëtan Kerschen, P. De Boe, and J. C. Golinval. Structural damage diagnosis under varying environmental conditions–part II: local PCA for non-linear cases. *Mechanical Systems and Signal Processing*, 19(4):865–880, 2005.

[123] W. H. Hu, D. H. Tang, Jun Teng, Samir Said, and Rolf Rohrmann. Structural health monitoring of a prestressed concrete bridge based on statistical pattern recognition of continuous dynamic measurements over 14 years. *Sensors*, 18(12):4117, 2018.

[124] E. García-Macías, A. Ruccolo, M. Angelo Zanini, C. Pellegrino, C. Gentile, F. Ubertini, and P. Mannella. P3P – A software suite for autonomous SHM of bridge networks. *Under Review*. *Journal of Civil Structural Health Monitoring*, 2022.

[125] J. N. Juang. *Applied system identification*. Prentice-Hall, Inc., Englewood Cliffs, NJ, USA, 1994.

[126] Carlo Rainieri and Giovanni Fabbrocino. Operational modal analysis of civil engineering structures. *Springer, New York*, 142:143, 2014.

[127] Rune Brincker, Lingmi Zhang, and Palle Andersen. Modal identification of output-only systems using frequency domain decomposition. *Smart materials and structures*, 10(3):441, 2001.

[128] S. R. Ibrahim. The experimental determination of vibration parameters from time responses. *Shock Vibration Bull.*, 46(5):187–196, 1976.

[129] Edwin Reynders, Guido De Roeck, and Geert Degrande. System identification and modal analysis in structural mechanics. In *National Congress*

on Theoretical and Applied Mechanics, Date: 2012/05/09-2012/05/10, Location: Brussels, Belgium, 2012.

[130] Edwin Reynders and Guido De Roeck. Reference-based combined deterministic-stochastic subspace identification for experimental and operational modal analysis. *Mechanical Systems and Signal Processing*, 22(3):617–637, 2008.

[131] Richard S. Pappa, Kenny B. Elliott, and Axel Schenk. Consistent-mode indicator for the eigensystem realization algorithm. *Journal of Guidance, Control, and Dynamics*, 16(5):852–858, 1993.

[132] Carlo Rainieri and Giovanni Fabbrocino. Influence of model order and number of block rows on accuracy and precision of modal parameter estimates in stochastic subspace identification. *International Journal of Lifecycle Performance Engineering 10*, 1(4):317–334, 2014.

[133] Elia Favarelli and Andrea Giorgetti. Machine learning for automatic processing of modal analysis in damage detection of bridges. *IEEE Transactions on Instrumentation and Measurement*, 70:1–13, 2020.

[134] EMPA work package. SIMCES Task A1 & A2 Longterm Monitoring and Bridge Tests. Technical report, Dübendorf, Switzerland, 1999.

[135] Lawrence A. Klein. *Sensor and data fusion: a tool for information assessment and decision making*, volume 138. SPIE press, 2004.

[136] R. T. Wu and Mohammad Reza Jahanshahi. Data fusion approaches for structural health monitoring and system identification: past, present, and future. *Structural Health Monitoring*, 19(2):552–586, 2020.

[137] Erdal Şafak. Wave-propagation formulation of seismic response of multistory buildings. *Journal of Structural Engineering*, 125(4):426–437, 1999.

[138] M. D. Trifunac, S. S. Ivanović, and M. I. Todorovska. Wave propagation in a seven-story reinforced concrete building: III. Damage detection via changes in wavenumbers. *Soil Dynamics and Earthquake Engineering*, 23(1):65–75, 2003.

[139] S. S. Ivanovic, M. D. Trifunac, and M. D. Todorovska. On identification of damage in structures via wave travel times. In *Strong Motion Instrumentation for Civil Engineering Structures*, pages 447–467. Springer, 2001.

[140] Mahdi Ebrahimian, Mohammadtaghi Rahmani, and Maria I. Todorovska. Nonparametric estimation of wave dispersion in high-rise buildings by seismic interferometry. *Earthquake Engineering & Structural Dynamics*, 43(15):2361–2375, 2014.

[141] R. Snieder and E. Şafak. Extracting the building response using seismic interferometry: Theory and application to the Millikan Library in Pasadena, California. *Bulletin of the Seismological Society of America*, 96(2):586–598, 2006.

[142] Maria I. Todorovska and Mihailo D. Trifunac. Impulse response analysis of the Van Nuys 7-storey hotel during 11 earthquakes and earthquake damage detection. *Structural Control and Health Monitoring: The Official Journal of the International Association for Structural Control and Monitoring and of the European Association for the Control of Structures*, 15(1):90–116, 2008.

[143] Nori Nakata and Roel Snieder. Monitoring a building using deconvolution interferometry. II: Ambient-vibration analysis. *Bulletin of the Seismological Society of America*, 104(1):204–213, 2013.

[144] German A. Prieto, Jesse F. Lawrence, Angela I. Chung, and Monica D. Kohler. Impulse response of civil structures from ambient noise analysis. *Bulletin of the Seismological Society of America*, 100(5A):2322–2328, 2010.

[145] G. Lacanna, M. Ripepe, M. Coli, R. Genco, and E. Marchetti. Full structural dynamic response from ambient vibration of Giotto's bell tower in Firenze (Italy), using modal analysis and seismic interferometry. *NDT & E International*, 102:9–15, 2019.

[146] Enrique García-Macías and Filippo Ubertini. Seismic interferometry for earthquake-induced damage identification in historic masonry towers. *Mechanical Systems and Signal Processing*, 132:380–404, 2019.

[147] Enrique García-Macías and Filippo Ubertini. Automated operational modal analysis and ambient noise deconvolution interferometry for the full structural identification of historic towers: A case study of the Sciri Tower in Perugia, Italy. *Engineering Structures*, 215:110615, 2020.

[148] Enrique Garcia-Macias, Alban Kita, and Filippo Ubertini. Synergistic application of operational modal analysis and ambient noise deconvolution interferometry for structural and damage identification in historic masonry structures: three case studies of Italian architectural heritage. *Structural Health Monitoring*, 19(4):1250–1272, 2020.

[149] Enrique García-Macías and Filippo Ubertini. Structural assessment of bridges through ambient noise deconvolution interferometry: application to the lateral dynamic behaviour of a RC multi-span viaduct. *Archives of Civil and Mechanical Engineering*, 21(3):1–20, 2021.

[150] Roel Snieder, Masatoshi Miyazawa, Evert Slob, Ivan Vasconcelos, and Kees Wapenaar. A comparison of strategies for seismic interferometry. *Surveys in Geophysics*, 30(4-5):503–523, 2009.

[151] Maria I. Todorovska and Mohammad T. Rahmani. System identification of buildings by wave travel time analysis and layered shear beam models–Spatial resolution and accuracy. *Structural Control and Health Monitoring*, 20(5):686–702, 2013.

[152] Mahdi Ebrahimian and Maria I. Todorovska. Wave propagation in a Timoshenko beam building model. *Journal of Engineering Mechanics*, 140(5):04014018, 2013.

[153] Jie Zhang, Edwin Reynders, Guido De Roeck, and Geert Lombaert. Model updating of periodic structures based on free wave characteristics. *Journal of Sound and Vibration*, 442:281–307, 2019.

[154] European Committee. Eurocode 4 EN 1994-1-1. Design of composite steel and concrete structures. *European Committee: Brussels, Belgium*, 2004.

[155] Mohammadtaghi Rahmani and Maria I. Todorovska. 1D system identification of buildings during earthquakes by seismic interferometry with waveform inversion of impulse responses–method and application to Millikan library. *Soil Dynamics and Earthquake Engineering*, 47:157–174, 2013.

[156] Julius Miklowitz. *The theory of elastic waves and waveguides*, volume 22. Elsevier, 2015.

[157] Hao Sun, Aurélien Mordret, Germán A. Prieto, M. Nafi Toksöz, and Oral Büyüköztürk. Bayesian characterization of buildings using seismic interferometry on ambient vibrations. *Mechanical Systems and Signal Processing*, 85:468–486, 2017.

[158] Nizar Faisal Alkayem, Maosen Cao, Yufeng Zhang, Mahmoud Bayat, and Zhongqing Su. Structural damage detection using finite element model updating with evolutionary algorithms: a survey. *Neural Computing and Applications*, 30(2):389–411, 2018.

[159] Tshilidzi Marwala. *Finite-element-model updating using computional intelligence techniques: Applications to structural dynamics*. Springer, 2010.

[160] Michael I. Friswell, John E. Mottershead, and Hamid Ahmadian. Finite-element model updating using experimental test data: parametrization

and regularization. *Philosophical Transactions of the Royal Society of London. Series A: Mathematical, Physical and Engineering Sciences*, 359(1778):169–186, 2001.

[161] B. Titurus and M. I. Friswell. Regularization in model updating. *International Journal for numerical methods in engineering*, 75(4):440–478, 2008.

[162] X. W. Zheng, H. N. Li, H. L. Lv, L. S. Huo, and Y. Y. Zhang. Bayesian-based seismic resilience assessment for high-rise buildings with the uncertainty in various variables. *Journal of Building Engineering*, page 104321, 2022.

[163] K. V. Yuen. *Bayesian methods for structural dynamics and civil engineering*. John Wiley & Sons, 2010.

[164] Yong Huang, Changsong Shao, Biao Wu, James L. Beck, and Hui Li. State-of-the-art review on Bayesian inference in structural system identification and damage assessment. *Advances in Structural Engineering*, 22(6):1329–1351, 2019.

[165] H. F. Lam, J. H. Yang, and S. K. Au. Markov chain Monte Carlo-based Bayesian method for structural model updating and damage detection. *Structural Control and Health Monitoring*, 25(4):e2140, 2018.

[166] Sai Hung Cheung and Sahil Bansal. A new Gibbs sampling based algorithm for Bayesian model updating with incomplete complex modal data. *Mechanical Systems and Signal Processing*, 92:156–172, 2017.

[167] Adolphus Lye, Alice Cicirello, and Edoardo Patelli. Sampling methods for solving Bayesian model updating problems: A tutorial. *Mechanical Systems and Signal Processing*, 159:107760, 2021.

[168] Roberto Rocchetta, Matteo Broggi, Quentin Huchet, and Edoardo Patelli. On-line Bayesian model updating for structural health monitoring. *Mechanical Systems and Signal Processing*, 103:174–195, 2018.

[169] Daniel Straub and Iason Papaioannou. Bayesian updating with structural reliability methods. *Journal of Engineering Mechanics*, 141(3):04014134, 2015.

[170] Lei Xu, Maomao Hu, and Cheng Fan. Probabilistic electrical load forecasting for buildings using Bayesian deep neural networks. *Journal of Building Engineering*, 46:103853, 2022.

[171] Jin Luo, Minshui Huang, Chunyan Xiang, and Yongzhi Lei. Bayesian damage identification based on autoregressive model and MH-PSO hybrid

MCMC sampling method. *Journal of Civil Structural Health Monitoring*, 12(2):361–390, 2022.

[172] Jian Li, Yong Huang, and Parisa Asadollahi. Sparse Bayesian learning with model reduction for probabilistic structural damage detection with limited measurements. *Engineering Structures*, 247:113183, 2021.

[173] Mayank Mishra, Paulo B. Lourenço, and Gunturi Venkata Ramana. Structural health monitoring of civil engineering structures by using the internet of things: A review. *Journal of Building Engineering*, page 103954, 2022.

[174] Mayank Mishra. Machine learning techniques for structural health monitoring of heritage buildings: A state-of-the-art review and case studies. *Journal of Cultural Heritage*, 47:227–245, 2021.

[175] Souvik Chakraborty, Sondipon Adhikari, and Ranjan Ganguli. The role of surrogate models in the development of digital twins of dynamic systems. *Applied Mathematical Modelling*, 90:662–681, 2021.

[176] Manuel Chiachío, María Megía, Juan Chiachío, Juan Fernandez, and María L. Jalón. Structural digital twin framework: Formulation and technology integration. *Automation in Construction*, 140:104333, 2022.

[177] Fei Tao, He Zhang, Ang Liu, and Andrew Y. C. Nee. Digital twin in industry: State-of-the-art. *IEEE Transactions on industrial informatics*, 15(4):2405–2415, 2018.

[178] Grigor Angjeliu, Dario Coronelli, and Giuliana Cardani. Development of the simulation model for Digital Twin applications in historical masonry buildings: The integration between numerical and experimental reality. *Computers & Structures*, 238:106282, 2020.

[179] Wei Zhao, Feng Fan, and Wei Wang. Non-linear partial least squares response surface method for structural reliability analysis. *Reliability Engineering & System Safety*, 161:69–77, 2017.

[180] Géraud Blatman and Bruno Sudret. An adaptive algorithm to build up sparse polynomial chaos expansions for stochastic finite element analysis. *Probabilistic Engineering Mechanics*, 25(2):183–197, 2010.

[181] J. M. Bourinet. Rare-event probability estimation with adaptive support vector regression surrogates. *Reliability Engineering & System Safety*, 150:210–221, 2016.

[182] Zeyu Wang and Abdollah Shafieezadeh. Highly efficient Bayesian updating using metamodels: An adaptive Kriging-based approach. *Structural Safety*, 84:101915, 2020.

[183] Pinghe Ni, Jun Li, Hong Hao, Qiang Han, and Xiuli Du. Probabilistic model updating via variational Bayesian inference and adaptive Gaussian process modeling. *Computer Methods in Applied Mechanics and Engineering*, 383:113915, 2021.

[184] Dimitris G. Giovanis, Iason Papaioannou, Daniel Straub, and Vissarion Papadopoulos. Bayesian updating with subset simulation using artificial neural networks. *Computer Methods in Applied Mechanics and Engineering*, 319:124–145, 2017.

[185] Chiara Pepi, Massimiliano Gioffre, and Mircea Grigoriu. Bayesian inference for parameters estimation using experimental data. *Probabilistic Engineering Mechanics*, 60:103025, 2020.

[186] Felix Schneider, Iason Papaioannou, Daniel Straub, Christoph Winter, and Gerhard Müller. Bayesian parameter updating in linear structural dynamics with frequency transformed data using rational surrogate models. *Mechanical Systems and Signal Processing*, 166:108407, 2022.

[187] Alessandro Cabboi, Carmelo Gentile, and Antonella Saisi. From continuous vibration monitoring to FEM-based damage assessment: application on a stone-masonry tower. *Construction and Building Materials*, 156:252–265, 2017.

[188] Enrique García-Macías, Laura Ierimonti, Ilaria Venanzi, and Filippo Ubertini. An innovative methodology for online surrogate-based model updating of historic buildings using monitoring data. *International Journal of Architectural Heritage*, pages 1–21, 2019.

[189] Enrique García-Macías and Filippo Ubertini. Real-time Bayesian damage identification enabled by sparse PCE-Kriging meta-modelling for continuous SHM of large-scale civil engineering structures. *Journal of Building Engineering*, page 105004, 2022.

[190] E. García-Macías, I. A. Hernández-González, E. Puertas, R. Gallego, R. Castro-Triguero, and F. Ubertini. Digital twin for vibration-based damage identification of a 13th-century rammed earth tower in the Alhambra monumental complex in Granada, Spain. *Under review. International Journal of Architectural Heritage*, 2022.

[191] Xin Zhou, Chul-Woo Kim, Feng-Liang Zhang, and K. C. Chang. Vibration-based bayesian model updating of an actual steel truss bridge subjected to incremental damage. *Engineering Structures*, 260:114226, 2022.

[192] Costas Argyris, Costas Papadimitriou, Panagiotis Panetsos, and Panos Tsopelas. Bayesian model–updating using features of modal data: Application to the Metsovo Bridge. *Journal of Sensor and Actuator Networks*, 9(2):27, 2020.

[193] Laura Ierimonti, Nicola Cavalagli, Ilaria Venanzi, Enrique García-Macías, and Filippo Ubertini. A transfer Bayesian learning methodology for structural health monitoring of monumental structures. *Engineering Structures*, 247:113089, 2021.

[194] Jinwoo Jang and Andrew Smyth. Bayesian model updating of a full-scale finite element model with sensitivity-based clustering. *Structural Control and Health Monitoring*, 24(11):e2004, 2017.

[195] H. F. Lam, Jiahua Yang, and S. K. Au. Bayesian model updating of a coupled-slab system using field test data utilizing an enhanced Markov chain Monte Carlo simulation algorithm. *Engineering Structures*, 102:144–155, 2015.

[196] Heikki Haario, Marko Laine, Antonietta Mira, and Eero Saksman. DRAM: efficient adaptive MCMC. *Statistics and computing*, 16(4):339–354, 2006.

[197] Andrew Gelman, John B. Carlin, Hal S. Stern, David B. Dunson, Aki Vehtari, and Donald B. Rubin. *Bayesian data analysis*. CRC press, 2013.

[198] Mehdi Nobahari and Seyed Mohammad Seyedpoor. An efficient method for structural damage localization based on the concepts of flexibility matrix and strain energy of a structure. *Structural Engineering and Mechanics*, 46(2):231–244, 2013.

[199] H. Ahmadian, G. M. L. Gladwell, and F. Ismail. Parameter selection strategies in finite element model updating. *Journal of Vibration and Acoustics*, 119(1):37–45, 1997.

[200] H. P. Wan and W. X. Ren. Parameter selection in finite-element-model updating by global sensitivity analysis using Gaussian process metamodel. *Journal of Structural Engineering*, 141(6):04014164, 2015.

[201] Daniel T. Bartilson, Jinwoo Jang, and Andrew W. Smyth. Finite element model updating using objective-consistent sensitivity-based parameter clustering and Bayesian regularization. *Mechanical Systems and Signal Processing*, 114:328–345, 2019.

[202] F. E. A. Abaqus. Abaqus analysis user's manual. *Dassault Systemes, Vélizy-Villacoublay, France*, 2009.

[203] Daniel T. Bartilson, Jinwoo Jang, and Andrew W. Smyth. Sensitivity-based singular value decomposition parametrization and optimal regularization in finite element model updating. *Structural Control and Health Monitoring*, 27(6):e2539, 2020.

[204] Robert R. Sokal. A statistical method for evaluating systematic relationships. *Univ. Kansas, Sci. Bull.*, 38:1409–1438, 1958.

[205] J. Lubliner, J. Oliver, Sand Oller, and E. Oñate. A plastic-damage model for concrete. *International Journal of Solids and Structures*, 25(3):299–326, 1989.

[206] Jeeho Lee and Gregory L. Fenves. Plastic-damage model for cyclic loading of concrete structures. *Journal of Engineering Mechanics*, 124(8):892–900, 1998.

[207] Reza Alizadeh, Janet K. Allen, and Farrokh Mistree. Managing computational complexity using surrogate models: a critical review. *Research in Engineering Design*, 31(3):275–298, 2020.

[208] Nestor V. Queipo, Raphael T. Haftka, Wei Shyy, Tushar Goel, Rajkumar Vaidyanathan, and P. Kevin Tucker. Surrogate-based analysis and optimization. *Progress in aerospace sciences*, 41(1):1–28, 2005.

[209] J. N. Fuhg, Amélie Fau, and Udo Nackenhorst. State-of-the-art and comparative review of adaptive sampling methods for Kriging. *Archives of Computational Methods in Engineering*, pages 1–59, 2020.

[210] Sushant S. Garud, Iftekhar A. Karimi, and Markus Kraft. Design of computer experiments: A review. *Computers & Chemical Engineering*, 106:71–95, 2017.

[211] Haitao Liu, Y. S. Ong, and Jianfei Cai. A survey of adaptive sampling for global metamodeling in support of simulation-based complex engineering design. *Structural and Multidisciplinary Optimization*, 57(1):393–416, 2018.

[212] Raymond H Myers, Douglas C Montgomery, and Christine M Anderson-Cook. *Response surface methodology: process and product optimization using designed experiments*. John Wiley & Sons, 4th edition, 2016.

[213] Ilaria Venanzi, Alban Kita, Nicola Cavalagli, Laura Ierimonti, and Filippo Ubertini. Continuous OMA for Damage Detection and Localization in the Sciri tower in Perugia, Italy. In *Proceedings of the 8th International Operational Modal Analysis Conference (IOMAC), Copenhagen, Denmark, 2019*, 13th - 15th May 2019.

[214] Z. H. Han and K. S. Zhang. Surrogate-based optimization. In *Real-world applications of genetic algorithms*. IntechOpen, 2012.

[215] Georges Matheron. Principles of geostatistics. *Economic geology*, 58(8):1246–1266, 1963.

[216] Michael L. Stein. *Interpolation of spatial data: some theory for kriging*. Springer Science & Business Media, 2012.

[217] Søren Nymand Lophaven, Hans Bruun Nielsen, and Jacob Søndergaard. DACE-A Matlab Kriging toolbox, version 2.0. Technical report, Technical University of Denmark, 2002.

[218] Jerome Sacks, William J. Welch, Toby J. Mitchell, and Henry P. Wynn. Design and analysis of computer experiments. *Statistical science*, 4(4):409–423, 1989.

[219] Christian Soize and Roger Ghanem. Physical systems with random uncertainties: chaos representations with arbitrary probability measure. *SIAM Journal on Scientific Computing*, 26(2):395–410, 2004.

[220] Norbert Wiener. The homogeneous chaos. *American Journal of Mathematics*, 60(4):897–936, 1938.

[221] Dongbin Xiu and George Em Karniadakis. The Wiener–Askey polynomial chaos for stochastic differential equations. *SIAM journal on scientific computing*, 24(2):619–644, 2002.

[222] Géraud Blatman and Bruno Sudret. Adaptive sparse polynomial chaos expansion based on least angle regression. *Journal of computational Physics*, 230(6):2345–2367, 2011.

[223] Vladimir Vapnik. *The nature of statistical learning theory*. Springer Science & Business Media, 2013.

[224] Olivier Chapelle, Vladimir Vapnik, and Yoshua Bengio. Model selection for small sample regression. *Machine Learning*, 48(1):9–23, 2002.

[225] Edwin Reynders, Mattias Schevenels, and Guido De Roeck. Macec 3.2: A matlab toolbox for experimental and operational modal analysis-user's manual. *Katholieke Universiteit, Leuven*, 2011.

[226] L. M. S. Test. Lab modal analysis user manual. *Siemens Industry Software NV*, 2015.

[227] SVS. *ARTeMIS Extractor Pro User's Manual, Release 3.5*. Structural Vibration Solutions A/S, 2006.

[228] Yongchao Yang and Satish Nagarajaiah. Blind denoising of structural vibration responses with outliers via principal component pursuit. *Structural Control and Health Monitoring*, 21(6):962–978, 2014.

[229] Abel Folch-Fortuny, Francisco Arteaga, and Alberto Ferrer. PCA model building with missing data: New proposals and a comparative study. *Chemometrics and Intelligent Laboratory Systems*, 146:77–88, 2015.

[230] Mahdi Ebrahimian and Maria I. Todorovska. Structural system identification of buildings by a wave method based on a nonuniform Timoshenko beam model. *Journal of Engineering Mechanics*, 141(8):04015022, 2015.

[231] Freeman Gilbert and George E. Backus. Propagator matrices in elastic wave and vibration problems. *Geophysics*, 31(2):326–332, 1966.